Characterization of magnetic nanoparticles as contrast agents and their application for quantitative magnetic susceptibility monitoring of the waterflooding of heavy oil in real time

by

Petar Anatoliev Petrov

A thesis submitted in partial fulfillment of the requirements for the degree of

Doctor of Philosophy

in
Geophysics

Department of Physics
University of Alberta

ABSTRACT

Waterflooding is one enhanced oil recovery process used in heavy oil reservoirs such as at Cold Lake in North-Eastern Alberta. However, little has been published in terms of imaging heavy oil waterfloods, mainly due to the similar densities of water and heavy oil, which makes it difficult to track the process by methods such as computer tomography (CT) scanning. This thesis will first present the results of physical and magnetic characterization of four magnetic nanoparticle compositions for potential use as magnetic contrast agent tracers for tracking the waterflooding of a heavy oil saturated sandpack. The magnetic properties of the nanoparticles were examined at both room temperature and typical reservoir temperatures. The most favourable candidate nanoparticle composition subsequently underwent stability experiments in order to produce long term stable dispersed nanoparticle suspensions.

The magnetic nano-fluid was then used in experiments to track the waterflooding of a heavy oil saturated sandpack in real time using magnetic susceptibility scanning. Attempts to track the process were also undertaken with CT scanning for comparison. The successful waterflood 2 experiment revealed the formation, growth and movement of a significant positive magnetic susceptibility peak. This peak formed at the injection end of the flow cell and migrated towards the production end as the waterflooding progressed. The peak was likely due to the higher concentration of nanoparticles collecting at the main water-heavy oil interface(s). This result was significant as it provided a means to quantitatively track the progression of the waterflood in real time. The increased accumulation of nanoparticles at the water-heavy oil interface(s) was further supported by the material collected in the production jars. While the CT attenuation profiles showed some correspondence with the magnetic results, they were not able to track the progression of the waterflood, most likely due to the low CT contrast between the nano-fluid and

the heavy oil. Once the main water-heavy oil interface(s) had passed through the sandpack the magnetic profiles had a constant shape similar to the porosity profile (as determined by the CT derived porosity variation). The results suggested that the magnetic technique has potential for monitoring larger scale commercial waterflooding operations.

The potential retention of magnetic nanoparticles after water-flushing was also examined. These results were then compared to a case study where naturally occurring hematite nanoparticles in a tight gas reservoir were shown to have a detrimental effect on the reservoir quality by reducing the permeability. The comparison showed that the concentrations of retained nanoparticles in a series of laboratory water flushing experiments were significantly less than the concentrations causing the detrimental effects in the tight gas reservoir case study.

A further study was conducted on the magnetic properties of hematite nanoparticles. Although hematite nanoparticles were initially considered as possible magnetic contrast agent tracers for reservoir characterization, one sample exhibited an unexpected diamagnetic magnetic susceptibility signal during initial room temperature measurements. A search of the literature also revealed another apparent “diamagnetic” result in another sample of hematite nanoparticles. These results were unusual as hematite is expected to have canted antiferromagnetic behaviour at room temperature. This led to an investigation of whether the hematite nanoparticles were behaving diamagnetically themselves or if the observed magnetic signal was due to the diamagnetic matrix overwhelming a weak canted antiferromagnetic signal from the hematite nanoparticles. After comprehensively investigating three different sizes of hematite nanoparticles it was concluded that the nanoparticles were not diamagnetic but that the “diamagnetic” magnetic susceptibility signal resulted from the diamagnetic matrix (in which the nanoparticles were dilutely dispersed) overwhelming the weak hematite signal.

PREFACE

This thesis is the original work by Petar Anatoliev Petrov. Any use of work conducted by other authors within this thesis is given proper acknowledgement at the point of their use.

The waterflood experiments in **Chapter 4** were done in collaboration with InnoTech Alberta (previously known as Alberta Innovates Technology Futures). During the collaboration the staff from InnoTech Alberta (Shauna Cameron, Mike London, James Donald, and Wade Waterman) were responsible for the collection and analysis of the computer tomography (CT) data, while I collected and analyzed the magnetic susceptibility data for the imaging of the waterflooding of heavy oil.

PUBLICATIONS ARISING FROM THIS THESIS

Parts of **Chapter 4** of this thesis have been published as:

Petrov, P. A., Potter, D. K., Cameron, S., London, M., Donald., J., and Waterman, W., 2015. Combined CT and magnetic scanning techniques for multimodal imaging of fluid flow in porous media: application to heavy oil waterflooding. Proceedings of the International Symposium of the Society of Core Analysts, St. John’s, Canada, SCA2015-012 (12 pages).

A version of **Chapter 6** has been published as:

Petrov, P. A., Ali, A., and Potter, D. K., 2017. Diamagnetic behavior in nanoparticle hematite? Journal of Modern Physics, **8**, 1013-1019. (Part of the Special Issue on “Magnetism and Magnetic Materials”).

PAPERS IN PREPARATION

Petrov, P. A., Potter, D. K., Cameron, S., and London, M. Magnetic scanning technique for imaging of fluid flow in porous media: application to heavy oil waterflooding.

Potter, D. K., Ali, A., Petrov, P. A., and Ivakhnenko, O. P. Quantifying the roles of hematite and illite on the permeability in red and white sandstone reservoir rocks.

DEDICATION

This thesis is dedicated to my parents, Anatoliy Petrov and Anka Petrova, and to my sister, Martina Petrova, as well as my partner Carrie Ng.

ACKNOWLEDGEMENTS

Firstly, I would like to thank my supervisor Dr. David K. Potter for giving me the opportunity to pursue this degree. I am grateful for his support and invaluable insights over the course of my research. I am also grateful to the members of my defense committee Dr. Mark Freeman, Dr. Bruce Sutherland, Dr. Ergun Kuru and Dr. Steven Bryant for carefully reviewing my thesis.

I would like to thank Shauna Cameron, Mike London, James Donald and Wade Waterman from InnoTech Alberta for their collaboration. I would also like to thank InnoTech Alberta for providing the funding towards the waterflood experiments.

I am grateful to Dr. Douglas Schmitt for allowing the use of some of his laboratory equipment.

I would also like to thank my family, friends and my partner for their support over the course of my studies. I am grateful for their support and encouragement over the years.

TABLE OF CONTENTS

LIST OF TABLES

Chapter 2 MATERIALS, EQUIPMENT AND EXPERIMENTAL PROCEDURES

Chapter 3 CHARACTERIZATION OF MAGNETIC NANOPARTICLES FOR POTENTIAL RESERVOIR APPLICATIONS

Chapter 4 STABILITY AND WATERFLOOD EXPERIMENTS APPLYING MAGNETIC SUSCEPTIBILITY AND CT SCANNING

Chapter 5 THE EFFECT OF NATURAL HEMATITE NANOPARTICLES ON RESERVOIR QUALITY AND ESTIMATION OF POTENTIAL MAGHEMITE NANOPARTICLE RETENTION DURING FLUID FLOW EXPERMENTS IN POROUS MEDIA

LIST OF FIGURES

Chapter 1 INTRODUCTION

Chapter 2 MATERIALS, EQUIPMENT AND EXPERIMENTAL PROCEDURES

Chapter 3 CHARACTERIZATION OF MAGNETIC NANOPARTICLES FOR POTENTIAL RESERVOIR APPLICATIONS

Chapter 4 STABILITY AND WATERFLOOD EXPERIMENTS APPLYING MAGNETIC SUSCEPTIBILITY AND CT SCANNING

Chapter 5 THE EFFECT OF NATURAL HEMATITE NANOPARTICLES ON RESERVOIR QUALITY AND ESTIMATION OF POTENTIAL MAGHEMITE NANOPARTICLE RETENTION DURING FLUID FLOW EXPERMENTS IN POROUS MEDIA

Chapter 6 DIAMAGNETIC BEHAVIOUR IN NANOPARTICLE HEMATITE? 151

NOMENCLATURE

LIST OF SYMBOLS

D_N	Density of Suspended Nanoparticles
F_H	Fraction of Hematite in the Sample
F_I	Fraction of Illite in the Sample
F_Q	Fraction of Quartz in the Sample
φ	Porosity
g	Acceleration due to Gravity
H	Applied Magnetic Field
k	Permeability
m	Mass
M	Induced Magnetization
M_{IN}	Mass of the Initial Nanoparticles Used in Creating the Nano-Fluid Suspension
M_{RN}	Mass of the Retained Nanoparticles After Water Flush
M_{RS}	Remanent Magnetization
M_S	Saturation Magnetization
μ	Dynamic Viscosity
$N_{\%}$	Volume Percent Concentration of Retained Nanoparticles
$NI_{\%}$	Volume Percent Concentration of Injected Nanoparticles
ρ	Density
ρ_f	Density of the Fluid
ρ_p	Density of the Particle
R	Radius of the Particle
Sor	Residual Oil Saturation
Sorw	Residual Oil Saturation After Waterflood
T_C	Curie Temperature
V_t	Terminal Velocity
χ_d	Drift Corrected Magnetic Susceptibility
χ_H	Volume Magnetic Susceptibility of Naturally Occurring Hematite
χ_I	Volume Magnetic Susceptibility of Illite

χ_m	Mass Magnetic Susceptibility
χ_N	Volume Magnetic Susceptibility at Mid-Point of the Flow Cell After Nano-Fluid Injection
χ_Q	Volume Magnetic Susceptibility of Quartz
χ_{raw}	Raw Volume Magnetic Susceptibility
χ_T	Total Volume Magnetic Susceptibility of the Sample
χ_v	Volume Magnetic Susceptibility
χ_W	Volume Magnetic Susceptibility at Mid-Point of the Flow Cell After Water Flush

LIST OF UNITS

A	Amperes
Am^{-1}	Amperes per metre
Am^2kg^{-1}	Amperes Metre Squared per Kilogram
cc	Cubic Centimetre
cm^3	Cubic Centimetre
cm $year^{-1}$	Centimetres per year
CGS	Centimetre-Gram-Second System of Units
cP	Centipoise
D	Darcy
mD	MilliDarcy
emu	Electromagnetic Unit
emu g^{-1}	Electromagnetic Units per Gram
eV	Electronvolt
keV	Kiloelectronvolts
Hz	Hertz
kHz	Kilohertz
HU	Hounsfield Units
kg	Kilograms
g	Grams
g L^{-1}	Grams per Litre
mg	Milligrams

L	Litre
ml	Millilitre
m	Metres
mm	Millimetre
µm	Micron (Micrometre)
nm	Nanometre
$m\ s^{-1}$	Metres per Second
$mL\ hr^{-1}$	Millilitre per Hour
mol	Mole
$mol\ L^{-1}$	Mole per Litre
Oe	Oersted
ppm	Parts per Million
s	Seconds
SI	Système Internationale
T	Tesla
mT	Millitesla
µT	Microtesla
V	Volt

GLOSSARY OF TERMS

CT	Computer Tomography
DDBS	Sodium Dodecylbenzenesulfonate
DI	De-Ionized
EDS	Energy Dispersive Spectroscopy
EOR	Enhanced Oil Recovery
IFT	Interfacial Tension
PV	Pore Volume
SEM	Scanning Electron Microscope
TEM	Transmission Electron Microscope
VFTB	Variable Field Translation Balance
XRD	X-ray Diffraction

Chapter 1

INTRODUCTION

1.1 Nanotechnology and its Applications in Reservoir Studies

Nanotechnology is starting to be increasingly applied to hydrocarbon reservoir studies. The following sections will review some of the recent developments.

1.1.1 Nanoparticle Applications for Enhanced Oil Recovery (EOR)

The application of nanotechnology in enhanced oil recovery (EOR) has been attracting interest due to its cost-effectiveness and environmentally friendly impact. Due to their small size nanoparticles have the potential to be injected into reservoir rock to help improve oil recovery. There are a number of different enhancement mechanisms which depend on the chosen composition of the nanoparticles. The main mechanisms were summarized by Negin et al. (2016) as viscosity reduction, interfacial tension (IFT) reduction, wettability alteration and efficiency in sweep and displacement. Certain nanoparticles (such as aluminum oxide, copper (II) oxide, iron oxide, nickel oxide, polymer coated nanoparticles, ethanol and magnesium oxide) can help to reduce the viscosity of the oil in the reservoir, and thus increase its mobility. Such a mechanism could be very useful in reservoirs containing heavy oil. The IFT reduction nanoparticles (such as SiO_2, ferrofluids, polymer coated nanoparticles and others) function by reducing the surface tension between the different phases present. This can be beneficial as it can be applied to both water-wet and oil-wet reservoirs (Kothari et al., 2010). Wettability altering nanoparticles (such as tin oxide, hydrophobic silicon oxide, alumina coated silica nanoparticles and others) operate by altering the wettability of the formation. Application of wettability altering nanoparticles generally aims to alter the formation from an oil-wet to a water-wet setting. Such alterations should be done after vigorous testing of the reservoir conditions in the area of interest. Also some studies (Onyaekonwu and Ogolo, 2010) have shown that changing a weakly water-wet rock to a strongly water-wet rock can in fact be detrimental to the formation and result in a poor recovery factor. Sweep and displacement efficiency nanoparticles (such as polymer nanoparticles, polymer coated nanoparticles and nano-sized colloidal dispersion gels) are used as sweep improving agents for displacing oil with low mobility ratio.

There have been numerous studies examining the oil recovery results from the injection of different nano-fluids in oil saturated sandpacks. Ogolo et al. (2012) looked into nine different nanoparticle compositions (aluminum oxide, magnesium oxide, iron oxide, nickel oxide, zinc oxide, zirconium oxide, tin oxide, silane treated silicon oxide and hydrophobic silicon oxide) dispersed in three different substances (distilled water, brine and ethanol). They observed that oil recovery experienced a boost of between 0.8 to 12.5 % (depending on the nanoparticle composition) from the control experiment when the sandpack was injected with different nanoparticle compositions dispersed in distilled water. When using brine as a dispersing matrix the oil recovery behavior was more complex with a maximum increase of 5% when using aluminum oxide nanoparticles. The complication in this case was that not all nanoparticle compositions had a positive effect on the oil recovery, in fact four nano-fluid compositions (magnesium oxide, zinc oxide, zirconium oxide and tin oxide) had a detrimental effect on the oil recovery ranging between -2.5 to -4.2%. Using ethanol as a dispersing matrix led to even poorer results with only two nano-fluid compositions (silane treated silicon oxide and hydrophobic silicon oxide) having a positive impact on the oil recovery of 5% and 1.7% respectively. All other nano-fluids led to a decrease in the oil recovery of between -0.9 to -13.4 % depending on the nanoparticle composition. Another study by Ponmani et al. (2013) came to a similar conclusion. The general impact on oil recovery for nano-fluids dispersed in distilled water had a positive impact, nanoparticles dispersed in brine showed a variable result depending on the nanoparticle composition, while nanoparticles dispersed in ethanol generally led to a negative impact on the oil recovery. The application of nano-fluids for enhanced oil recovery has shown much promise, although further study is required.

1.1.2 Magnetic Nanoparticle Contrast Agents

Another potential application of nanoparticles in the oil and gas industry is their utilization as sensing or contrast agents (Barron et al., 2010; Johnson, 2010). Superparamagnetic nanoparticles have magnetic susceptibilities orders of magnitude higher than any normally occurring minerals and fluids within a hydrocarbon reservoir (**Figure 1.1**), making them ideal contrast agents. With their high magnetic susceptibilities superparamagnetic nanoparticles could be utilized for mapping of fractures mixture during a fracture job (Barron et al., 2010). By mixing the fracture fluid, proppant and magnetic nanoparticles (by either coating the proppant with the magnetic nanoparticles or directly dispersing them in the fracture fluid) a magnetic susceptibility tool could be utilized to detect the size of a fracture (which would be proportional to the nanoparticle content in the "sensing" proppant) at the end of the fracture job (**Figure 1.2**). Such fracture detection would be indispensable in the mapping of the fractures and determining the effectiveness of the fracture job.

Superparamagnetic nanoparticles could also be used to detect any permeability anisotropy within an active well (Johnson, 2010). If a magnetic nano-fluid was injected within a hydrocarbon reservoir then observations of the 3D flow of the nano-fluid in real time can potentially detect any flow pathways and permeability anisotropy within the well bore. Areas of low permeability would have a slow flow of the nano-fluid, therefore leading to a higher nanoparticle concentration and higher magnetic susceptibilities with time, while areas of high permeability would have a faster flow rate leading to lower overall magnetic susceptibilities and a constant value with time.

Finally such magnetic contrast agents could potentially track the progression of the waterflooding process in hydrocarbon reservoirs (see **Figure 1.3**). A highly magnetic nano-fluid can provide a very clear contrast once injected into an oil flooded sandpack. This can potentially allow for the real time tracking of the progression of the waterflood in the laboratory by monitoring the magnetic susceptibility profile of the sandpack at regular time intervals. This is one of the main objectives of this thesis. The profile monitoring of a real hydrocarbon reservoir could potentially be utilized by having monitoring magnetic susceptibility sensors installed between the injection and production wells, thus allowing for the detection of the progression of the water/oil interfaces(s).

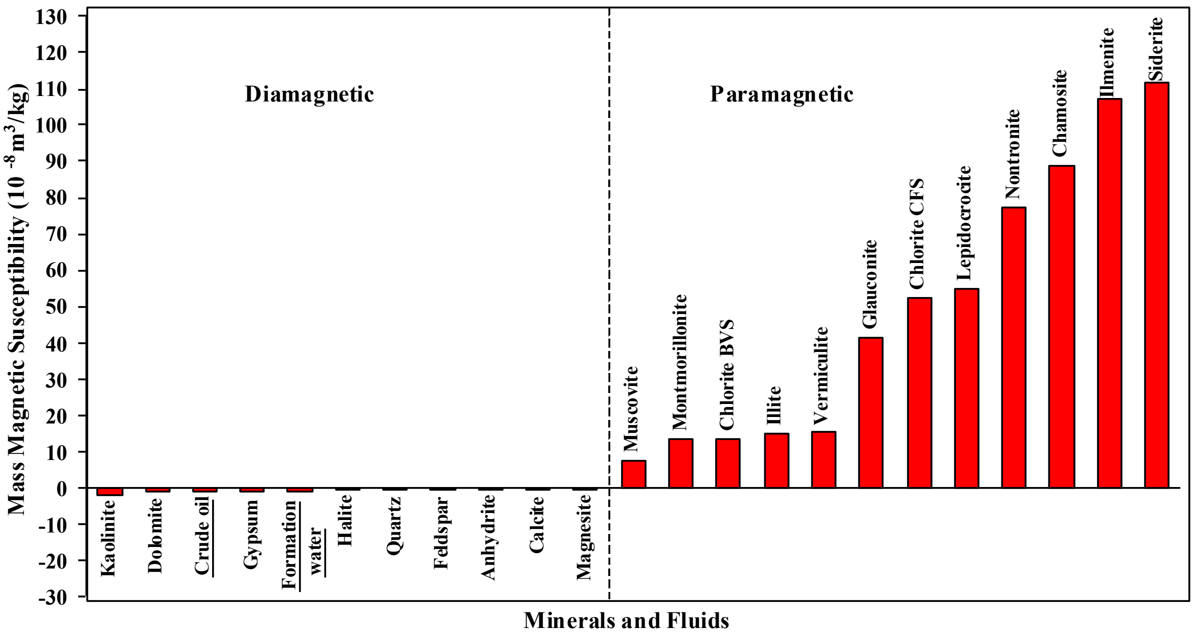

Figure 1.1: Magnetic susceptibility of common reservoir minerals and fluids (Ivakhnenko and Potter, 2004).

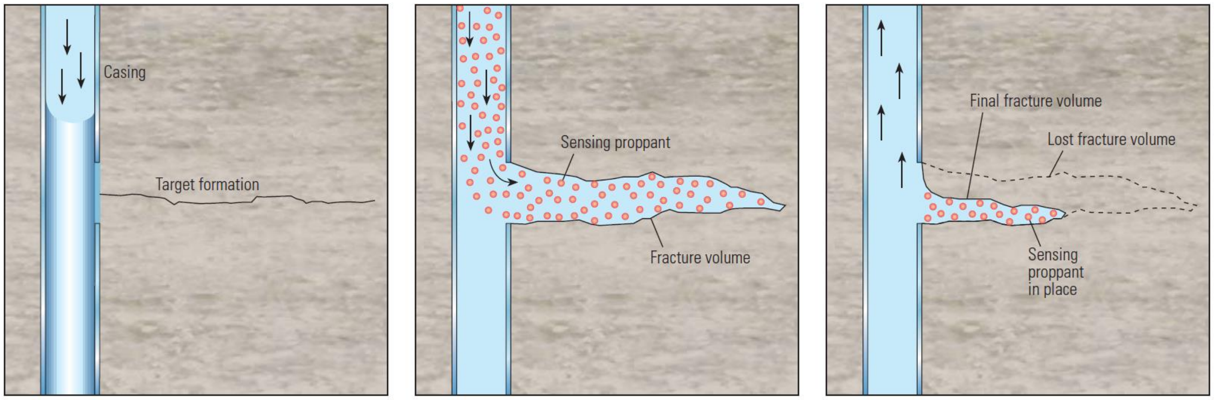

Figure 1.2: Utilization of sensing proppant during a fracture job. Left: the target formation. Middle: the sensing proppant entering the fracture during the fracture job. Right: the proppant stabilizes under the high pressure and partially closes the fracture (Barron et al., 2010).

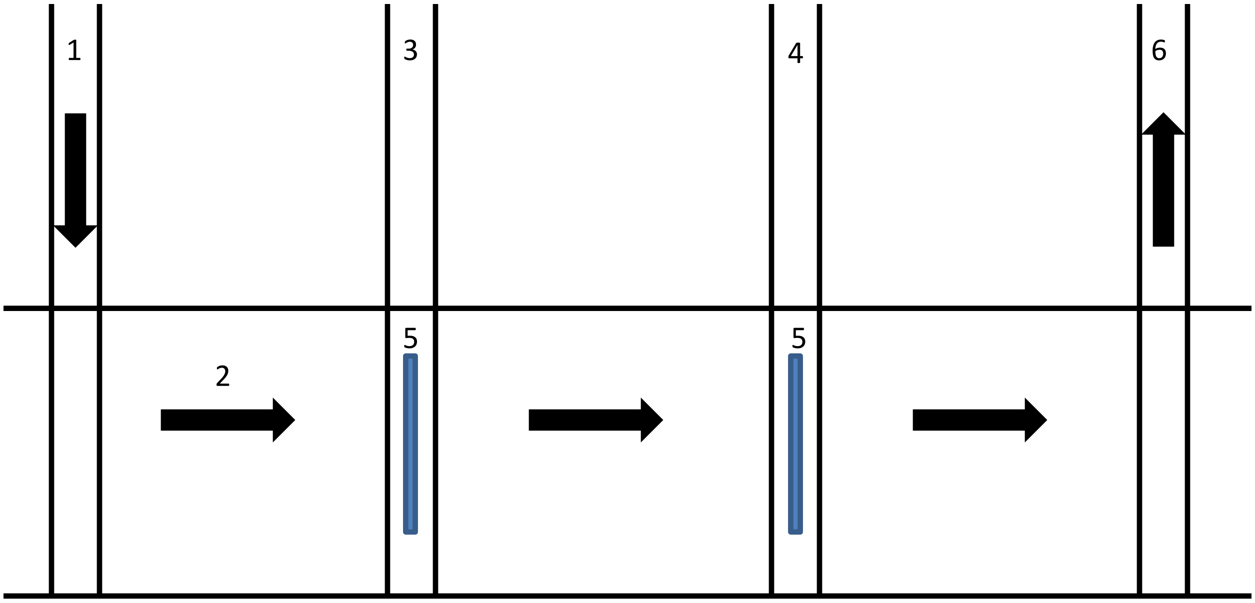

Figure 1.3: Field utilization of magnetic sensing waterflood. (1) Is the injection well where the magnetic sensing fluid is pumped in, (2) is the target formation where the waterflood fluid is displacing the oil in place, (3) and (4) are one or more monitoring wells between the injection and production well, (5) are downhole magnetic susceptibility wireline tools for magnetic monitoring in real time that would detect the arrival of the magnetic nanoparticles, (6) is the production well where oil is brought to the surface.

1.2 Study Focus

This thesis investigates the suitability of high magnetic susceptibility superparamagnetic and stable single domain nanoparticles to use as tracers (contrast agents) for imaging fluid flow in porous media. The main focus is to apply magnetic nanoparticles to quantitatively monitor in real time the process of waterflooding a heavy oil saturated sandpack (which simulates one of the oil recovery techniques used in heavy oil reservoirs by Cold Lake in North-Eastern Alberta). The success of such a monitoring technique would be significant since quantitative monitoring of heavy oil waterflooding is difficult and there is little in literature regarding this issue, even though there are numerous studies on the viscous fingering that arises due to the higher viscosity of heavy oil (Da Costa e Silva, 1995; Jamaloei, 2016). Thus the first goal of this study was to identify and characterize a suitable nanoparticle composition. The second goal was to develop a dispersed, stabilized suspension of the nanoparticles to monitor the progression of a waterflood in a heavy oil saturated sandpack in real time.

Such a magnetic contrast agent tracer would have multiple advantages if the experiment proves to be successful. Firstly, nanoparticles with superparamagnetic behavior would have magnetic susceptibilities orders of magnitude larger than most naturally occurring reservoir minerals and fluids, and thus are expected to be easy to detect. Secondly, some potential nanoparticle compositions are naturally occurring minerals with low toxicity, and thus would have a minimal environmental impact. Thirdly, as mentioned is **Section 1.1.1**, nano-fluid waterflooding can potentially enhance the oil recovery of a reservoir, and although this is not the focus of this PhD study future nanoparticle dispersions could potentially be generated that would act both as a tracer and an enhanced oil recovery nano-fluid. Note that the presence of naturally occurring nanoparticles in the formation would cause a larger background signal. In order to address this issue a detailed background magnetic susceptibility scan should be conducted on the hydrocarbon reservoir prior to injecting the magnetic nano-fluid.

There are a number of other techniques that could also potentially act as a tracer for heavy oil waterflooding. One such technique is computer tomography (CT), whose viability will also be tested simultaneously with the magnetic scanning during the waterflooding experiments in this thesis. CT scanning utilizes X-rays to measure the attenuation of the material and is dependent on the density. The images produced by a CT scanner can interrogate a very thin slice of material. CT scanning also has some disadvantages. In the case of heavy oil waterflooding the injection fluid will need the addition of a CT contrast agent. This is due to the low contrast between water and heavy oil as both have very similar densities. A further disadvantage is the cost and size of the equipment. The price of a high quality CT scanner can reach over 2 million dollars and even the cheaper models tend to be over 50,000 dollars. The large size of the CT scanner would also mean that CT scanning could not at present be implemented in actual hydrocarbon reservoirs.

Other potential techniques include chemical tracers or radioactive isotope tracers. Both techniques are believed to be inferior to the magnetic susceptibility technique as they have a number of disadvantages. Chemical tracers can cause contamination, and can degrade (due to oxidation, bacteria or precipitation out of solution) or adsorb onto the rock (Bennion et al., 1995). The radioactive tracers may pose an environmental risk depending on the type of isotope used, with the beta ray emitters being the safer option over the gamma ray ones.

Thus magnetic nanoparticle tracers are considered to be a potentially superior choice. As this is a new approach the magnetic nanoparticles needed to be thoroughly tested in order to find an optimal nanoparticle composition. Moreover, the magnetic properties of the nanoparticles needed to be examined under high temperature conditions in order to simulate those in a typical reservoir environment. Withstanding higher temperatures is crucial as some studies have shown (Hong et. al., 2009 and Auge et. al., 2010) that exposure to higher temperatures can have a detrimental effect on magnetic nanoparticles, causing a layer of oxidation on the outer surface of the nanoparticles which affects their overall magnetic properties. Another crucial requirement is the generation of a stable suspension of dispersed nanoparticles. The nano-fluid suspension will need to be able to flow through the formation without generating any particle aggregates (Abramas et al., 1977), otherwise such agglomerates may cause impairment to flow and damage the quality of the reservoir by plugging up the porethroats and thus reducing the permeability. Although some nanoparticle retention is expected to occur during waterflooding there are already multiple studies looking into this issue and attempting to model their behavior (Caldelas, 2010; Yu, 2012; Zhang et al., 2015; Zhang et al., 2016), many of which are showing favorable results under the right conditions.

1.3 Magnetic Properties

1.3.1 Introduction

This thesis has a large focus on the magnetic properties of nanoparticles and thus an understanding of the basic magnetic properties of materials is crucial. Magnetism is an intrinsic property of all matter.

1.3.2 Magnetic Susceptibility

Once a material is exposed to an external magnetic field the motion of the electrons in the electron shell is affected, resulting in the generation of an internal magnetic field within the material defined as induced magnetization. The magnetic susceptibility of a material is defined as the ratio between the induced magnetization and the external magnetic field. The volume magnetic susceptibility of a material is dimensionless (in SI) and is defined as follows:

$$\chi_{\mathrm{v}} = \frac{\mathrm{M}}{\mathrm{H}} \tag{1.1}$$

Where:

- χ_v is the volume magnetic susceptibility (SI)
- M is the induced magnetization of the material (Am^{-1})
- H is the applied external field on the material (Am^{-1})

The volume magnetic susceptibility can also be converted into mass magnetic susceptibility as follows:

$$\chi_{\mathrm{m}} = \frac{\chi_{\mathrm{v}}}{\rho} \tag{1.2}$$

Where:

- χ_v is the volume magnetic susceptibility (SI)
- χ_m is the mass magnetic susceptibility ($\mathrm{m}^3\mathrm{kg}^{-1}$)
- ρ is the density of the material ($\mathrm{kg\ m}^{-3}$)

The induced magnetization as well as the magnetic susceptibility of a material is highly dependent on the class of magnetic material as well as the magnetic domain state of the material, which is controlled by the size of the particles.

1.3.3 Classes of Magnetic Materials

There are five main classes of magnetic materials diamagnetic, paramagnetic, ferromagnetic, ferrimagnetic, and antiferromagnetic (with canted antiferromagnetic as a sub class), based on their response to an applied external magnetic field.

Diamagnetic Materials

In diamagnetic materials the atomic shells are filled with all electrons being paired. Thus in the absence of a magnetic field the magnetic moments produced from the electron motion cancels out resulting in a zero internal magnetization (**Figure 1.4** left). When subjected to an applied magnetic field the orbital motion of the electrons alters and leads to the generation of a weak magnetic dipole which opposes the applied magnetic field direction (**Figure 1.4** middle). Materials that behave diamagnetically include oil, water as well as most non-iron minerals such as quartz, calcite and feldspar (Dunlop and Özdemir, 1997; Thompson and Oldfield, 1986). Diamagnetic materials are temperature independent, and thus do not show any changes in magnetic susceptibility during heating or cooling. The magnetic hysteresis curve of a diamagnetic material results in a straight line which has negative slope, having negative magnetization to applied field (**Figure 1.4** right).

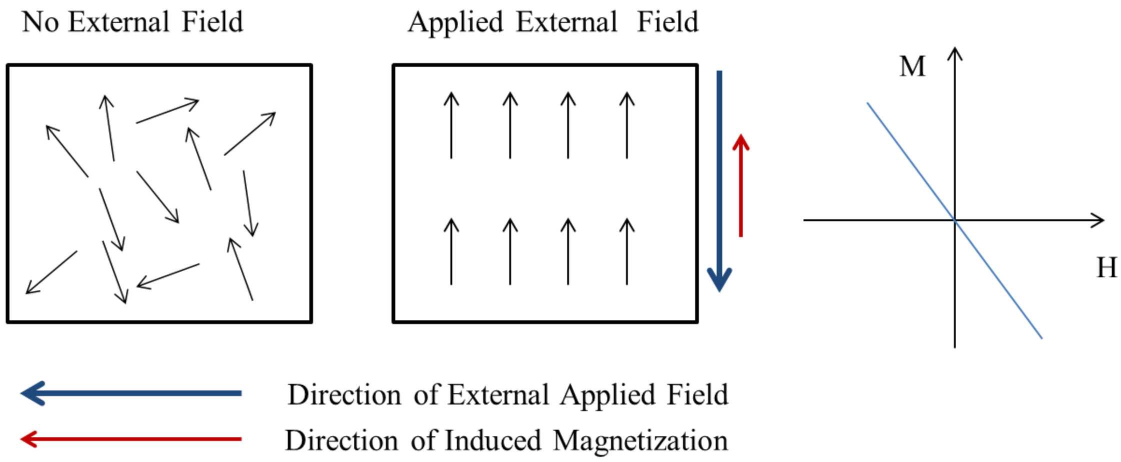

Figure 1.4: Behaviour of diamagnetic material under no applied field (left), an applied field (middle), as well as the magnetization (M) versus applied field (H) as shown in a typical magnetic hysteresis curve (right). The small arrows within the squares (left and middle) represent the magnetic moments.

Paramagnetic Materials

Paramagnetic materials have partially filled electron shells and unpaired electron spins. In the absence of an applied field the magnetic moments orient randomly and cancel each other out (**Figure 1.5** left). Thus paramagnetic materials have zero net magnetization in the absence of an applied field. Once an external field is applied the atomic moments tend to align towards the direction of the applied field producing a small positive magnetization (**Figure 1.5** middle). The degree of alignment and the resultant net magnetization is proportional to the strength of the applied field. Thus a stronger applied magnetic field will induce a larger net magnetization in a paramagnetic material and the magnetic hysteresis curve is a straight line with positive slope (**Figure 1.5** far right). Once the applied field is removed the thermal motion of the atoms randomizes the magnetic moments leading to a zero net magnetization state. Paramagnetic minerals include illite, chlorite and siderite (Ivakhnenko and Potter, 2004). Their magnetic susceptibilities are generally small compared to ferrimagnetic materials but are still 10-100 times larger (and in a positive sense) than diamagnetic materials (Dunlop and Özdemir, 1997). Paramagnetic materials have an inverse relationship between magnetic susceptibility and temperature following the Curie law. Thus an increase in temperature results in an increase in the thermal agitation which would decrease the ordering of the atomic moments and lower the magnetic susceptibility.

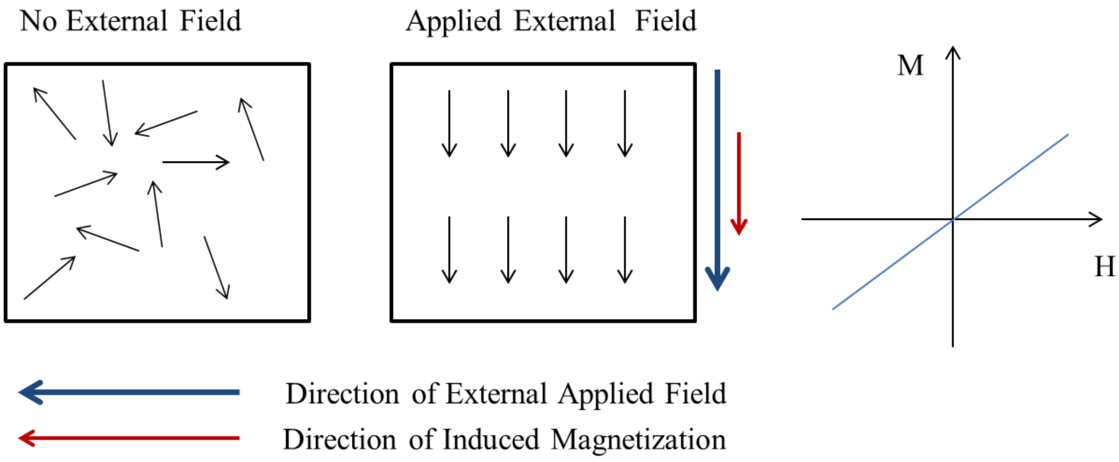

Figure 1.5: Behaviour of paramagnetic material under no applied field (left), an applied field (middle), as well as the magnetization (M) versus applied field (H) as shown in a typical magnetic hysteresis curve (right).

Ferromagnetic Materials

Ferromagnetic materials such as pure iron and nickel have a strong interaction between neighbouring magnetic moments leading to the parallel alignment of the magnetic moments within the material (**Figure 1.6** left). When an external field is applied all magnetic moments align parallel to the applied field, resulting in a large magnetization of the material (**Figure 1.6** middle). Once the external magnetic field is removed the material retains part of the magnetization (called a remanent magnetization M_{RS}) with the magnitude being dependent on the size of the magnetic particles. With increasing applied field strength the magnetization of the material eventually reaches a maximum value (called the saturation magnetization M_S), with all of the magnetic moments in the material aligned in the direction of the applied field. Ferromagnetic materials have large magnetic susceptibilities, orders of magnitude larger than paramagnetic materials. Ferromagnetic materials only behave as such below the Curie temperature. Once heated above their Curie temperature the thermal energy disrupts the interaction of the magnetic moments, and the material then behaves as a paramagnet, requiring an external field to induce magnetization.

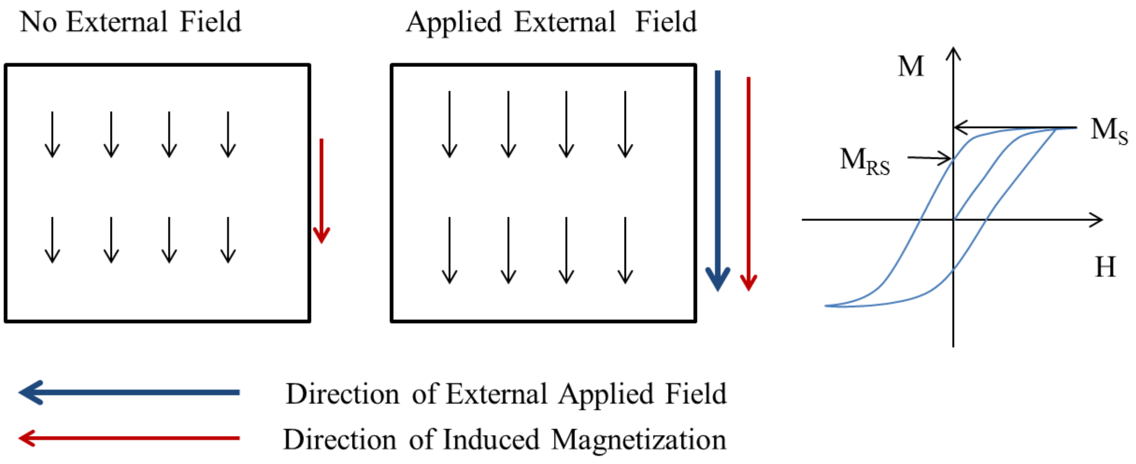

Figure 1.6: Behaviour of ferromagnetic material under no applied field (left), an applied field (middle), as well as magnetization (M) versus applied field (H), with saturation magnetization (M_S) and remanent magnetization (M_{RS}) showing a characteristic magnetic hysteresis loop (right).

Ferrimagnetic Materials

Ferrimagnetic materials are oxides of metals such as iron and nickel (such as magnetite, maghemite). Ferrimagnets exhibit strong interaction between neighbouring magnetic moments although in this case the directionality is anti-parallel (**Figure 1.7**). The strength of the magnetic moments is unequal which leads to a net magnetization of the material even after the removal of an applied field (**Figure 1.7** left), although in this case the magnitude of the magnetization is lower than in ferromagnetic cases. Once an external field is applied the magnetization in the applied field direction increases (**Figure 1.7** middle). Ferrimagnets behave as paramagnetic materials above their Curie temperature similar to the behavior of ferromagnets.

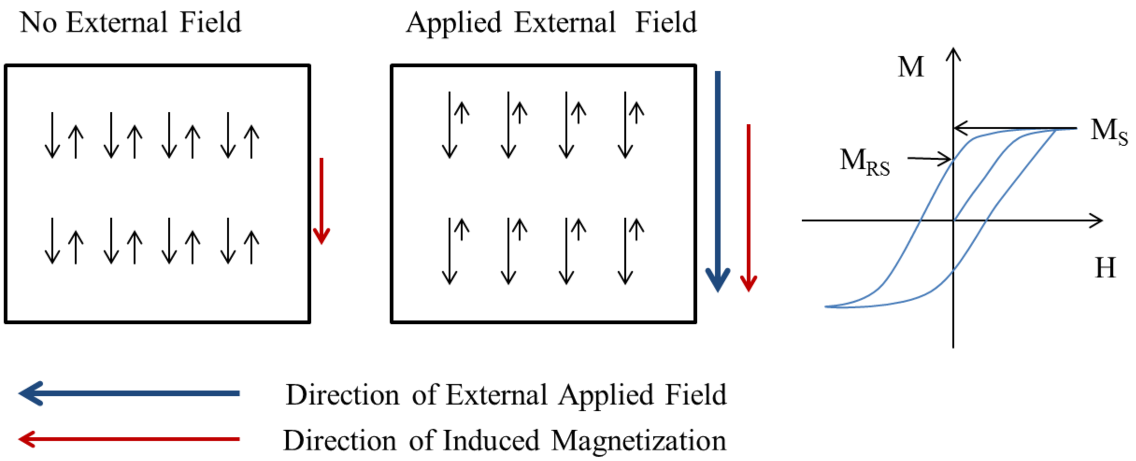

Figure 1.7: Behaviour of ferrimagnetic material under no applied field (left), an applied field (middle), as well as magnetization (M) versus applied field (H), with maximum saturation magnetization (M_S) and remanent magnetization (M_{RS}) as shown in a typical magnetic hysteresis curve (right).

Antiferromagnetic Materials

Antiferromagnetic materials have strong neighbouring interactions between magnetic moments. In this case the directionality of the magnetic moments is anti-parallel with equal strength. Thus once an applied field is removed the net magnetization of the material reverts to zero (**Figure 1.8** left). Once an external magnetic field is applied the material gains a small magnetization in the same direction as the applied field (**Figure 1.8** right). In some cases the direction of the magnetic moments is not completely antiparallel, but is slightly canted. Such materials are referred to as canted antiferromagnetic materials and can retain a weak net magnetization once the applied field has been removed. The critical magnetic temperature in this case is called the Néel temperature. Above the Néel temperature the thermal energy disrupts the magnetic ordering in the material thus causing the material to behave paramagnetically. An example of a canted antiferromagnetic material is hematite, while a pure antiferromagnetic material is ilmenite.

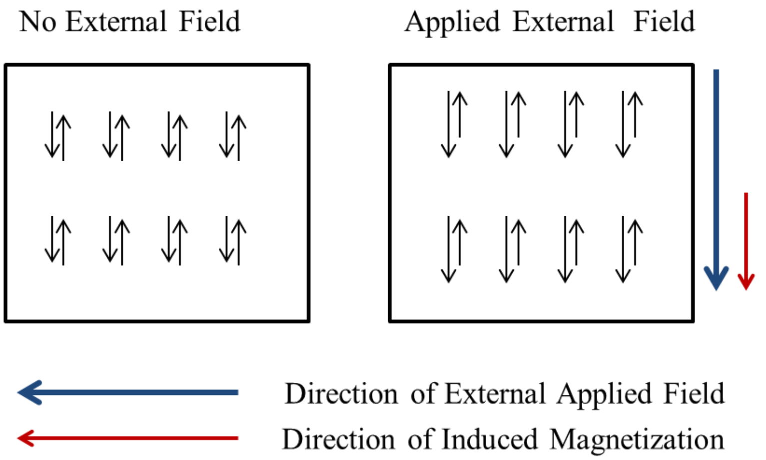

Figure 1.8: Behaviour of antiferromagnetic material under no applied field (left), and an applied field (right).

1.3.4 Magnetic Domains

The magnetic susceptibility of materials other than diamagnets and paramagnets are dependent on both the class of magnetic material as well as the size of the magnetic particle. Based on the size of the particles the material can be either in the multidomain or single domain state. Multidomain behavior occurs above a critical size, and single domain behavior below this critical size, depending on the composition and magnetic class (ferromagnetic, ferrimagnetic or antiferromagnetic).

Multidomain

The critical size above which particles become multidomain varies depending on the magnetic material and can be anywhere from 0.017 µm for iron (Butler and Banerjee, 1975) or as large as 15 µm for hematite (Banerjee, 1971). **Table 2.6** in **Chapter 2** will show the critical stable single domain/multidomain boundaries for the nanoparticle compositions studied in this thesis. Multidomain particles (**Figure 1.9 (b)**) have domain walls and more than one magnetization direction within a single particle. They are not of much interest for this thesis as the particles are much larger than the nanoparticles required for reservoir applications (the nanoparticles need to have high magnetic susceptibilities and be small in size so they don't plug up the pore throats in the reservoir).

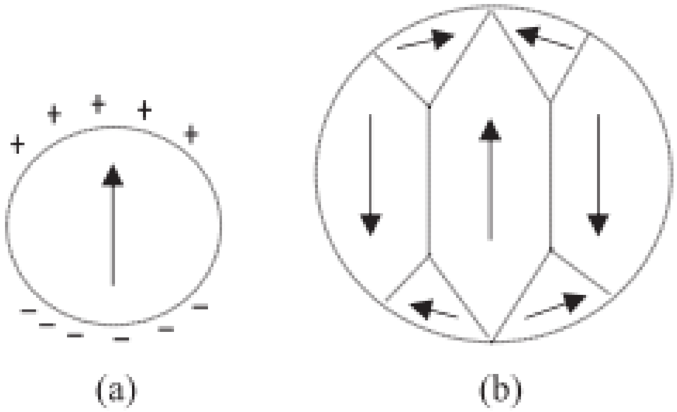

Figure 1.9: (a) Spherical stable single domain grain with magnetization shown by the arrow and surface charge indicated. (b) A spherical multidomain grain with arrows indicating the magnetization direction in each domain and domains are separated by domain walls (Butler, 1992).

Stable Single Domain

Below the critical grain size single domain particles have lower energy than a two-domain particle (Dunlop and Özdemir, 1997). Such particles have only one magnetization direction

(**Figure 1.9 (a)**). Stable single domain particles have long relaxation times and can hold a remanent magnetization over geological time periods. A distribution of randomly oriented (i.e., isotropic) uniaxial stable single domain particles have a remanent magnetization (M_{RS}) approximately half the saturation magnetization (M_S) (**Figure 1.10**).

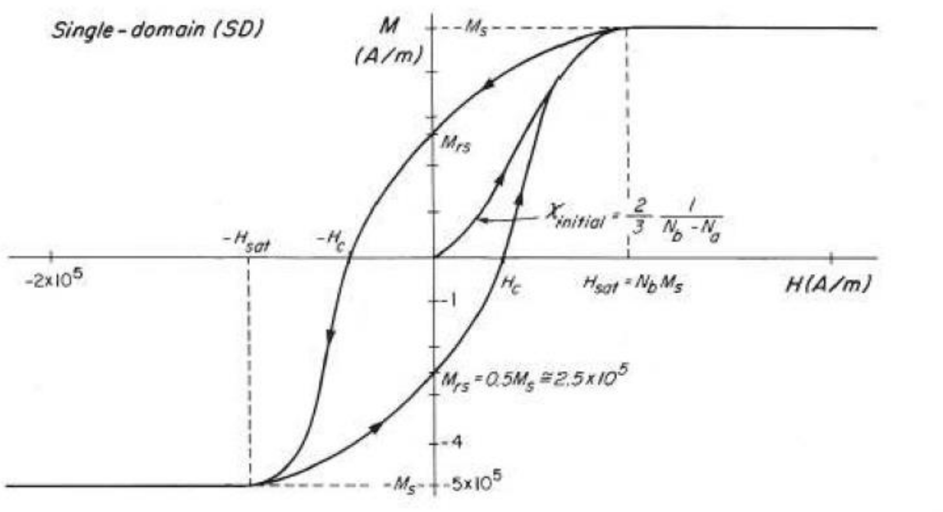

Figure 1.10: Idealized magnetic hysteresis of randomly oriented uniaxial stable single domain particles. Numerical values are representative of magnetite (Dunlop and Özdemir, 1997).

Superparamagnetic Behaviour

Superparamagnetism occurs in single domain particles once their size decreases below a critical size. The critical superparamagnetic/stable single domain boundaries for the nanoparticle compositions studied in this thesis will be given in **Table 2.6** (see **Chapter 2**). Superparamagnetic particles have zero remanence in the absence of an applied field (**Figure 1.11**). Once an external field is applied they gain a rapid magnetization. The magnetic susceptibilities of superparamagnetic particles can be orders of magnitude larger than a typical stable single domain or multidomain particle of the same material (Dunlop and Özdemir, 1997). Therefore a small concentration of superparamagnetic particles can completely dominate the magnetic susceptibility signal of a sample. Thus the small size and high magnetic susceptibility properties of superparamagnetic particles potentially make them ideal candidates as magnetic tracers.

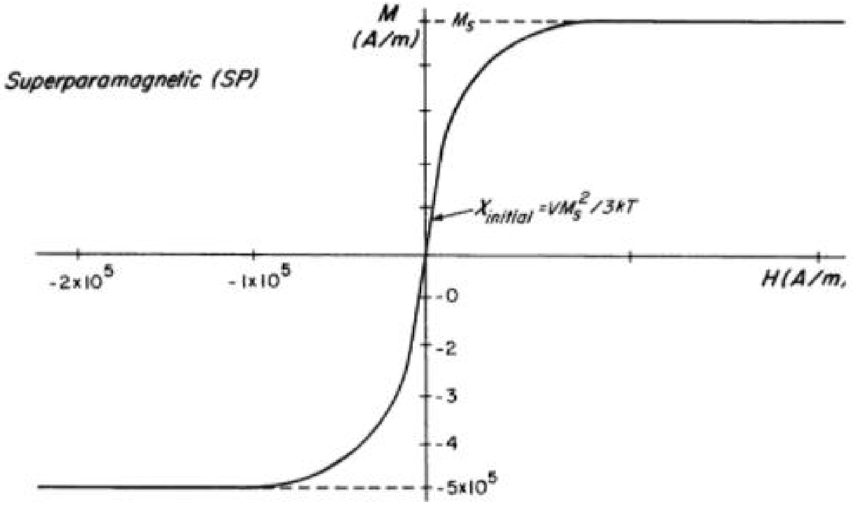

Figure 1.11: Idealized magnetization curve for superparamagnetic magnetite particles (Dunlop and Özdemir, 1997).

1.4 Main Objectives

The main objectives of this study were as follows:

- To characterize four types of magnetic nanoparticles in order to identify the most suitable type for use as a magnetic contrast agent in reservoirs at reservoir temperatures. The characterization would involve the following aspects:
    i. General physical and chemical characterizations (scanning electron microscopy, transmission electron microscopy, energy dispersive spectroscopy, X-ray diffraction).
    ii. Magnetic characterization (magnetic susceptibility at room temperature and reservoir temperatures when dispersed in different solid and liquid materials, and magnetic hysteresis).
- To undertake stability experiments on the most suitable type of magnetic nanoparticle, with the aim of developing a method of generating a stable dispersed suspension of the nanoparticles. The nanoparticles would need to stay dispersed and in suspension for at

least several days during a typical waterflooding process (either experimentally in the laboratory or in a typical field application) without forming large agglomerates or settling out of suspension.

- To use the most suitable magnetic nanoparticles as contrast agents during waterflooding experiments that simulate the waterflooding of heavy oil, which is a type of enhanced oil recovery (EOR) that is used in some heavy oil wells. The main aim was to monitor the waterflooding in real time by multimodal scanning using both magnetic susceptibility scanning and computer tomography (CT) scanning. In the past CT scanning has been relatively ineffective in this type of application due to the low contrast between water and heavy oil (since they both have very similar densities). Therefore one major objective was to determine whether magnetic susceptibility scanning of the magnetic nanoparticle contrast agents was more effective at monitoring the progress of the waterflooding (and in particular the progression of the water-heavy oil interface(s)).
- To determine the retention of magnetic nanoparticles after water flushing in some previous fluid flow experiments (since nanoparticle retention may degrade the quality of a reservoir), and to investigate the role of natural hematite nanoparticles in a tight gas reservoir.
- A further objective was to determine whether some observations of apparent unusual "diamagnetic" behavior in nanoparticle hematite are due to the hematite nanoparticles themselves or due to the matrix in which they are dispersed.

1.5 Organization of Thesis

This thesis is divided into seven chapters:

Chapter 1 gives the background of the research area and introduces the research objectives. The first chapter also gives an overview of the basics of the magnetic properties of materials.

Chapter 2 firstly introduces the main materials and equipment used in the experiments. The chapter then describes in detail the experimental methodology used in this project.

Chapter 3 details the results of the nanoparticle characterization of the four main nanoparticle compositions examined. The chapter first introduces the results of the general nanoparticle characterization which looked at the size, shape and chemical composition of the nanoparticles. Following this the magnetic properties of the nanoparticles were examined both at room temperature and potential reservoir temperatures when dispersed in different materials. The Curie temperature of the nanoparticles was also examined. At the end of the characterization the most suitable nanoparticle composition (from those studied) was chosen for the subsequent stability and waterflood experiments.

Chapter 4 focuses on the stability and waterflood experiments. Firstly, the chosen nanoparticle composition underwent a number of stability experiments in order to generate a dispersed nanoparticle suspension with long term stability. The nano-fluid was then used to trace the progress of the waterflooding of a heavy oil saturated sandpack. The waterflood experiments were monitored by multimodal scanning using both magnetic susceptibility and computer tomography (CT) scanning equipment.

Chapter 5 analyses the potential nanoparticle retention following waterflooding experiments, as well as the impact of naturally occurring hematite nanoparticles on the quality of a clastic tight gas reservoir. The quantity of nanoparticles retained after water flushing was examined in an attempt to evaluate any potential threat to the quality of a reservoir due to the injection of the nano-fluids.

Chapter 6 examines the unusual apparent “diamagnetic” behavior of some hematite nanoparticle samples, which were initially the fifth potential candidate for a contrast agent tracer nanoparticle composition. The chapter investigates whether the apparent diamagnetic behavior of some samples containing hematite nanoparticles (one of the samples examined in this thesis, and also a sample reported by Mi et al., 2006) is actually due to the hematite nanoparticles themselves or due to the dispersing matrix that contained the nanoparticles.

Chapter 7 summarizes all of the conclusions and gives recommendations for further studies.

1.6 References

- Abrams A., SPE-AIME and Shell Development Co., 1977. Mud Design to Minimize Rock Impairment Due to Particle Invasion. Journal of Petroleum Technology, **29**, 586-592.
- Auge, A., Weddemann, A., Vogel, D., Wittbracht, F., and Hutten, A., 2010. A level set base approach for modeling oxidation processes of ligand stabilized metallic nanoparticles. Applied Physics Letters, **96**, ID093111, 3 pp.
- Banerjee, S. K., 1971. New grain size limits for palaeomagnetic stability in hematite. Nature Physical Science, **232**, 15-16.
- Barron, A. R., Tour, J. M., Busnaina, A. A., Jung, Y. J., Somu, S., Kanj, M. Y., Potter, D. K., Resasco, D., and Ullo, J., 2010. Big things in small packages. Oilfield Review, Schlumberger, **22**, 38-49.
- Bennion, B. D., Thomas, B. F., Crowell, E. C., amd Freeman B., 1995. Applications for tracers in reservoir conformance predictions and initial saturation determinations. Annual International Conference on Reservoir Conformance, Profile Control Water and Gas Shutoff, Houston, 14 pp.
- Butler, R. F., 1992. Paleomagnetism, magnetic domains to geologic terranes. Blackwell Scientific Publications, 319 pp.
- Butler, R. F., and Banerjee, S. K., 1975. Theoretical single-domain grain-size rangein magnetite and titanomagnetite. Journal of Geophysical Research, **80**, 4049-4058.
- Caldelas, F. M., 2010. Experimental parameter analysis of the nanoparticle retention in porous media. M.S. thesis, University of Texas at Austin, Austin, USA, 145 pp.
- Da Costa e Silva, A. 1995. Analysis of viscous fingering reproducibility in consolidated natural porous media. Society of Core Analysts conference, Paper Number 9504, 1–10.
- Dunlop, D. J., and Özdemir, Ö., 1997. Rock Magnetism. Cambridge University Press, 565 pp.
- Hong S. J., Pyun J., Park W. Y., Kim S. C. and Shim I., 2009. Oxidation Effect in Cobalt Nanoparticles Magnetic Fluids, IEEE Transactions on Magnetics, **45**, 2464-2466.
- Ivakhenko, O. P., and Potter, D. K., 2004. Magnetic susceptibility of petroleum reservoir fluids. Physics and Chemistry of the Earth, **29**, 899-907.

- Jamaloei, B. Y., Babolmorad, R., and Kharrat, R., 2016. Correlations of viscous fingering in heavy oil waterflooding. Fuel, **179**, 97-102.
- Johnson, K., 2010. Advances in nanotechnology hold huge potential promise in upstream applications. The American Oil & Gas Reporter, 113-123.
- Kothari, N., Raina, B., Chandak, K. B., Iyer, V., and Mahajan, H. P., 2010. Application of ferrofluids for enhanced surfactant flooding in IOR. Society of Petroleum Engineers, SPE EUROPEC/EAGE Annual Confenrece and Exhibition, Barcelona, 14-17.
- Mi, Y., Zhang, X., Luo, J., Zhou, S., Zhang, H., Cheng, J. and Liu, F., 2006. Hydrothermal fabrication of spindle-type α-Fe2O3 nanoparticle and its magnetic property. Proceedings of the 1st IEEE International Conference on Nano/Micro Engineered and Molecular Systems, Zhuhai, 519-522.
- Negin, C., Ali, S., and Xie, Q., 2016. Application of nanotechnology for enhancing oil recovery – A review. Petroleum, **2**, 324-333.
- Ogolo, N. A., Olafuyi, O. A., and Onyekonwu, M. O., 2012. Enhanced oil recovery using nanoparticles. Society of Petroleum Engineers, SPE Saudi Arabia Section Technical Symposium and Exhibition, Al-Khobar, 9 p.
- Onyekonwu, M. O., and Ogolo, N. A., 2010. Investigating the use of nanoparticles in enhancing oil recovery. Society of Petroleum Engineers, Nigeria Annual International Conference and Exhibition, Tinapa-Calabar, 14 pp.
- Ponmani, S., Nagarajan, R., and Sandwai, J., 2013. Applications of nanotechnology for upstream oil and gas industry. Journal of Nano Research, **24**, 7-15.
- Thompson, R., and Oldfield, F., 1986. Environmental Magnetism. Allen and Unwin, London, 243 pp.
- Yu, H., 2012. Transport and retention of surface-modified nanoparticles in sedimentary rocks. Ph.D. thesis, University of Texas at Austin, Austin, USA, 257 pp.
- Zhang, T., Murphy, M. J., Yu, H., Bagaria. H. G., Yoon, K. Y., Neilson, B. M., Bielawski, C. W., Johnston, K. P., Huh, C., and Bryant, S. L., 2015. Investigation of nanoparticle adsorption during transport in porous media. Society of Petroleum Engineers, SPE Annual Technical Conference and Exhibition, New Orleans, 667-677.
- Zhang, T., Murphy, M., Yu, H., Huh, C., and Bryant, S. L., 2016. Mechanic model for nanoparticle retention in porous media. Transport in Porous Media, **115**, 387-406.

Chapter 2

MATERIALS, EQUIPMENT AND EXPERIMENTAL PROCEDURES

2.1 Introduction

This chapter will describe the materials, equipment and procedures that were used in the experiments. As the nanoparticles were synthesized out of house the manufacturer specifications will be described in detail. Following the nanoparticle description, the main chemicals and dispersants used will be introduced. Next the chapter will describe in detail the relevant pieces of equipment that were utilized in the conducted experiments. Finally the methodology and techniques used over the course of this research will be introduced. The main experimental procedures as well as analytical methods will be described in detail.

2.2 Materials

2.2.1 Magnetic Nanoparticles

Five magnetic nanoparticle powder compositions synthesized by the SOL-GEL method were procured from the MTI Corporation (**Tables 2.1 to 2.5**). The nanoparticles were thoroughly characterized in order to determine their suitability for the intended application of a contrast agent for magnetic monitoring in hydrocarbon reservoirs.

Four key considerations were taken into account in choosing the nanoparticle compositions:

- First and foremost was their magnetic properties; almost all of the nanoparticles (with the exception of hematite) were expected to be ferro- or ferrimagnetic. High magnetic susceptibility is a vital requirement for a potential contrast agent as this would provide a strong signal that is easy to detect. Thus ferro- or ferrimagnetic materials would be prime candidates for such applications due to their high magnetic susceptibilities.

Table 2.1: Material characteristics of magnetite (20 nm) nanoparticles.

Characteristic	**Description**
Chemical Formula	Fe_3O_4
Purity	99.9%
Color	Black
Morphology	Spherical
Average Particle Size	20 nm
Bulk Density	0.84 g cm^{-3}
True Density	4.8-5.1 g cm^{-3}

Table 2.2: Material characteristics of nickel ferrite (30 nm) nanoparticles.

Characteristic	**Description**
Chemical Formula	$NiFe_2O_4$
Purity	99.5%
Color	Dark Brown
Morphology	Nearly Spherical
Average Particle Size	30 nm
Bulk Density	0.89 g cm^{-3}
True Density	5.368 g cm^{-3}

Table 2.3: Material characteristics of maghemite (20 nm) nanoparticles.

Characteristic	Description
Chemical Formula	γ-Fe_2O_3
Purity	99.5%
Color	Red Brown
Morphology	Spherical
Average Particle Size	20 nm
Bulk Density	1.20 g cm^{-3}
True Density	5.24 g cm^{-3}

Table 2.4: Material characteristics of cobalt ferrite (40 nm) nanoparticles.

Characteristic	Description
Chemical Formula	$CoFe_2O_4$
Purity	99.5%
Color	Black
Morphology	Spherical
Average Particle Size	40 nm
Bulk Density	0.41-0.51 g cm^{-3}
True Density	5.3 g cm^{-3}

Table 2.5: Material characteristics of hematite (30 nm) nanoparticles.

Characteristic	**Description**
Chemical Formula	α-Fe_3O_4
Purity	99.5%
Color	Red Brown
Morphology	Spherical
Average Particle Size	30 nm
Bulk Density	1.24 g cm^{-3}
True Density	5.24 g cm^{-3}

- The next consideration taken into account was the potential environmental impact of the nanoparticles when injected into an actual hydrocarbon reservoir. In order to minimize any environmental impact three out of the five potential candidates (magnetite, maghemite and hematite) were chosen as they are naturally occurring compounds in reservoir rocks and have low toxicity. Note that magnetite and maghemite are also used for various biomedical applications (Roger et al., 1999; Halbreich et al., 1998; Ghazanfari et al., 2016).
- The final two requirements for the nanoparticles considered were their morphology and size. The ideal candidates were required to be small enough in order to be in their superparamagnetic state. Such superparamagnetic nanoparticles have much larger magnetic susceptibilities compared to their stable single-domain or multidomain counterparts, and would thus make better contrast agents as they would provide strong magnetic susceptibility signal even with lower concentrations. The morphology of the chosen particles was spherical. The small size and morphology would allow for smoother flow of the nanoparticles through the porous media and reduce the risk of clogging the pore throats of a potential reservoir. The critical theoretical (or in some cases

experimentally observed) sizes for the superparamagnetic/stable single-domain and the stable single-domain/multidomain boundaries for the various nanoparticles are shown in **Table 2.6**.

Table 2.6: Critical boundaries for the superparamagnetic/stable single domain and stable single domain/multidomain sizes of the examined nanoparticles.

Mineral	**Superparamagnetic/Stable Single-Domain boundary size (µm)**	**Stable Single-Domain/Multidomain boundary size (µm)**
Magnetite	0.025-0.030[1-3]	0.05-0.06[2,4]
Maghemite	0.03[5]	0.06[6]
Nickel Ferrite	0.01[7]	0.042[8]
Cobalt Ferrite	0.04[9]	0.1[5]
Hematite	0.025-0.030[10,11]	15[11]

[1]McNab et al. (1968) – experimental; [2]Dunlop (1973) – experimental; [3]Dunlop and Bina (1977) – experimental; [4]Argyle and Dunlop (1984) – theoretical; [5]Krishan (2010) – theoretical; [6]Morrish and Yu (1955) – theoretical; [7]Kamble et al. (2015) – reported; [8]Jiang and Yang (2007) – experimental; [9]Chinnasamy et al. (2003) – experimental; [10]Bando et al. (1965) – experimental; [11]Banerjee (1971) – experimental.

In order to further examine the magnetic behaviour of nano-sized hematite two more dilutely dispersed nanoparticle sizes (8 nm and 40 nm) were analyzed. The compositions were purchased from Particular GmbH, where they were synthesized via laser ablation in water. Unlike the previous nanoparticles which were provided in a powder form, the particles synthesized via the laser ablation method were already stabilized and dispersed in a water matrix by the manufacturer. The characteristics of these hematite dispersions are shown in **Tables 2.7 & 2.8**.

Table 2.7: Material characteristics of hematite (8 nm) nanoparticles.

Characteristic	**Description**
Chemical Formula	α-Fe_3O_4
Dispersant	Water
Particle Concentration	140 mg L^{-1}
Color	Red Brown
Morphology	Spherical
Average Particle Diameter	8 nm

Table 2.8: Material characteristics of hematite (40 nm) nanoparticles.

Characteristic	**Description**
Chemical Formula	α-Fe_3O_4
Dispersant	Water
Particle Concentration	160 mg L^{-1}
Color	Red Brown
Morphology	Spherical
Average Particle Diameter	40 nm

2.2.2 Chemicals and Dispersants

Methyl methacrylate ($C_5H_8O_2$) and cold mounting resin were used to disperse the nanoparticles in a diamagnetic (i.e., low negative magnetic susceptibility) matrix. When combined these substances form a hard resin that can be used to contain the dispersed nanoparticles. This form of dispersion is useful in simulating a consolidated reservoir rock with dispersed nanoparticles (since quartz in clastic reservoirs and calcite in carbonate reservoirs are also diamagnetic). Methyl methacrylate is a liquid which can be mixed with a small concentration of nanoparticles to disperse them. Cold mounting resin is a white powder that was the second component used, in order to set the nanoparticles in place. The magnetic susceptibility of these samples was subsequently measured in a Molspin susceptibility bridge (see **Section 2.3.1**).

Calcium fluoride (CaF_2) was used as another diamagnetic dispersing matrix in a number of room temperature and high temperature magnetic susceptibility experiments. It was chosen as it was an ideal dispersant for high temperature experiments (whereas the previous cold mounting resin would have melted). Calcium fluoride has a high melting point of 1418 ˚C which was sufficiently above the maximum Curie temperatures of the nanoparticles (which was approximately 700 ˚C). The compound has a very low diamagnetic susceptibility response and thus would have an insignificant contribution to the total magnetic susceptibility of the dispersed samples.

Sodium chloride (NaCl) and sodium iodide (NaI) were two salt compounds which were used as contrast agents for the CT scanner during the waterflooding of heavy oil experiments. They were separately tested to see if they increased the CT contrast, when added to water, between water and heavy oil. When added to a nanoparticle suspension these salts also lead to an increase in the ionic strength of the solution. Both salts are diamagnetic exhibiting a small negative magnetic susceptibility when exposed to an applied magnetic field.

Sodium dodecylbenzenesulfonate ($C_{18}H_{29}NaO_3S$, DDBS) is a white, granular organic surfactant. This anionic compound was used as a stabilizing agent in order to prevent nanoparticle agglomerations and maintain the stability of the nanoparticle suspensions before and during waterflooding. The surfactant coats the nanoparticles during the dispersion process and creates an electric surface charge. This increases the repulsive force between nanoparticles and helps prevent the formation of nanoparticle agglomerates. The compound is biodegradable with a relatively short half-life of approximately 1 to 3 weeks, thus it is unlikely to have any negative environmental impacts when injected into a hydrocarbon reservoir (Jensen, 1999).

2.3 Equipment

2.3.1 Molspin Susceptibility Bridge

The Molspin susceptibility bridge is a low frequency magnetic susceptibility sensor system (**Figure 2.1**). The system is comprised of a sample chamber enclosed by a sensor which is connected to a control computer unit. The specimen in the sample chamber is subjected to a weak applied magnetic field, which produces a magnetization in the sample. The magnetic susceptibility is the magnetization divided by the applied field.

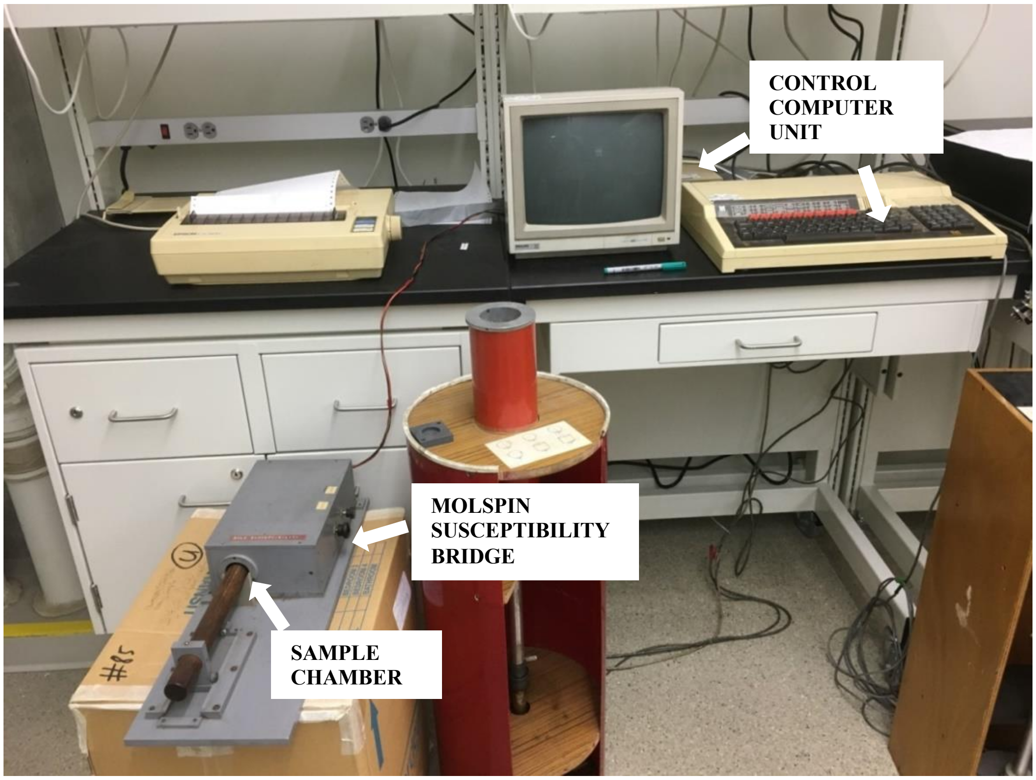

Figure 2.1: Molspin susceptibility bridge system.

2.3.2 Bartington Dual Frequency Magnetic Susceptibility System (MS2B)

The Bartington MS2B sensor experimental system was used to measure the magnetic susceptibility of the 30 nm hematite sample at room temperature conditions. The system has two main components: a MS2B dual frequency sensor (**Figure 2.2**) connected to a MS2 meter (**Figure 2.3**). The sample chamber of the sensor is designed to accommodate cubic boxes with dimensions of 25.4 mm and 23 mm, cylindrical bottles with sizes of 20 cc and 10 cc as well as cylindrical 25.4 mm diameter cores. The sensor is specifically calibrated for use with a 10 cc cylindrical sample container with internal diameter of 24 mm and height of 23 mm. The operating frequency for the MS2B sensor has two optional settings: a low operating frequency of 0.465 kHz and a high operating frequency of 4.65 kHz. The sensor operates by applying a magnetic field to the sample, which in turn causes an induced magnetization. The magnetization of the sample is determined from the frequency of oscillation detected by an inductor in the MS2B sensor. The magnetic susceptibility is then calculated from the induced magnetization of the sample and the applied field.

The MS2 meter is connected to the MS2B sensor via a coaxial cable and displays the magnetic susceptibility readings (**Figure 2.3**). The meter can be set to display the measurements in both SI and CGS units, with high and low resolution options. In high resolution mode the susceptibility reading takes 15 seconds to complete with the MS2B sensor, whilst the low resolution mode takes 1.5 seconds under the SI setting. The MS2 meter has a volume magnetic susceptibility range between 1 and 9999 x 10^{-5} when set to SI, and betweeen 1 and 9999 x 10^{-6} when set to CGS.

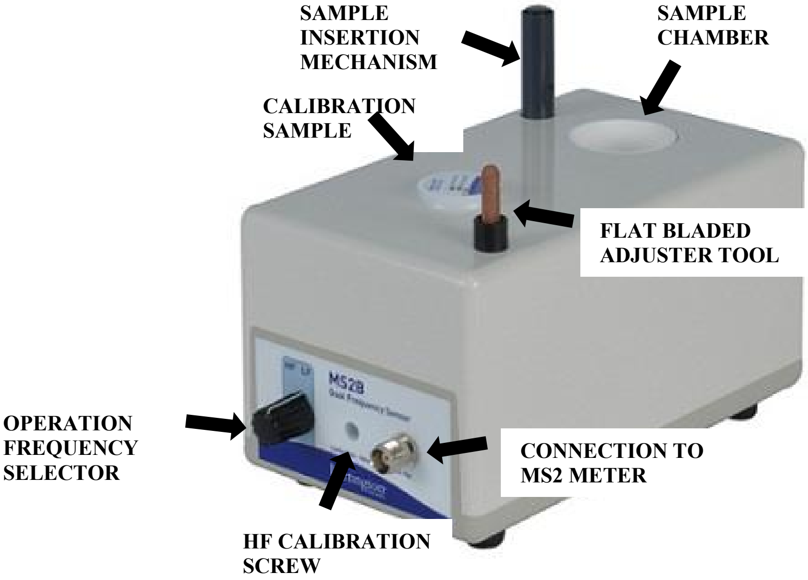

Figure 2.2: Bartington MS2B dual frequency magnetic sensor.

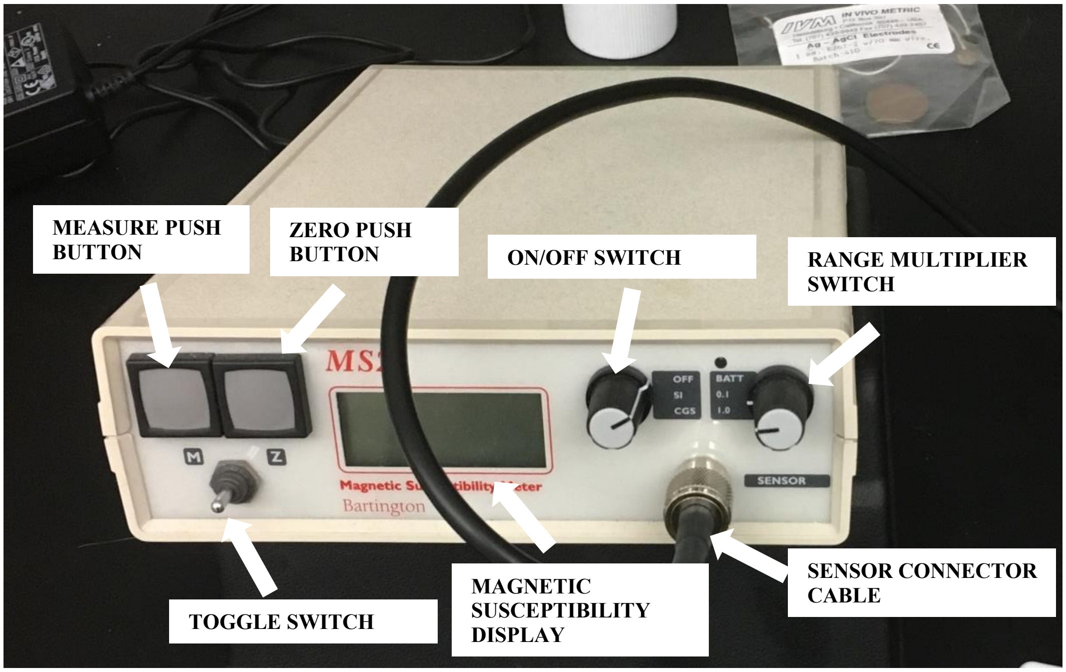

Figure 2.3: Bartington MS2 meter.

2.3.3 Bartington Magnetic Susceptibility Core Logging System (MS2C)

The magnetic susceptibility core logging sensor (MS2C) was used for the stability and waterflood experiments. The system has two main components (**Figure 2.4**). The MS2C core scanning sensor used has an 80 mm aperture. It was manufactured to order to surround the PEEK flow cell used in the waterflood experiment, and to surround the jars for the static stability tests. The sensor works by generating a weak applied field (of 250 μT), which in turn magnetizes the sample. The magnetization of the sample is determined from the frequency of oscillation detected by an inductor in the MS2C sensor. The magnetic susceptibility is then determined as a function of the magnetization of the sample and the applied field.

The MS2 meter is connected to the MS2C sensor and displays the magnetic susceptibility readings. In high resolution mode the susceptibility reading takes 11 seconds to complete with the MS2C sensor, whilst the low resolution mode takes 1.1 seconds under the SI setting.

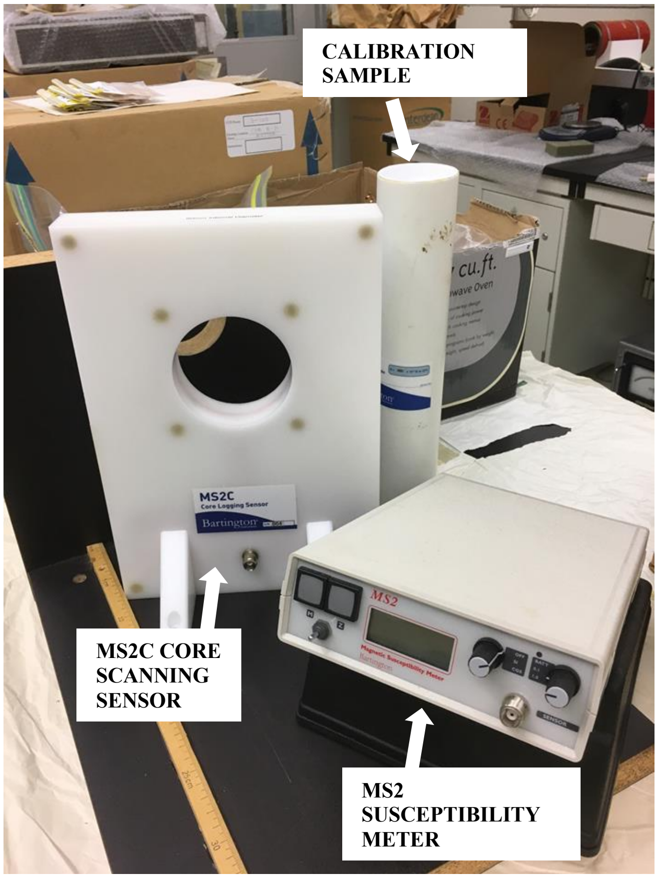

Figure 2.4: Bartington magnetic susceptibility core logging system (MS2C).

2.3.4 Bartington Magnetic Susceptibility Surface Scanning System (MS2E)

The surface scanning magnetic susceptibility system allows for the fast magnetic susceptibility measurements of flat surfaces (**Figure 2.5**). The system was used for the measurement of the magnetic susceptibility of a sample of the hematite nanoparticles. The system has two main components. The MS2E is a high sensitivity sensor used to measure the magnetic susceptibility of flat surfaces. The sensor has an operating frequency of 2 kHz and works by generating a weak applied field in the sample. The applied field then magnetizes the sample, the magnetization of the sample is then detected by a sensor and converted into magnetic susceptibility. The sensing area has a rectangular profile with dimentions 3.8 mm by 10.5 mm. The MS2E sensor has a maximum depth of signal penetration of approximately 6 mm, although the response is reduced by approximately 50% at 1 mm depth and almost by 90% at 3.5 mm depth.

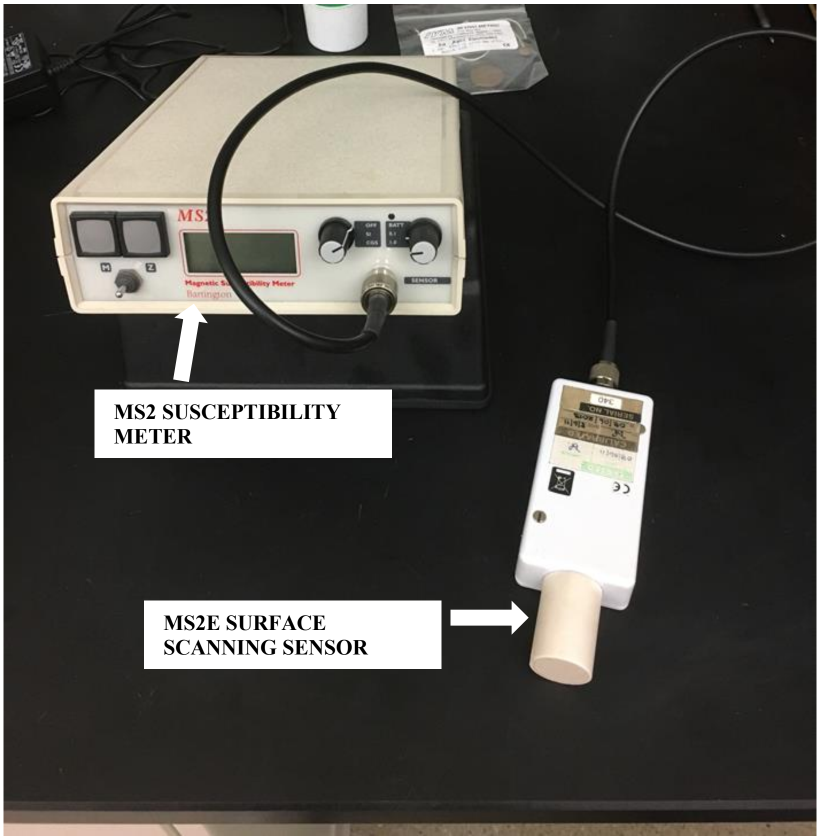

Figure 2.5: Bartington magnetic susceptibility surface scanning system (MS2E).

The second component of the system is an MS2 susceptibility meter to which the sensor is connected via a coaxial cable (similar to the connections for the MS2B and MS2C sensors). When set to high resolution mode the susceptibility reading with the MS2E sensor takes 15 seconds to complete, while the low resolution mode requires 1.5 seconds when using the SI unit setting.

2.3.5 Bartington Magnetic Susceptibility-Temperature System (MS2WF)

The experimental system used for the temperature dependent magnetic susceptibility experiments was purchased from Bartington and consists of five main components (**Figure 2.6**). The MS2WF furnace is a non-inductively wound platinum wire furnace with maximum operational temperature of 900 ˚C and a maximum sample capacity of 15 mm diameter. The furnace is mounted on a metal base, which has a digital temperature display.

The magnetic susceptibility readings are obtained via a MS2W water-jacket sensor. The sensor is mounted on the furnace platform and has a 30 mm internal diameter cavity allowing it to fit around the sample chamber. Water is continuously cycled through the sensor during its operation in order to maintain a stable temperature of the sensor and prevent temperature damage. The sensor is calibrated for a sample size of 10 cubic centimetres and has an operating frequency of 696 Hz. The sensor operates by generating an applied field through the sample in order to magnetize it. The sample magnetization is then determined from the frequency of oscillation detected by the sensor inductor. The magnetic susceptibility is displayed on an MS2 meter.

The MS2WFP is the power supply and control unit. It is directly connected to the furnace and supplies the electrical power for its operation. The unit also contains manual thermostatic controls such as ramp rate setting, linear increase or decrease of the temperature, as well as temperature hold setting. The MS2WFP power supply unit also supplies electricity and controls the water pump which circulates water through the MS2W sensor. The power supply unit also allows for an optional connection to a computer via a serial interface connection.

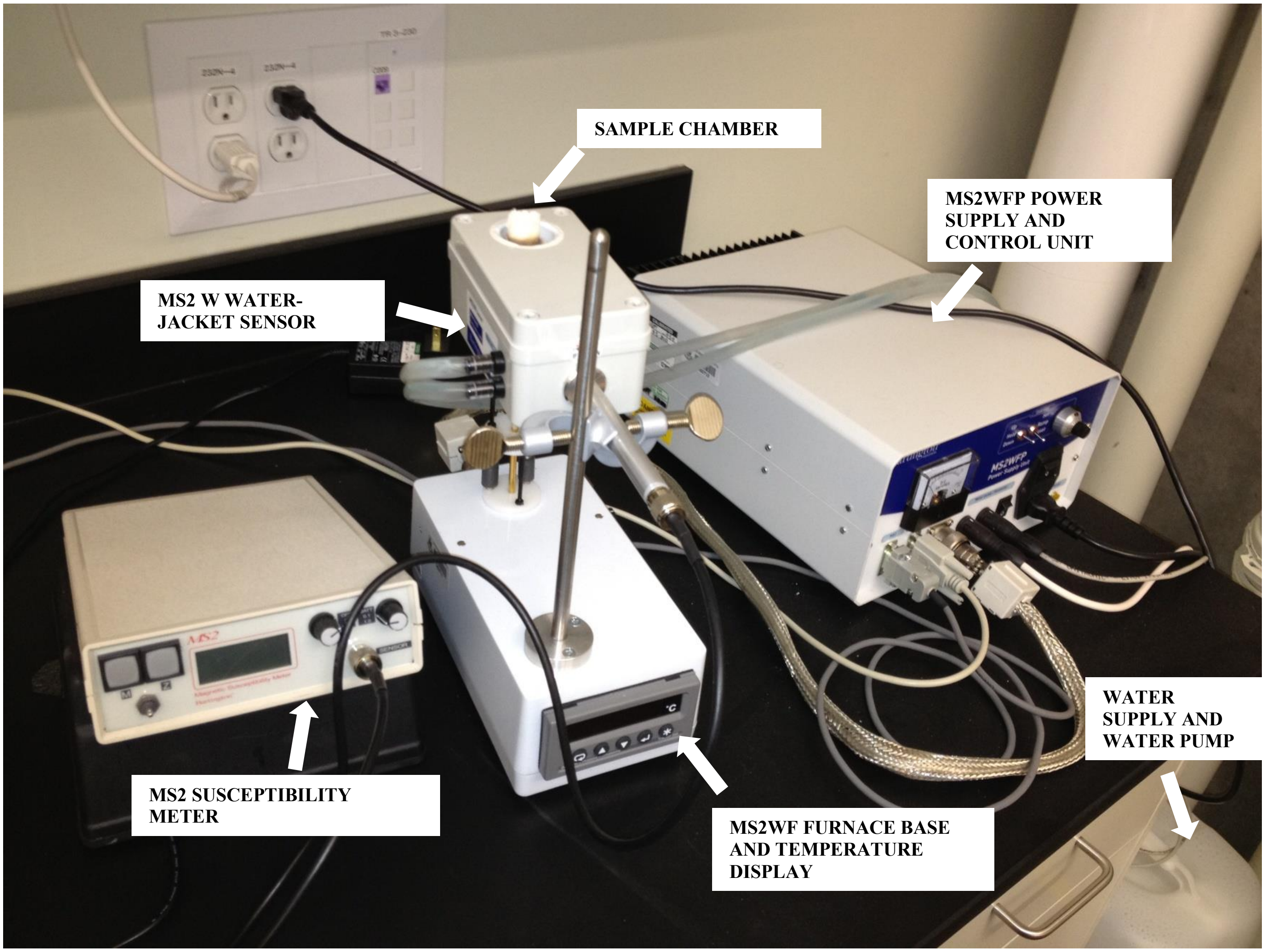

Figure 2.6: Bartington MS2 magnetic susceptibility-temperature system.

The water supply unit consists of a large container filled with water at room temperature and a pump which circulates the water through the MS2W sensor. The pump itself is located in the water container and is controlled and supplied with electricity from the MS2WFP power supply unit.

The MS2W sensor is connected to an MS2 meter which displays a digital read out of the magnetic susceptibility readings. In high resolution mode the susceptibility reading takes 24 seconds to complete, whilst the low resolution mode takes 2.4 seconds under the SI setting.

2.3.6 Variable Field Translation Balance

The Variable Field Translation Balance (VFTB) is a multifunctional magnetic system (**Figure 2.7**). It is generally used to measure the acquisition of isothermal remanent magnetization (IRM) and magnetic hysteresis curves in variable applied fields up to 1 Tesla. It can also be used for investigating the temperature dependence of those parameters. The VFTB produces separate inducing and gradient fields. The gradient field is produced by four gradient coils, which oscillate with a certain frequency (2-4 Hz). The oscillating part of the instrument contains the specimen in a weakly magnetic (actually diamagnetic) quartz glass sample holder. The gradient coils exert a periodic force on the specimen and excite the motion of the system. The motion is monitored by a linear variable differential transformer, whose signal is then processed and converted into the magnetization of the sample. The system contains a heating/cooling unit surrounding the sample holder which allows the temperature to be varied between -190 ˚C and 800 ˚C. This enables the recording of magnetic measurements at different temperatures, which means that reservoir temperatures can be simulated.

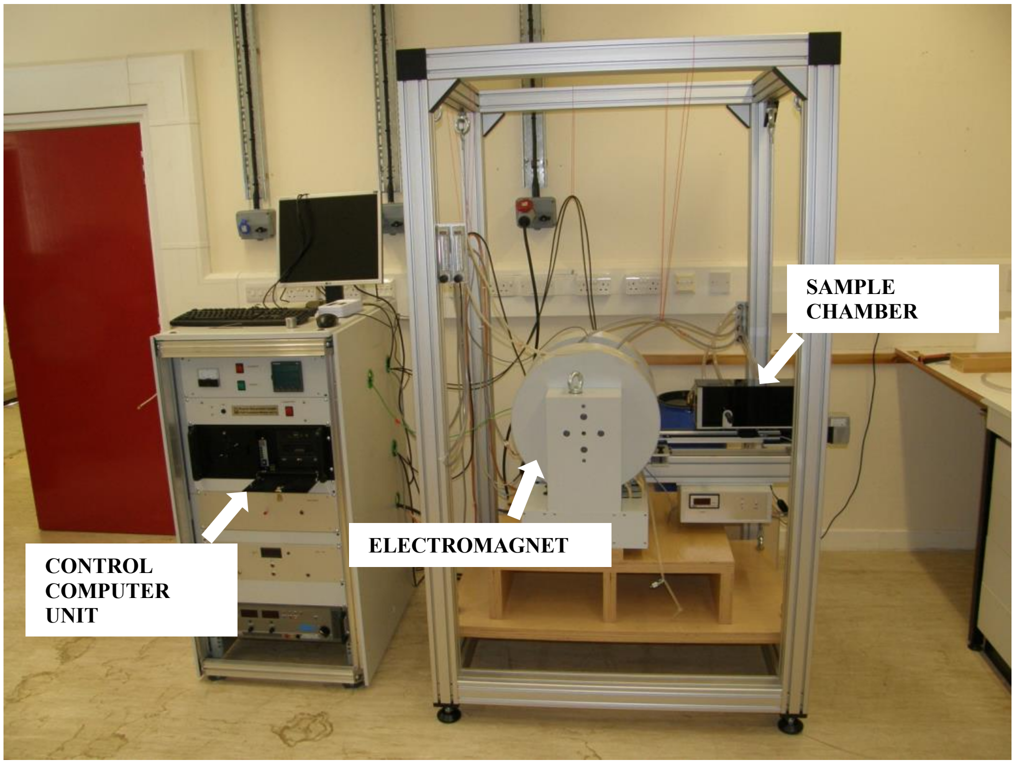

Figure 2.7: Variable Field Translation Balance (VFTB) system.

2.3.7 Sonicator

A Qsonica 500 (Q500) sonicator was used in the preparation of the nanoparticle suspensions (**Figure 2.8**). The sonicator consists of four main components. The power supply and control unit inputs standard AC current. It is rated for both the North American standard (100-120 V at 50/60 Hz) as well as the European standard (220-240 V at 50/60 Hz). The input energy is converted to an output voltage 1000 Vrms (max) with 20 kHz frequency. The convertor is connected to the power supply unit via a converter cable. Here the electric signal is converted by a transducer to mechanical vibrations. The vibrations are amplified and transmitted to the probe. The probe then longitudinally expands and contracts its tip. The distance the tip travels is proportional to the selected amplitude setting (higher amplitude results in an increase of sonication intensity). The stand holds the converter and probe upright and holds the sample container.

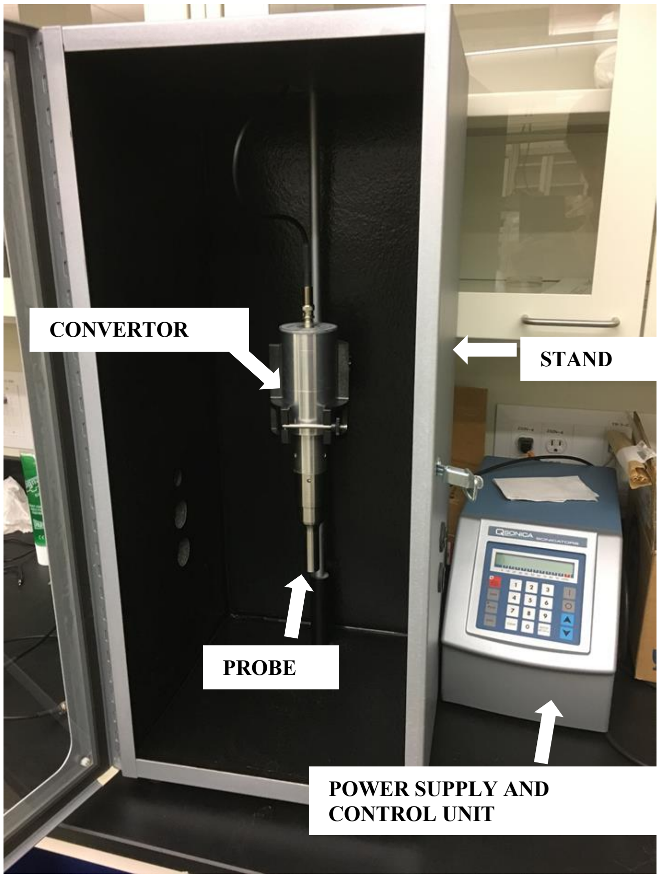

Figure 2.8: Qsonica 500 sonicator.

The system operates by generating microscopic bubbles at the tip of the probe. The collapse of those bubbles generates shock waves which break up and disperse nanoparticle agglomerates. The volume and intensity of this process is dependent on the amplitude setting of the system as well as the diameter of the probe tip in use. A larger tip diameter is able to process larger fluid volumes at the cost of sonication intensity. On the other hand lower tip diameters offer higher sonication intensity, but the energy is focused in a smaller area.

2.3.8 Weighing Balances

Two weighing balances were used for weighing the different materials. The Ohaus Pioneer PA64 scale was used for precise measurements of the nanoparticles, due to its high accuracy of up to 0.0001 g. Due to the low maximum capacity of the PA64 (of only 65 grams) the Ohaus Scout Pro was used when measuring heavier samples. The Scout Pro has a lower accuracy of 0.01 g but much greater capacity of up to 200 g.

2.3.9 Flow Cell

A PEEK flow cell was specially manufactured for the waterflood experiments, rather than a standard stainless steel flow cell, in order to be able to take magnetic susceptibility measurements with the surrounding MS2C coil sensor as the fluids were flowing. PEEK has a low magnetic susceptibility, thus allowing the signal from the nanoparticles to be readily seen. The PEEK flow cell was a Hassler-type vessel that allowed a confining pressure of 600 kPa (**Figure 2.9**). It was able to hold approximately 78 g of packed sand surrounded by a viton sleeve. The sandpack itself was 114.3 mm long with a diameter of approximately 22.2 mm (for waterflood 2). Additional end fittings were installed on both the injection and production ends of the flow cell. In the first waterflood experiment the fittings were metallic with high magnetic susceptibility giving an unwanted high background signal, while in the second waterflood experiment new PEEK end fittings were manufactured in order to reduce the background magnetic susceptibility signal.

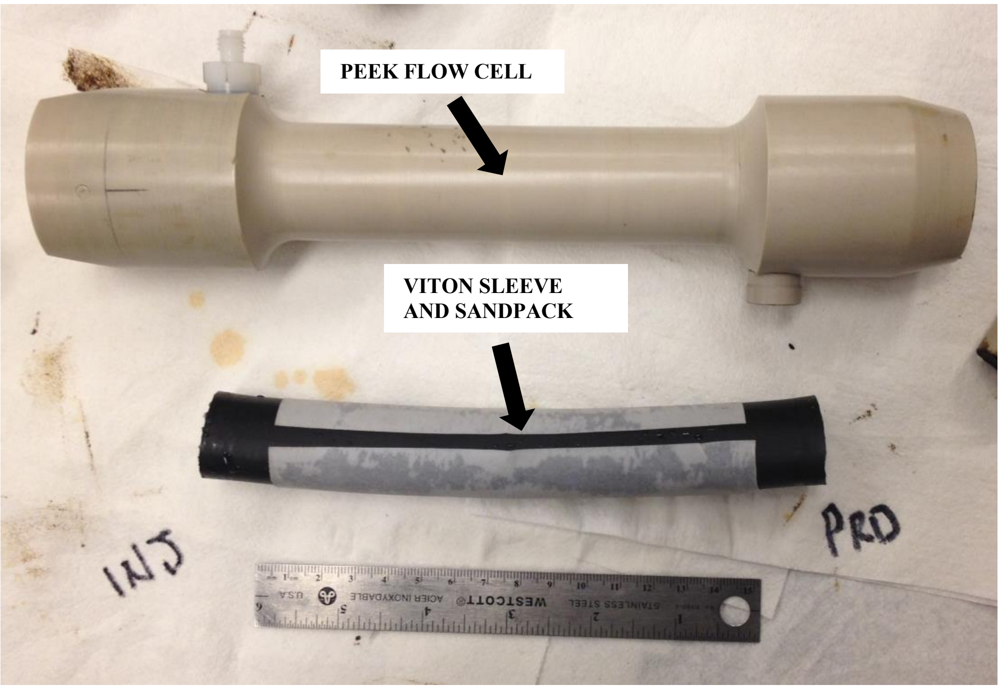

Figure 2.9: PEEK flow cell and viton sleeve. INJ and PRO refer to the injection and production ends respectively.

2.3.10 Core Plug Gas Permeability

Core plug permeability measurements were undertaken on some red sandstones (see **Chapter 5**), using a Hassler type flow cell and a Ruska type gas permeameter. Nitrogen gas was used and a Darcy type equation to obtain the permeability.

2.4 Methods and Experimental Procedures

This section will introduce the methods and experimental procedures performed over the course of this project. The first experimental procedures that will be covered are the ones for the general characterization of the magnetic nanoparticles followed by their magnetic characterization at room temperature. Then the magnetic experimental procedures for the nanoparticles under potential reservoir temperatures using different types of dispersants will be described. As hydrocarbon reservoirs generally have higher temperature conditions than those at the surface these experiments were critical in determining whether the nanoparticles could perform their function under reservoir temperatures. Once suitable nanoparticle compositions were determined stability experiments were performed in order to derive a suitable method for creating a stable dispersed nanoparticle suspension for injection into a sandpack. Finally the nanoparticle suspension was injected into a heavy oil saturated sandpack in an attempt to use the nanoparticle suspension as a tracer during the waterflooding process. Previous conventional tracers, such as CT scanning, had been ineffective due to the low CT contrast between the water and heavy oil (due to their similar densities).

2.4.1 Scanning Electron Microscopy (SEM) Procedures

In the SEM analysis a sample of an individual nanoparticle powder composition was mechanically dispersed and placed directly on the observation plate. The observation plates were then inserted into a Field Emission Scanning Electron Microscope and micrograph images of the individual samples were collected and analyzed. The samples were also subjected to an energy dispersive spectroscopy (SEM/EDS) microanalysis, which was used to provide the compositional makeup of the nanoparticles for comparison with the manufacturer specifications.

2.4.2 Transmission Electron Microscopy (TEM) Procedures

The Transmission Electron Microscopy (TEM) analysis allowed for the collection of micrographs of the nanoparticle samples at a much higher magnification compared to the SEM. The untreated nanoparticles were immersed in ethanol solution and then sonicated for 40 minutes in a bath sonicator. Following the sonication a drop of the solution was placed on an observation plate and allowed to air dry in order to allow the nanoparticles to settle out. The observation plate was then inserted in the TEM and micrographs of the individual samples were collected and analyzed.

TEM was also conducted on samples of maghemite, nickel ferrite and magnetite that had undergone a heating cycle. In these cases the nanoparticles had already been mixed with calcium fluoride powder (CaF_2) for their temperature dependent magnetic susceptibility measurements. The powder mixture was then immersed in ethanol and then sonicated for 40 minutes in a bath sonicator. A drop of each solution was placed on an observation plate and allowed to air dry. The observation plate was then inserted in the TEM and images of the individual samples were collected for analysis.

2.4.3 Molspin Susceptibility Bridge Experimental Procedure

A Molspin susceptibility bridge was used to measure the room temperature magnetic susceptibility of the nanoparticle samples dispersed in resin. In this measurement known amounts of nanoparticles were placed in plastic container tubes designed specifically to fit inside the Molspin susceptibility bridge (**Table 2.9**). Methyl methacrylate solution was then added to the nanoparticles. Following this cold mounting resin was continuously added to the container, while mechanically agitating the mixture. The addition of the cold mounting resin led to the thickening of the solution, and was continuously added until the desired viscosity was achieved (approximately 10000 cps, close to the viscosity of honey). The containers were then capped and the resin allowed to set hard. Subsequently their bulk magnetic susceptibilities were measured using the Molspin susceptibility bridge. The raw volume magnetic susceptibility values were converted using equation (2.1) in order to get the mass magnetic susceptibility for each sample as follows:

$$\chi_m = \frac{\chi_{raw} * 9.702 * 10^{-8}}{m} \tag{2.1}$$

Where:

- χ_m is the corrected mass magnetic susceptibility of the nanoparticles (10^{-8} m^3kg^{-1})
- χ_{raw} is the raw volume magnetic susceptibility measured by the Molspin susceptibility bridge (10^{-5} SI)

- $9.702 * 10^{-8}$ is the conversion factor for the Molspin susceptibility bridge for a 1 inch cylindrical sample (cm^3)
- m is the mass of the nanoparticles (g)

Table 2.9: Molspin susceptibility bridge experimental parameters.

Mineral	Mineral Mass (mg)	Volume Concentration (%)
Magnetite	53.6	0.08
Maghemite	53.5	0.08
Nickel Ferrite	55.9	0.08
Cobalt Ferrite	56.3	0.08

2.4.4 Bartington (MS2B Sensor) Volume Magnetic Susceptibility Analysis Procedure

This analysis was used to measure the volume magnetic susceptibility of the 30 nm hematite nanoparticles using a second independent instrument. This independent measurement was done because the Molspin results gave an unusual apparently diamagnetic (low negative magnetic susceptibility) signal, and thus the MS2B analysis was conducted on the hematite nanoparticles (without the resin) in order to test if it gave a similar result (this will be discussed in more detail in **Chapter 6**). The sample was prepared by mechanically dispersing a known amount of 30 nm hematite nanoparticles in a calcium fluoride powder (CaF_2) matrix. The MS2B sensor was zeroed and used to take an air magnetic susceptibility background measurement prior to the insertion of the sample container. The hematite sample was then inserted into the sample chamber and a magnetic susceptibility reading was taken using the low frequency setting of the sensor. Finally another air magnetic susceptibility measurement was taken in order to account for any instrumental drift while measuring the sample.

2.4.5 Bulk Volume Magnetic Susceptibility Experimental Procedure (MS2E Sensor)

In this experiment the bulk volume magnetic susceptibility of the powder hematite (30 nm spherical) nanoparticles in a calcium fluoride matrix (same concentration of nanoparticles as for the MS2B measurement above) was measured at room temperature using a Bartington MS2E probe sensor connected to a Bartington MS2 meter. This additional independent measurement was done to further examine the magnetic behavior of nanoparticle hematite following the unusual apparently diamagnetic signal results from the Molspin analysis (discussed in more detail in **Chapter 6**). The MS2E sensor was firstly zeroed away from any sources of interference, following which an air magnetic susceptibility background measurement was taken. The magnetic susceptibility of various parts of a large undispersed sample of the hematite nano-powder was then measured. Finally another air magnetic susceptibility measurement was taken in order to account for any instrumental drift while measuring the sample.

2.4.6 Magnetic Hysteresis Analysis Experimental Procedure

In this experimental procedure a Variable Field Translation Balance (VFTB) was used in order to measure the magnetization of the nanoparticles versus a variable applied field. The samples were prepared by mechanically mixing a known amount of nanoparticles with a known amount of calcium fluoride in order to increase the nanoparticle dispersion (see **Table 2.10**). The samples were then placed in quartz sample holders and inserted into the VFTB and their mass magnetization was measured versus an applied magnetic field at room temperature conditions.

The 8 nm and 40 nm hematite nanoparticles synthesized by laser ablation were already dispersed in water. In this case the dispersed suspensions were placed in the quartz sample containers and positioned in the VFTB. Again the mass magnetization of the dispersions was measured versus applied field at room temperature. Another set of measurements was conducted on the water sample used for dispersion for comparison with the two nanoparticle suspension results.

Table 2.10: Variable field translation balance (VFTB) experimental parameters.

Mineral	Mineral Mass (mg)	Mass of CaF_2 (mg)	Mass Concentration (%)
Magnetite	29	222	11.6
Maghemite	29	222	11.6
Nickel Ferrite	29	222	11.6
Cobalt Ferrite	29	222	11.6

2.4.7 Temperature Dependent Magnetic Susceptibility Measurements Experimental Procedures

This experiment used a Bartington MS2 Magnetic Susceptibility-Temperature System in order to determine the magnetic susceptibility of the nanoparticle suspensions under different simulated temperatures. The nanoparticles were also dispersed in different substances in order to determine the effect on the magnetic susceptibility response.

Curie Point Experimental Procedures (Calcium Fluoride Matrix)

The aim of this experiment was to compare the measured Curie temperatures of the nanoparticle powder samples to their expected theoretical values. This set of experiments was conducted to independently confirm the composition of the samples. Such high temperatures are not expected in actual oil and gas reservoirs. All the nanoparticle powders were tested with the exception of the hematite sample (as it was earlier established that the magnetic susceptibility of the hematite sample was too low to be useful as a tracer).

In this experiment a known amount of the nanoparticle powder was placed in a ceramic test container, following which a known amount of calcium fluoride (CaF_2) powder was added to act as a dispersing matrix (see **Table 2.11**). The two powders were mechanically mixed in order to increase the nanoparticle dispersion. After mixing the ceramic test containers were capped and placed inside the Bartington MS2WF furnace. The furnace was prepared by zeroing the magnetic sensor prior to the nanoparticle insertion and taking air measurements for drift correction before and after the experiment. Once inserted the samples were heated steadily at a rate of 5˚C/min in air. Measurements of the magnetic susceptibility were taken at regular intervals as the temperature was increased until the Curie point was reached for each sample. The magnetic susceptibility was also recorded during the cooling cycle of the samples in order to check for any chemical changes (such as nanoparticle oxidation). The nanoparticles examined in this set of experiments had high positive magnetic susceptibilities, whilst the ceramic sample container and calcium fluoride matrix were diamagnetic.

The raw data was corrected for instrumental drift using the initial and final air magnetic measurements, and the mass magnetic susceptibilities of the nanoparticle samples were calculated using equation (2.2).

$$\chi_m = \frac{\chi_d * 10}{m} \tag{2.2}$$

Where:

- χ_m is the mass magnetic susceptibility of the nanoparticles (10^{-8} m^3kg^{-1})
- χ_d is the drift corrected magnetic susceptibility measured by the MS2W sensor (10^{-5} SI)
- 10 is the calibration sample size for the MS2W sensor (cm^3)
- m is the mass of the nanoparticles (g)

Table 2.11: Curie point experimental parameters.

Mineral	Mineral Mass (mg)	Mass of CaF_2 (mg)	Mass Concentration (%)
Magnetite	136.9	858.8	13.7
Maghemite	131.8	891.6	12.9
Nickel Ferrite	79.3	1246.4	6.0
Cobalt Ferrite	164.1	801.6	17.0

Reservoir Temperature Magnetic Susceptibility Experimental Procedures (Calcium Fluoride Matrix)

This set of experiments aimed to determine the magnetic susceptibility response of the nanoparticles at reservoir temperatures. A known amount of nanoparticles was placed in a ceramic sample container and mechanically mixed in a known amount of calcium fluoride dispersing matrix (see **Table 2.12**). The containers were then capped and placed inside the Bartington MS2WF furnace. The nanoparticles were heated steadily at a rate of 5˚C/min, while measurements of their magnetic susceptibility were taken at regular intervals as the temperature was increased to approximately 200 ˚C (this maximum temperature was chosen as hydrocarbon reservoirs generally have in situ temperatures below this). The magnetic susceptibility was also recorded during the cooling cycle in order to check for any chemical changes. As most nanoparticle compositions exhibited high magnetic susceptibilities compared to the diamagnetic ceramic sample container and calcium fluoride dispersing matrix, their mass magnetic susceptibilities were calculated using equation (2.2). The one exception was the hematite (30 nm particle) sample. The results for the 30 nm hematite nanoparticles were discarded as the sample failed to produce a detectable result (due to its low magnetic susceptibility).

Table 2.12: Experimental parameters for reservoir temperature magnetic susceptibility experiments in calcium fluoride dispersing matrix.

Mineral	Mineral Mass (mg)	Mass of CaF_2 (mg)	Mass Concentration (%)
Magnetite	103.4	1160.8	8.2
Maghemite	82.3	992.7	7.7
Nickel Ferrite	50.6	1231.7	3.9
Cobalt Ferrite	72.7	1170.3	5.8

Reservoir Temperature Magnetic Susceptibility Experimental Procedures (Water Matrix)

As the main potential application for the magnetic nanoparticles is as contrast agents during waterflooding of heavy oil, and also in situations involving water based drilling muds or hydraulic fracturing fluids, understanding their behavior when mixed with water was paramount.

In these experiments a known amount of nanoparticles was first placed in a crystal sample container (see **Table 2.13**). A known amount of water then was added and mechanically mixed with the nanoparticles. The containers were then capped and inserted into the Bartington MS2WF furnace. The nanoparticles were heated steadily at a rate of 5˚C/min, and measurements of their magnetic susceptibility were taken at regular intervals as the temperature was increased to approximately 95 ˚C (in order to avoid evaporation which could potentially damage the furnace). The magnetic susceptibilities were recorded during the cooling cycle as well in order to check for any chemical changes. The data was drift corrected, following which, the mass magnetic susceptibilities of the nanoparticle samples were calculated using equation (2.2) directly.

Table 2.13: Experimental parameters for reservoir temperature magnetic susceptibility experiments in water dispersing matrix.

Mineral	**Mineral Mass (mg)**	**Mass of Water (mg)**	**Mass Concentration (%)**
Magnetite	48.7	1248.9	3.8
Maghemite	33.2	1444.1	2.2
Nickel Ferrite	49.8	1387.1	3.5
Cobalt Ferrite	79.5	1409.6	5.3

Reservoir Temperature Magnetic Susceptibility Experimental Procedures (Oil Based Drilling Mud Matrix)

In some cases it may be useful to use nanoparticles with oil based drilling mud (for example when there are swelling clays present when it is not suitable to use water based drilling mud). The procedure was similar to that for the water matrix experiments (see **Table 2.14** for experimental parameters).

Table 2.14: Experimental parameters for reservoir temperature magnetic susceptibility experiments in oil based drilling mud dispersing matrix.

Mineral	Mineral Mass (mg)	Mass of Oil Mud (mg)	Mass Concentration (%)
Magnetite	15.7	1716.3	0.9
Maghemite	57.9	1845.1	3.0
Nickel Ferrite	32.4	1723.1	1.8
Cobalt Ferrite	9.9	1780.7	0.6

Reservoir Temperature Magnetic Susceptibility Experimental Procedures (Stabilized Nanoparticle Dispersions)

After generating stabilized nanoparticle dispersions it was imperative to test their magnetic susceptibility behavior under reservoir temperatures. Thus in this experiment stabilized dispersed nanoparticle suspensions were prepared using deionized water and DDBS using the Trial #5 stability experimental procedure (see **Section 2.4.8** below). The stability procedure for Trial #5 was chosen as it proved effective in creating maghemite dispersions, which were stable over long periods of time. The magnetic susceptibility measurement procedure was similar to that in the previous two sections.

Table 2.15: Experimental parameters for reservoir temperature magnetic susceptibility experiments in oil based drilling mud dispersing matrix.

Mineral	Mineral Mass (g)	Mass of Water (g)	Mass of DDBS (g)	Mass Concentration (%)
Magnetite	0.078	130.56	0.6498	0.06
Maghemite	0.1033	130.72	0.7608	0.08
Nickel Ferrite	0.126	127.5	0.6286	0.10

2.4.8 Stability Experiments Procedures

The aim of these experiments was to provide dispersed nanoparticle suspensions that were stable over long time periods of days to weeks. Since the nanoparticle suspensions were to be used ultimately as contrast agents for imaging the waterflooding of heavy oil, it was important that the nanoparticles remained stable (i.e., suspended) and did not settle out during the course of the waterflooding. The procedures for the production of the stabilized suspensions were modified from the initial ones proposed by Khan (2012a), Khan (2012b) and Khan et al. (2015). The stabilized suspensions were to be used for multimodal imaging of fluid flow combining magnetic susceptibility and CT scanning in the imaging of heavy oil waterflooding. Due to the similar densities of heavy oil and water, sodium iodide was another necessary ingredient as a contrast agent for the CT scanner. The dispersions needed to include this component.

Stability Experiment Trial #1

In this experiment a known amount of maghemite nanoparticles were mixed in a beaker with a known amount of deionized water, and mechanically mixed. A known amount of the anionic dispersant DDBS was added to the mixture, and after mechanical agitation the desired amount of sodium iodide was added. The final mixture was placed in the Qsonica sonicator and sonicated for 40 minutes at a pulse setting of 10 seconds on and 10 seconds off. The dispersion was then transferred into a graduated cylinder and its volume magnetic susceptibility was measured at different heights using the MS2C core logging magnetic sensor. **Figure 2.10** shows the experimental set up used for the stability Trials. The MS2C sensor was zeroed prior to each measurement and a background air measurement was taken before and after each sample reading in order to account for instrumental drift. The behavior of the suspension was observed with time both qualitatively (by photographing the graduated cylinder) and quantitatively (by measuring the magnetic susceptibility profile of the graduated cylinder at later times).

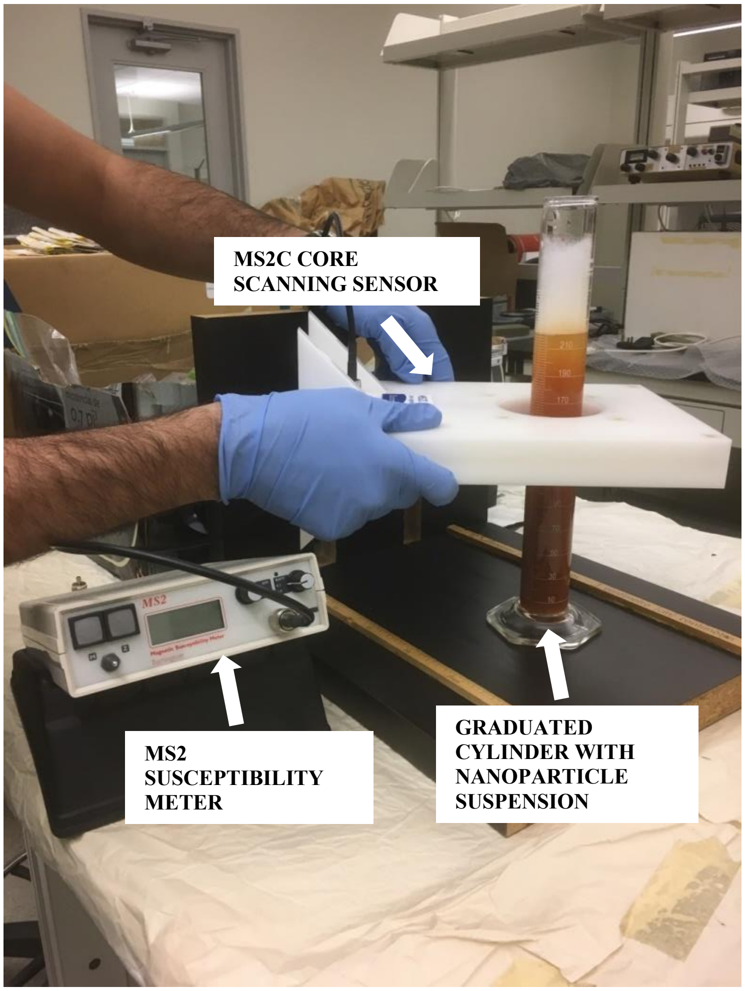

Figure 2.10: Experimental set up for stability experiments.

Stability Experiment Trial #2

In this experiment the desired amount of sodium iodide was mixed in a beaker with a known amount of deionized water. After mechanical agitation of the solution a known amount of maghemite nanoparticles was mixed in. While mechanically agitating the mixture a known amount of DDBS was added in. The final mixture was placed in the Qsonica sonicator and sonicated for 40 minutes at a pulse setting of 10 seconds on and 10 seconds off. The suspension was then transferred into a graduated cylinder and its magnetic susceptibility was measured at different heights using the MS2C core logging magnetic sensor. The behavior of the suspension was observed with time both quantitatively and qualitatively.

Stability Experiment Trial #3

In this experiment a known amount of maghemite nanoparticles were mixed in a beaker with a known amount of deionized water, and mechanically mixed. A known amount of DDBS was added to the mixture and after mechanical agitation the desired amount of sodium iodide was mixed in. The final mixture was put in an ice bath (the ice bath was introduced in order to limit the Brownian motion due to heating during the sonication process) and placed in the Qsonica sonicator and sonicated for 20 minutes using a continuous setting. The suspension was then transferred into a graduated cylinder and its magnetic susceptibility was measured at different heights using the MS2C core logging magnetic sensor. The behavior of the suspension was observed with time both quantitatively and qualitatively.

Stability Experiment Trial #4

In this experiment the desired amount of sodium chloride was mixed in a beaker with a known amount of deionized water. After mechanical agitation of the solution a known amount of maghemite nanoparticles was mixed in. While mechanically agitating the mixture a known amount of DDBS was added in. The final mixture was put in an ice bath and placed in the Qsonica sonicator and sonicated for 20 minutes using a continuous setting. The suspension was then transferred into a graduated cylinder and its magnetic susceptibility was measured at different heights using the MS2C core logging magnetic sensor. The behavior of the suspension was observed with time both quantitatively and qualitatively.

Stability Experiment Trial #5

In this experiment a known amount of maghemite nanoparticles were mixed in a beaker with a known amount of deionized water, and mechanically mixed. The desired amount of DDBS was then added in and the suspension was mechanically agitated again. The final suspension was put in an ice bath and then placed in the Qsonica sonicator and sonicated for 20 minutes using a continuous setting. The suspension was then transferred into a graduated cylinder and its magnetic susceptibility was measured at different heights using the MS2C core logging magnetic sensor. The behavior of the suspension was observed with time both quantitatively and qualitatively.

Stability Experiment Trial #6

In this experiment a larger amount of maghemite nanoparticles were mixed in a beaker with a known amount of deionized water, and mechanically mixed. The desired amount of DDBS was then added and the suspension was mechanically agitated again. The final suspension was put in an ice bath and then placed in the Qsonica sonicator and sonicated for 20 minutes using a continuous setting. The suspension was then transferred into a graduated cylinder and its magnetic susceptibility was measured at different heights using the MS2C core logging magnetic sensor. The behavior of the suspension was observed with time both quantitatively and qualitatively.

2.4.9 Waterflood Experiment 1 Procedure

In this experiment a viton sleeve was packed with 78 grams of F110 sand and then inserted into the PEEK flow cell (**Figures 2.11 & 2.12**). The sandpack was 109.5 mm long and approximately 22 mm in diameter. The core material is water wet Ottawa sand, F110 from the U.S. Silica Company. F110 is a pure quartz sand (99.8% SiO_2) with minor amounts of Fe_2O_3, Al_2O_3 (<0.1% each), and other oxides. Grain diameter is 50–150 µm. Particles are subangular, and the size distribution is as follows: 8% 53–75 µm, 25% 75–106 µm, 44% 106–150 µm, 18% 150–212 µm, and 4% 150–212 µm, with <1% beyond the upper and lower limits. The median particle diameter is 85 µm, the median pore diameter 46 µm, and the median throat diameter 18 µm. The absolute permeability was estimated to be 5 Darcy (which was calculated from the size distribution of the sand grains and the resulting porethroats distribution). A set of dry CT scans were collected as a baseline of the sand packed flow cell prior to flooding. Following the CT scans the flow cell was injected with two pore volumes of brine solution. The composition of the brine solution was 6.5 wt. % NaI and 1800 ppm Flopaam 3630 s polymer in deionized water. The polymer was added to the brine as it was also added to the nanoparticle suspension (that was later injected) in an attempt to increase the viscosity of the nanoparticle suspension and potentially help its stability. This step was necessary as the presence of sodium iodide was deemed crucial for the CT scanner contrast ratio and had to be included in the nanoparticle suspension even though it had proved to destabilize the suspension and lead to the settling out of the nanoparticles. The solution was injected at approximately 60 mL/hr, and each pore volume was approximately 15 cc (the constant flow rate was achieved by using a computer controlled pump that ensured a constant volume flux). Following the brine injection another set of CT scans was collected as brine baseline values. The flow cell was then oil flooded with heavy oil (with viscosity 20,000 cP) at a rate of approximately 1mL/hr for two pore volumes. This was followed by another set of CT scans for the oil baseline values. A magnetic susceptibility baseline of the oil flooded cell was also collected using the MS2C magnetic sensor. The sensor was firstly zeroed and an air measurement was taken for the drift correction of the data. The volume magnetic susceptibility profile of the flow cell was then measured at 5 mm intervals using the high sensitivity setting. The baseline readings in this experiment were high due to the metallic end fittings to the flow cell. This made it somewhat difficult to distinguish the signal due to the nanoparticle dispersion during injection in the sandpack.

The dispersed nanoparticle suspension was created using maghemite and a modified version of the Trial #2 stability experiment. In this case Flopaam 3630 s polymer was diluted to 1800 ppm in deionized water. Sodium iodide was the added to the solution at approximately 6.5 wt. % and the mixture was mechanically agitated. Maghemite nanoparticles were then added at 0.05 wt. % to the brine solution and then mechanically agitated followed by a 1 minute sonication in the Qsonica sonicator. Finally the DDBS surfactant was mechanically mixed in the nanoparticle-brine suspension. The final mixture was sonicated in the Qsonica sonicator for 40 minutes using a pulse setting of 10 seconds on and 40 seconds off.

The nanoparticle suspension was then placed in the injection accumulator container and attached to a KS500 IKA-WERK shaker assembly, which was continually moving in an effort to keep the nanoparticles suspended during the injection phase. Two pore volumes of the nanoparticle suspension were injected into the flow cell with an approximate injection rate of 1.45 mL/hr. During the injection CT scans and volume magnetic susceptibility sensor measurements were collected at regular intervals of approximately 1 hour during the daily observations.

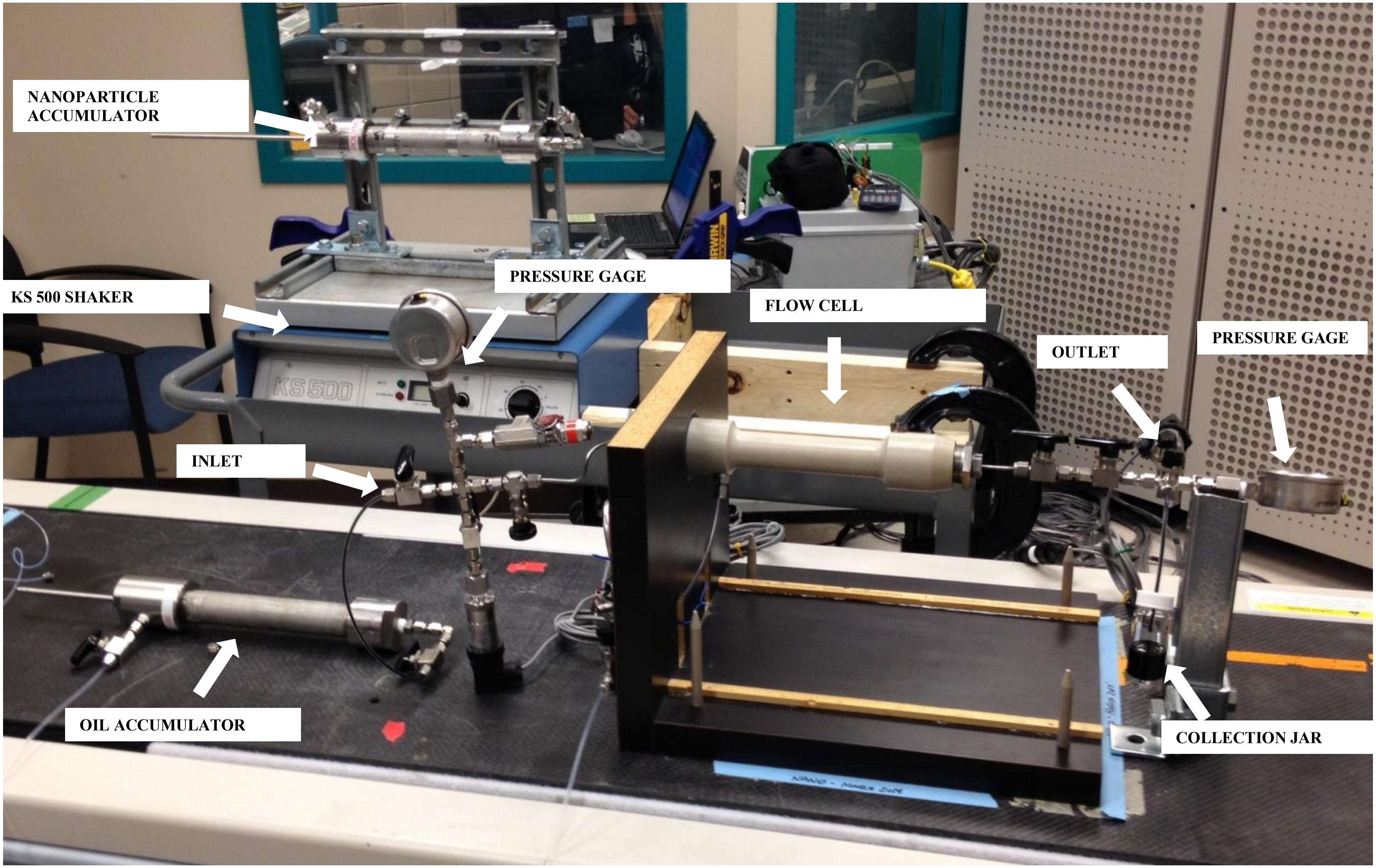

Figure 2.11: Experimental set up for Waterflood 1 experiment.

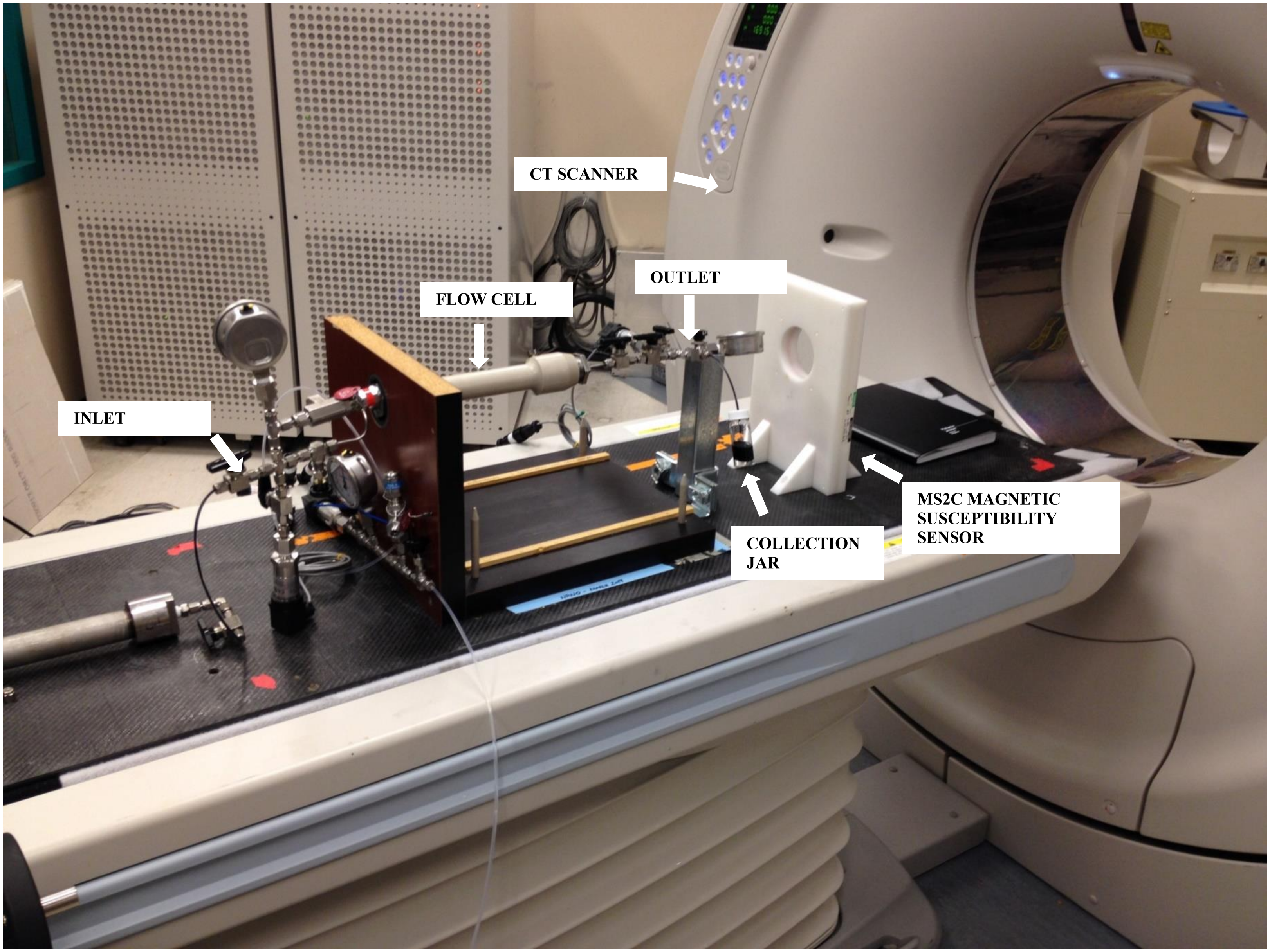

Figure 2.12: Experimental set up for Waterflood 1 experiment (second angle).

A background magnetic air measurement was taken at the end of each day, which was combined with the background magnetic air measurement at the beginning of each day in order to subtract any instrumental drift.

2.4.10 Waterflood Experiment 2 Procedure

The second waterflood experiment aimed to improve on the procedure of the waterflood 1 experiment. In this experiment the metallic end fittings of the flow cell were replaced by PEEK end fittings. This significantly reduced the baseline magnetic susceptibility readings, making it much easier to track the subsequent injection of the nanoparticles.

In this experiment a Viton sleeve was packed with 79.9 grams of F110 sand and then inserted into the PEEK flow cell (**Figures 2.13 - 2.15**). The sandpack was 114.3 mm long and approximately 22.2 mm in diameter. The other properties of the sandpack were similar to those of Waterflood 1. A set of dry CT baseline scans were collected, following which the flow cell was injected with two pore volumes of deionized water, with each pore volume being approximately 16.7 cc. Following the water injection a set of CT scans were collected as wet baseline values. The flow cell was then flooded with heavy oil at a rate of approximately 0.5 mL/hr for 1.2 pore volumes. Sets of CT and volume magnetic susceptibility sensor baseline scans were collected of the flow cell prior to the nanoparticle injection.

The nanoparticle suspension for this experiment was created using maghemite nanoparticles at a concentration of 0.6 wt. % and the experimental procedure of the Trial #6 stability experiment. This procedure dramatically improved the stability of the nanoparticles over long periods of time, and meant that there was no need for a shaker assembly to keep the nanoparticles suspended this time. The nanoparticles were then injected at a rate of 1mL/hr for a total of 1.75 pore volumes. During the injection CT scans and volume magnetic susceptibility sensor measurements were collected at regular intervals of approximately 1 hour during the daily observations. A magnetic air measurement was taken before and after each profile scan in order to calculate the instrumental drift correction.

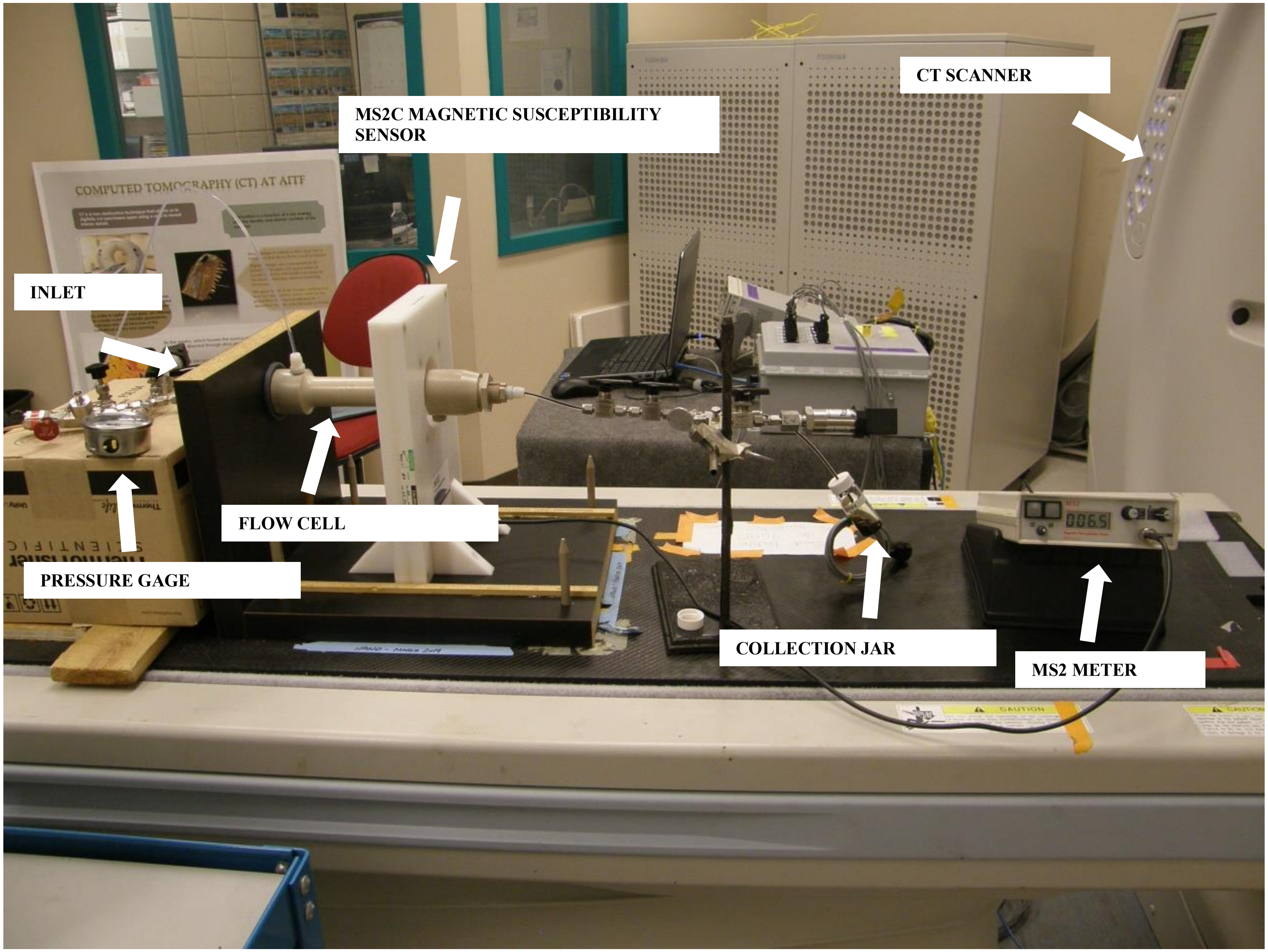

Figure 2.13: Experimental set up for Waterflood 2 experiment.

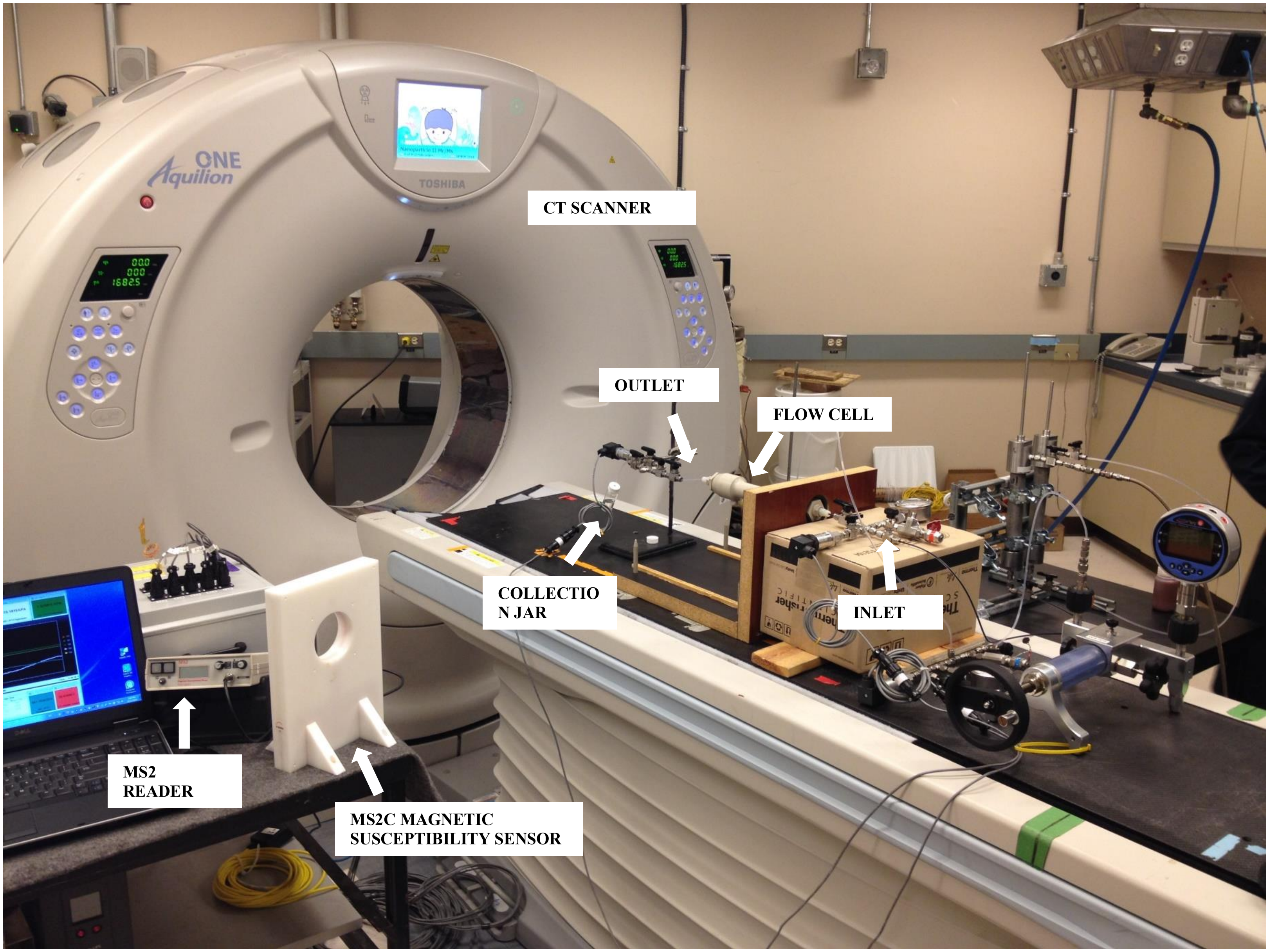

Figure 2.14: Experimental set up for Waterflood 2 experiment (second angle).

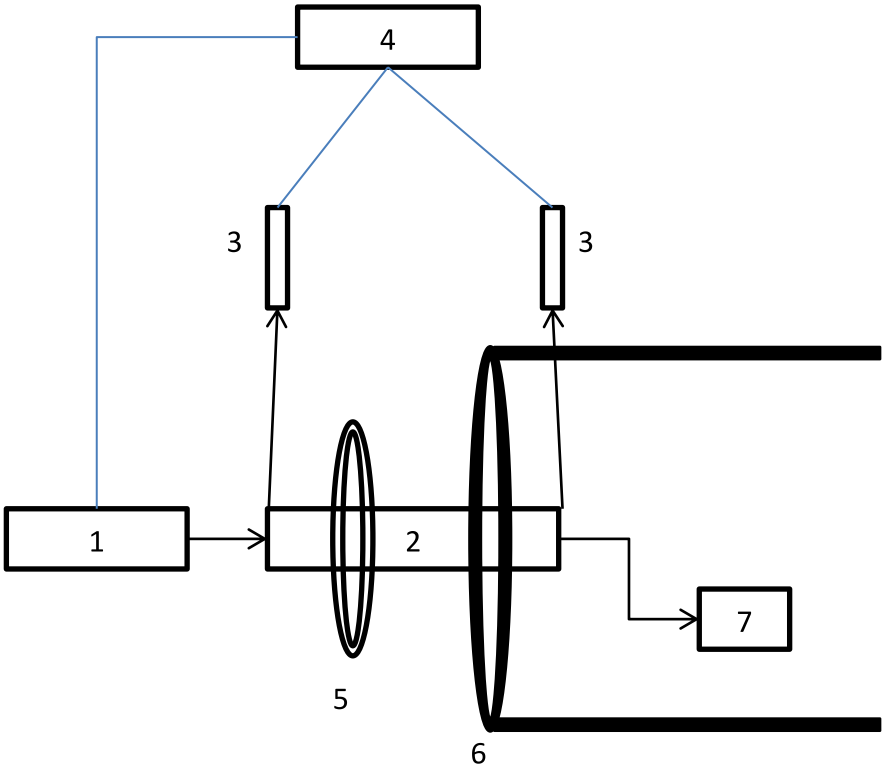

1. Nano-fluid accumulator
2. Oil flooded sandpack
3. Inlet and outlet pressure sensors
4. Flow rate control and pressure data logging computer
5. MS2C magnetic susceptibility sensor
6. CT scanning sensor
7. Production collection jar

Figure 2.15: Experimental schematic for Waterflood 2 experiment.

2.4.11 Core Plug Gas Permeability Experimental Procedure

Core plug permeability measurements were taken on some red sandstones (see **Chapter 5**). Nitrogen gas was flowed through the core plugs. The flow rate and initial and final pressures were measured and input into a Darcy type equation to obtain the permeability. The values were not Klinkenberg corrected, since the uncorrected values were a better comparison with probe permeability measurements on slabbed core of the same material previously undertaken by Potter et al. (2009).

2.5 References

- Argyle, K. S., and Dunlop, D. J., 1984. Theoretical domain structure in multidomain magnetite particles. Geophysical Research Letters, **95**, 7069-7083.
- Bando, Y., Kiyama, M., Yamamoto, N., Takada, T., Sjinjo, T., and Takaki, H., 1965. Magnetic properties of α-Fe_2O_3 fine particles. Journal of the Physical Society of Japan, **20**, 2086.
- Banerjee, S. K., 1971. New grain size limits for palaeomagnetic stability in hematite. Nature Physical Science, **232**, 15-16.
- Chinnasamy, C. N., Jeyadevan, B., Shinoda, K., Djayaprawira, D. J., Takahashi, M., Joseyphus, R. J., and Narayanasamy, A., 2003. Unusually high coercivity and critical singe-domain size of nearly monodisperesed $CoFe_2O_4$ nanoparticles. Applied Physics Letters, **83**, 2862-2864.
- Dunlop, D. J., 1973. Superparamagnetic and single-domain threshold sizes in magnetite. Journal of Geophysical Research, **78**, 1780-1793.
- Dunlop, D. J., and Bina, M-M. 1977. The coercive force spectrum of magnetite at high temperatures: evidence for thermal activation below blocking temperature. Geophysical Journal International, **51**, 121-147.
- Ghazanfari, M. R., Kashefi, M., Shams, S. F., and Jaafari, M. R., 2016. Perspective of Fe_3O_4 nanoparticles role in biomedical applications. Biochemistry Research International, **2016**, Article ID 7840161, 32 pp.
- Halbreich, A., Roger, J., Pons, J. N., Geldwerth, D., Da Silva, M. F., Roudier, M., and Bacri, J. C., 1998. Biomedical applications of maghemite ferrofluid. Biochimie, **80**, 5-6, 379-390.
- Jensen, J., 1999. Fate and effects of linear alkylbenzene sulphonates (LAS) in the terrestrial environment. Science of The Total Environment, **226**, 2-3, 93-111.
- Jiang, J. and Yang, Y-M., 2007. Facile synthesisof nanocrystalline spinel $NiFe_2O_4$ via a novel soft chemistry route. Material Letters, **61**, 4276-4279.
- Kamble, R. B., Varade, V., Ramesh, K. P., and Prasad, V., 2015. Domain size correlated magnetic properties and electrical impedance of size dependent nickel ferrite nanoparicles. AIP Advances, **5**, 017119-1 – 017119-13.

- Khan, M. M., 2012b. A laboratory study of the effect of ionic strength on the stability of nanoparticle suspensions using a magnetic technique. M. Eng. report, University of Alberta, Department of Civil and Environmental Engineering, Edmonton, Canada, 25 pp.
- Khan, S., 2012a. A laboratory study of the stability and flow of nanoparticle suspensions through porous media using magnetic techniques. M.S. thesis, University of Alberta, Department of Civil and Environmental Engineering, Edmonton, Canada, 147 pp.
- Khan, S., Potter, D. K., and Kuru, E., 2015. Quantifying the transport of superparamagnetic nanoparticles in porous media using an acrylic flow cell and integrated magnetic susceptibility sensor technique. Transport in Porous Media, **106**, 691-705.
- Krishnan, K. M., 2010. Biomedical Nanomagnetics: a spin through possibilities in imaging, diagnostics, and therapy. IEEE Transactions on Magnetics, **46**, 2523-2558.
- MacNab, T. K., Fox, R. A., and Boyle, A. J. F., 1968. Some magnetic properties of magnetite (Fe_3O_4) microcrystals. Journal of Applied Physics, **39**, 5703-5711.
- Morrish, A. H., and Yu, S. P., 1955. Dependance of the coercive force on the density of some iron oxide powders. Journal of Applied Physics, **26**, 1049-1055.
- Nordin, M., and Frankel, V. H., 2001. Basic biomechnics of the musculoskeletal system. Lippincott Williams and Wilkins, 467 pp.
- Roger, J., Pons, J. N., Massart, R., and Halbreich A., 1999. Some biomefical applications of ferrofluids. The European Physical Journal Applied Physics, **5**, 321-325.

Chapter 3

CHARACTERIZATION OF MAGNETIC NANOPARTICLES FOR POTENTIAL RESERVOIR APPLICATIONS

3.1 Introduction

Advances of nanoparticle applications within the oil and gas industry have been relatively slow, even though nanotechnology is already being utilized in the medical and electronics sectors. The slow progress of nanoparticle applications is partly due to the harsh environmental conditions of hydrocarbon reservoirs. If nanoparticles are to be successfully utilized they would need to be able to withstand the high temperatures and pressures of oil and gas reservoirs. A further concern when injecting nanoparticles within a hydrocarbon reservoir is the possibility of forming larger particle agglomerates that could damage the reservoir quality. If those issues can be addressed nanoparticles would have a number of potential practical applications such as magnetic sensing or enhancing the oil recovery of a reservoir (Barron et al., 2010; Johnson 2010). Thus any potential nanoparticle composition would need to undergo rigorous laboratory testing before being suitable for field applications.

This chapter will detail the results of the characterization of the magnetic nanoparticles. There were four potential magnetic nanoparticle compositions that were considered: magnetite, maghemite, nickel ferrite and cobalt ferrite. Hematite nanoparticles were initially purchased as a fifth potential candidate, but will be examined separately (in **Chapter 6**) due to their very different behaviour that they displayed during their characterization. The four nanoparticle compositions were subjected to two types of characterization. First they underwent general microscopic physical characterization. This was followed by examination of their magnetic properties. The key purposes of the magnetic characterization were (1) to see whether their magnetic susceptibilities were sufficiently high to be used as contrast agents when injected in a hydrocarbon reservoir, and (2) to determine how their magnetic susceptibilities would be affected under reservoir temperature conditions in different solid and liquid matrix materials.

3.2 Initial Microscopic Characterization of Magnetic Nanoparticle Compounds

3.2.1 Scanning Electron Microscopy (SEM)

Scanning electron microscopy (SEM) was the first characterization that the nanoparticles underwent. Using an SEM the nanoparticles first underwent an energy dispersive spectroscopy (SEM/EDS) analysis. The SEM/EDS micro-analysis was conducted on all nanoparticle powders in order to confirm their elemental composition (**Figures 3.1-3.4**) and compare it to the manufacturer specifications. Although SEM/EDS is not as accurate as X-ray diffraction analysis, it was still able to identify all of the nanoparticle compositions successfully. All four of the nanoparticles examined in this section displayed elemental peaks which were consistent with the expected results from their chemical compositions and the manufacturers' specifications.

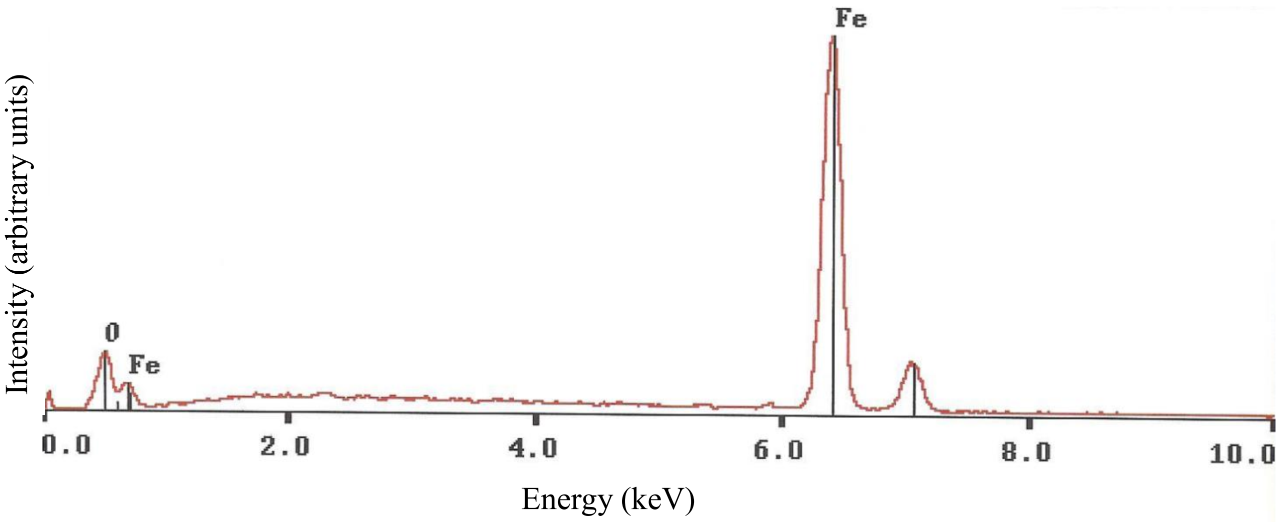

Figure 3.1: SEM/ESD micro-analysis of the 20 nm magnetite nanoparticle powder. The experimental red curve coincides with the expected black peaks for the examined nanoparticle powder composition.

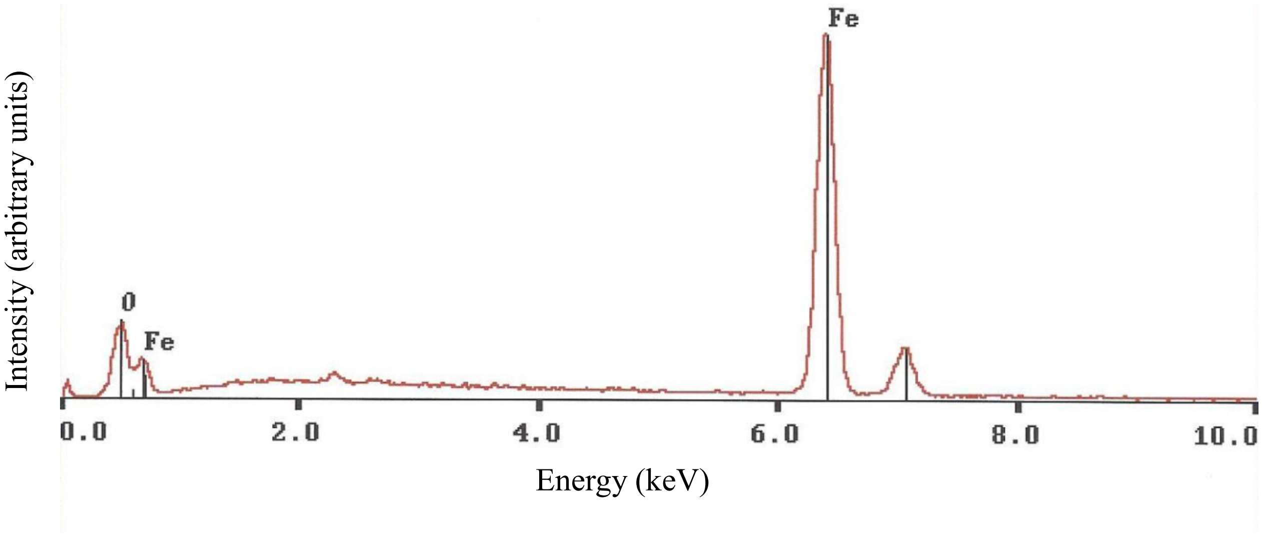

Figure 3.2: SEM/ESD micro-analysis of the 20 nm maghemite nanoparticle powder. The experimental red curve coincides with the expected black peaks for the examined nanoparticle powder composition.

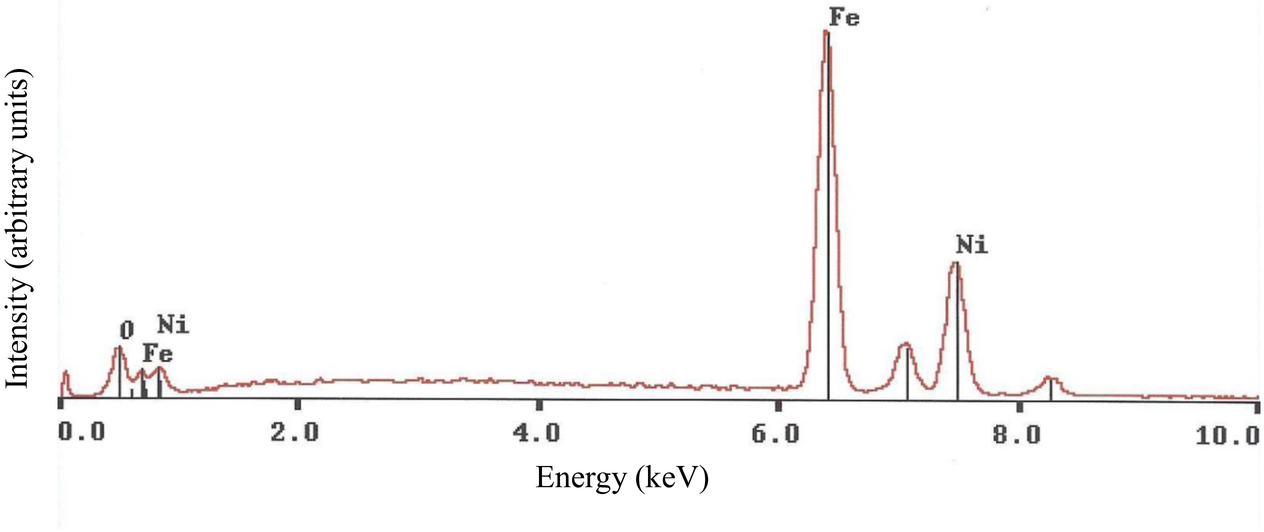

Figure 3.3: SEM/ESD micro-analysis of the 30 nm nickel ferrite nanoparticle powder. The experimental red curve coincides with the expected black peaks for the examined nanoparticle powder composition.

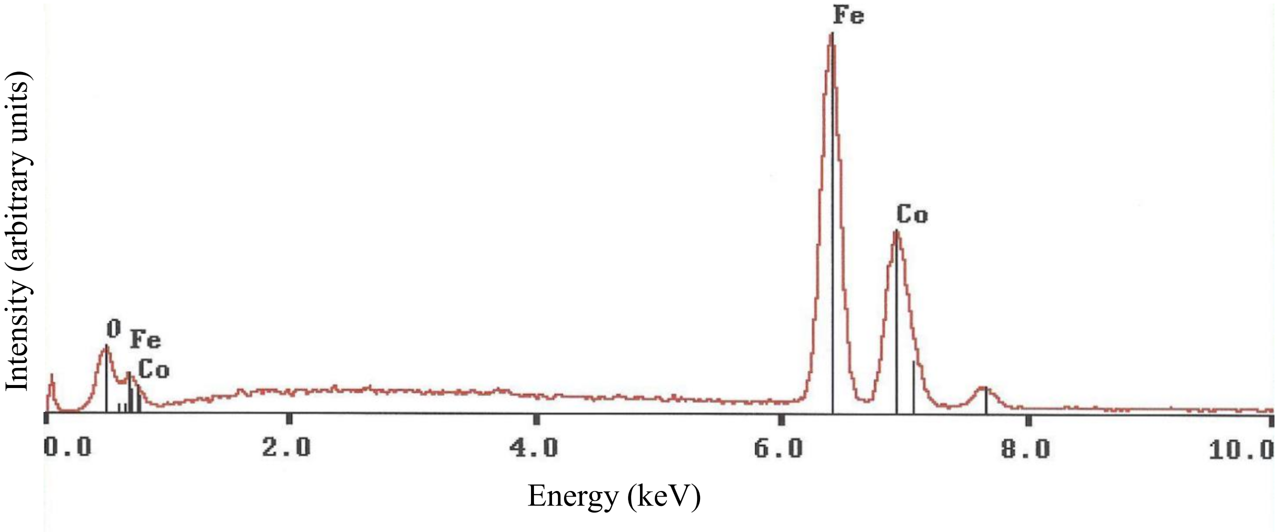

Figure 3.4: SEM/ESD micro-analysis of the 40 nm cobalt ferrite nanoparticle powder. The experimental red curve coincides with the expected black peaks for the examined nanoparticle powder composition.

Following the SEM/EDS the scanning electron microscope was used to collect micrographs of the four nanoparticle samples (**Figure 3.5**) in an attempt to compare the particle sizes to the provided particle data. All four nanoparticle samples revealed the formation of agglomerates with sizes from less than 1 micrometre to over 100 micrometre diameters. From the SEM alone it was difficult to identify individual nanoparticles in the samples. The reason for the observed particle agglomerations was most likely due to an increase in the attraction forces such as the Van der Waals adhesion forces (Schubert, 1981) with a decrease in particle size. The observed variation in nanoparticle agglomerate sizes could cause an irregular distribution in the nanoparticle flow when injected into a hydrocarbon reservoir, leading to a misrepresentation of the actual reservoir conditions. More importantly the agglomerates would likely have a detrimental effect on the reservoirs' permeability if they were large enough to plug up the pore throats. Therefore a technique was developed to disperse and stabilize the nanoparticles in order to prevent the formation of the observed agglomerates (see **Chapter 4**).

average particle size of the nano-powders and compare them to the manufacturer specifications. The TEM magnification proved powerful enough to distinguish the individual particles (**Figure 3.6**). The average nanoparticle size diameter was observed to be approximately 20 nm in line with the manufacturer specifications. Although successful in identifying individual nanoparticles the TEM also showed the tendency of the nanoparticles to form larger particle agglomerates, similar to the SEM observations.

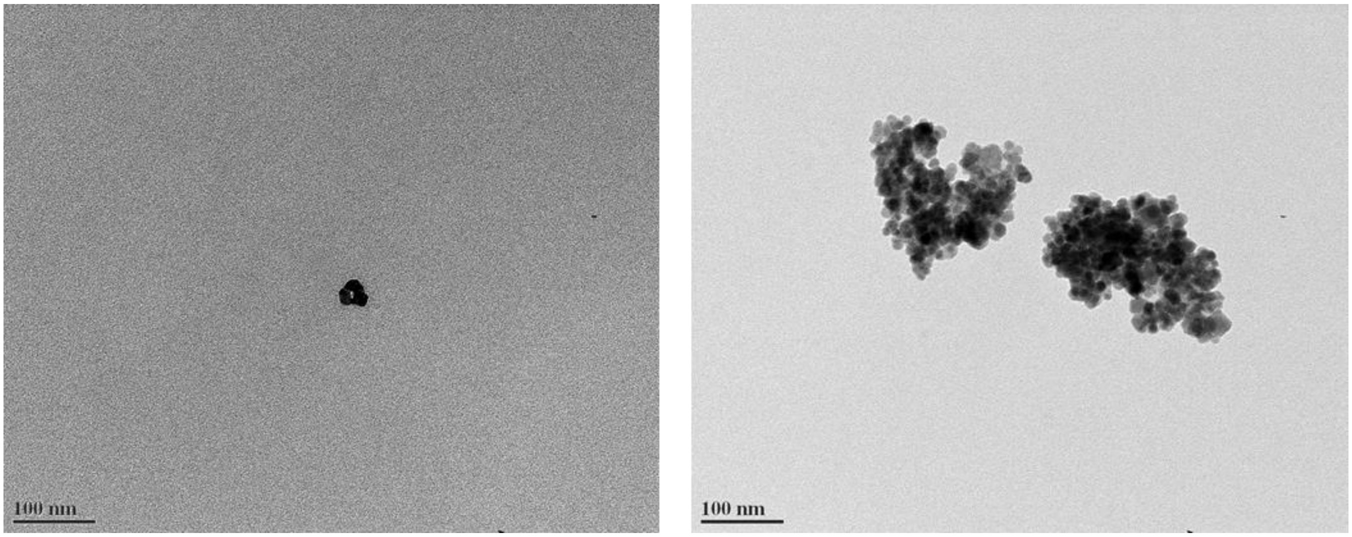

Figure 3.6: TEM micrographs of 20 nm maghemite nanoparticles, scale bar 100 nanometres. The observed darker areas are caused by some nanoparticles overlaying one another.

The nanoparticle agglomerates observed under the TEM tended to be much smaller than the ones seen under the SEM. While the SEM particle agglomerates reached sizes of over 100 microns, the ones observed under TEM were generally less than 1 micron. This difference is attributed to the sonication step of the nanoparticles implemented in the TEM procedure. The results suggested that the agitation of the nanoparticles in a liquid medium can greatly improve their dispersion. Nevertheless the formation of nanoparticle agglomerates was not prevented completely. The observed maghemite nanoparticle agglomerates most likely formed during the air drying step and aggregated when they settled out of the suspension. These observations further stressed the importance of generating a dispersed nano-fluid suspension that would remain stable (without the nanoparticles aggregating) when they were injected into a hydrocarbon reservoir.

TEM was also conducted on three temperature treated nanoparticle samples. The nanoparticles had previously been mixed with calcium fluoride and gradually heated to approximately 200 ºC. Previous studies have shown positive results in visually observing oxidation of temperature treated nanoparticles (Auge et al., 2010 and Hong et al., 2009). In those cases, TEM micrographs allowed one to visually observe structural differences in the nanoparticles. The particles displayed a distinguishable core-shell structure, where the core was made up of the original material while the shell was made of an oxidized layer.

In the present study most of the micrographs revealed homogenous nanoparticles without a clear core-shell structure (**Figure 3.7**). The distinguishable nanoparticles also appeared to be close to the manufacturer specifications of 20-30 nanometres depending on their composition. The absence of an observable core-shell structure suggested that the nanoparticles did not experience any large scale oxidation during the heating, although this conclusion will be re-assessed after examining their magnetic susceptibility response during their heating and cooling cycles (see **Section 3.4**). The nanoparticle powders all displayed large scale agglomeration similar to the unheated maghemite sample **(Figure 3.6**), further stressing the importance of creating a stable nano-fluid dispersion. This problem was eventually solved by dispersing the nanoparticles in de-ionized water, adding an anionic stabilizing surfactant (sodium dodecylbenzenesulfonate, DDBS), and probe sonication of the suspension (see **Chapter 4**).

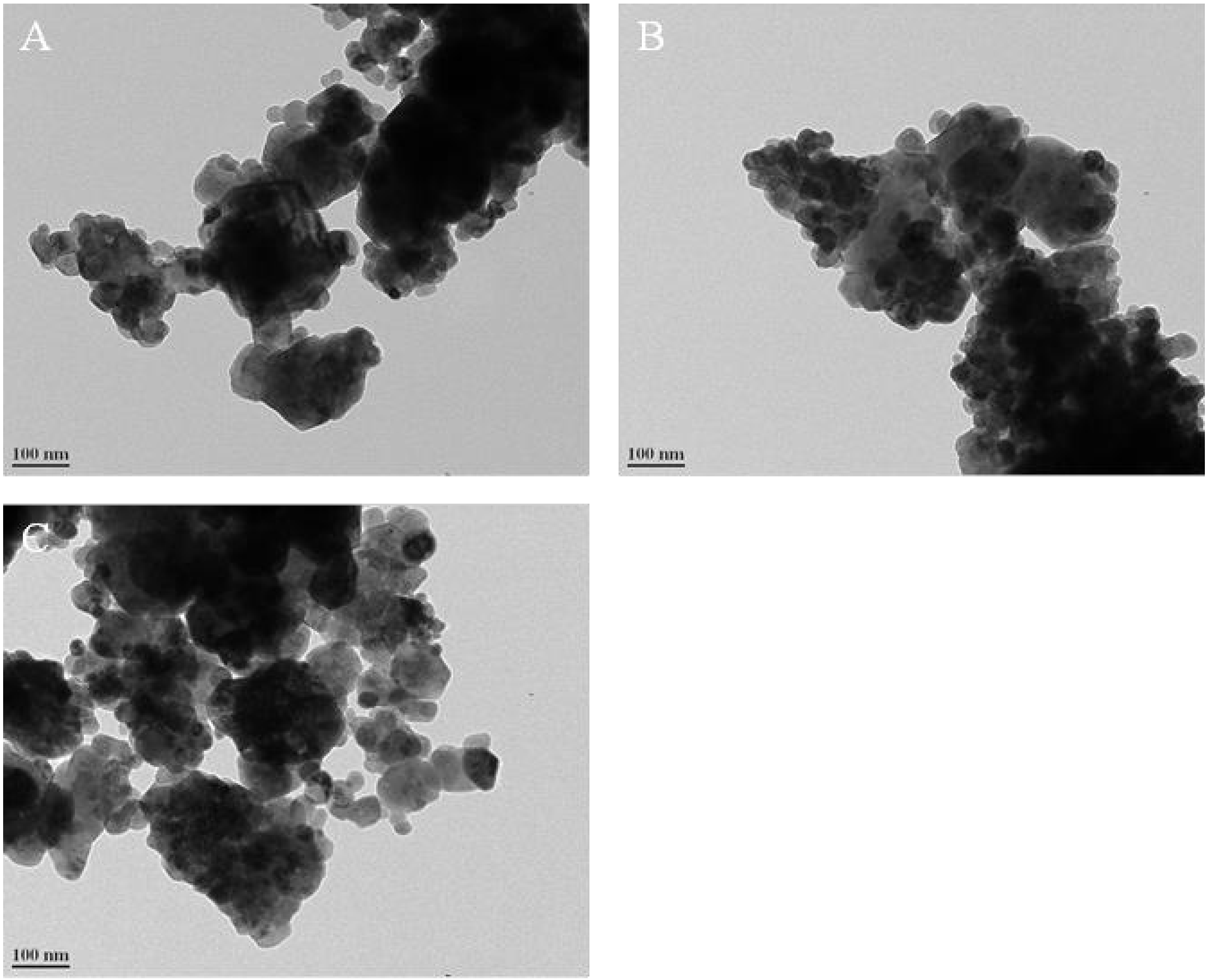

Figure 3.7: TEM micrographs of nanoparticles and calcium fluoride mixtures after heating: (A) 20 nm magnetite, scale bar 100 nanometres (B) 30 nm nickel ferrite, scale bar 100 nanometres (C) 40 nm cobalt ferrite, scale bar 100 nanometres. The observed darker areas are caused by some nanoparticle overlaying one another.

3.3 Magnetic Characterization of the Nanoparticle Powders at Room Temperature

3.3.1 Introduction

Following the initial characterization of the nanoparticles the next step was to examine their magnetic properties. In order to be useful as contrast agents the nanoparticles needed to have suitably high magnetic susceptibilities. Thus this section aimed to determine the room temperature magnetic properties of the four nanoparticle compositions. Following these initial observations the magnetic hysteresis curves of the nanoparticles were examined in order to verify the domain state of the magnetic nanoparticles.

3.3.2 Molspin Susceptibility Bridge Results and Discussion

The mass magnetic susceptibilities of the four potential nanoparticle compositions at room temperature were firstly determined (**Table 3.1**). These were the samples dispersed in resin (by dispersing in methyl methacrylate and adding cold mounting resin). From the four nanoparticle compositions examined the magnetite nanoparticles exhibited the highest magnetic susceptibility value 68200 x 10^{-8} m^3kg^{-1}. The nickel ferrite and maghemite nanoparticles also displayed relatively high values. The cobalt ferrite nanoparticles, on the other hand, displayed a value which was approximately 10 times lower than the other three compositions. All four nanoparticle compositions displayed mass magnetic susceptibilities orders of magnitude larger than those of common reservoir minerals (**Figure 3.8**, from Ivakhnenko and Potter, 2004). However, the magnetite, maghemite and nickel ferrite nanoparticles clearly are the best potential contrast agents in reservoirs due to their high magnetic susceptibilities (compared to reservoir minerals and fluids) and small sizes (20-30 nm).

Table 3.1: Bulk magnetic susceptibility using a Molspin susceptibility bridge.

Nanoparticle Composition	Nanoparticle Powder Mass (mg)	Mass Magnetic Susceptibility (10^{-8} m^3kg^{-1})
Magnetite	53.6	68200
Maghemite	53.5	54900
Nickel Ferrite	55.9	56700
Cobalt Ferrite	56.3	5860

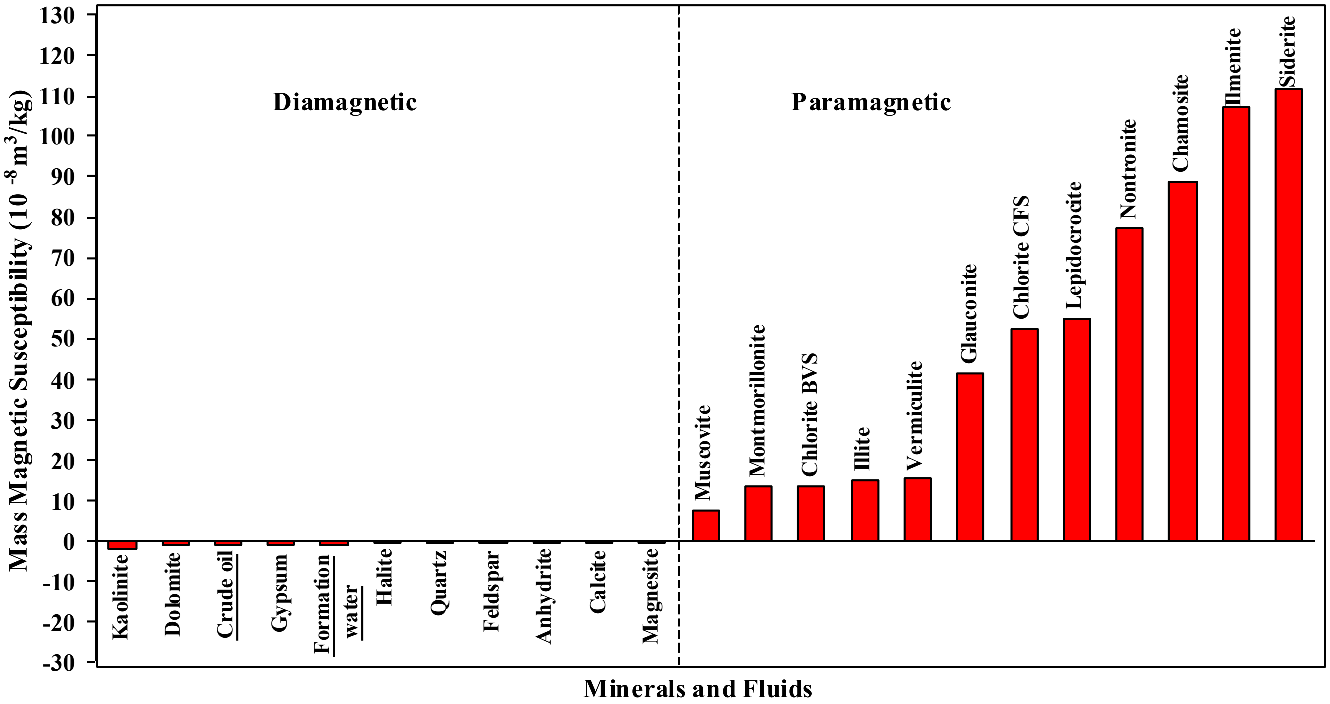

Figure 3.8: Magnetic Susceptibility of common reservoir minerals and fluids (Ivakhnenko and Potter, 2004).

3.3.3 Magnetic Hysteresis Analysis Results and Discussion

The magnetization of the nanoparticles was tested under varying applied magnetic fields using a Variable Field Translation Balance (VFTB). The observed hysteresis curves were then used to identify the magnetic domain state of the four nanoparticle samples.

The magnetite, maghemite and nickel ferrite nanoparticle samples had saturation magnetizations (M_S) of approximately 45 Am^2kg^{-1}, 30 Am^2kg^{-1} and, 45 Am^2kg^{-1} respectively (**Figures 3.9-3.11**). The magnetic hysteresis curves for all three samples passed through the origin (indicating no remanent magnetization, M_{RS}) and did not exhibit any loop. This demonstrated that all three types of nanoparticles were superparamagnetic. Their magnetic hysteresis curves were almost identical with the idealized magnetization curve for superparamagnetic particles (**Figure 1.9)** **(**Dunlop and Özdemir, 1997). Since superparamagnetic particles have both higher magnetic susceptibilities and smaller particle sizes compared to stable single domain particles, they would be easier to detect against the background minerals and fluids, and less likely to obstruct the pore network connections in the hydrocarbon reservoir that they were injected into.

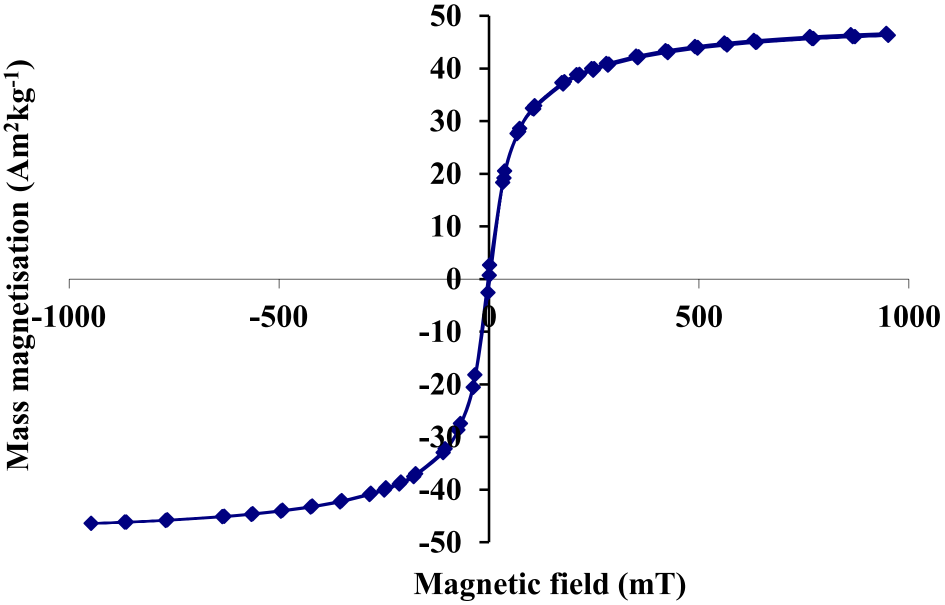

Figure 3.9: Magnetic hysteresis curve of the superparamagnetic 20 nm magnetite nanoparticles.

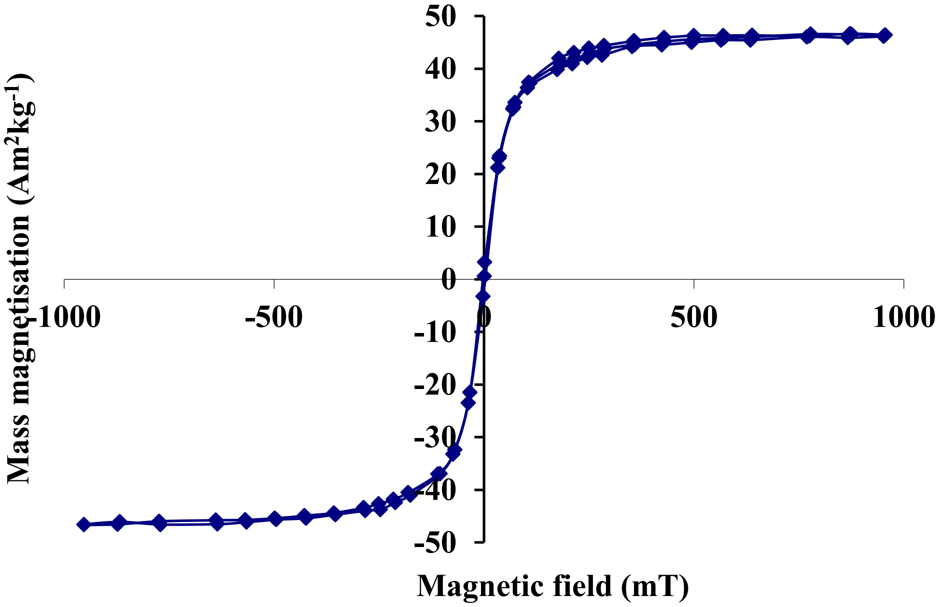

Figure 3.10: Magnetic hysteresis curve of the superparamagnetic 20 nm maghemite nanoparticles.

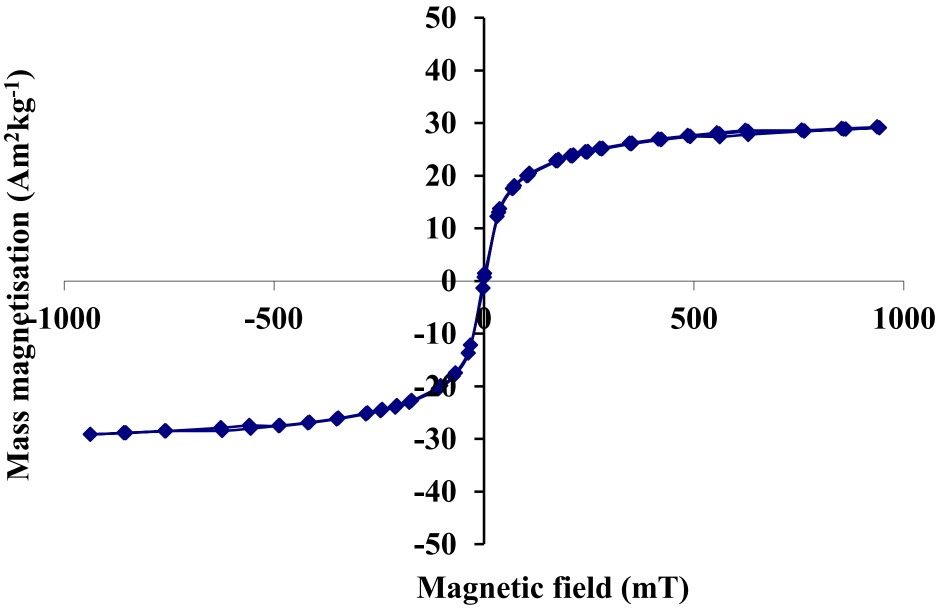

Figure 3.11: Magnetic hysteresis curve of the superparamagnetic 30 nm nickel ferrite nanoparticles.

The cobalt ferrite sample, however, displayed an open magnetic hysteresis loop (**Figure 3.12**). The cobalt nanoparticles have a saturation magnetization close to 50 Am^{2}kg^{-1} and a remanent magnetization of approximately 27 Am^{2}kg^{-1}. This demonstrates that the 40 nm cobalt nanoparticles are stable single domain. This explains why the cobalt nanoparticle sample has a bulk magnetic susceptibility an order of magnitude lower than the other three samples, as stable single domain particles have lower magnetic susceptibilities compared to superparamagnetic ones. The fact that the remanent magnetization is close to half the saturation magnetization also shows that the nanoparticles are randomly (isotropically) dispersed (see **Figure 1.8**).

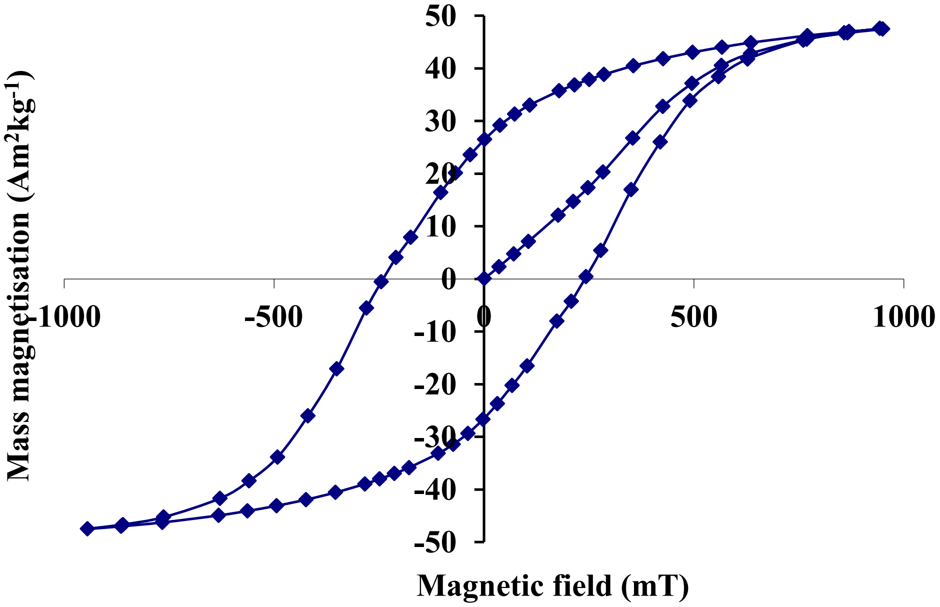

Figure 3.12: Magnetic hysteresis loop of stable single domain 40 nm cobalt ferrite nanoparticles.

3.4 Temperature Dependent Magnetic Susceptibility Measurements

3.4.1 Introduction

The magnetic nanoparticles would need to be able to withstand the harsh environmental conditions of hydrocarbon reservoirs if they were to be successfully utilized within the oil and gas industry. Thus the magnetic properties of the potential candidates needed to go through rigorous testing under potential reservoir conditions. This section examined the effects of the higher reservoir temperatures on the magnetic properties of the four nanoparticle candidates. The effect of the type of dispersing matrix (calcium fluoride, water or oil) on the magnetic susceptibility of the nanoparticles with temperature was also tested.

3.4.2 Curie Point Experiments in Calcium Fluoride Matrix

This set of experiments was conducted merely to check the composition of the nanoparticles (oil and gas reservoirs would never reach such high temperatures). The nanoparticles were mixed with calcium fluoride and their magnetic susceptibility with temperature was measured using the Bartington temperature susceptibility system described in **Sections 2.3.5 and 2.4.7**. The results are shown in **Figure 3.13**. The Curie temperatures of the nano-sized materials are expected to be lower than that of the bulk materials (Rong et al., 2006). **Table 3.2** compares the measured Curie temperatures from **Figure 3.13** with some published values for similar materials.

Table 3.2: Experimental and expected (based on previously published values) Curie temperatures of the magnetic nanoparticles.

Nanoparticle Composition	Measured Tc (˚C)	Expected Tc (˚C)
Magnetite	575	580[1]
Maghemite	570 and 655	590-675[1]
Nickel Ferrite	540	634[2]
Cobalt Ferrite	500	552[3]

[1]Dunlop and Özdemir, (1997) – experimental; [2]Joshi et al. (1986) – experimental; [3]Paulsen et al. (2003) – experimental.

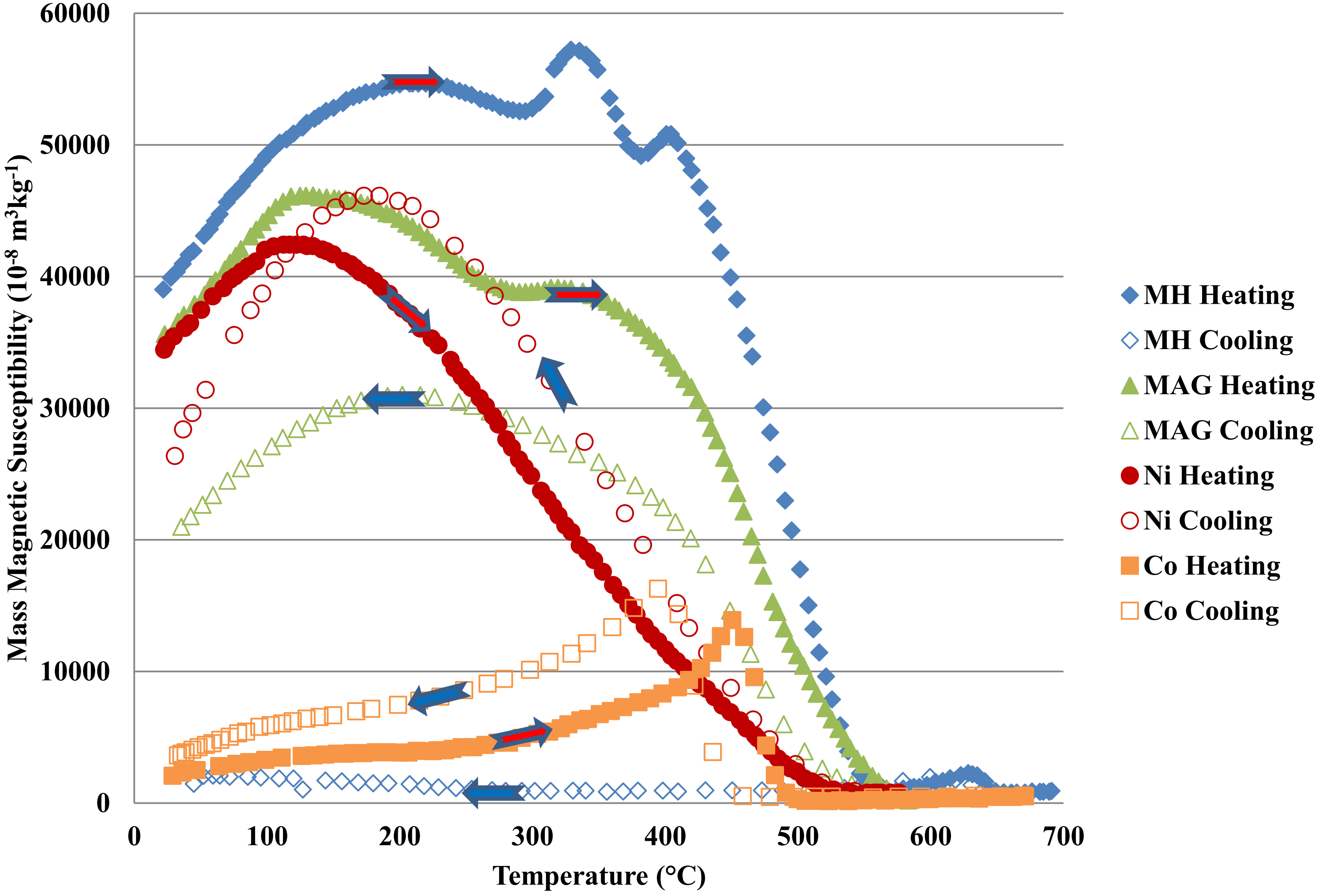

Figure 3.13: Mass magnetic susceptibility of the nanoparticle compounds when heated to their Curie temperatures. MH refers to the 20 nm maghemite, MAG refers to the 20 nm magnetite, Ni refers to the 30 nm nickel ferrite, and Co refers to the 40 nm cobalt ferrite..

The magnetite nanoparticles exhibited relatively higher magnetic susceptibilities during their heating cycle compared to the cooling cycle values, suggesting the nanoparticles underwent partial oxidation during the heating in air. The experimental Curie temperature was 575 ˚C which was only slightly lower than the bulk temperature of 580 ˚C given by Dunlop and Özdemir (1997).

The maghemite sample displayed the overall highest mass magnetic susceptibilities from the four nanoparticle compositions examined. Note that these samples were dispersed in calcium fluoride, and slight differences in the dispersions between these samples and those dispersed in the resin (**Table 3.1**) might explain the differences in magnetic susceptibility between the two sets of samples. The magnetic susceptibility of the maghemite sample dropped significantly during the cooling cycle. The nanoparticles also displayed two Curie temperatures, one at 570 ˚C and one at approximately 655 ˚C. The lower temperature was slightly lower than the 590-675 ˚C Curie range reported by Dunlop and Özdemir (1997), while the higher Curie point is close to that of hematite (Curie temperature around 675 ˚C, reported by Dunlop and Özdemir, 1997). The second Curie temperature and the large decrease in magnetic susceptibility during cooling were most likely a result of oxidation of the maghemite nanoparticles to hematite during the heating in air. In order to avoid oxidation while heating in air the experiment would need to be performed in a vacuum or the sample put in an evacuated sealed capsule.

For the nickel ferrite sample the cooling cycle magnetic susceptibility values were higher than those for the heating cycle within the range 150-540 ˚C. At lower temperatures the magnetic susceptibilities of the cooling cycle became lower than those of the heating cycle. This behaviour may have been partly the result of a temperature lag of the sample during the cooling cycle. The observed Curie temperature of the nickel ferrite sample was approximately 540 ˚C which was almost 100 ˚C lower than the 634 ˚C reported by Joshi et al. (1986) for the bulk material.

The cobalt ferrite nanoparticles exhibited the lowest mass magnetic susceptibilities. Like the nickel ferrite sample, the cooling cycle curve of the cobalt ferrite displayed higher magnetic susceptibility values over much of the temperature range 20-400 ˚C when compared to the heating cycle. This may have been caused by a slight temperature lag of the sample (the cooling curve appears slightly shifted to lower temperatures compared to the heating curve), or potentially by slight oxidation of the nanoparticles resulting in somewhat smaller particle cores which may be closer to being superparamagnetic, and therefore would have higher magnetic susceptibility values than the original particles. The Curie temperature of the cobalt ferrite nanoparticles was measured to be approximately 500 ˚C which was lower than the reported 552 ˚C reported by Paulsen at al. (2003).

The results of the experiments revealed that the Curie temperatures of all the nanoparticle compositions were indeed lower than the previously reported values for bulk materials. The oxidation in air of the magnetite and maghemite nanoparticles is unlikely to be an issue in hydrocarbon reservoirs at typical reservoir temperatures. Nevertheless, the magnetic susceptibility response of the nanoparticles at typical reservoir temperatures in different types of dispersing matrices were then tested.

3.4.3 Reservoir Temperature Experiments in Calcium Fluoride Matrix

In this set of experiments the magnetic susceptibility of the nanoparticles was examined when mixed in a solid matrix of calcium fluoride and heated to potential hydrocarbon reservoir temperatures. The calcium fluoride matrix was used as it is chemically inert at these temperatures and has a low diamagnetic susceptibility, and thus its contribution to the overall magnetic susceptibility would be insignificant. It also has a high melting point. The calcium fluoride heating allows one to see the effect of heating in air so that those results can then be compared to those where the nanoparticles are dispersed in fluids typical of those in reservoirs (water and oil). The magnetic susceptibility of the nanoparticles were measured as the mixtures were heated to approximately 200 ˚C and then cooled back to room temperature. The errors in magnetic susceptibility measurements were calculated for both heating and cooling cycle curves. The measurement error was taken to be the smallest unit of measurement or the calibration accuracy of the magnetic sensor (whichever of the two values was larger) and the smallest unit of measurement for the weight balance. The measurement error was then used to calculate the error in mass magnetic susceptibility of the samples by deriving an error formula from equation (2.2). The error bars were slightly larger than the symbol sizes and included for the magnetite heating and cooling cycles on the figure (**Figure 3.14**) for this set of experiments.

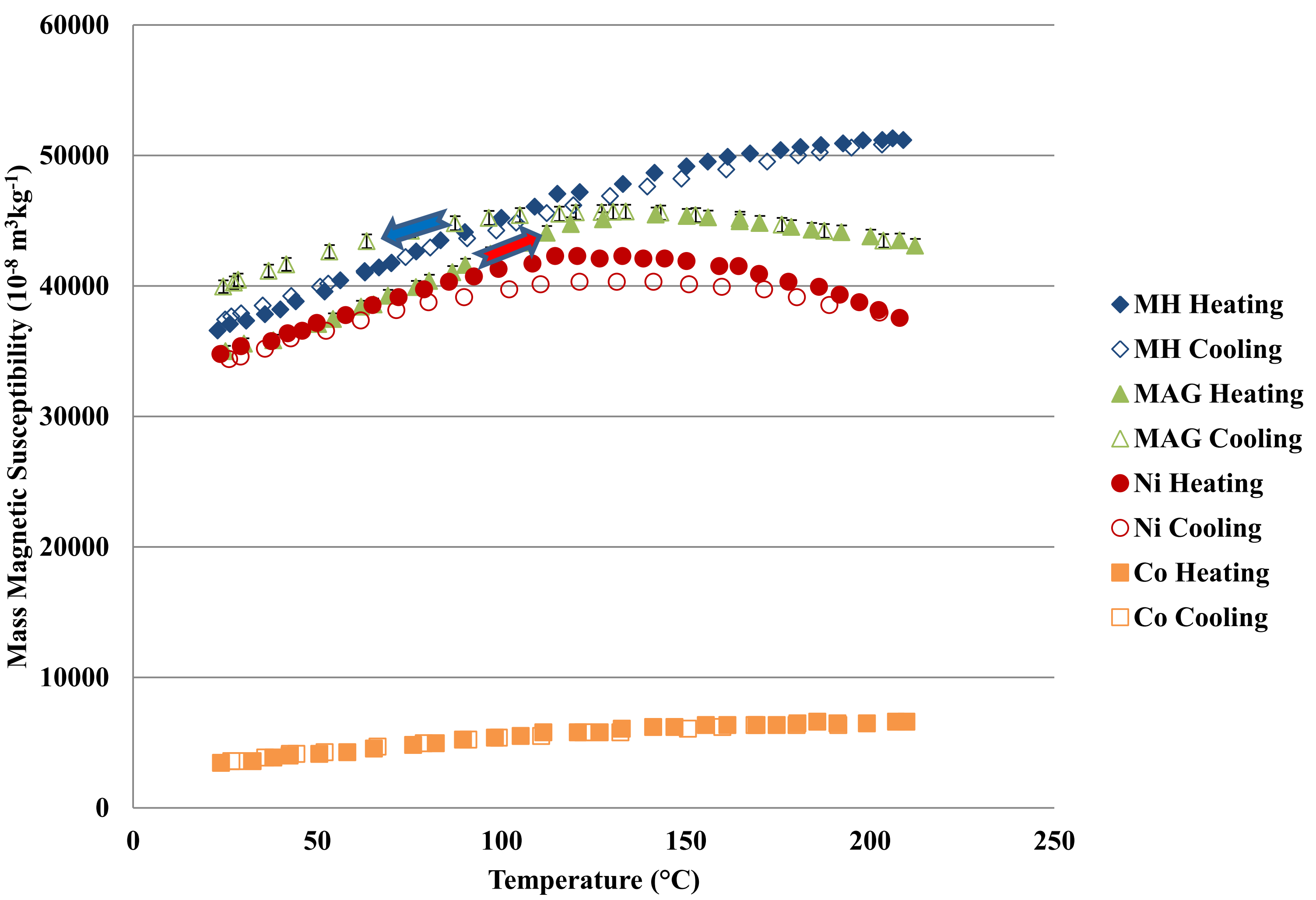

Figure 3.14: Temperature dependence of the mass magnetic susceptibility of the nanoparticle compounds when heated to reservoir temperatures in a calcium fluoride matrix. MH refers to the 20 nm maghemite, MAG refers to the 20 nm magnetite, Ni refers to the 30 nm nickel ferrite, and Co refers to the 40 nm cobalt ferrite.

The magnetite nanoparticles showed a linear increase in magnetic susceptibility with increasing temperature between 25 and 130 ˚C (**Figure 3.14**). When heated above 130 ˚C the nanoparticles exhibited a slight linear decrease in magnetic susceptibility, which continued for the rest of the heating cycle. The magnetic susceptibilities values of the cooling cycle were initially comparable to the ones observed during the heating cycle. When cooled below 130 ˚C though the magnetic susceptibilities showed higher values compared to the heating cycle. This cycle could potentially be explained if the magnetite nanoparticles underwent partial oxidation to maghemite. If the oxidation was minor the resulting nanoparticles would have smaller magnetite cores with thin maghemite outer shells (see the schematic shown in **Figure 3.15**). Both minerals have high magnetic susceptibility when they are superparamagnetic. The small superparamagnetic maghemite shells and the resulting magnetite cores (which would be smaller than the initial 20 nm magnetite particles, and may have stronger superparamagnetic properties) may possibly explain the higher susceptibility on cooling.

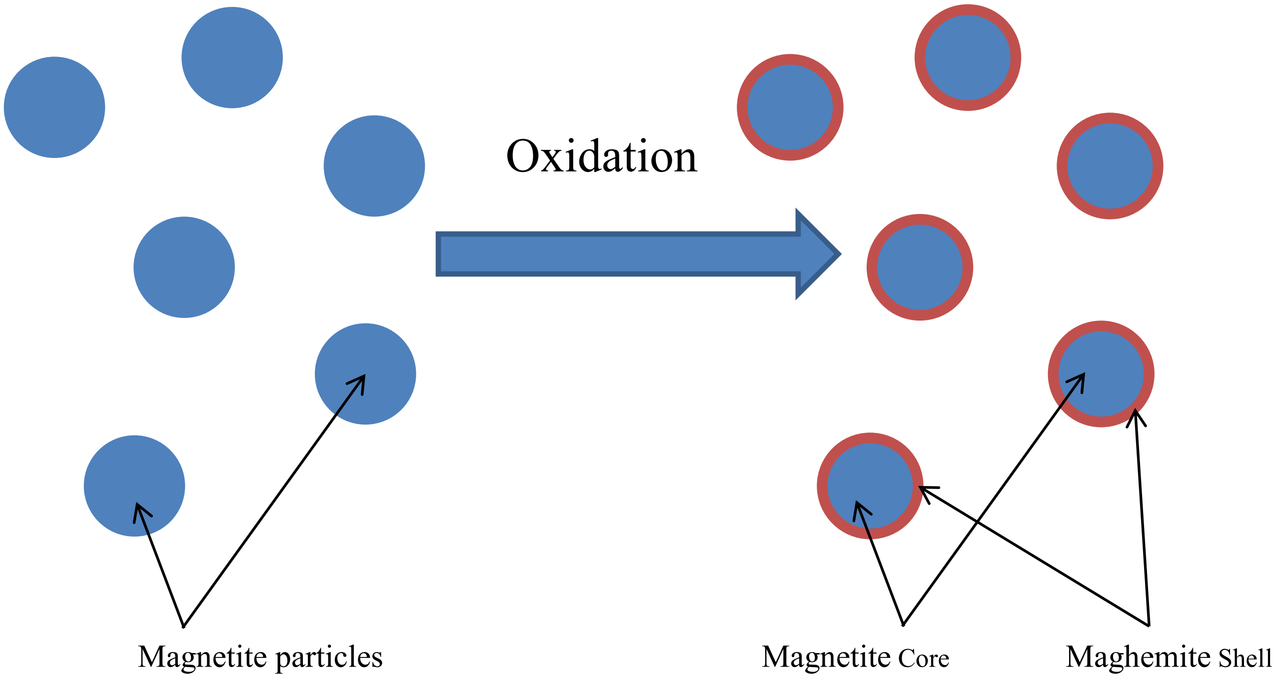

Figure 3.15: Schematic illustrating partial oxidation of magnetite nanoparticles into a core-shell structure of magnetite and maghemite.

The maghemite nanoparticles displayed an initial linear trend of increasing magnetic susceptibility with increasing temperature, which became slightly non-linear after about 120 ˚C (**Figure 3.14**). The magnetic susceptibilities of the cooling cycle were very similar to those during the heating cycle suggesting the maghemite nanoparticles underwent little to no chemical change on heating to 200 ˚C.

The nickel ferrite nanoparticle sample also displayed an initial linear trend of increasing magnetic susceptibility with increasing temperature (**Figure 3.14**) between 25 and 120 ˚C. Above the 120 ˚C the particles displayed a gradual decrease of magnetic susceptibility with temperature for the rest of the heating cycle. The cooling cycle curve displayed similar trends to the heating one, although with sometimes slightly lower magnetic susceptibilities, with the final value after cooling close to the initial value.

The cobalt ferrite nanoparticles displayed a curved trend of increasing magnetic susceptibilities with increasing temperatures throughout the full heating cycle (**Figure 3.14**). The cooling cycle resembled the heating cycle suggesting the particles underwent little to no chemical change.

The magnetic susceptibility curves displayed an overall trend of increasing with temperature especially for the first 120 ˚C of the heating cycle. This increase in magnetic susceptibility is most likely due to the Hopkinson effect, where ferromagnetic or ferrimagnetic materials experience increase in magnetic susceptibility between their blocking temperature and Curie temperature giving rise to a magnetic susceptibility peak. This effect is more pronounced in superparamagnetic particles leading to a magnetic susceptibility peak of up to two orders of magnitude higher than the values of the thermally blocked particles (Dunlop and Özdemir 1997), and as shown by Dunlop (1974) single domain grains can be affected at lower temperature and begin to show increase in magnetic susceptibility shortly after heating is initiated. This effect may be in part due to the shortening of the relaxation time when a particle is heated, such changes in relaxation time may be leading to more superparamagnetic behavior and an overall higher magnetic susceptibility.

3.4.4 Reservoir Temperature Experiments in Water Matrix

This set of experiments examined the temperature dependence of the magnetic susceptibility of the nanoparticle samples when they were mixed in a water matrix. The water matrix was chosen as it is used for enhanced oil recovery waterflooding, and in water based drilling muds. In this case the heating was kept to below 100 ˚C in order to avoid evaporation. Errors were calculated and included for the magnetite and maghemite magnetic susceptibility measurements (**Figure 3.16**) demonstrating that the chosen symbol sizes were close to the size of the errors (calculations were conducted in the same way as **Section 3.4.3**).

The magnetite nanoparticles showed mainly a linear increase in magnetic susceptibilities with increasing temperature (**Figure 3.16**) during the heating cycle. The cooling cycle magnetic susceptibilities were generally larger, suggesting again that the magnetite may be oxidizing partially into maghemite.

The maghemite nanoparticles also displayed an overall increase in magnetic susceptibility with increasing temperature during the heating cycle (**Figure 3.16**). The cooling curve values were not too different from the heating cycle ones (as was the case with the maghemite in the calcium fluoride matrix) within the uncertainties of the measurement. The nickel ferrite nanoparticles also displayed a general linear increase in magnetic susceptibility during heating (**Figure 3.16**). The cooling curve values were generally very similar within the uncertainties of the measurement. The cobalt ferrite nanoparticles displayed a linear increase in magnetic susceptibility during heating (**Figure 3.16**). The cooling curve values were almost identical, indicating no chemical changes.

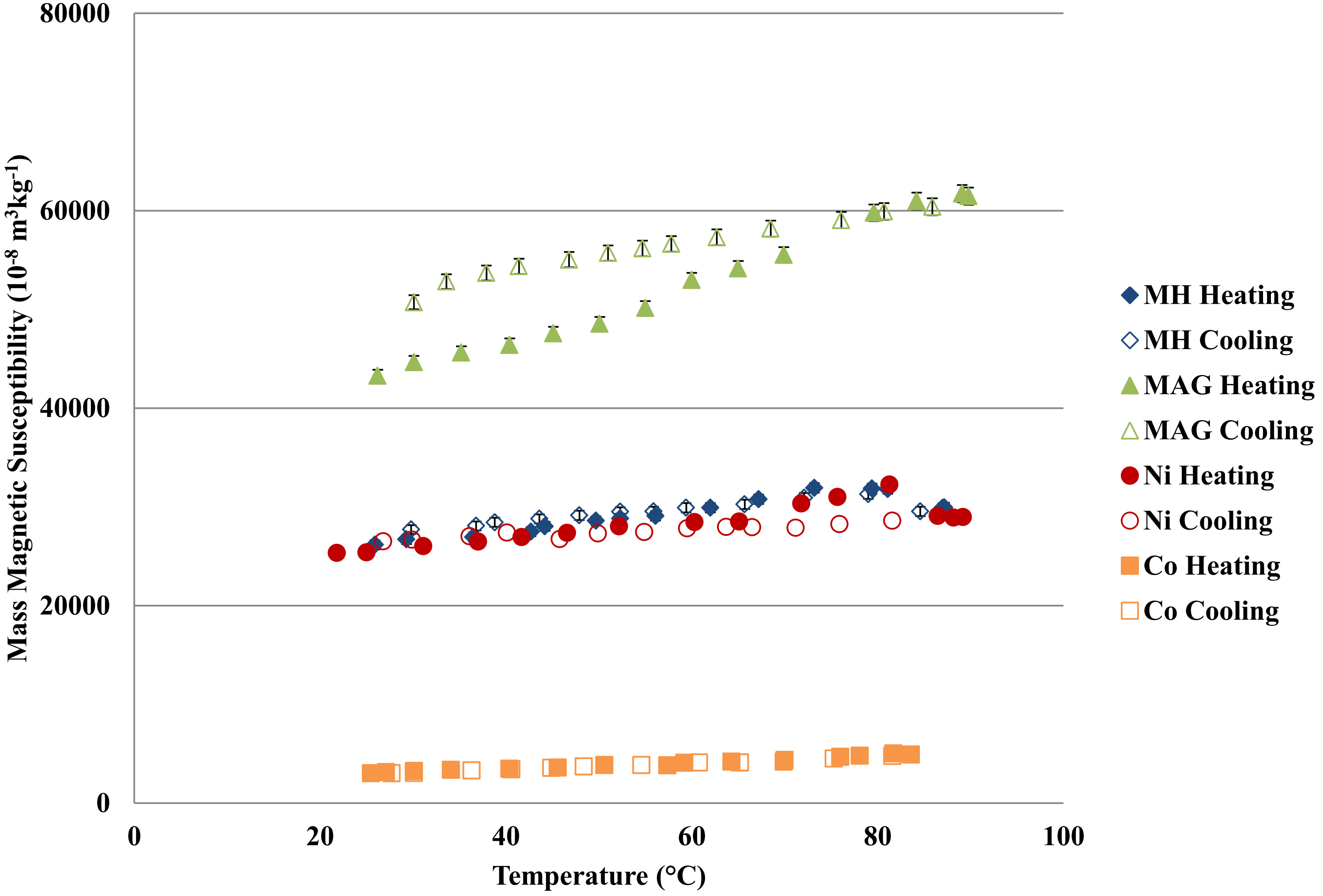

Figure 3.16: Temperature dependence of the mass magnetic susceptibility of the nanoparticle compounds when heated to reservoir temperatures in a water matrix. MH refers to the 20 nm maghemite, MAG refers to the 20 nm magnetite, Ni refers to the 30 nm nickel ferrite, and Co refers to the 40 nm cobalt ferrite.

3.4.5 Reservoir Temperature Experiments in Oil Based Drilling Mud Matrix

This set of experiments examined the magnetic susceptibility behaviour of the nanoparticles, when they were mixed in an oil based drilling mud matrix. Oil based drilling mud is commonly used in wellbores especially where swelling clays are present when water based drilling mud is not recommended. The samples were heated to approximately 90 ˚C in order to avoid evaporation.

The magnetite nanoparticles displayed an increase in magnetic susceptibility with increasing temperature (**Figure 3.17**). The magnetic susceptibility values of the cooling cycle were fairly similar to the heating cycle (unlike the cases when the nanoparticles were mixed with calcium fluoride and water). This suggests that oxidation was not taking place when the nanoparticles were mixed with oil based drilling mud.

Furthermore, the magnitude of the magnetic susceptibility was significantly higher when the magnetite nanoparticles were mixed with the oil based drilling mud, compared to when they were mixed with calcium fluoride or water. This suggests that the oil based drilling mud dispersed the nanoparticles better than the calcium fluoride or water (where there may be more particle agglomerates leading to lower magnetic susceptibility).

The maghemite nanoparticles also displayed an overall linear increase in magnetic susceptibility with temperature during their heating cycle (**Figure 3.17**). The cooling cycle magnetic susceptibility values were almost identical to those of the heating cycle, suggesting the nanoparticles underwent no chemical change.

The nickel ferrite nanoparticles also displayed a relatively linear increase in magnetic susceptibility with temperature during heating (**Figure 3.17**). The cooling cycle values were very similar suggesting little to no chemical change.

The cobalt ferrite nanoparticles also displayed an overall increase in magnetic susceptibility with increasing temperature during their heating cycle (**Figure 3.17**). The magnetic susceptibilities of the cooling cycle were slightly larger than those in the heating cycle, but the differences may not be significant in terms of the uncertainties in the measurements.

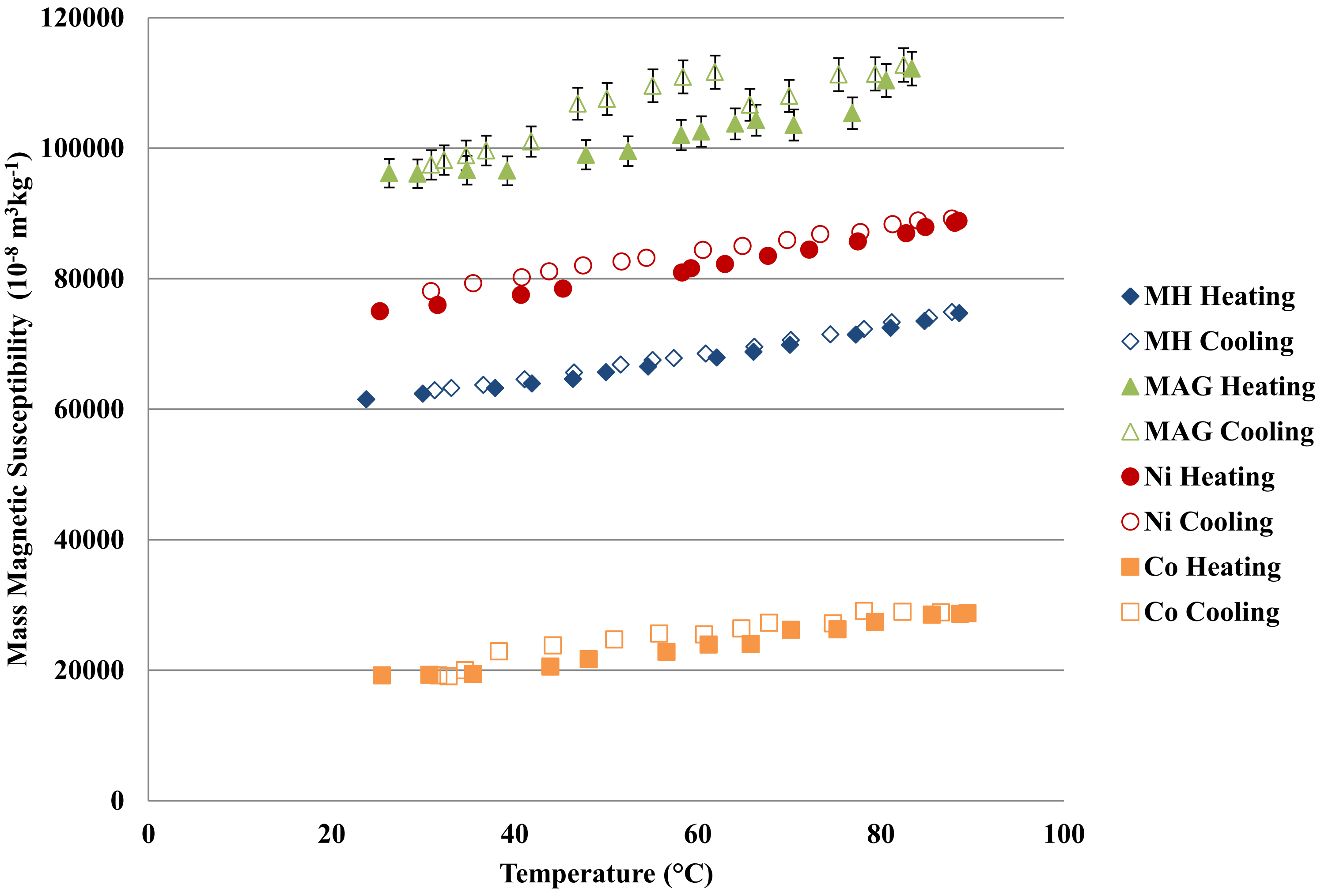

Figure 3.17: Temperature dependence of the mass magnetic susceptibility of the nanoparticle compounds when heated to reservoir temperatures in an oil based drilling mud matrix. MH refers to the 20 nm maghemite, MAG refers to the 20 nm magnetite, Ni refers to the 30 nm nickel ferrite, and Co refers to the 40 nm cobalt ferrite.

3.4.6 Reservoir Temperature Experiment in Stabilized Solution

This experiment aimed to observe the magnetic susceptibility behaviour of the nanoparticles once they had been stabilized in deionized water with the anionic chemical surfactant sodium dodecylbenzenesulfonate (DDBS), using the stability procedures creating maghemite dispersions that were stable over long periods of time (see **Chapter 4 Section 4.2.2**). A stable magnetic signal is crucial for the nanoparticles' reservoir applications. The stabilized, dispersed nanoparticle suspensions utilized a low concentration (0.597 g L^{-1} for magnetite, 0.790 g L^{-1} for maghemite and 0.988 g L^{-1} for nickel ferrite), and the concentrations were specifically chosen to be all above the required concentration for differentiation against the background magnetic signal of sand that was calculated by Morrow et al. (2015) for magnetite nanoparticles of 0.269 g L^{-1}. Only the three superparamagnetic nanoparticles samples (magnetite, maghemite and nickel ferrite) were examined. The cobalt ferrite nanoparticles of this concentration had a magnetic susceptibility too low to be accurately detected. The uncertainties in the mass magnetic susceptibilities were larger than previous experiments due to the lower concentrations. The uncertainty values were included for the nickel ferrite heating cycle while the rest were comparable in value but left out of the figure to avoid overcrowding (**Figure 3.18**). Instrumental drift was taken into account for all presented values.

The magnetite and maghemite nanoparticles samples displayed fairly similar high magnetic susceptibilities (**Figure 3.18**). At first glance the magnetic susceptibility values for both samples show a slight decrease with increasing temperature. There is also the possibility that the magnetic susceptibility is stable with increasing temperature and the observed "decrease" is merely due to measurement uncertainties in this experiment. The cooling curves of the magnetite and maghemite samples are similar to their heating curves within these larger uncertainties.

The nickel ferrite nanoparticles displayed lower magnetic susceptibility values from the other two compositions (**Figure 3.18**). This may be due to lower particle dispersion and stability of the nano-fluid as the procedure developed in **Chapter 4 Section 4.2.2** was developed for maghemite nanoparticles and may be less effective for the nickel ferrite. Similar to the magnetite and maghemite samples the nanoparticles appeared to show a decreasing magnetic susceptibility with increasing temperature, although again this may be due to the larger measurement uncertainties.

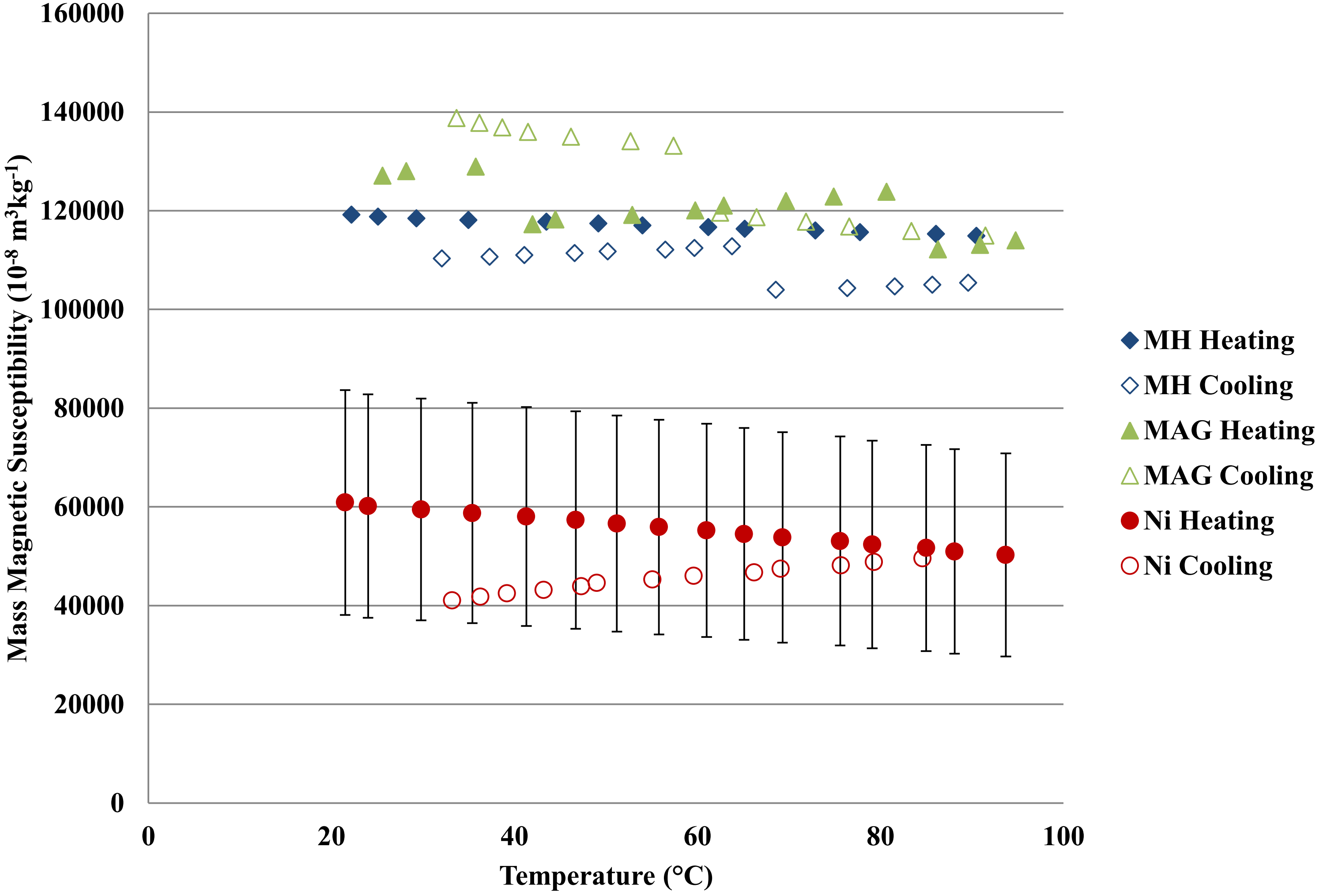

Figure 3.18: Temperature dependence of the mass magnetic susceptibility of the nanoparticle compounds when heated to reservoir temperatures dispersed with DDBS. MH refers to the 20 nm maghemite, MAG refers to the 20 nm magnetite, and Ni refers to the 30 nm nickel ferrite.

3.4.7 Comparison of Dispersion Matrix Effectiveness for Reservoir Temperature Experiments

The various dispersing matrices for the nanoparticles caused differences in the mass susceptibility values. It is expected that samples containing particle agglomerates will have lower magnetic susceptibility values (since the magnetic moments of adjacent particles can interfere with one another leading to an overall lower magnetic susceptibility of the aggregate; Stauch et al. (2017) showed how the agglomeration degree of magnetite nanoparticles can affect their magnetic properties as well as their blocking temperature), while samples that are better dispersed will have higher magnetic susceptibilities. Thus the magnetic susceptibility heating curves will be used to compare the quality of the nanoparticle dispersions in different dispersing matrices.

The magnetite nanoparticles displayed the highest magnetic susceptibility values when stabilized and dispersed with DDBS (**Figure 3.19**), although due to the large uncertainties of the DDBS temperature experiment the values could potentially be comparable to those of the oil based drilling mud experiment. The calcium fluoride and water dispersing matrices, on the other hand, proved less effective in dispersing the nanoparticles as their magnetic susceptibility curves exhibited lower values.

The maghemite nanoparticles also showed the highest magnetic susceptibilities when stabilized and dispersed with DDBS, suggesting the best dispersion was achieved in this sample (**Figure 3.20**). The second highest magnetic susceptibilities were when the maghemite nanoparticles were dispersed in the oil based drilling mud matrix, while dispersion of the maghemite nanoparticles in calcium fluoride and water gave the lowest magnetic susceptibility values similar to the magnetite case.

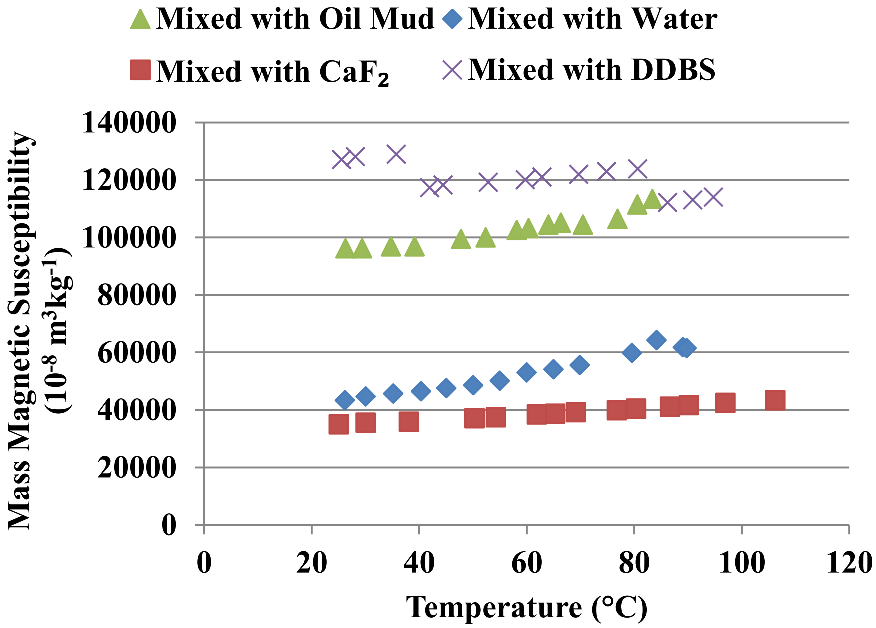

Figure 3.19: Mass magnetic susceptibilities of 20 nm magnetite nanoparticles in different dispersing matrices.

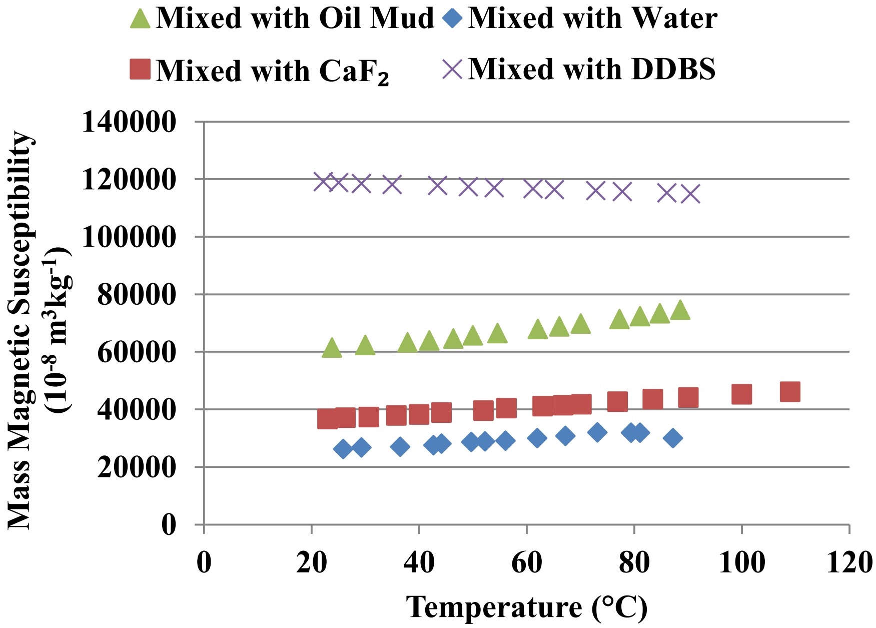

Figure 3.20: Mass magnetic susceptibilities of 20 nm maghemite nanoparticles in different dispersing matrices.

The nickel ferrite nanoparticles, on the other hand, had highest magnetic susceptibilities when mixed in oil based drilling mud (**Figure 3.21**) indicating that in this case the drilling mud was the most effective dispersing matrix. The DDBS stabilized dispersion gave the second highest magnetic susceptibilities. This indicates that the DDBS stabilization procedure was not as effective for the nickel ferrite nanoparticles and if they are to be utilized as tracers for hydrocarbon reservoirs they would need to undergo separate stability testing. The calcium fluoride and water dispersing matrices gave the lowest magnetic susceptibilities similar to magnetite and maghemite.

In the case of the cobalt ferrite nanoparticles the highest magnetic susceptibilities were seen when mixed in the oil based drilling mud matrix (**Figure 3.22**). The calcium fluoride and water samples gave lower results. The cobalt ferrite nanoparticles were not tested when stabilized with DDBS as their magnetic susceptibilities were too low to be accurately detected at those concentrations.

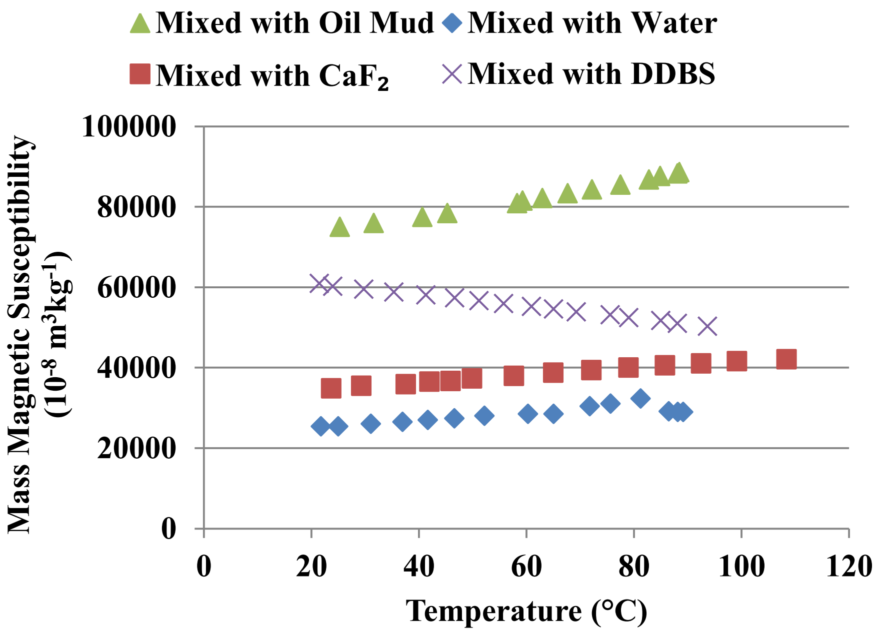

Figure 3.21: Mass magnetic susceptibilities of 30 nm nickel ferrite nanoparticles in different dispersing matrices.

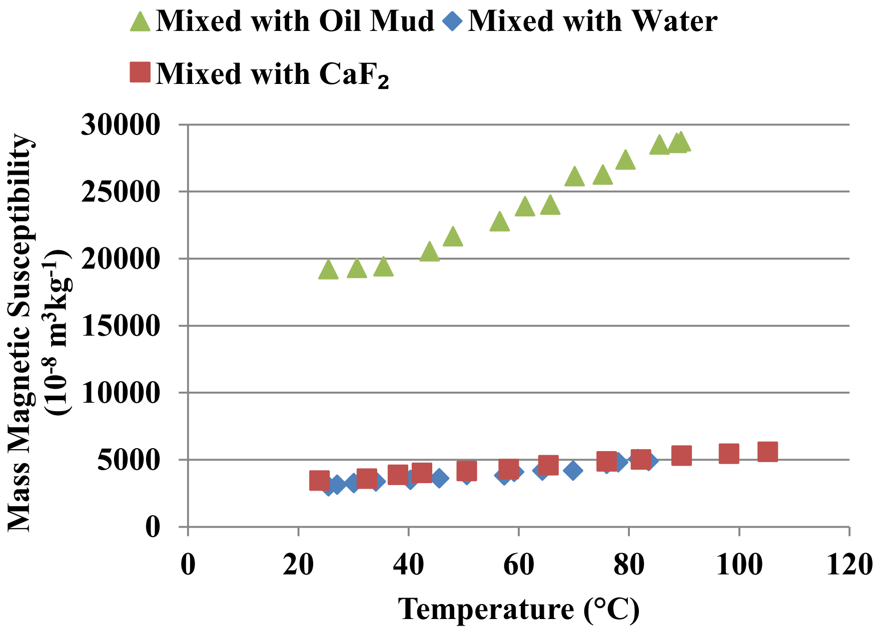

Figure 3.22: Mass magnetic susceptibilities of 40 nm cobalt ferrite nanoparticles in different dispersing matrices.

3.5 Conclusions

1. The SEM and TEM experiments confirmed the nanoparticle compositions and average particle sizes, as specified by the manufacturers. The VFTB experiments revealed that three of the nanoparticle compositions were superparamagnetic (the magnetite, nickel ferrite and maghemite), while the cobalt ferrite nanoparticles were in a stable single domain state.
2. The room temperature magnetic susceptibility measurements revealed that the three superparamagnetic nanoparticle compositions all have potentially high enough mass magnetic susceptibilities to be good contrast agents, while the stable single domain cobalt ferrite nanoparticles exhibited mass magnetic susceptibilities approximately an order of magnitude lower than the three superparamagnetic samples.
3. From the three superparamagnetic nanoparticle compositions maghemite exhibited the most stable behaviour with reservoir temperatures. The heating and cooling curves did not show much deviation for maghemite regardless of the dispersing matrix (calcium

fluoride, water, or oil based drilling mud) or the use of the dispersant DDBS. The maghemite nanoparticles also exhibited high mass magnetic susceptibilities (maghemite and magnetite gave the two highest values). Due to their stability and high magnetic susceptibilities the maghemite nanoparticles were subsequently chosen as the best candidate (from these studied) for potential reservoir applications. Maghemite was therefore used for the contrast agent multimodal imaging for the waterflooding of heavy oil experiments in **Chapter 4**. Note also that maghemite is present naturally in many reservoir rocks, and so using small quantities as a contrast agent in future reservoir applications in the field is unlikely to cause environmental issues.

4. The various dispersing matrices for the nanoparticles caused different degrees of dispersion, as indicated by differences in the mass magnetic susceptibility values. Dilute concentrations of the superparamagnetic nanoparticles mixed with DDBS gave the highest mass magnetic susceptibility values for most samples with the exception of the nickel ferrite nanoparticle composition.
5. Whilst the magnetite nanoparticles also exhibited high mass magnetic susceptibilities, they were less stable with reservoir temperatures than the maghemite particles (particularly when mixed with calcium fluoride and heated in air, and when mixed with water).
6. The nickel ferrite and cobalt ferrite samples were quite stable in all reservoir temperature experiments.

3.6 References

- Auge, A., Weddemann, A., Vogel, D., Wittbracht, F., and Hutten, A., 2010. A level set base approach for modeling oxidation processes of ligand stabilized metallic nanoparticles. Applied Physics Letters, **96**, ID093111, 3 pp.
- Barron, A. R., Tour, J. M., Busnaina, A. A., Jung, Y. J., Somu, S., Kanj, M. Y., Potter, D. K., Resasco, D., and Ullo, J., 2010. Big things in small packages. Oilfield Review, Schlumberger, **22**, 38-49.
- Dunlop. D. J., 1974. Thermal enhancement of magnetic susceptibility. Journal of Geophysiscs, **40**, 439-451.

- Dunlop, D. J., and Özdemir, Ö., 1997. Rock Magnetism. Cambridge University Press, 565 pp.
- Hong, S. J., Pyun, J., Park, W. Y., Kim, S. C., and Shim, I., 2009. Oxidation effect in cobalt nanoparticles magnetic fluids. IEEE Transactions on Magnetics, **45**, 2464-2466.
- Ivakhenko, O. P., and Potter, D. K., 2004. Magnetic susceptibility of petroleum reservoir fluids. Physics and Chemistry of the Earth, **29**, 899-907.
- Johnson, K., 2010. Advances in nanotechnology hold huge potential promise in upstream applications. The American Oil & Gas Reporter, 113-123.
- Joshi, G. K., Khot, A. Y., and Sawant, S. R., 1986. Magnetization, Curie temperature and Y-K angle studies of Cu substituted and non substituted Ni-Zn mixed ferrites. Solid State Communications, **65**, 1593-1595.
- Morrow, L., Potter, D. K., and Barron, A. R., 2015. Detection of magnetic nanoparticles against proppant and shale reservoir rocks. Journal of Experimental Nanoscience, **10**, 1028-1041.
- Paulsen, J. A., Lo, C. C. H., Snyder, J. E., Ring, P., Jones, L. L., and Jiles, D. C., 2003. Study of the curie temperature of cobalt ferrite based composites for stress sensor applications. IEEE Transactions on Magnetics, **39**, 3316-3318.
- Rong, C., Li, D., Nandwana, V., Poudyal, N., Ding, Y., Wang, Z. L., Zeng, H., and Liu, J. P., 2006. Size-dependant chemical and magnetic ordering in $L1_0$-FePt nanoparticles. Advanced Materials, **18**, 2984-2988.
- Schubert, H., 1981. Principles of agglomeration. International Chemical Engineering, **21**, 363-377.
- Stauch, C., Spath, S., Ballweg, T., Luxenhofer, R., and Mandel, K., 2017. Nanostructured micro-raspberries from superparamagnetic iron oxide nanoparticles: studying agglomeration degree and redispersibility of nanoparticulate powders via magnetization measurements. Journal of Colloid and Interface Science, **505**, 605-614.

Chapter 4

STABILITY AND WATERFLOOD EXPERIMENTS APPLYING MAGNETIC SUSCEPTIBILITY AND CT SCANNING

Part of this chapter was published (and fully peer reviewed) as follows:

Petrov, P. A., Potter, D. K., Cameron, S., London, M., Donald., J., and Waterman, W., 2015. Combined CT and magnetic scanning techniques for multimodal imaging of fluid flow in porous media: application to heavy oil waterflooding. Proceedings of the 2015 International Symposium of the Society of Core Analysts, 16-21 August 2015, St. John's, Canada, Paper SCA2015-012 (12 pages).

4.1 Introduction

The work in the previous chapter identified three potential nanoparticle compositions for application within the oil and gas industry. The most suitable nanoparticle powder chosen for further examination was maghemite. This decision was based on its high magnetic susceptibility (being superparamagnetic), small particle size, as well as the stability of its magnetic susceptibility under reservoir temperatures. In order to inject the nano-fluid into a hydrocarbon reservoir the nanoparticles would first need to be dispersed in a suitable stable suspension. Morrow et al. (2015) investigated the required concentrations of magnetite nanoparticles to produce a differentiable signal against sand to be 0.269 g L^{-1}. This concentration was used as a reference point when conducting the nanoparticle stability experiments, as the magnetic susceptibility of the chosen maghemite nanoparticles were not significantly different from the magnetite nanoparticles examined (see **Chapter 3**). The aim of the stability experiments was to create a stable dispersed maghemite nanoparticle suspension to be used later in the waterflood experiments.

Once a stable dispersed nanoparticle suspension was created it was used to monitor the progress of waterflooding of a heavy oil saturated sandpack. Quantitative imaging of heavy oil waterflooding is difficult due to the similar densities of heavy oil (0.99 g cm^{-3}) and water (1.00 g cm^{-3}) and there is little in the literature regarding this issue, even though there are several studies on the viscous fingering that arises due to the higher viscosity of heavy oil (Da Costa e Silva, 1995; Jamaloei et al., 2016). The main aim of this research project was to provide a means to quantitatively image the waterflooding of a heavy oil saturated sandpack, by tracking the water-heavy oil interface or interfaces in real time. The multimodal imaging utilized both magnetic susceptibility and CT scanning using the dispersed maghemite nanoparticles as a contrast agent. The waterflood experiments aimed to simulate the oil recovery process employed for heavy oil waterflooding used as an enhanced oil recovery process in places such as the heavy oil reservoirs by Cold Lake in North-Eastern Alberta. The future aim of this research is to establish a method for the tracking the waterflooding of heavy oil in actual hydrocarbon reservoirs.

4.2 Nanoparticle Stability Experiments

4.2.1 Introduction

The purpose of the nanoparticle stability experiments was to determine a reliable procedure for generating a stable dispersed nanoparticle suspension. This step was critical as multiple studies have already shown how nanoparticle suspensions can aggregate due to instability if they are inadequately dispersed (Khan, 2012a; Khan et al., 2015; Prigiobbe et al., 2015). Prigiobbe et al. (2015) developed a mathematical model for the settling of suspended superparamagnetic iron oxide nanoparticles coated with cationic surfactant that were subjected to a continuous applied magnetic field. An ideal maghemite suspension would need to have good nanoparticle dispersion without any agglomerates. Once suspended the terminal velocity of the spherical particles can be calculated using Stoke's equation for a sphere falling in a fluid:

$$V_t = \frac{2(\rho_p - \rho_f) g R^2}{9\mu} \tag{4.1}$$

Where:

- V_t is the terminal velocity of the particle (m s^{-1})

- ρ_p is the density of the particle (kg m^{-3})
- ρ_f is the density of the fluid (kg m^{-3})
- g is the acceleration due to gravity (m s^{-2})
- R is the radius of the particle (m)
- μ is the dynamic viscosity (kg $m^{-1}s^{-1}$)

Using Stoke's equation for an individual maghemite nanoparticle suspended in water gives a terminal velocity of 9.22×10^{-10} m s^{-1} or 2.91 cm $year^{-1}$. Therefore if the nanoparticles were to be properly dispersed and suspended the nano-fluid has the potential for long term stability. It should be noted that at such particle sizes the effects of Brownian motion can become the dominant factor that governs the nanoparticle motion (Ferguson et al., 2013). This may lead to the gravitational force being completely unbalanced by continuous collisions of the nanoparticle molecules with the fluid molecules, thus confining the motion of the nanoparticles. Collisions between different nanoparticles themselves would be undesirable as this may lead to the formation of nanoparticle agglomerates, which would have larger terminal velocities. Coating the nanoparticles with a surfactant would thus be beneficial as it would ideally prevent the collision between nanoparticles, and thus hindering the formation of larger nanoparticle agglomerates.

4.2.2 Stability Trial Experimental Summary Results and Discussion

Refer to **Section 2.4.8** for the details of the stability Trials #1-6. The suspension for the first trial was comprised of deionized water, maghemite nanoparticles, sodium dodecylbenzenesulfonate (DDBS) and sodium iodide (**Table 4.1**). The DDBS surfactant was used to maintain the nanoparticle dispersion, while the sodium iodide was used in order to increase the ion concentration in the suspension. Due to the similar densities of the heavy oil and water that were to be used in the waterflood experiments the sodium iodide was believed to be a necessary contrast agent for the CT scanner. The resulting suspension proved to be unstable in this case. Nanoparticle agglomerates could be clearly seen on the bottom of the graduated cylinder (**Figure 4.1**).

Table 4.1: Compositions for the dispersed nanoparticle suspension stability experiments.

	Trial #1	**Trial #2**	**Trial #3**	**Trial #4**	**Trial #5**	**Trial #6**
Deionized Water (g)	191.03	191.51	261.84	237.76	242.33	226.83
Deionized Water (wt%)	93.140	93.172	93.144	97.103	99.599	96.903
Maghemite (g)	0.120	0.094	0.130	0.163	0.165	2.170
Maghemite Concentration (wt%)	0.059	0.046	0.047	0.067	0.068	0.927
Maghemite Concentration (g L^{-1})	0.628	0.491	0.496	0.686	0.681	9.567
DDBS (g)	0.640	0.660	0.870	0.850	0.810	5.080
DDBS (wt%)	0.312	0.321	0.309	0.347	0.333	2.170
Sodium Iodide (g)	13.310	13.280	18.270	N/A	N/A	N/A
Sodium Iodide (wt%)	6.489	6.461	6.500	N/A	N/A	N/A
Sodium Chloride (g)	N/A	N/A	N/A	6.080	N/A	N/A
Sodium Chloride (wt%)	N/A	N/A	N/A	2.483	N/A	N/A

The magnetic susceptibility profile of the graduated cylinder (determined using the Bartington MS2C sensor) was also consistent with the visual observation. The initial magnetic susceptibility profile of the cylinder was relatively consistent along its length with values between 8.5 and 10 x 10^{-5} SI **(Figure 4.2**). Error bars were calculated and included for the magnetic susceptibility values to show that they were not substantially larger than the symbol sizes of the graph. The magnetic susceptibility values throughout much of the cylinder after a time interval of 49 hours consistently gave values close to 0 x 10^{-5} SI reinforcing the visual observation that the majority of the nanoparticles had settled out of the suspension. These observations revealed settling rates that were much faster than those expected theoretically. Two possible reasons seemed likely for this. Either the nanoparticle dispersion was inadequate leading to the presence of large maghemite agglomerates which would have larger terminal velocities, or something was destabilizing the suspension leading to the formation of nanoparticle agglomerates after the dispersion of the particles (or a combination of the two reasons).

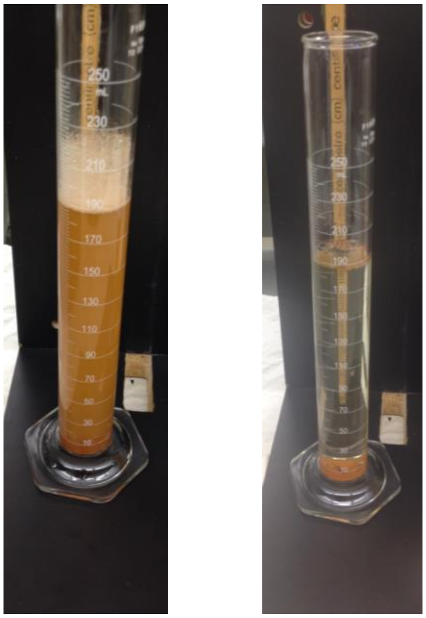

0 hours 49 hours

Figure 4.1: Stability experiment Trial #1 of maghemite nanoparticles.

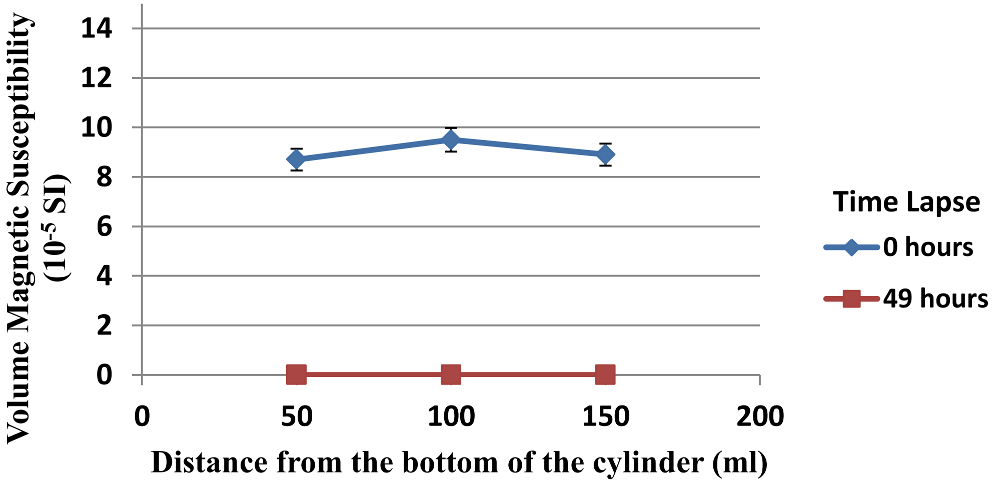

Figure 4.2: Magnetic susceptibility response (using the Bartington MS2C sensor) of stability experiment Trial #1 of maghemite nanoparticles (concentration 0.628 g L^{-1}).

Trial #2 had a slightly different mixing procedure from Trial #1 (see **Section 2.4.8** of **Chapter 2**), while keeping comparable amounts of the components (**Table 4.1**). Similar to Trial #1 there was observable settlement of the nanoparticles (**Figure 4.3**). After less than 24 hours there were visible changes to the suspension with distinguishable particle agglomerates that had settled out of suspension. The magnetic susceptibility profiles of the graduated cylinder were also consistent with these observations (**Figure 4.4**). The initial magnetic susceptibility profile of the cylinder had values between 4.5 and 5.4 x 10^{-5} SI, which were lower than the initial measurements of Trial #1 suggesting a poorer nanoparticle dispersion. The second measurement taken after 22.5 hours had a magnetic susceptibility value throughout much of the cylinder of 0 x 10^{-5} SI and confirmed that the majority of the suspended nanoparticles had settled out.

Trial #3 modified the mixing procedure further by altering the mixing order of the components and introducing an ice bath during the sonication process (the ice bath was introduced in order to limit the Brownian motion of the nanoparticles), while keeping the suspension composition similar to the first two trials (**Table 4.1**). The method proved unreliable as the nanoparticles had dropped out of suspension and settled to the bottom of the cylinder within 48 hours (**Figure 4.5**). The magnetic susceptibility profile measurements also confirmed the visual observation. The initial volume magnetic susceptibility of the cylinder was between 7.8 and 10.5 x 10^{-5} SI (**Figure 4.6**). The second magnetic susceptibility profile was taken after 44 hours and it failed to detect a magnetic susceptibility response throughout much of the cylinder confirming that most of the nanoparticles had settled out of the suspension.

The purpose of Trial #4 was to test the viability of using sodium chloride instead of sodium iodide as a potential contrast agent for the CT scanner. The procedure used for this trial was a modification of the methodology used for Trials #2 and #3. The nanoparticle suspension in this trial proved unstable again, with observable settlement of the nanoparticles within 20 hours (**Figure 4.7**). The visual observations were supported by the magnetic susceptibility profiles of the suspension (**Figure 4.8**). The initial magnetic susceptibility values of the suspension were between 9 and 11.6 x 10^{-5} SI, while the second magnetic susceptibility profile failed to detect a magnetic susceptibility response throughout much of the cylinder confirming that most of the nanoparticles had settled out of suspension.

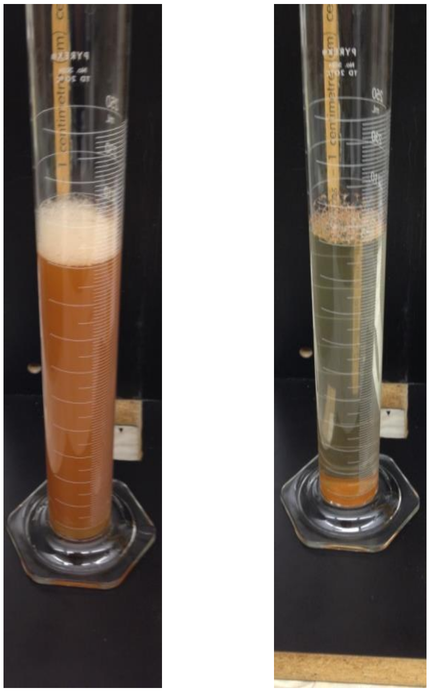

0 hours 22.5 hours

Figure 4.3: Stability experiment Trial #2 of maghemite nanoparticles.

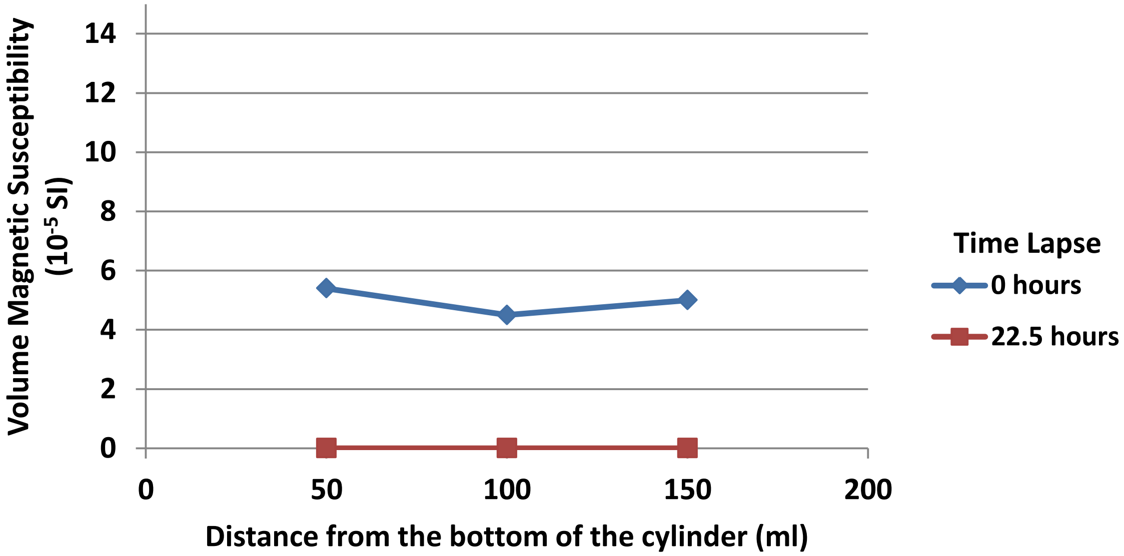

Figure 4.4: Magnetic susceptibility response of stability experiment Trial #2 of maghemite nanoparticles (concentration 0.491 g L^{-1}).

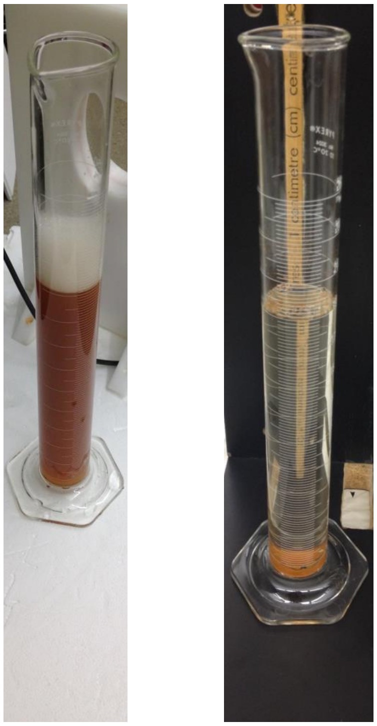

0 hours 44 hours

Figure 4.5: Stability experiment Trial #3 of maghemite nanoparticles.

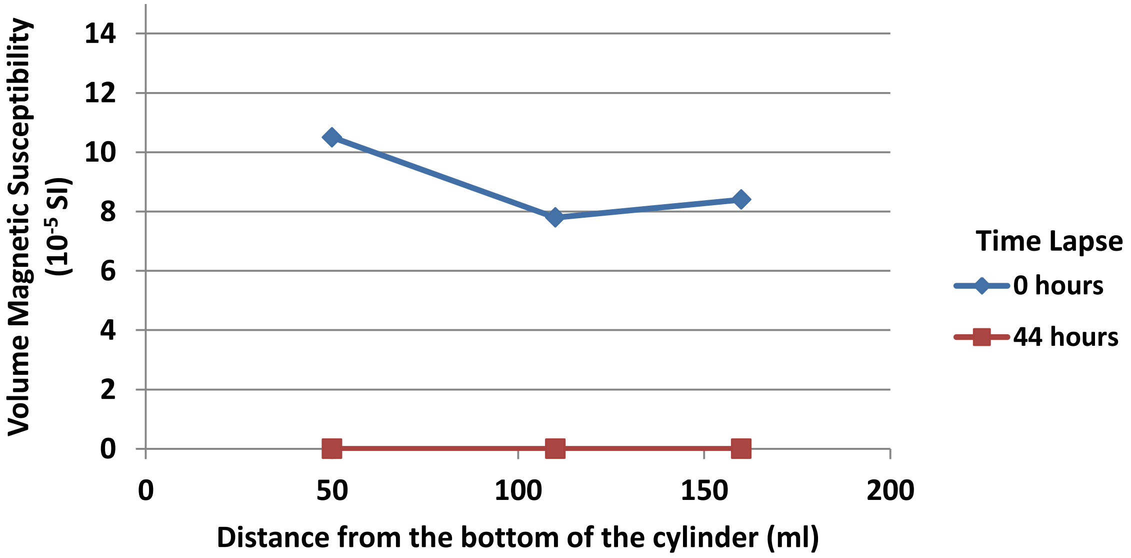

Figure 4.6: Magnetic susceptibility response of stability experiment Trial #3 of maghemite nanoparticles (concentration 0.496 g L^{-1}).

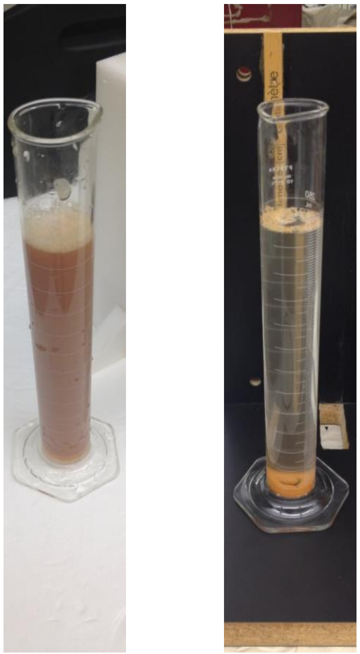

0 hours 20 hours

Figure 4.7: Stability experiment Trial #4 of maghemite nanoparticles.

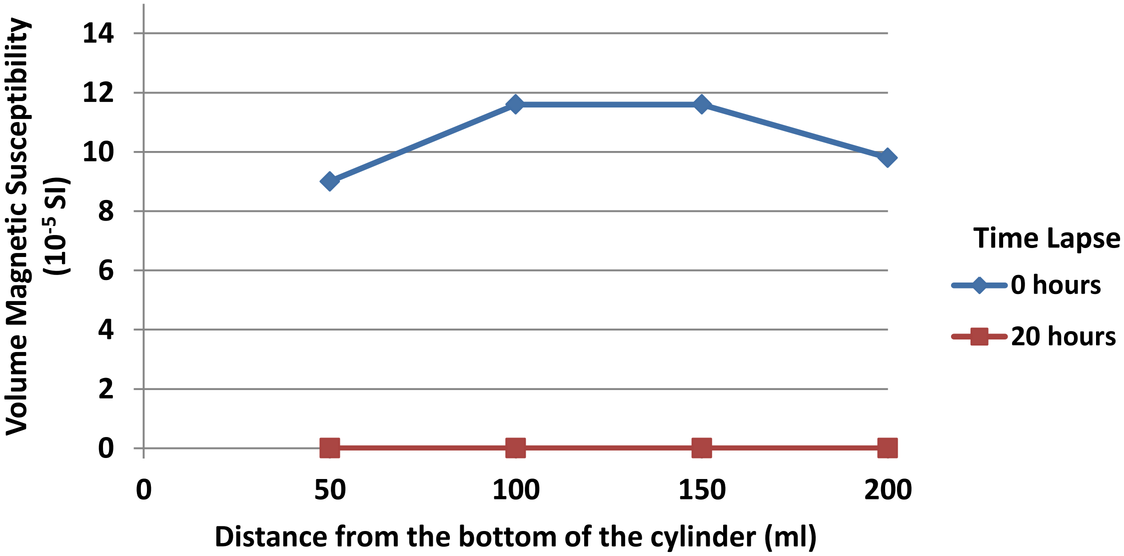

Figure 4.8: Magnetic susceptibility response of stability experiment Trial #4 of maghemite nanoparticles (concentration 0.686 g L^{-1}).

The methodology used for Trial #5 was similar to the one used for Trial #3. The modification for this trial was the composition of the suspension. It consisted of maghemite nanoparticles, DDBS dispersant and deionized water. The sodium iodide was excluded in order to examine the suspension stability without it. In this trial the maghemite suspension appeared to be visually stable over time (**Figure 4.9**). The initial magnetic susceptibility profile of the cylinder had values between 35.9 and 37.3 x 10^{-5} SI (**Figure 4.10**). The second magnetic susceptibility profile was taken 19 hours after the first one and displayed a slight drop of in magnetic susceptibility values (between 29.5 and 31.2 x 10^{-5} SI), which was most likely the result of some undispersed nanoparticle agglomerates settling out of suspension. The agglomerates would have greater terminal velocities than the individual nanoparticles leading to accelerated settling out. The third and fourth magnetic susceptibility profiles (collected at 55 and 195 hours) were both consistent with the second one, with magnetic susceptibility values between 28.9 and 31.6 x 10^{-5} SI. This would suggest that after the initial settling of the larger nanoparticle agglomerates, the remaining suspension was stable. As the trial utilized a procedure similar to previously tested methods (Khan, 2012a; Khan et al., 2015) the observed suspension stability was attributed to the alteration of the suspension composition. This led to the conclusion that the cause for instability in previous trials was due to the presence of sodium iodide (or sodium chloride for Trial #4).

Trial #6 utilized a similar procedure and suspension composition to Trial #5. The main difference in this trial was the increased concentration of the maghemite nanoparticles and the DDBS dispersant. The main objective of this trial was to explore the possibility of using a higher concentration of nanoparticles in order to replace the use of sodium iodide. The resulting suspension appeared visually stable even with the increased nanoparticle concentrations (**Figure 4.11**). The initial magnetic susceptibility profile of the cylinder had values between 296 and 360 x 10^{-5} SI (**Figure 4.12**). The second magnetic susceptibility profile was taken 48 hours after the initial one and showed a slight drop in magnetic susceptibility values while keeping the same trend. After the initial drop in magnetic susceptibility the suspension appeared to stabilize as the magnetic susceptibility profiles taken at the 48 and 166 hour marks were almost identical. Similar to Trial #5 the observed drop of magnetic susceptibility values between the initial profile and the ones taken at later times was attributed to a few particle agglomerates which settled out quickly. The magnetic susceptibility values were higher than for Trial #5 due to the higher maghemite concentration.

0 hours 19 hours 55 hours 195 hours

Figure 4.9: Stability experiment Trial #5 of maghemite nanoparticles.

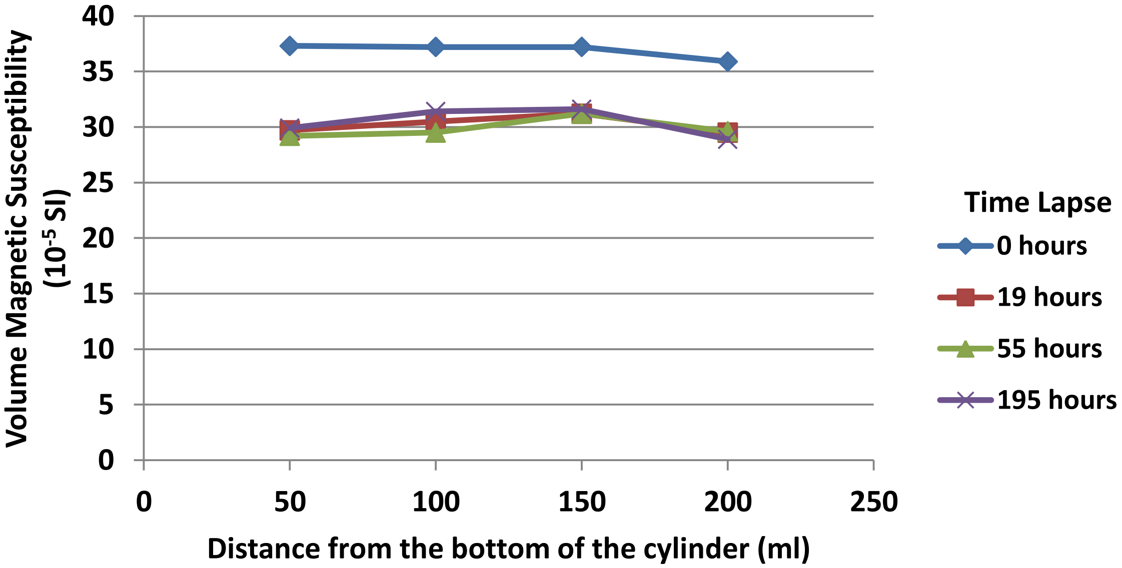

Figure 4.10: Magnetic susceptibility response of stability experiment Trial #5 of maghemite nanoparticles (concentration 0.681 g L^{-1}).

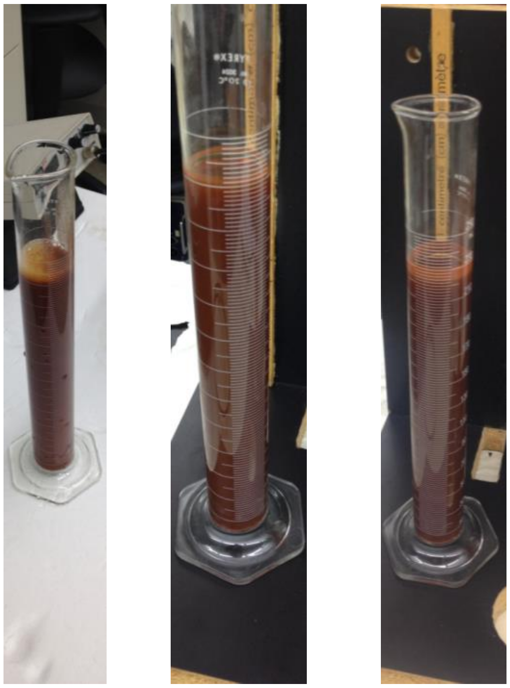

0 hours 48 hours 166 hours

Figure 4.11: Stability Experiment Trial #6 of maghemite nanoparticles.

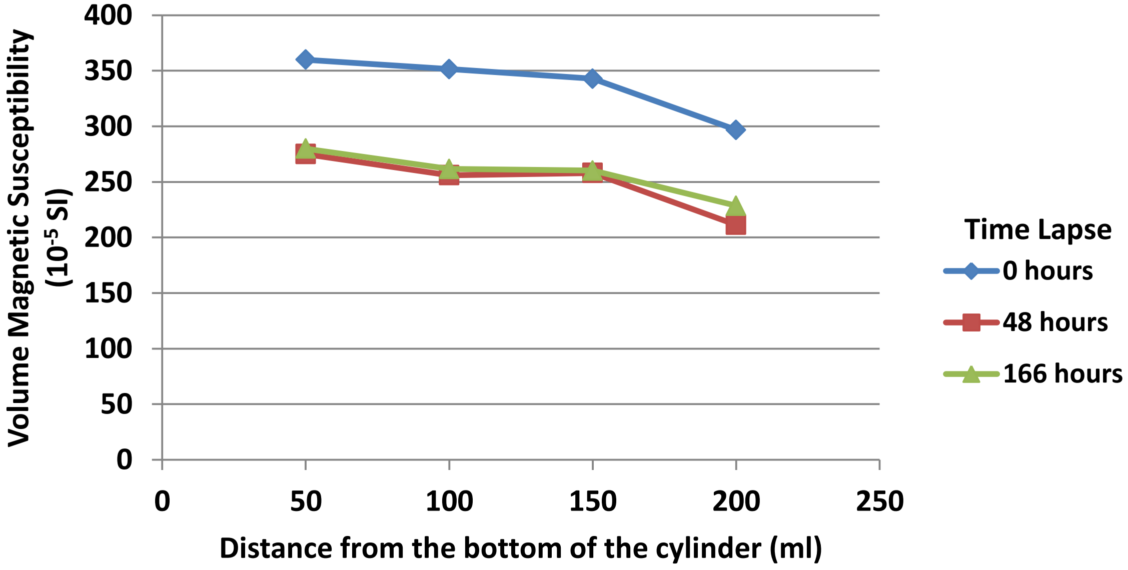

Figure 4.12: Magnetic susceptibility response of stability experiment Trial #6 of maghemite nanoparticles (concentration 9.567 g L^{-1}).

The experiments showed instability in the trials containing salts (sodium iodide or sodium chloride). This behaviour could be explained by the DLVO (named after Boris Derjaguin, Lev Landau, Evert Verwey, and Theodoor Overbeek) theory which describes the interaction forces between charged particles in a liquid medium. It combines the attractive van der Waals forces and repulsive electrostatic forces caused from the electrical double layer present around the particles. The electrical double layer results from an electric potential near the surface of the particles. **Figure 4.13** shows the electrical double layer which gives rise to a repulsive force between particles, and the strength of the repulsive force is directly connected to the thickness of the electrical double layer. Previous studies have shown (French et al., 2009; Jingkun et al., 2009; Khan, 2012b) that ionic strength can lead to particle agglomeration by decreasing the strength of the repulsive force from the electrical double layer (by decreasing the radius of the double layer). Khan (2012b) studied the effect of sodium chloride concentration on the stability of nanoparticle suspensions and found that an increase in ionic strength is proportionally detrimental to the stability of nanoparticle suspensions. What the present thesis did differently was test the effects of different dispersion techniques.

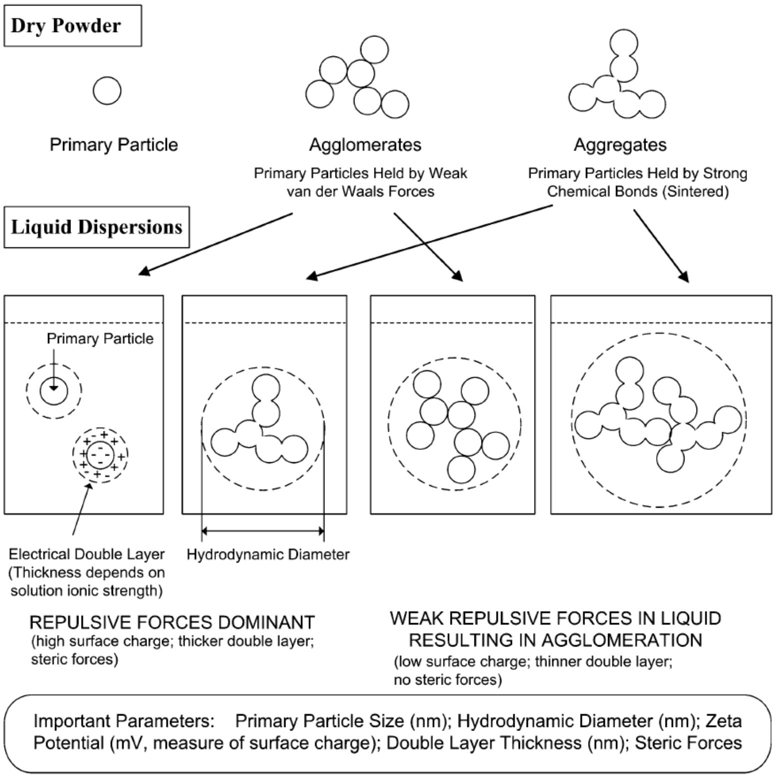

Figure 4.13: Electrical double layer model for particles (Jingkun et al., 2009).

4.2.3 Conclusions of Stability Tests

1. The stability experiments revealed that the presence of sodium iodide or sodium chloride caused rapid destabilization of the nanoparticle suspensions. The trials containing these salts (Trials #1, 2, 3, and 4) exhibited major settling out of the nanoparticles due to the formation of maghemite agglomerates. The results were consistent with previous work by French et al. (2009), and Khan (2012b), which demonstrated that the formation of nanoparticle agglomerates is related to the ionic strength and type of the electrolyte comprising the suspension. This was attributed to the weakening of the electrical double layer repulsive force due to the ionic strength of the suspension.
2. In the absence of sodium iodide and sodium chloride (Trial #5 and Trial #6) the maghemite suspensions had long term stability. The observed drop of magnetic susceptibility from the initial profile was attributed to the settling out of a few particle agglomerates which failed to disperse during the sonication process. The magnetic susceptibility profiles taken after that were consistent with each other, indicating that the suspension stabilized with no formation of new agglomerates. Therefore the suspension process was deemed quite successful, although there was still some room for improvement to 100% dispersion of the nanoparticles without any agglomerates.

4.2 Waterflood Experiment 1

4.2.1 Introduction

Waterflood experiment 1 was the first attempt to track the progression of the water-heavy oil interfaces(s) during a waterflood of a heavy oil saturated sandpack. The first waterflood experiment had three stages (**Table 4.2**). In the first stage the flow cell was saturated with water. In the second stage the flow cell was saturated with heavy oil. The final third stage was the waterflood stage when the maghemite nanoparticle suspension was injected and heavy oil was recovered from the production end. The waterflood 1 experiment was undertaken at InnoTech Alberta (formerly AITF). The flow cell and magnetic susceptibility sensor were set up on their

Table 4.2: Waterflood 1 experimental summary.

Injection Stage and Conditions		
1. Water Saturation Stage		
Injection Fluid:	De-ionized Water containing:	
	Sodium Iodide	6.5 wt%
	FLOPAAM	1800 ppm
Permeability (k)		5 Darcy
Injection Rate		60 ml hr^{-1}
2. Oil Saturation Stage		
Injection Fluid:	Heavy Oil	
Injection Rate		1 ml hr^{-1}
Total Injection		2 PV
3. Waterflood Stage		
Injection Fluid:	De-ionized Water containing:	
	Maghemite Concentration	0.05 wt%
	DDBS	0.31 wt%
	Sodium Iodide	6.48 wt%
	FLOPAAM	1800 ppm
	Sonication Time	40 min
Shaker Assembly		Yes
Injection Rate (Average)		1.45 ml hr^{-1}
Breakthrough Volume		1.1 PV
Total Volume Injected		3 PV
Total Oil Produced		0.4 PV

CT table (see **Chapter 2 Figures 2.10** and **2.11**) so that magnetic susceptibility and CT scans could be taken at closely comparable times.

Even though the stability experiments proved sodium iodide to be detrimental to the stability of the maghemite suspension, the presence of sodium iodide was initially thought necessary by InnoTech Alberta for the CT scanner's ability to distinguish water from heavy oil. Therefore the procedure used for the suspension generation was the same as for stability experiment Trial #1. In order to delay the settling of the nanoparticles the viscosity of the suspension was increased using FLOPAAM. The nanoparticle injection canister was also fitted to a shaker assembly in an attempt to maintain the suspension stability during the injection in the flow cell.

4.2.2 CT Scanning Results and Discussion

The porosity profile of the sandpack in the flow cell was generated using the CT scanner (calculated from the attenuation voxels and averaged over each slice) (**Figure 4.14**). From the injection end (left side) the porosity profile was relatively consistent until reaching a slight drop in porosity observed after the 65 mm mark. This may either be due to slightly inconsistent packing when creating the sandpack or a migration of sand particles during the initial water and oil saturation stages.

The total nano-fluid injected during the waterflood stage was 3 pore volumes (3PV) with oil production levelling off at about 0.4 PV (**Figure 4.15**). As breakthrough of water was expected to have a slope of one, the breakthrough was estimated to have occurred at about 1.1 PV of nano-fluid injection. The displacement of the curve towards higher injected volume versus produced volume suggested the presence of a compressible element in the system, most likely due to trapped gas.

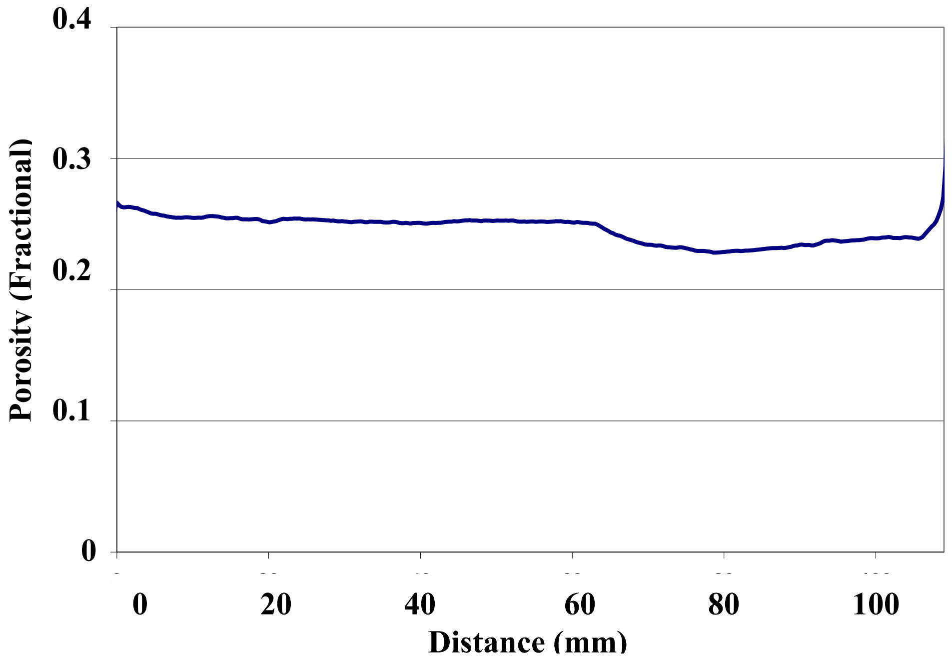

Figure 4.14: Porosity profile of the sandpack (saturated with heavy oil) along the axis of the flow cell (injection is left to right).

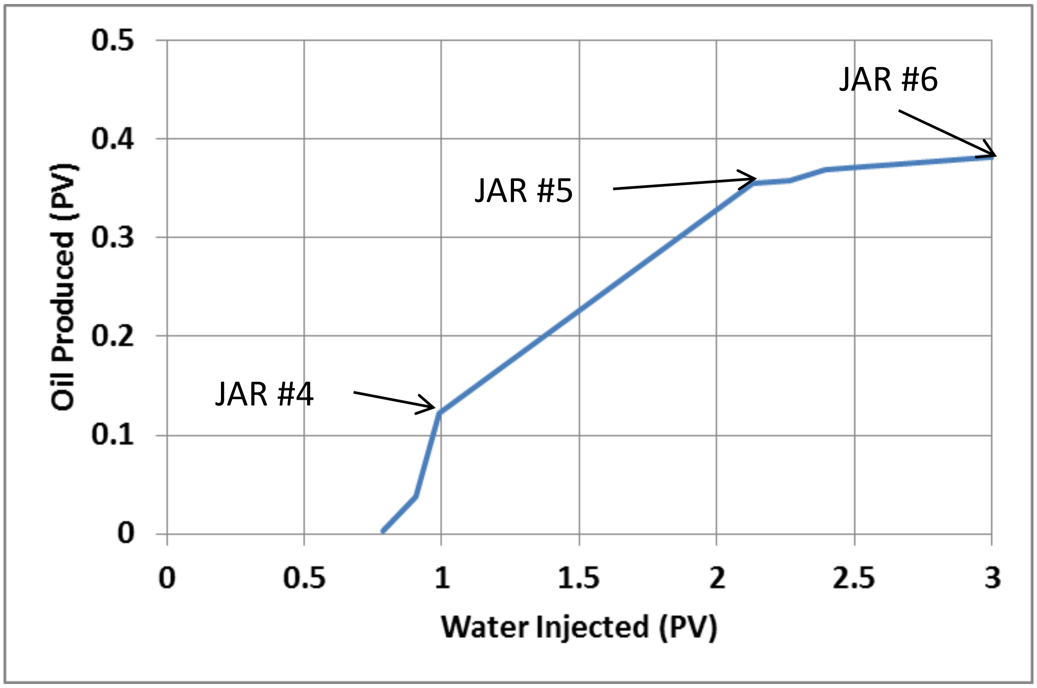

Figure 4.15: Produced oil versus injected water in waterflood 1. (PV refers to pore volume and JAR# refers to when a production jar was collected).

The CT profiles were taken at 1 hour intervals (**Figure 4.16**) and are representative of the porosity and water saturation along the flow cell. Nano01 to Nano07 were taken during the first day of waterflooding (representing hours 1 through 7 from the start of the waterflood). Profiles Nano08 to Nano15 were taken on the second day of the waterflooding and represent hours 24 through 31 from the start of the waterflooding.

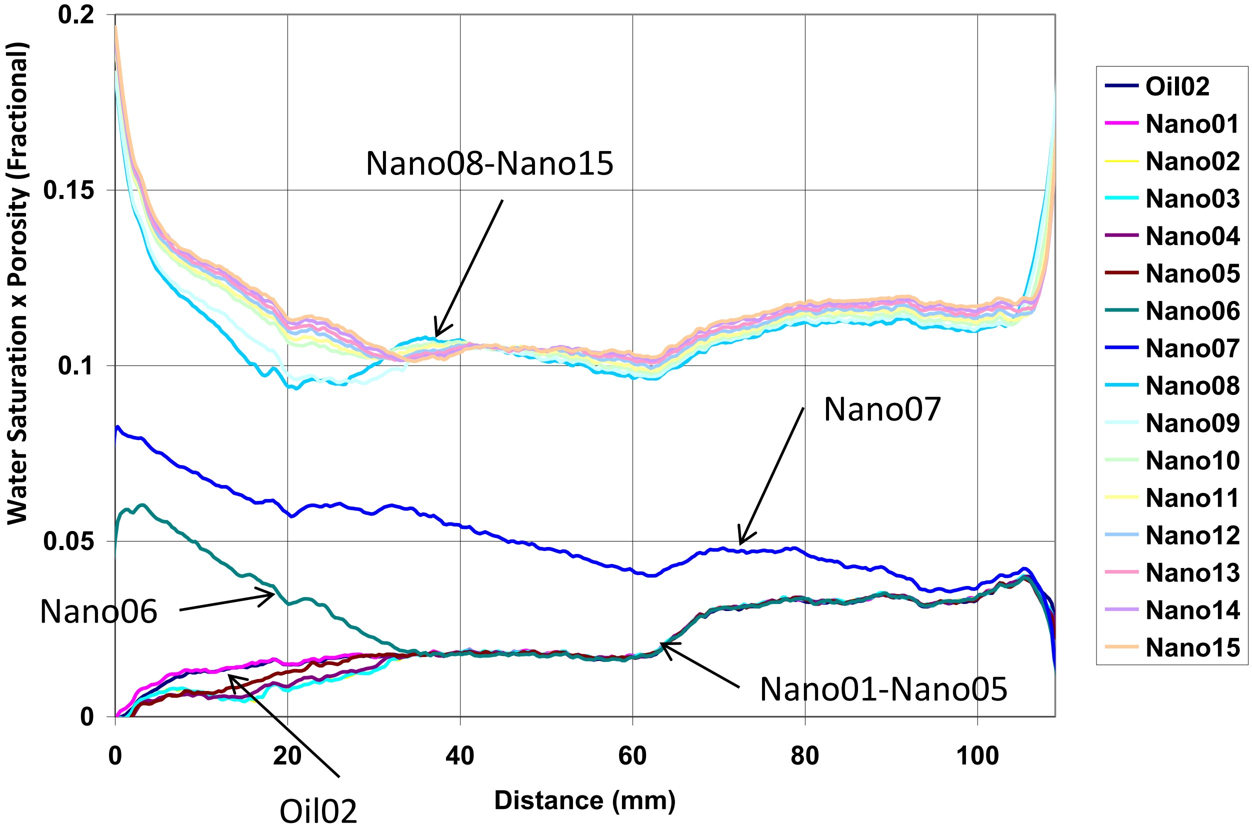

Figure 4.16: Water content profiles during the nanoparticle waterflood. Injection is from left to right. The Oil02 profile represents the baseline profile when the sandpack was saturated with heavy oil taken prior to the nano-fluid injections. Profiles Nano01 to Nano07 were taken at one hour intervals between hours 1 through 7 from the start of the nano-fluid injection. Profiles Nano08 to Nano15 were taken at one hour intervals during hours 24 through 31 from the start of the nano-fluid injection.

The first five water saturation profiles (Nano01–Nano05) taken over the first five hours from the start of the nano-fluid waterflooding revealed negligible deviation from the base flow cell profile Oil02. Nano06 taken at the 6 hour mark was the first profile to show a difference in water saturation from the base Oil02 profile. In this case an increase in water saturation can be seen over the first 30mm from the injection end of the flow cell. This was the first CT profile to clearly show the presence of the injected nanoparticle suspension inside the flow cell. The profile of Nano07 was taken at the 7 hour mark and showed a further increase in water saturation. The increase in water saturation observed in this case was almost along the full length of the flow cell profile, suggesting that breakthrough of the nanoparticle suspension was imminent. Even though there is some indication of increased saturation of the nano-fluid the CT scan profiles failed to successfully track the progression of the water-heavy oil interface(s) prior to the breakthrough.

Profiles Nano08 through to Nano15 were taken on the second day of measurements and they correspond to hours 24 through 31 from the beginning of the waterflood. The shape of the profiles in this case was relatively consistent with general increases of water saturation with time. This behaviour was consistent with the experimental expectations, as more oil was produced and more water (nano-fluid) was introduced in the flow cell to replace the displaced oil.

4.2.3 Magnetic Susceptibility Scanning Results and Discussion

A volume magnetic susceptibility profile of the flow cell with the heavy oil saturated sandpack was first undertaken (**Figure 4.17**) prior to injection of the nanoparticle suspension. The "U" shaped profile and large magnetic susceptibility values at each end of the flow cell were due to the metallic end fittings. The large background signals proved problematic in obtaining a clearly identifiable signal due to the nanoparticle suspension when it was injected into the flow cell.

Seven volume magnetic susceptibility profiles were taken at one hour intervals (immediately after each CT scanning profile) during the first day of waterflooding (**Figure 4.18**). The magnetic susceptibility values shown represent those after subtraction of the background signal shown in **Figure 4.17**. These initial results showed that some nanoparticles were collecting and aggregating near the metallic end fittings (giving higher magnetic susceptibility readings). The middle section of the flow cell (25-75 mm from the inlet) was less influenced by the end fittings and the lower magnetic susceptibility values were expected to be a better indication of the amount of nanoparticles injected into the sandpack. However, it was difficult to see any discernible change on the first day as all the profiles in the middle of the flow cell were quite similar. The error bars are shown in **Figure 4.18** for the hour 1 profile scan, and show that the metal end fittings resulted in larger uncertainties compared to the middle section.

On the second day of the waterflooding the eight volume magnetic susceptibility profiles in the middle of the flow cell (around 25-80 mm in this case) showed much more distinct differences with time (**Figure 4.19**). As time progressed, and therefore more nanoparticle suspension was injected into the sandpack, the magnetic susceptibility values generally increased, as one might expect. This increase in magnetic susceptibility with time was a clear indication of the increase in magnetic nanoparticle concentration within the flow cell, as the nano-fluid was replacing the heavy oil within the flow cell. The profiles still showed artefacts, however, at each end of the flow cell (due to the metallic end fittings) where aggregates of nanoparticles were formed. Errors were based on the calibration accuracy of the Bartington MS2C sensor.

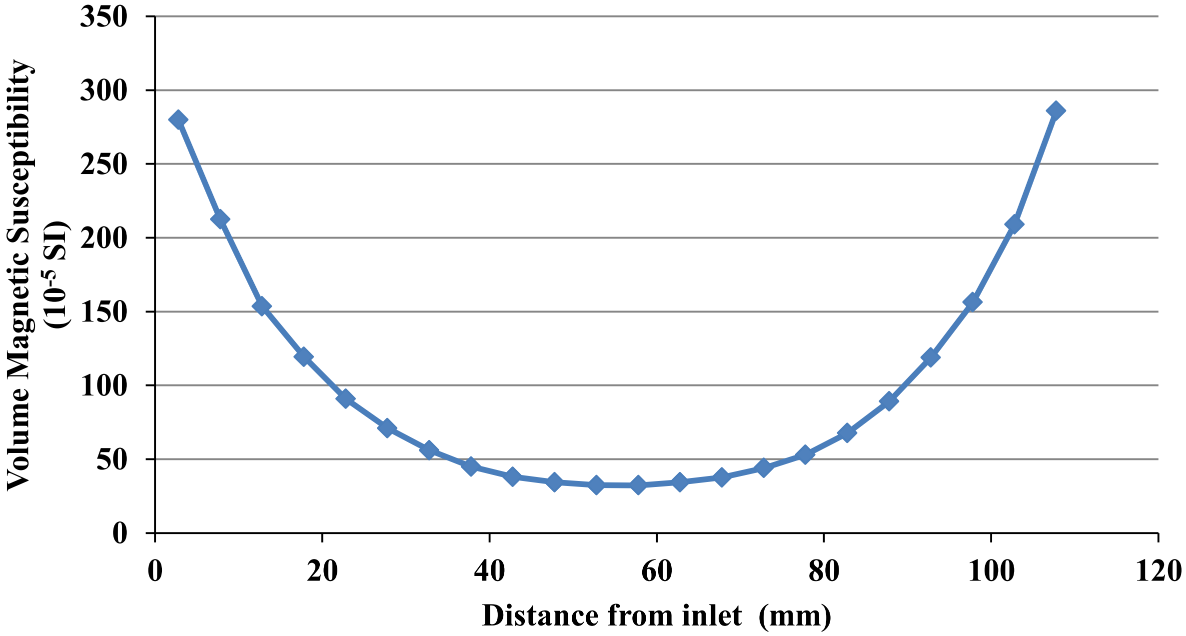

Figure 4.17: Volume magnetic susceptibility profile of the flow cell with the heavy oil saturated sandpack prior to nanoparticle suspension injection.

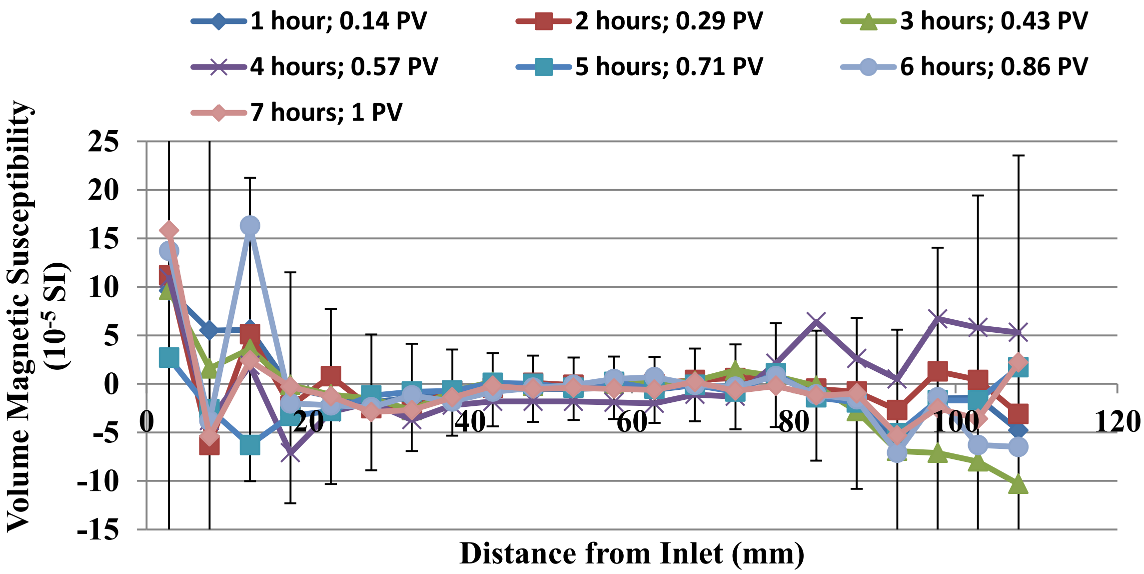

Figure 4.18: Volume magnetic susceptibility profiles (using the Bartington MS2C sensor) taken during day one of nanoparticle suspension flooding of a heavy oil saturated sandpack. Injection is from left to right. Legend is the time lapse from the beginning of waterflooding (PV refers to injected pore volumes).

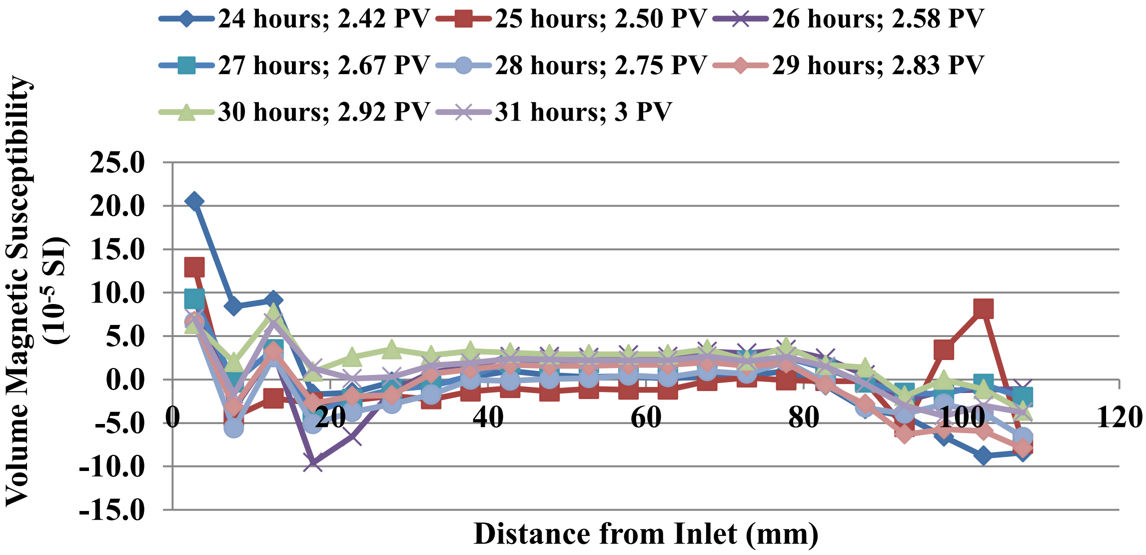

Figure 4.19: Volume magnetic susceptibility profiles taken during day two of the nanoparticle suspension flooding of a heavy oil saturated sandpack. Injection is from left to right. Legend is the time lapse from the beginning of waterflooding (PV refers to injected pore volumes).

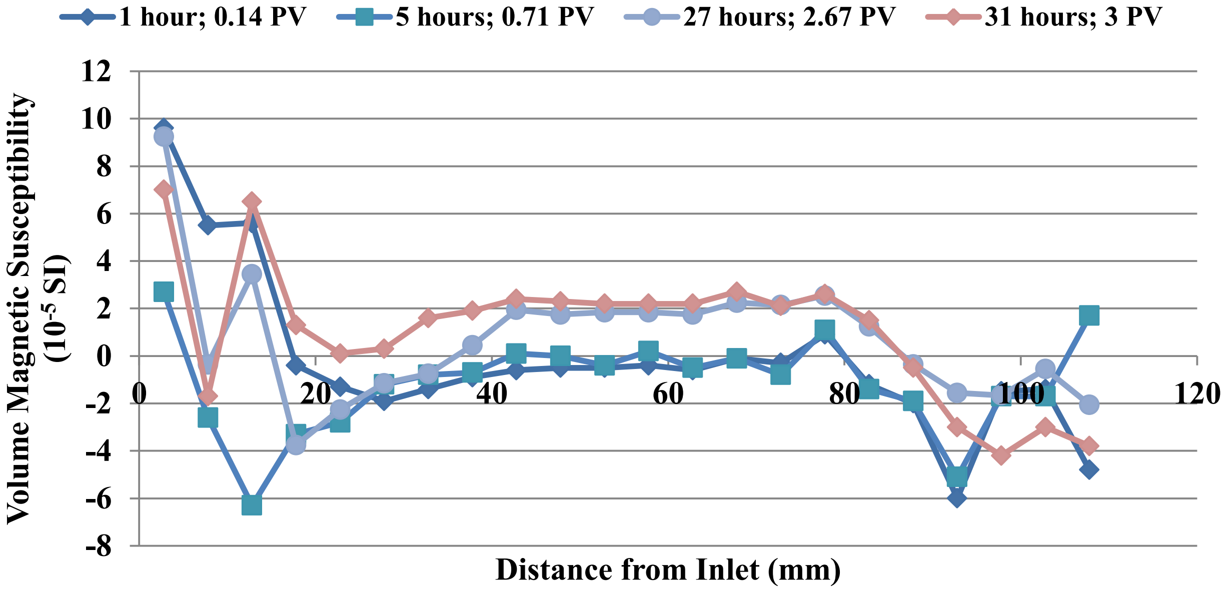

Figure 4.20: Comparison of some of the volume magnetic susceptibility profiles on days one and two of the nanoparticle suspension flooding of a heavy oil saturated sandpack. Injection is from left to right. Legend is the time lapse from the beginning of waterflooding.

The change with time can more clearly be seen by plotting some of the magnetic susceptibility profiles from both days (**Figure 4.20**). The increases of magnetic susceptibility with time for the middle part of the flow cell are clearly evident.

Even though the experiment could detect the presence of nanoparticles within the flow cell a number of issues were identified. The shaker assembly appeared to be ineffective in maintaining the dispersed nanoparticle suspension. There were two observations pointing to this conclusion. First the maghemite suspension left over in the injection accumulator revealed large nanoparticle agglomerates (**Figure 4.21A**). Second, when examining the production jars of the waterflood experiment (**Figure 4.21B**) JARS #5 and #6 appear relatively clear suggesting a low concentration of maghemite nanoparticles when compared to the initial dispersed nanoparticle suspension (JAR #7). The low concentration of nanoparticles was attributed to the presence of the sodium iodide additive in the maghemite suspension, which had already been proved to be detrimental to the stability of the suspensions but was thought necessary by InnoTech Alberta for the CT scanning. Another issue which was identified during the first waterflood experiment was the effect on the magnetic susceptibility of the metal end connection fittings. Their large magnetic susceptibilities made it difficult to distinguish the signal of the nanoparticles from the background "noise", and their metallic nature appeared to attract the nanoparticles and cause agglomerates to accumulate at the ends of the flow cell. The formation of agglomerates was also largely caused by the addition of the sodium iodide.

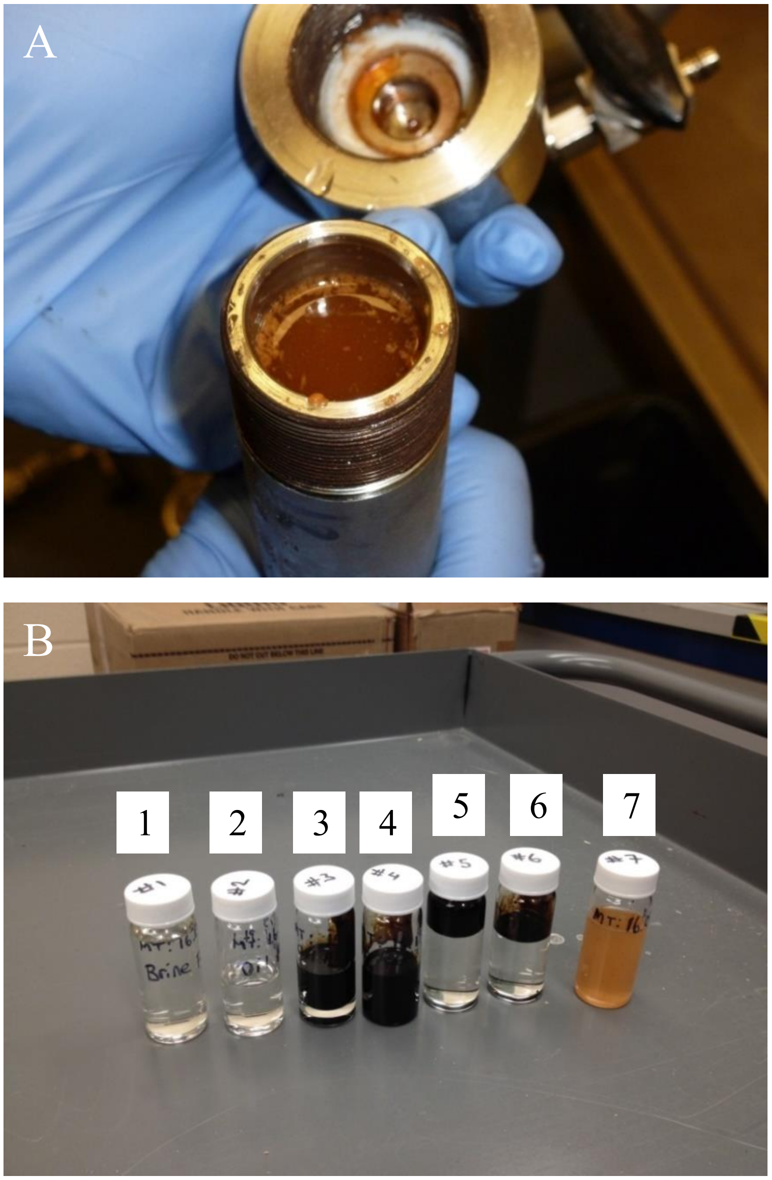

Figure 4.21: (A) Maghemite nano-fluid left over in the accumulator following waterflood 1 experiment. (B) Production jars during waterflood 1 experiment. A description of their contents, and the relation to the various stages of the experiment, is given in **Table 4.3**.

Table 4.3: Production jars stage summary.

JAR #	Stage (Fluid Injected and Collected at PV Injected)	Fluid Produced in JARS
1	Initial Waterflood	Brine
2	Oil Saturation	Brine
3	Oil Saturation	Brine and Oil
4	Nano-Fluid Waterflood day 1 (1PV)	Oil
5	Nano-Fluid Waterflood day 1- day 2 (2.2 PV)	Oil and Nano-Fluid
6	Nano-Fluid Waterflood day 2 (3 PV)	Oil and Nano-Fluid
7	Initial Dispersed Nanoparticle Suspension	N/A

4.2.4 Conclusions of Waterflood 1

In the first waterflood experiment both CT and magnetic scanning techniques were not very effective at tracking the progression of the water-heavy oil interfaces(s) during of the waterflooding process.

1. Two CT scanning profiles (Nano06 and Nano07) did show some minor indication of the progression of the waterflooding, but CT was unable to track the full process in real time.
2. The magnetic susceptibility scanning was able to distinguish small changes in the nanoparticle concentration over the two days, despite the large background signal from the metallic end fittings. However the results were far from ideal, and the experiment highlighted key areas where significant improvements could be made.
3. Waterflood 1 revealed two major issues that needed to be addressed. First, the metal end fittings of the PEEK flow cell generated an unwanted high background magnetic susceptibility signal. These end fittings were replaced with PEEK ones in waterflood 2. Second, the maghemite nanoparticle suspension was highly unstable from the addition of the sodium iodide leading to the formation of aggregates. Measures taken to keep the

nanoparticles suspended (using the shaker) also proved ineffective. These issues had to be addressed prior to conducting the next waterflood experiment.

4.3 Waterflood Experiment 2

4.3.1 Introduction

The second waterflood experiment (also undertaken at InnoTech Alberta) aimed to address the issues identified during the waterflood 1 experiment. In waterflood 2 the metallic end fittings at the inlet and outlet of the flow cell were replaced by customized PEEK ones. This was done in order to reduce the large background magnetic susceptibility. The second improvement was in the composition of the dispersed nanoparticle suspension used for the waterflooding stage (**Table 4.4**). In this case the maghemite suspension used a higher concentration of nanoparticles and abandoned the use of sodium iodide. The higher nanoparticle concentration was used to increase the magnetic susceptibility signal, as well as being a substitute contrast agent for the CT scanner in place of the sodium iodide. The new stable suspension was created using the procedure for stability experiment Trial #6 (see **Chapter 2 Section 2.4.8**).

Previous studies (Jamaloei et al., 2016), and observations from waterflood 1, recognized that the waterflooding of heavy oil does not seem to produce a recognizable “flow front” separating the water from the heavy oil, but can result in viscous fingering or thin films of fluid flow. Thus this section will not refer to a “flow front” but instead will use the term “water-heavy oil interface(s)” since there may be more than one water-heavy oil interface.

Table 4.4: Waterflood 2 experimental summary.

Injection Stage and Conditions		
1. Water Saturation Stage		
Injection Fluid:	De-ionized Water containing:	
Permeability (k)		5 Darcy
Injection Rate		60 ml hr^{-1}
2. Oil Saturation Stage		
Injection Fluid:	Heavy Oil	
Injection Rate		0.5 ml hr^{-1}
Total Injection		1.2 PV
3. Waterflood Stage		
Injection Fluid:	De-ionized Water containing:	
	Maghemite Concentration	0.6 wt%
	DDBS	0.81 wt%
	Sonication Time	20 min
Injection Rate		1 ml hr^{-1}
Breakthrough Volume		0.44 PV
Total Volume Injected		1.75 PV
Total Oil Produced		0.2 PV

4.3.2 CT Scanning Results and Discussion

The fractional porosity of the oil saturated sandpack in the flow cell was calculated using the CT scanner prior to the waterflooding (calculated from the attenuation voxels and averaged over each slice) (**Figure 4.22**). The porosity of the sandpack was calculated to be between 29 and 34%, with a low porosity zone just before the 60 mm mark. The irregular porosity profile was most likely the result of slightly non-uniform packing of the flow cell or migration of sand particles during the initial water and oil saturation stages.

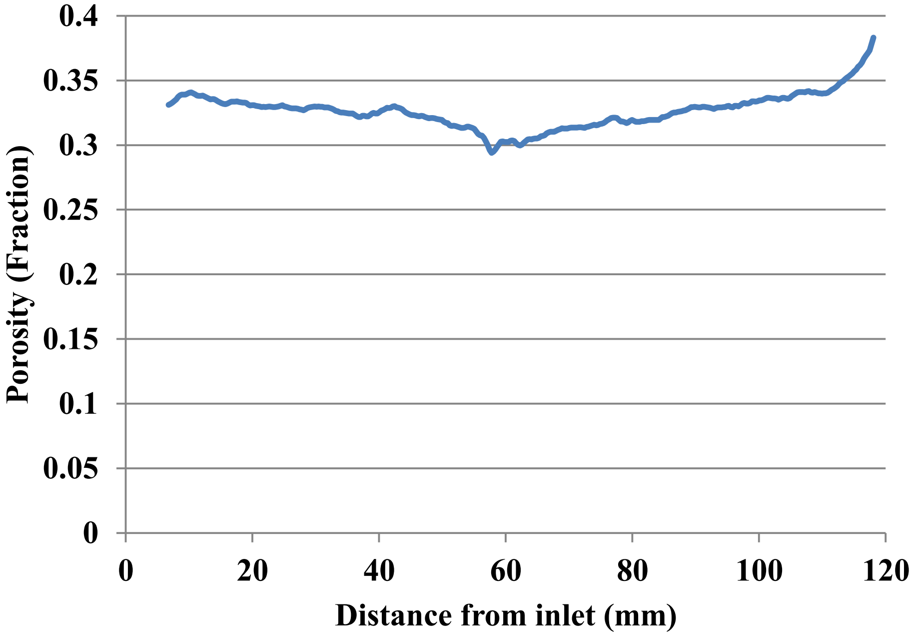

Figure 4.22: CT scanning porosity profile of the oil saturated sandpack. Injection is from left to right.

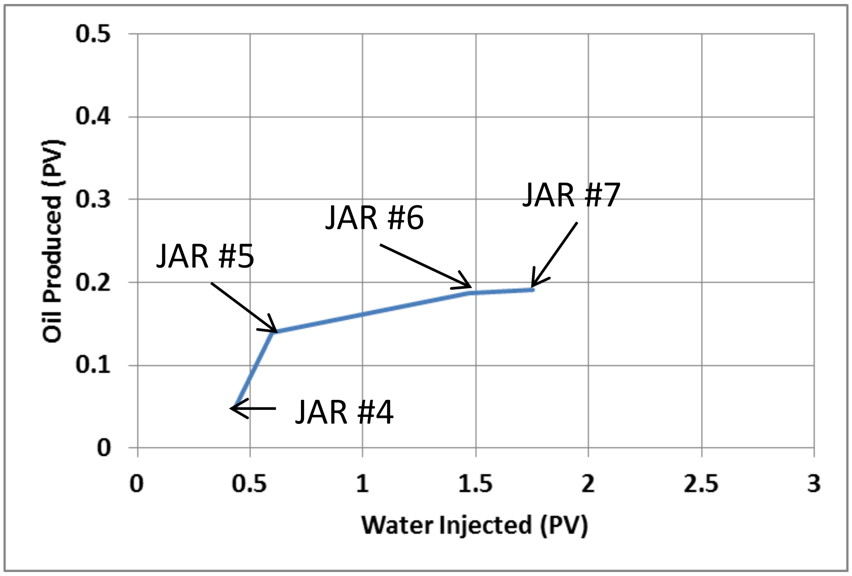

Figure 4.23: Produced oil versus injected nano-fluid during the waterflood 2 experiment (PV refers to pore volume and JAR# refers to when a production jar was collected).

The total injection volume during this waterflood experiment was 1.75 PV (**Figure 4.23**). Breakthrough volume was at 0.04 PV produced or 0.44 PV of injected nano-fluid at which point the production jar was replaced with a new one. The displacement of the curve towards higher injected volume versus produced volume suggested the presence of a compressible element in the system, most likely due to trapped gas.

The CT scanner contrast agent in this case was provided by the nanoparticles themselves. The attenuation values were calculated in Hounsfield units (HU). The CT scanner profiles (**Figure 4.24**) all revealed a low attenuation section after the 60 mm mark, which may have been caused by gas trapped during the initial water saturation and not fully swept out by the oil saturation of the sandpack. **Figure 4.25** is a 3D rendering generated by calculating the difference between the oil saturated CT scan and scan thirteen (final state) with the red section indicating decreased attenuation (possibly gas). This interpretation is further reinforced by the observed discrepancy between the injected and produced volumes. The observed low downstream attenuation (**Figure 4.24**) prevented any meaningful calculation of saturation profiles downstream of the 60 mm mark. Resolving the upstream portion (first 60 mm) of the CT profiles required further analysis as the nanoparticle-oil contrast was not very strong.

To further analyse the CT scanner profiles the first 60 mm of the sandpack were examined in more detail (**Figure 4.26**). Looking closer at the upstream profiles it was determined that the attenuation increased by up to approximately 4 HU between the first and last CT scan. Based on the calibrated nanoparticle-oil contrast of 24 Hounsfield units (HU) and a porosity of about 1/3, the peak value of 4 HU corresponds to an increase in saturation of 50%. The CT profiles clearly showed an increase in the attenuation between profiles 1 and 7 consistent with an increased magnetic susceptibility (due to injection of nanoparticles) as shown later in **Figure 4.28**. Moreover, the CT attenuation dropped once the main water-heavy oil interface(s) (identified from the magnetic susceptibility results and the material collected in the production jars) passed through the sandpack, consistent with the later magnetic susceptibility profiles of **Figure 4.29**. However, the CT profiles were unable to pinpoint the location and progression of the main water-heavy oil interface(s).

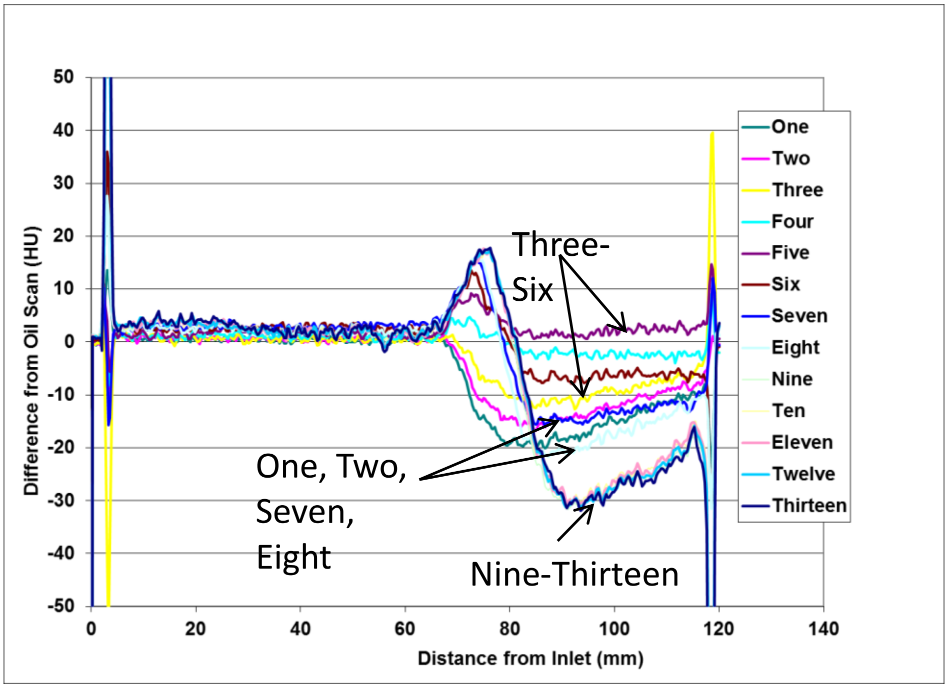

Figure 4.24: CT attenuation profiles (the difference from the initial CT scan with the sandpack in the oil saturated state) given in Hounsfield units (HU) for the waterflood 2 experiment. Profiles 1 to 8 were taken at one hour intervals from 1.5 to 8.5 hours from the start of injection. Profiles 9 to 12 were taken at one hour intervals from 23.5 to 27.5 hours from the start of injection. Injection is from left to right.

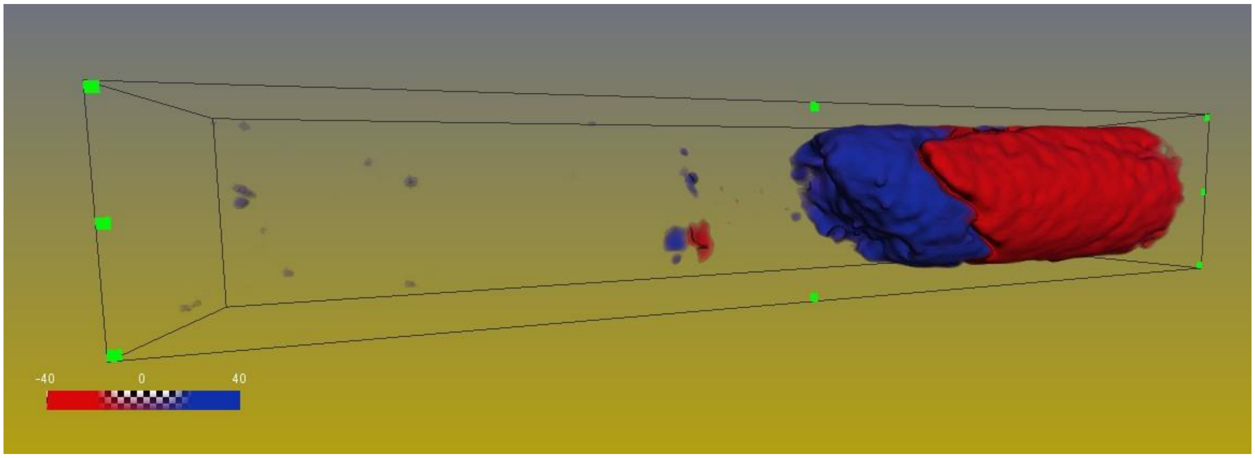

Figure 4.25: 3D rendering of the difference of the oil saturated CT scan and scan thirteen (final state). Blue indicates increased attenuation (unexplained peak) and red indicates decreased attenuation (possibly gas). Injection is left to right.

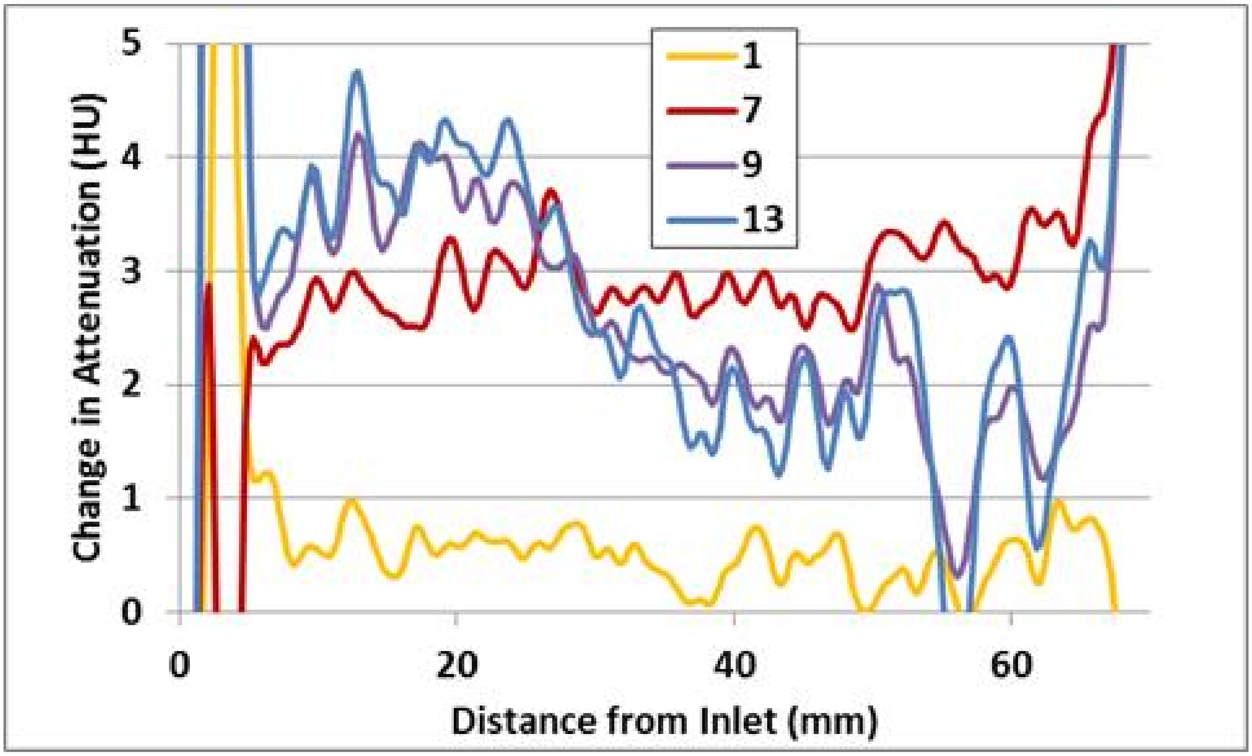

Figure 4.26: CT attenuation profiles (the change from the initial CT scan with the sandpack in the oil saturated state) for the upstream portion of the sandpack. Profiles 1, 7, 9 and 13 were taken at 1.5, 7.5, 23.5 and 27.5 hours from the start of the waterflooding respectively. Injection is from left to right.

4.3.3 Magnetic Susceptibility Scanning Results and Discussion

The background magnetic susceptibility profile prior to injection of the nanoparticle suspension was much lower with the new PEEK end fittings (**Figure 4.27**) of the flow cell compared to the background magnetic susceptibility profile of waterflood 1 which used the metallic end fittings (**Figure 4.17**) (the magnetic susceptibilities at the inlet and outlet of the flow cell were between 21 and 42 times lower after the PEEK end fitting replacement).

Eight volume magnetic susceptibility profiles were measured during the first day of nano-fluid injection (**Figure 4.28** shows profiles 3-8). The points on the profiles directly represent the content of maghemite nanoparticles at each point in the sandpack along the flow cell. The profiles revealed the progressive formation, growth and movement of a significant positive magnetic susceptibility peak, which initially formed on the left injection side of the flow cell (**Figure 4.28**, profiles 3 and 5) and migrated towards the right production (outlet) side as the injected volume of dispersed nanoparticle suspension increased (**Figure 4.28**, profiles 6-8). Due to the difference in viscosity between the nano-fluid and heavy oil the waterflood was likely to lead to viscous fingering rather than a single front during the oil production (Jamaloei et al., 2016). Therefore the magnetic susceptibility peak is likely the result of a higher concentration of nanoparticles collecting at the site of the main water-heavy oil interface(s) during the flooding process. This interpretation is based on the observation of the magnetic peak itself (a higher volume magnetic susceptibility suggests a higher concentration of nanoparticles are present), as well as the material collected in the production jars. The peak may not necessarily reflect higher water saturation (compared to portions of the sandpack closer to the inlet), since it appears that the nanoparticles agglomerate at the water-heavy oil interface(s) (from material collected in the production jars as discussed later). Typical error bars are shown for scan profile 8. Error bars were similar for the other profiles, but omitted in **Figure 4.28** (and **Figure 4.29**) for clarity. The measurement errors were lower than waterflood 1 experiment, which was attributed to the lower background noise in waterflood 2.

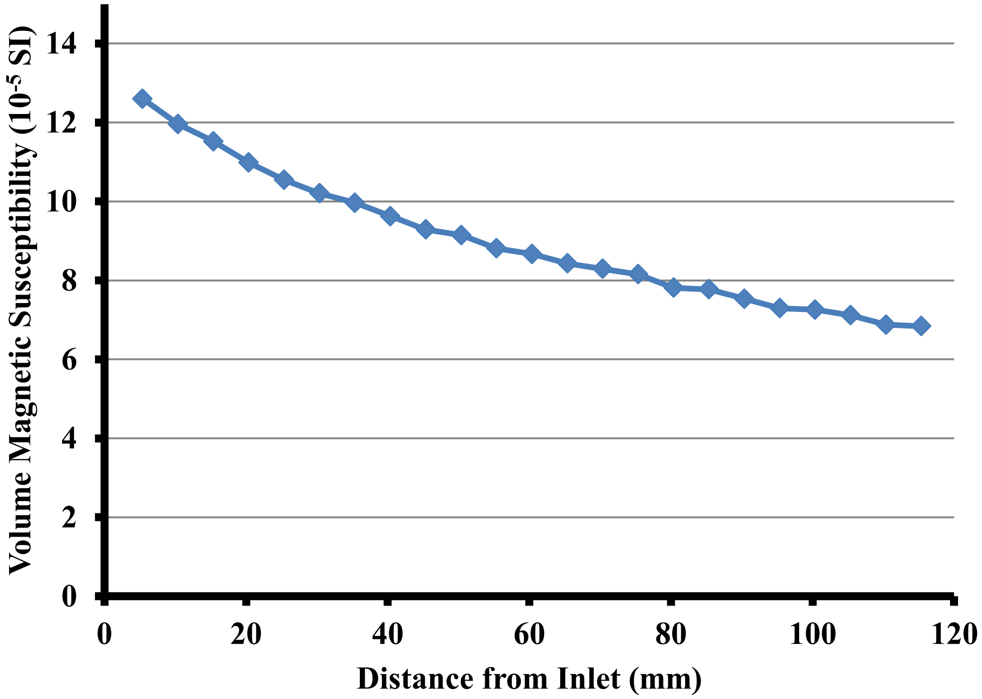

Figure 4.27: Volume magnetic susceptibility profile of the flow cell with the heavy oil saturated sandpack prior to nanoparticle suspension injection.

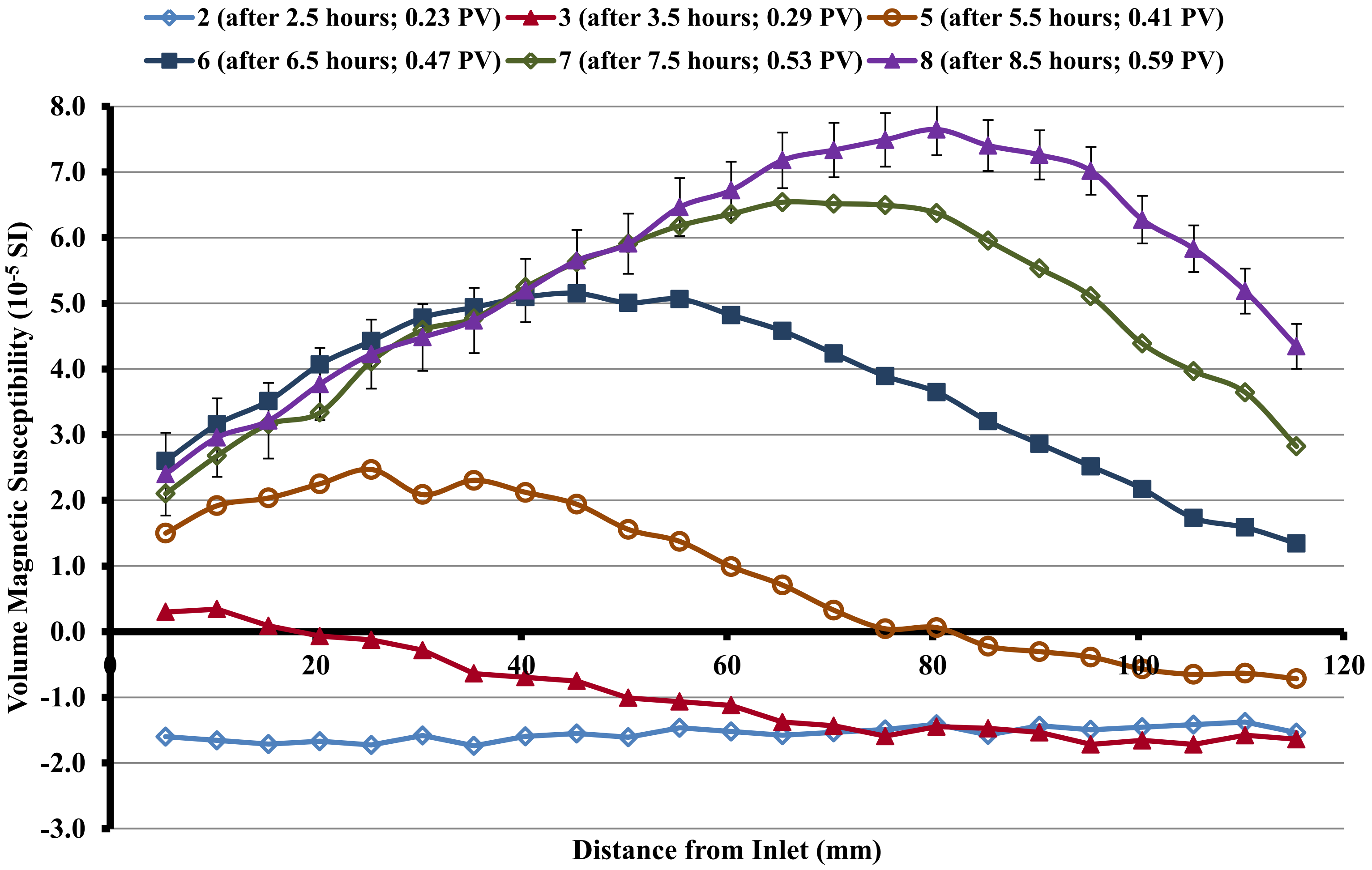

Figure 4.28: Volume magnetic susceptibility profiles taken during day one of the nano-fluid flooding of the heavy oil saturated sandpack. Legend is the time lapse from the beginning of waterflooding, as well as injected pore volumes of nano-fluid. Injection is from left to right. Typical error bars are shown on one of the profiles (similar error bars for the other profiles are omitted for clarity).

First breakthrough (nano-fluid recovered at the production end) was observed after an injection of approximately 7.34 ml (0.44 PV injected or 0.04 PV produced) halfway between profiles 5 and 6 and was accompanied by a drop in the pressure difference between the injection and production ends of the sand pack (**Figure 4.30**). This is consistent with the observed magnetic susceptibility profiles. Profile 5 shows negative magnetic susceptibility at the production end (right side of the graph) indicative of the absence of nanoparticles, while profile 6 has a clear positive magnetic susceptibility signal on the production end, which can only occur if nanoparticles are flowing through that section. Therefore it appears that breakthrough of the nanoparticle suspension occurred before the main water-heavy oil interface(s), whose progress was tracked by the magnetic susceptibility peak, reached the production end. This may happen if, for instance, viscous fingering is occurring. The results of **Figure 4.28** show how magnetic sensing of a nanoparticle suspension can track the progress of the main water-heavy oil interface(s) during water flooding of a heavy oil saturated sandpack. This would appear to be a significant result. The shape of the water-heavy oil interface(s) is likely to be complex (not a simple "flow front"), but the overall position of the main water-heavy oil interface(s) appears to be tracked by the peak in magnetic susceptibility in each of the curves of **Figure 4.28**. One analogy could be that the water-heavy oil interface(s), represented by the magnetic susceptibility peak, are akin to where fingers attach to the palm of one's hand. The "fingers" in this experiment are probable viscous fingers and where they begin is a "line" representing the water-heavy oil initial interface or interfaces (analogous to where fingers attach to the palm of one's hand). This "line" of interface(s) would seem to be a likely explanation for the peak in magnetic susceptibility. One can imagine the maghemite nanoparticles coming up against the heavy oil and accumulating there. Some of the nano-fluid suspension may break through in the form of viscous fingering or possibly thin films of fluid, but many of the nanoparticles will likely "stick" to the heavy oil layer immediately after they come into contact with it. In this scenario the magnetic susceptibility peak should increase with time (as more nano-fluid is injected) and also move from the inlet to the outlet end of the flow cell as the heavy oil is gradually displaced. This is exactly what is observed in **Figure 4.28**. The physical mechanism as to why the nanoparticles agglomerate at the water-oil interface(s) is not completely understood at present. It may be due to a weakening of the repulsive electrical double layer around the nanoparticles, making them more likely to agglomerate. One possible cause of the weakening of the electrical double layer could be due to adsorption of hydroxyl ions at oil-water interfaces as described by Marinova et al (1996).

The magnetic susceptibility peak progressed at an average rate of 1.7 cm hr^{-1}, while the interstitial velocity (assumes piston like front) for the sandpack was expected to be 0.8 cm hr^{-1} (calculated by dividing the flow rate by the cross-section of the sandpack and the porosity fraction). The difference between the two values was most likely due to the viscous fingering of the heavy oil waterflood. The viscous fingers tend to form preferential flow channels, which do not utilize the full cross sectional area of the sandpack. This would lead to a higher flow velocity through those channels, as seen in the observed average velocity of the magnetic susceptibility peak, which was approximately two times faster than the expected interstitial velocity.

After the main water-heavy oil interface(s) had passed through the production end of the flow cell the magnetic profiles of **Figure 4.29**, taken on the second day, show that the maximum magnetic susceptibility was lower than the peak observed in **Figure 4.28**. This would be expected if nanoparticles are no longer collecting at a major water-heavy oil interface or interfaces. The magnetic profiles shown in **Figure 4.29** also had a relatively constant shape, which was expected to reflect the porosity profile. Higher porosity areas should give larger magnetic signals due to the higher volume of nanoparticles. The CT scanning derived porosity profile (**Figure 4.29**) confirmed that the porosity profile was quite similar to the magnetic profiles. In particular, the decrease in magnetic susceptibility (**Figure 4.29**) just before 60 mm from the inlet end seems to correspond with a similar decrease in the CT porosity profile (**Figure 4.29**). There is also a correspondence because the residual oil saturation (Sor) value is quite homogeneous within the sandpack because the nano-fluid volume measured is locally a function of phi x (1-Sorw) and not phi only, where Sorw is the residual oil saturation after a waterflood. Note that the magnetic and CT values are the result of different “thickness slices” at each point (16 mm for the magnetics versus 0.35 mm for the CT), and this might explain differences between the two types of profile. Note also that the magnetic susceptibility values decrease slightly at both the inlet and outlet ends of the flow cell because the sensor is sensing outside the region of the sandpack at these points. **Figure 4.29** also indicates that there were slight increases in magnetic susceptibility with time. This is likely due to an increase in the volume of magnetic nanoparticles within the pore spaces, as nano-fluid was continuously displacing the oil.

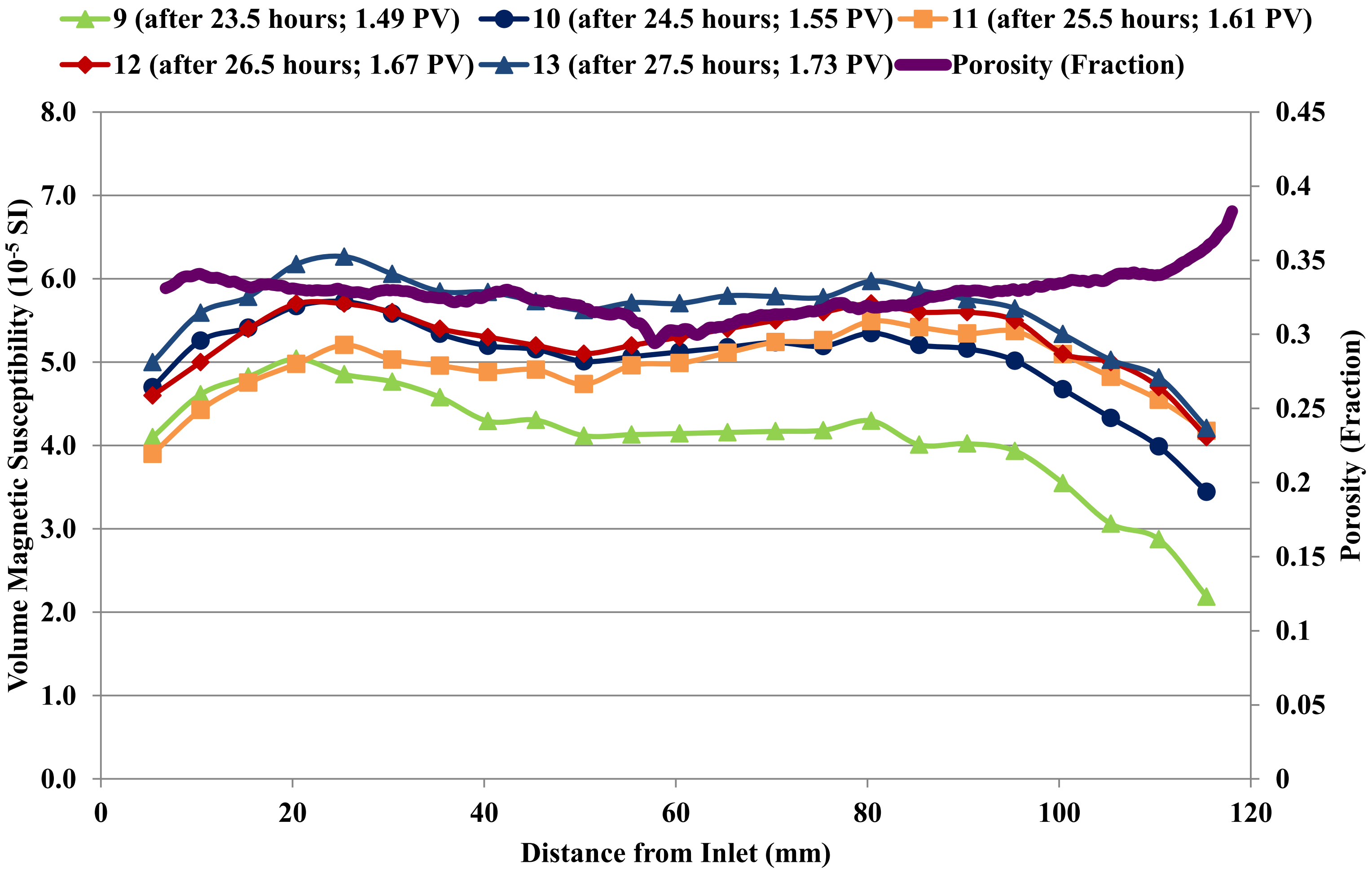

Figure 4.29: Volume magnetic susceptibility profiles taken during day two of the nano-fluid flooding of heavy oil saturated sandpack. The porosity profile of the sandpack determined from CT is also shown for comparison. Legend is the time lapse from the beginning of waterflooding, as well as injected pore volumes of nano-fluid. Injection is from left to right.

The growth and migration of the magnetic susceptibility peak shown in **Figure 4.28** strongly suggests that the nanoparticles accumulated at the main water-heavy oil interface(s). This was further supported by observations of the material in the production jars (**Figure 4.31**). The production jar relating to the main water-heavy oil interface(s) (JAR #5) contained nanoparticle agglomerates that had settled out of suspension (consistent with aggregation at these interface(s)). Such agglomerates were not subsequently seen in the later production jars after the main water-heavy oil interface(s) had passed through the production end. These later jars (JARS #6 and #7) had nanoparticles still in suspension. Therefore the nanoparticle suspension proved to be stable throughout the experiment as no major agglomerates were observed in these later production JARS or the nano-fluid left over in the accumulator (**Figure 4.32**).

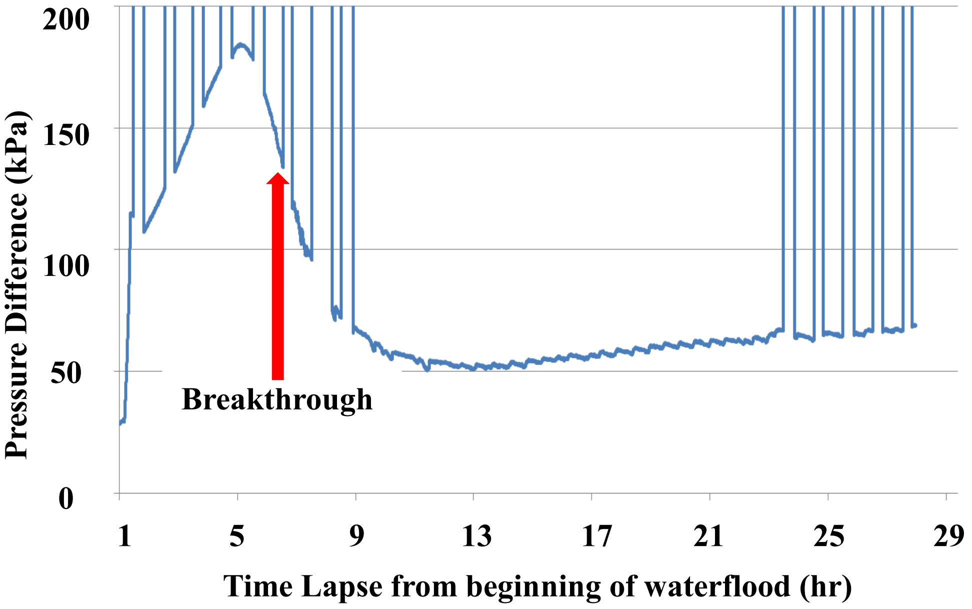

Figure 4.30: Pressure difference between inlet and outlet during the injection of nano-fluid of waterflood 2. Red arrow indicates the time the nano-fluid broke through the production end of the sandpack.

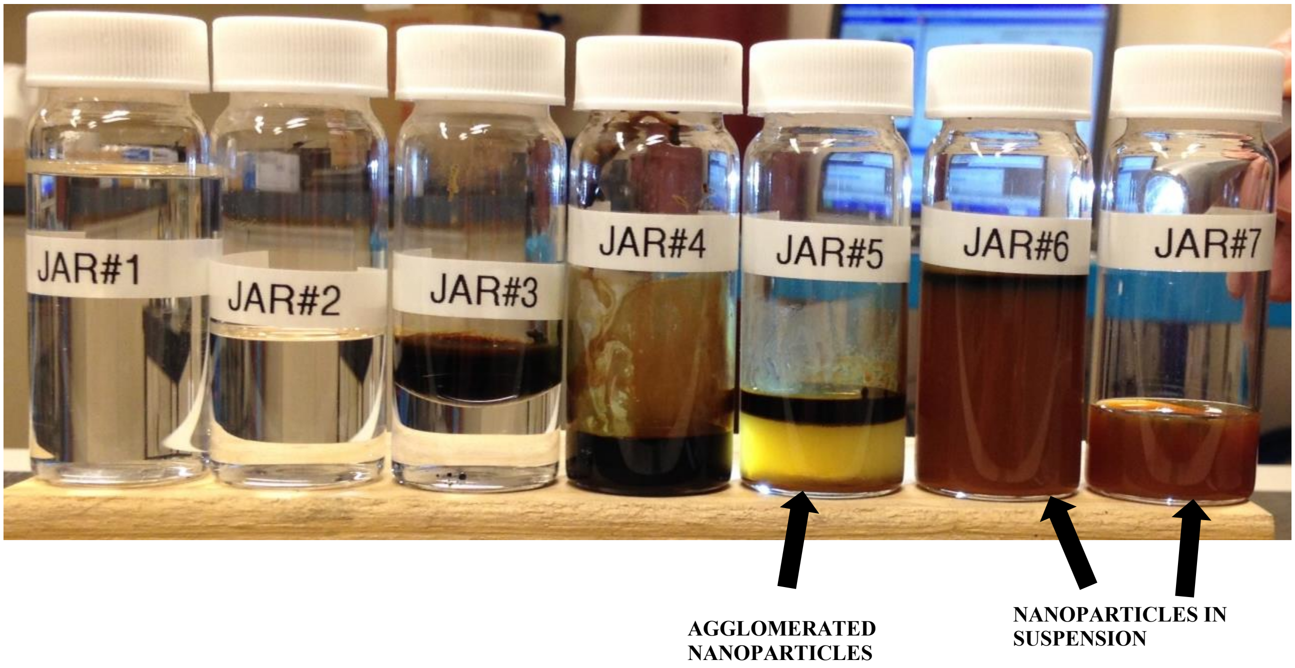

Figure 4.31: Production jars from the waterflood 2 experiment. A description of their contents, and the relation to the various stages of the experiment, is given in **Table 4.5**.

Table 4.5: Production jars stage summary.

JAR #	Stage (Fluid Injected and Collected at PV Injected)	Fluid Produced in JARS
1	Initial Waterflood	DI Water
2	Oil Saturation	DI Water
3	Oil Saturation	DI Water and Oil
4	Nano-Fluid Waterflood day 1 (0.44PV)	Oil
5	Nano-Fluid Waterflood post breakthrough day 1 (0.62 PV)	Oil and Nano-Fluid
6	Nano-Fluid Waterflood day 1 – day 2 (1.46 PV)	Oil and Nano-Fluid
7	Nano-Fluid Waterflood day 2 (1.75 PV)	Oil and Nano-Fluid

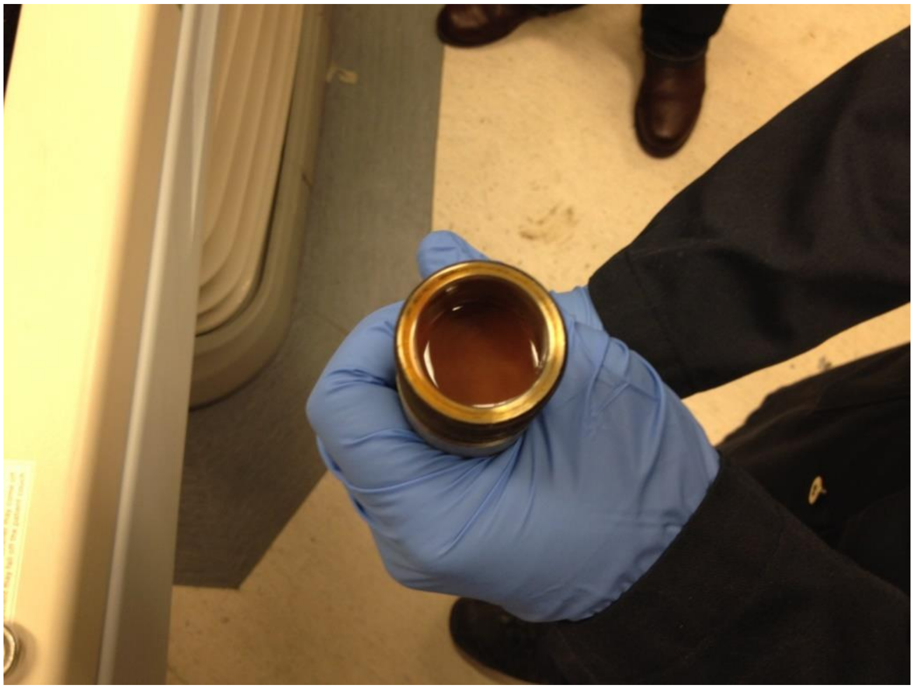

Figure 4.32: Maghemite suspension left over in the accumulator following waterflood 2 experiment.

4.3.4 Conclusions from Waterflood 2

The results of the waterflood 2 experiment led to the following conclusions:

1. The CT attenuation profiles did not clearly identify the progression of the water-heavy oil interfaces(s) during the nano-fluid injection process. This may be partially due to the relatively low CT contrast between the nano-fluid and the heavy oil. The CT results did show an increase in the attenuation as the nano-fluid was injected for some hours (at a time when the nanoparticles were expected to be collecting at the water-heavy oil interface(s)), and subsequently showed a drop in attenuation over part of the sandpack as the oil was displaced and the accumulated nanoparticles at the water-heavy oil interface(s) passed through the flow cell. Additionally the CT attenuation results appear to have been corrupted by trapped gas in the downstream part of the sandpack.
2. The magnetic scans, on the other hand, were able to trace the progression of the nanoparticles due to their high magnetic susceptibility. The magnetic scans of **Figure**

4.28 displayed the formation, growth and progression of a magnetic susceptibility peak during the waterflood, which is consistent with a higher concentration of nanoparticles collecting at the sites of the main water-heavy oil interface(s) during the waterflooding process. This result appears to provide a quantitative means of tracking the progression of the water-heavy oil waterflood in real time.

3. The material collected in the production jars provided further evidence for the higher concentration of nanoparticles accumulating at the main water-heavy oil interface(s).
4. The nanoparticle aggregation at the water-heavy oil interface(s) however may mean that the magnetic susceptibility values are not likely to be related quantitatively to the water saturation at that stage of the waterflood.
5. Once the main water-heavy oil interface(s) had passed through the production end of the sandpack the magnetic susceptibility profiles had a relatively constant shape, which reflected the porosity profile of the sandpack derived from the CT results. Thus after the passing of the main water-heavy oil interface(s) through the sandpack the magnetic profiles should potentially provide a quantitative measure of the water saturation, since the nanoparticles were dispersed and in suspension at this stage (as seen from the nano-fluid collected in the production JARS #6 and #7) similar to the originally injected nano-fluid.

4.4 General Conclusions From Chapter 4

After performing a number of stability experiments and the main waterflood experiments the following conclusions could be made:

1. Maghemite nanoparticles could be successfully dispersed in a deionized water matrix into a long lasting stable suspension with the use of sodium dodecylbenzenesulfonate (DDBS) surfactant. On the other hand, nanoparticle suspensions with high ionic strength (when sodium iodide or sodium chloride was added to the suspension) led to the formation of nanoparticle agglomerates, which resulted in the settling of the nanoparticles.

2. The CT and magnetic susceptibility scans in the first waterflood experiment were very ineffective in tracking the water-heavy oil progression. The magnetic scans suffered from the instability of the nanoparticle suspension as well as the large background signal of the metal end fittings. The CT scans only showed minor changes without being able to fully track the waterflooding process.
3. The magnetic susceptibility scans of the second waterflood experiment clearly showed the formation, growth and progression of a magnetic susceptibility peak, which was consistent with the collection of nanoparticles at the water-heavy oil interface(s). This potentially provides a quantitative means of tracking the progression of the water-heavy oil waterflood in real time. The material from the production jars provided further evidence for a higher accumulation of nanoparticles at the main water-heavy oil interface(s).
4. The shape of the magnetic susceptibility profiles collected after the main water-heavy oil interface(s) had passed through the production end of the sandpack was relatively constant and largely reflected the porosity profile of the sandpack as determined from the CT. Thus the magnetic profiles at this stage should potentially provide a quantitative measure of the water saturation of the sandpack.
5. The CT attenuation profiles of the second waterflood experiment did not clearly indicate the progression of the water-heavy oil interface(s) during the nano-fluid injection process, most likely due to the low CT contrast between the nano-fluid and the heavy oil.

4.5 References

- Da Costa e Silva, A. 1995. Analysis of viscous fingering reproducibility in consolidated natural porous media. Society of Core Analysts conference, Paper Number 9504, 1–10.
- French, R. A., Jacobson, A. R., Kim, B., Isley, S. L., Penn, R. L., and Baveye P. C., 2009. Influence of ionic strength, pH and cation valence on aggregation kinetics of titanium dioxide nanoparticles. Environmental Science and Technology, **43**, 1354-1359.
- Jamaloei, B. Y., Babolmorad, R., and Kharrat, R., 2016. Correlations of viscous fingering in heavy oil waterflooding. Fuel, **179**, 97-102.

- Jingkun, J., Günter, O., and Pratim, B., 2009. Characterization of size, surface charge, and agglomeration state of nanoparticle dispersions for toxicological studies. Journal of Nanoparticle Research, **11**, 79-89.
- Khan, M. M., 2012b. A laboratory study of the effect of ionic strength on the stability of nanoparticle suspensions using a magnetic technique. M. Eng. report, University of Alberta, Department of Civil and Environmental Engineering, Edmonton, Canada, 25 pp.
- Khan, S., 2012a. A laboratory study of the stability and flow of nanoparticle suspensions through porous media using magnetic techniques. M.S. thesis, University of Alberta, Department of Civil and Environmental Engineering, Edmonton, Canada, 147 pp.
- Khan, S., Potter, D. K., and Kuru, E., 2015. Quantifying the transport of superparamagnetic nanoparticles in porous media using an acrylic flow cell and integrated magnetic susceptibility sensor technique. Transport in Porous Media, **106**, 691-705.
- Marinova, K. G., Alargova, R. G., Dencov, N. D., Velev, O. D., Petsev, D. N., Ivanov, I. B., and Borwankar, R. P. 1996. Charging of oil-water interfaces due to spontaneous adsorption of hydroxyl ions. Langmiur, **12**, 2045-2051.
- Morrow, L., Potter, D. K., and Barron, A. R., 2015. Detection of magnetic nanoparticles against proppant and shale reservoir rocks. Journal of Experimental Nanoscience, **10**, 1028-1041.
- Prigiobbe, V., Ko, S., Huh, C., and Bryant, S. L., 2015. Measuring and modeling the magnetic settling of superparamagnetic nanoparticle dispersions. Journal of Colloid and Interface Science, **447**, 58-67.

Chapter 5

THE EFFECT OF NATURAL HEMATITE NANOPARTICLES ON RESERVOIR QUALITY AND ESTIMATION OF POTENTIAL MAGHEMITE NANOPARTICLE RETENTION DURING FLUID FLOW EXPERMENTS IN POROUS MEDIA

5.1 Introduction

The magnetic susceptibility monitoring of the waterflooding of heavy oil using a maghemite nanoparticle suspension in waterflood 2 proved to be successful. The experiment also showed a correlation between the porosity profile of the sandpack with the magnetic susceptibility profiles taken after the passing of the main magnetic susceptibility peak (which signified the passing of the main water-heavy oil interface(s)). Although successful in accomplishing the desired result, questions arose from the waterflood experiments which needed to be addressed. In particular, what kind of impact do injected nanoparticles have on the quality of the sandpack (or potentially a hydrocarbon reservoir if applied in the field), and what proportion of nanoparticles are retained in the sandpack (or hydrocarbon reservoir) after a subsequent waterflood to attempt to flush them out? This chapter will try to address these issues by looking at some other published studies, as water flushing was not performed in our current experiments due to time scheduling constraints in the use of the InnoTech Alberta CT laboratory.

Comprehensive studies on the retention parameters and forces affecting nanoparticle retention in porous media have been conducted by Caldelas (2010) and Murphy (2012). Yu (2012) showed that when injecting iron oxide nanoparticles under optimum conditions he was able to achieve particle retentions of only 4 % and 5.2% (in the cases where the nanoparticles were treated with extra coatings), although the same iron oxide nanoparticles also exhibited cases in which they failed to flow through the injection core. Models for nanoparticle retention are still in the early stages and generally require history matching with prior experimental results. The independent two-site model proposed by Zhang et al. (2016) has had success by asserting two types of sites for retention on the grain surfaces of the matrix.

5.2 The effect of natural hematite nanoparticles on reservoir quality

5.2.1 Case Study 1 (Tight Gas Reservoir in the North Sea)

In order to study the potential effects that nanoparticles can have on a hydrocarbon reservoir this section will first look at a case study (performed by Potter et al., 2009) of a clastic tight gas reservoir located in the North Sea. The study focused on the effects on permeability of naturally occurring hematite nanoparticles. Although hematite does not have the exact same crystal structure as the maghemite used in the waterflood experiments, both minerals are forms of iron (III) oxide and the effects on permeability of nanoparticles of the two minerals would be expected to be quite similar. The reason for examining a reservoir with naturally occurring iron oxide was because no study to date (that I am aware of) has examined the large scale impact of injected nanoparticles within an existing hydrocarbon reservoir.

The tight gas reservoir was comprised of red and white sandstones, where the red sandstone sections contain grain-rimming naturally occurring hematite nanoparticles. The white sandstones, on the other hand, are believed to have formed through a bleaching process by the migration of acidic fluids (Richardson, 2005), which removed the hematite nanoparticles. The Potter et al. (2009) study used non-destructive magnetic susceptibility measurements to analyze the reservoir samples. Previous studies had shown how magnetic susceptibility can be correlated to key petrophysical parameters (Potter et al., 2004; Potter, 2005, 2007; Ivakhnenko, 2006). The magnetic susceptibility of the tight gas reservoir samples was used to assess the relative roles of hematite and illite on the reservoir permeability. The study found that the permeability of the white sandstone sections was generally higher than that of the adjacent red sandstone sections, and was controlled by the illite content. In contrast, the red sandstone sections had systematically lower permeabilities than the adjacent white sandstone sections, and it was demonstrated that this was due to the presence of fine-grained hematite nanoparticles in the red sandstones.

The study first analyzed the magnetic hysteresis response of the white and red sandstones (**Figure 5.1**) using a variable field translation balance (VFTB). This measured the mass magnetization of the samples in response to a variable applied field. The results for two white sandstones (**Figure 5.1(a)**) displayed relatively straight line hysteresis plots with no hysteresis loop. The slope represents the magnetic susceptibility. The difference in slope between the two samples indicates a difference in illite content. A larger positive slope indicates a higher paramagnetic mineral content (in this case illite) in the sample. Higher illite content also correlated with lower permeability as one might expect. Sample 13-57 had a larger slope, thus a higher illite concentration, and a permeability of only 0.41 mD. Sample 13-249, on the other hand, had a lower slope indicating a lower illite content, and had a higher permeability of 4.36 mD.

Similar analysis was performed on samples of the red sandstones (**Figure 5.1(b)**). In this case all samples exhibited hysteresis loops consistent with the canted antiferromagnetic behaviour of hematite. A key observation from the VFTB results was that the red sandstone samples had lower permeability compared to white sandstone samples with similar illite content (similar high field slopes). For example, red sandstone sample 13-162 (**Figure 5.1(b)**) has a very similar illite content to white sandstone sample 13-249 (**Figure 5.1(a)**), but the red sandstone has a lower permeability of 0.58 mD compared to the 4.36 mD permeability of the white sandstone. This strongly suggested that the hematite was responsible for lowering the permeability in the red sandstone.

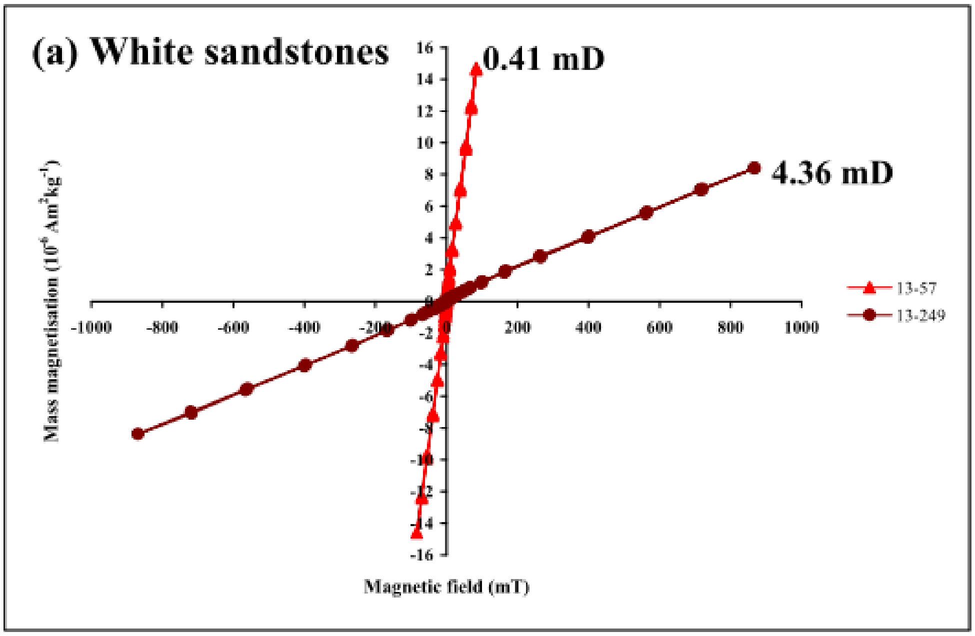

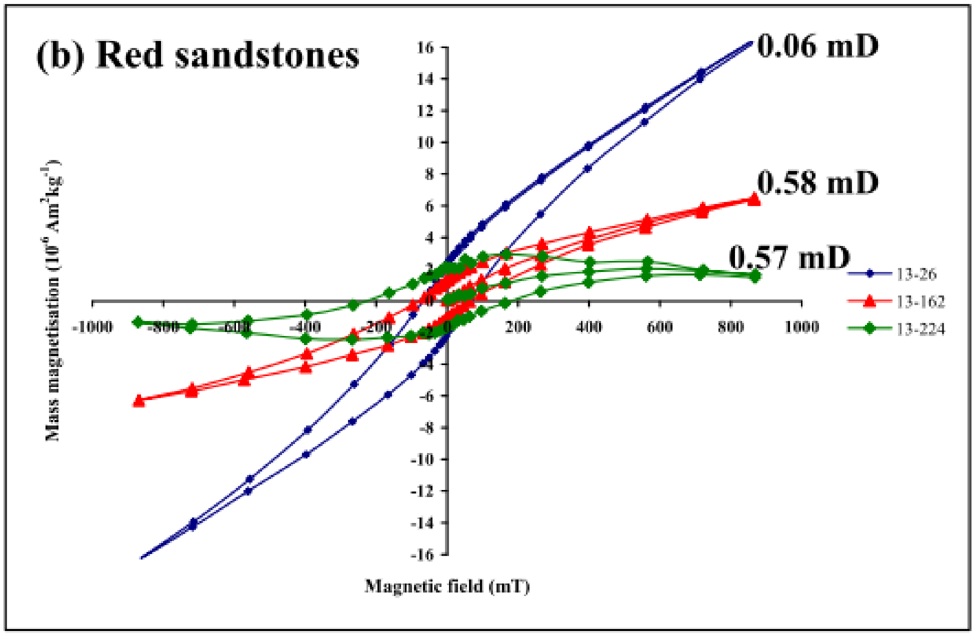

Figure 5.1: Magnetic hysteresis measurements of some North Sea tight gas reservoir samples for (a) white sandstones with a mineralogy comprised mainly of quartz and illite (higher slopes correlated with higher illite content and lower permeability) and (b) red san sandstones with a mineralogy comprised of quartz, illite and hematite. These samples had generally lower permeability than the white sandstones, which was linked to the hematite content of the red sandstones (Potter et al., 2009).

5.2.2 Case Study 2 (Another Gas Reservoir in the North Sea)

This reservoir also contained red and white sandstones, but had higher permeabilities than Case Study 1. To rapidly examine a large number of samples Potter et al. (2009) devised a method for estimating the illite and hematite content of the samples using low field magnetic susceptibility measurements. X-ray diffraction (XRD) analysis was used to determine the exact composition of the white sandstones. This revealed that the primary components were quartz and illite with small amounts of other minerals. Ignoring these other minerals (which would not influence the results significantly) equations for the fractions of quartz and illite were derived from Potter (2007):

$$F_I = \frac{\chi_Q - \chi_T}{\chi_Q - \chi_I} \tag{5.1}$$

$$F_Q = 1 - F_I \tag{5.2}$$

Where:

- F_I is the fraction of illite in the sample
- F_Q is the fraction of quartz in the sample
- χ_Q is the volume magnetic susceptibility of quartz -1.5×10^{-5} SI (Hunt et al., 1995)
- χ_I is the volume magnetic susceptibility of illite 41×10^{-5} SI (Hunt et al., 1995)
- χ_T is the total volume magnetic susceptibility of the sample SI

To analyze the red sandstones a more complex methodology had to be derived as the XRD analysis in this case showed that their main components were hematite, illite and quartz. Thus in this case the total magnetic susceptibility signal was due to the combination of all three minerals. In order to calculate the fractional content of illite and hematite an assumption had to be made about the quartz concentration, that it was 0.9 (or 90%) in all cases. This assumption was based on the average quartz content from the XRD measurements. Another issue was establishing the volume magnetic susceptibility of the naturally occurring hematite. Unlike illite and quartz, which both have set values for their volume magnetic susceptibilities, the value for hematite is largely dependent on the size of the particles. Thus the volume magnetic susceptibility of the hematite had to be determined and was estimated to be 400 x 10^{-5} SI (which was established by investigating the volume magnetic susceptibility of the hematite present in core samples from the reservoir). The fraction of illite could then be estimated from the following equation:

$$F_I = \frac{\chi_T - F_Q(\chi_Q - \chi_H) - \chi_H}{\chi_I - \chi_H} \tag{5.3}$$

Where:

- F_I is the fraction of illite in the sample
- F_Q is the fraction of quartz in the sample
- χ_Q is the volume magnetic susceptibility of quartz -1.5 x 10^{-5} SI (Hunt et al., 1995)
- χ_I is the volume magnetic susceptibility of illite 41 x 10^{-5} SI (Hunt et al., 1995)
- χ_H is the volume magnetic susceptibility of the naturally occurring hematite measured for the reservoir in question 400 x 10^{-5} SI
- χ_T is the total volume magnetic susceptibility of the sample SI

Using the assumption that the fraction of the quartz in the samples is 0.9 the hematite content was obtained from the following equation utilizing the calculated illite content from the previous equation using:

$$F_H = 0.1 - F_I \tag{5.4}$$

Using the equations above the hematite and illite contents were calculated (by Potter et al., 2009) for a number of slabbed core sections and compared to probe permeability measurements at the same locations. **Figure 5.2** shows the first core section that was analyzed. Comparing the observed permeabilities to the mineral contents there is a clear correlation between the hematite content and the permeability. All points of higher hematite content correspond to lower permeability values and vice versa. The illite content, on the other hand, does not appear to have any clear correlation to the permeability profile. **Figure 5.3** shows a similar pattern for one of the other core sections.

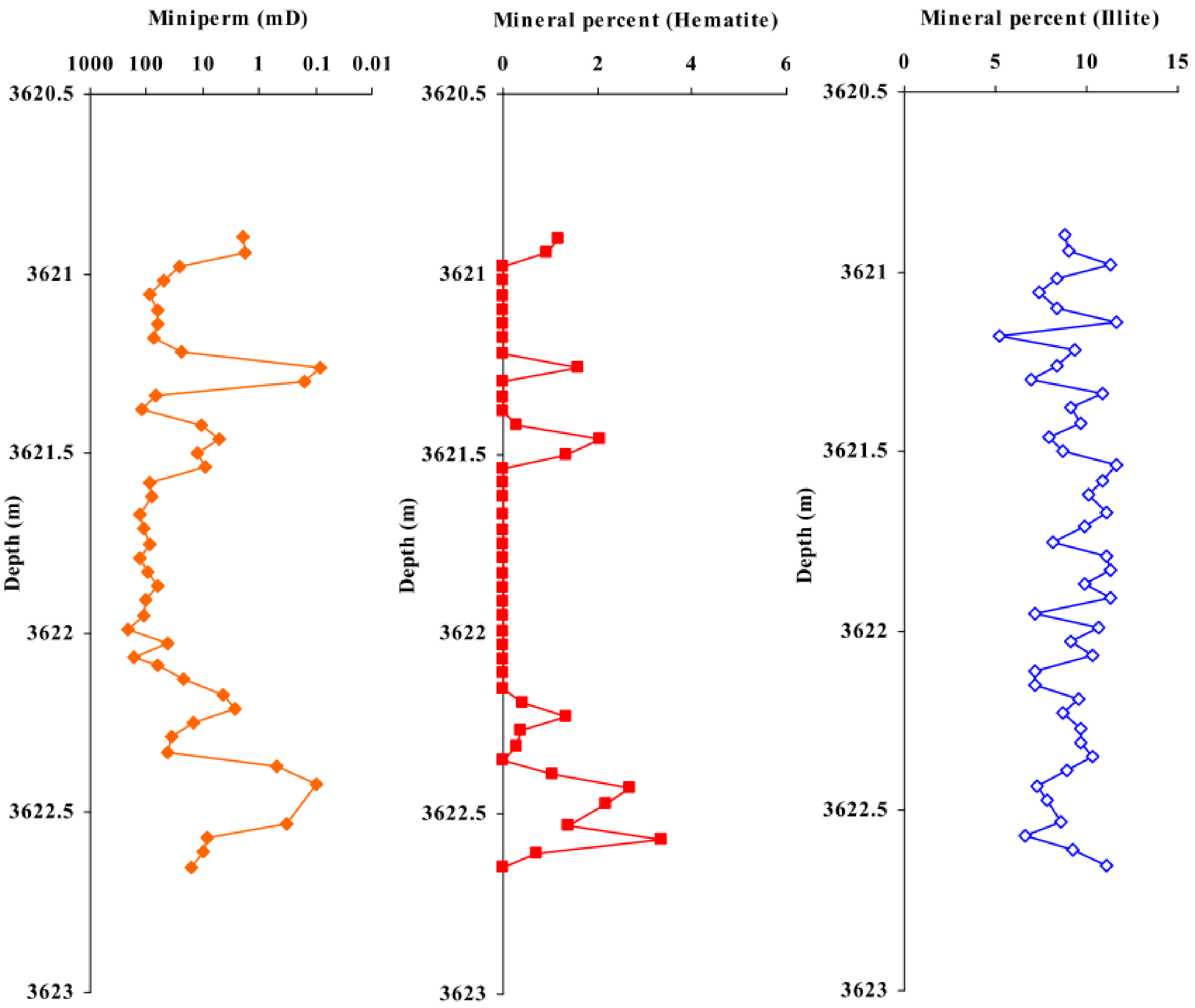

Figure 5.2: Probe permeability and magnetically derived hematite and illite content for a slabbed core section of the North Sea gas reservoir in Case Study 2. Permeability shows an inverse correlation to the hematite content along the profile, while no correlation can be seen with the illite content (Potter et al., 2009). The red sandstones contain hematite, whereas the white sandstones have close to zero percent hematite.

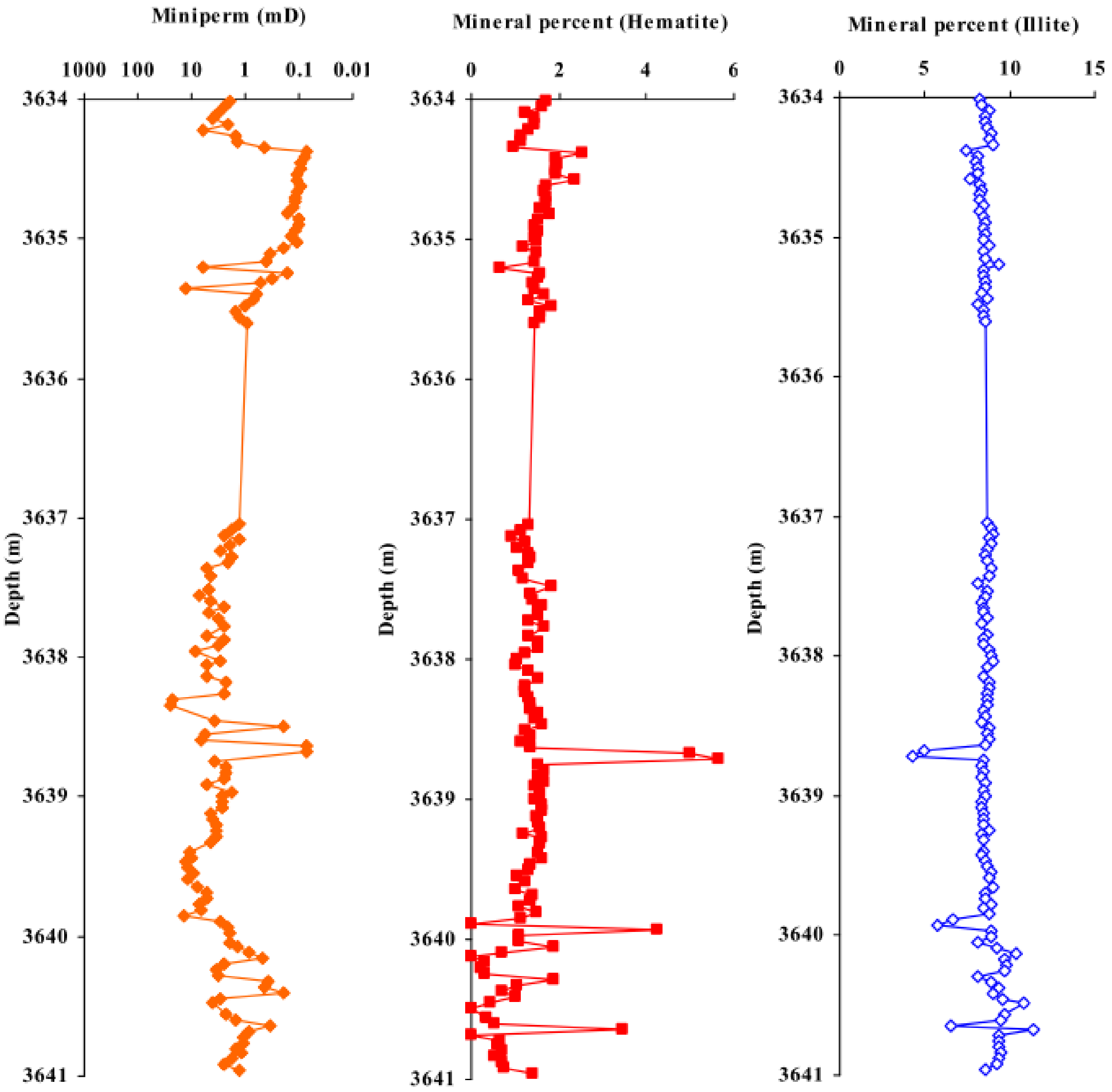

Figure 5.3: Probe permeability and magnetically derived hematite and illite content for another slabbed core section of the North Sea gas reservoir in Case Study 2. Permeability shows an inverse correlation to the hematite content along the profile (Potter et al., 2009).

For this thesis some red sandstone core plug samples were analyzed from this reservoir. The plug samples were examined in order to provide a larger volume scale from which to estimate hematite content from magnetic susceptibility, and compare with permeability (compared to the probe magnetic susceptibility and probe permeability of Potter et al., 2009). **Figure 5.4** shows a plot of plug permeability versus hematite content computed from equations (5.3) and (5.4). The total volume magnetic susceptibilities of the core plugs (χ_T) were measured using the Molspin susceptibility bridge. **Figure 5.4** shows that small concentrations of hematite can drastically decrease the permeability, and that the correlation coefficient between increasing hematite content and decreasing permeability is reasonably high ($R^2 = 0.77$). The maximum permeability in this reservoir is about 100 mD in the white sandstones where the hematite content is close to zero (see **Figure 5.2**). From **Figure 5.4** a value of 100 mD corresponds to a hematite content of about 0.16% ± 0.03% fitting confidence. One might expect, therefore, that hematite contents less than this value would have a limited effect on the permeability. In the next section this concentration will be compared to the calculated concentrations of retained nanoparticles after water flushing in some previous fluid flow experiments.

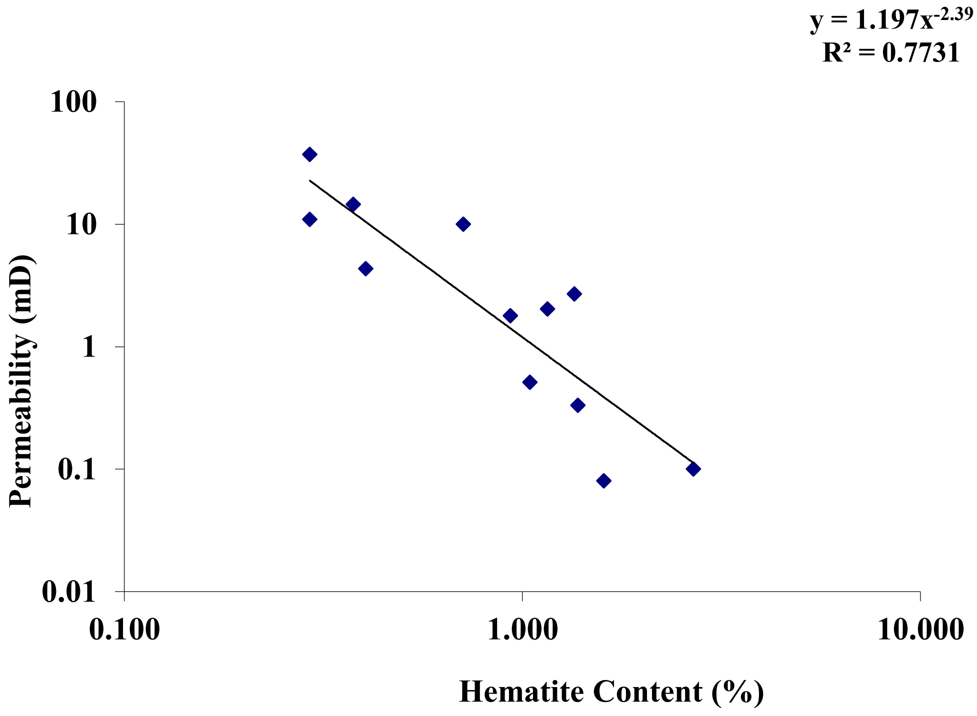

Figure 5.4: Permeability versus hematite content for some red sandstone core plugs from the gas reservoir in Case Study 2.

5.3 Retention of nanoparticles in porous media

The previous section showed that very small amounts of naturally occurring hematite can have a detrimental effect on the permeability and therefore quality of a gas reservoir. Thus the question was raised of whether a nano-fluid waterflood could potentially have a detrimental effect on a hydrocarbon reservoir. Due to time constraints at InnoTech Alberta no water-flush was performed after the nano-fluid waterflood experiments 1 and 2 of the heavy oil sandpack. Thus in order to estimate the nanoparticle retention of the sandpack a different study was examined. Khan (2012) examined the flow of nanoparticle suspensions through porous media (glass beads and sand). He focused on flowing maghemite nanoparticle suspensions through a water filled acrylic flow cell, following which he attempted to water-flush the nano-fluid out of the flow cell. He tested a number of different parameters such as nanoparticle concentration, effect of injection rate, effect of permeability and effect of the type of matrix. Since he did not calculate the amount of nanoparticles retained in the flow cell after the water-flush, his data will be used to calculate the nanoparticle retention for cases using as similar as possible suspension conditions as used during my heavy oil waterflood experiments 1 and 2.

The first step was to measure the maximum magnetic susceptibility value after the 3rd pore volume nano-fluid injection profile. This was done at 100mm along the flow cell, which is the approximate halfway point between the inlet and outlet of the flow cell in Khan's experiment (**Figure 5.5**). Following this a similar measurement was taken at the same halfway point after the 4th pore volume water flush magnetic susceptibility profile (**Figure 5.5**). These magnetic susceptibility values were assumed to be solely due to the nanoparticles as no information about the magnetic susceptibility response of the flow cell or the glass bead or sand matrix was provided by Khan (2012). Such an assumption was deemed acceptable as both the matrix and acrylic flow cell would have a very weak (diamagnetic) signal compared to the superparamagnetic nanoparticles. Using the magnetic susceptibility values, together with the porosity and amount of nanoparticles dispersed in suspension, the mass of the nanoparticles left in the flow cell was calculated using equation (5.5):

$$M_{RN} = \frac{\chi_W}{\chi_N}\frac{M_{IN}521\varphi}{600} \tag{5.5}$$

Where:

- M_{RN} is the mass of the retained nanoparticles after the 4th pore volume water flush (g)
- χ_W is the volume magnetic susceptibility at the mid-point of the flow cell after the 4th pore volume water flush (10^{-5} SI)
- χ_N is the volume magnetic susceptibility at the mid-point of the flow cell after the 3rd pore volume nano-fluid injection (10^{-5} SI)
- M_{IN} is the mass of initial magnetic nanoparticles used in creating the nano-fluid suspension (g)
- 521 is the volume of the acrylic flow cell (cm^3)
- φ is the porosity of the current trial (fractional)
- 600 is the volume of nano-fluid suspension originally made (ml)

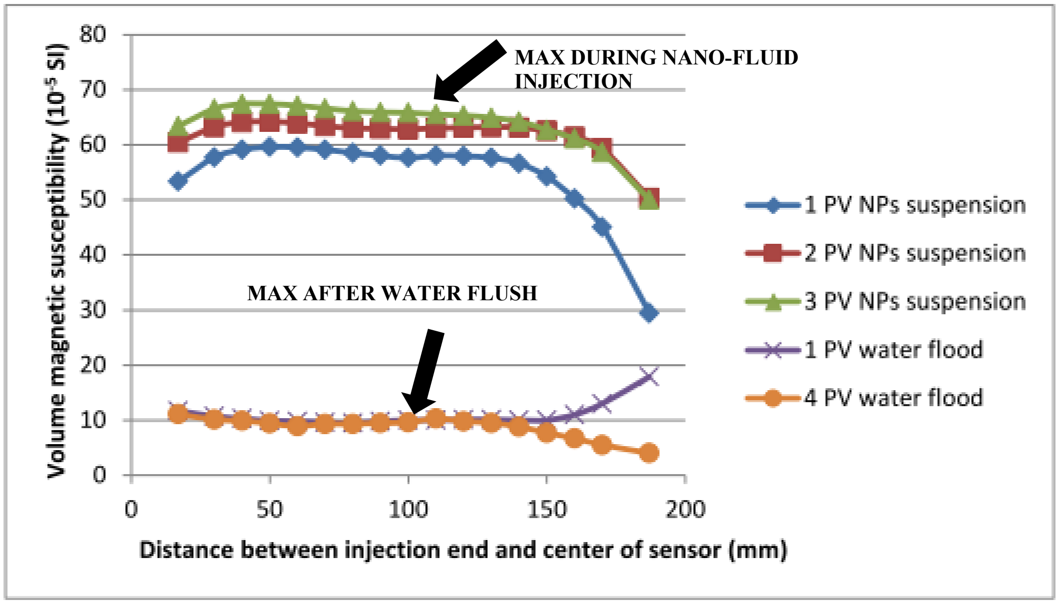

Figure 5.5: Example for taking the maximum magnetic susceptibility value for the injected nanoparticles and the maximum magnetic susceptibility for the 4th water flush (modified from Khan, 2012).

Following the calculation of the mass of the retained nanoparticles they were converted into volume using their specific density. Using the volume of the retained nanoparticles and the volume of the matrix (which was calculated from the volume of the acrylic flow cell and the porosity of the glass bead/sandpack volume percentage) the concentration of the retained nanoparticles (for the solids only) was calculated using equation (5.6):

$$\mathrm{N}_{\%} = \frac{\frac{\mathrm{M_{RN}}}{\mathrm{D_N}}}{\frac{\mathrm{M_{RN}}}{\mathrm{D_N}}+(1-\varphi)521} 100\% \qquad (5.6)$$

Where:

- $\mathrm{N}_{\%}$ is the volume percent concentration of retained nanoparticles (for solids only)
- $\mathrm{M_{RN}}$ is the mass of the retained nanoparticles after the 4th pore volume water flush (g)
- $\mathrm{D_N}$ is the density of the suspended nanoparticles (5.24 g cm^{-3} for maghemite)
- 521 is the volume of the acrylic flow cell (cm^3)
- φ is the porosity of the current trial (fractional)

The volume percentage concentration of the initially injected nanoparticles was also calculated for comparison as follows:

$$\mathrm{NI}_{\%} = \frac{\frac{(M_{IN}521\varphi)/600}{\mathrm{D}_N}}{\frac{(M_{IN}521\varphi)/600}{\mathrm{D}_N}+(1-\varphi)521} 100\% \qquad (5.7)$$

Where:

- $\mathrm{NI}_{\%}$ is the volume percent concentration of injected nanoparticles (for solids only)
- $\mathrm{M_{IN}}$ is the mass of magnetic nanoparticles used in creating the nano-fluid suspension (g)
- 521 is the volume of the acrylic flow cell (cm^3)
- φ is the porosity of the current trial (fractional)
- 600 is the volume of nano-fluid suspension originally made (ml)
- $\mathrm{D_N}$ is the density of the suspended nanoparticles (5.24 g cm^{-3} for maghemite)

Using equations (5.4), (5.5) and (5.6) the volume percent concentration of both the injected and the retained nanoparticles were calculated for a number of cases where Khan (2012) had performed water flushes (**Table 5.1**). The volume percentage concentration of the retained nanoparticles was found to be between 2.43 x 10^{-4} % and 4.59 x 10^{-3} %. These values are low compared to the amount of natural nanoparticle hematite required to make significant changes to the permeability (found to be over 0.16% **Figure 5.4**) in Case Study 2 described earlier. Whilst Khan's (2012) experiments and Case Study 2 are not directly comparable, the intrinsic permeabilities of Khan's samples are much higher (**Table 5.1**) and so the small concentrations of retained nanoparticles are unlikely to have a detrimental effect on the permeability of his samples. Note also that in the case of naturally occurring hematite the nanoparticles lack a dispersant and are thus more prone to aggregate into larger agglomerates, which can in turn lead to the blocking of the pore throats and decrease the formation permeability. When injecting nanoparticle suspensions the nanoparticles are treated with dispersant to prevent the formation of such aggregates. The nanoparticle volume percent concentrations of the injected nano-fluid prior to the water-flush were higher (**Table 5.1**) ranging between 6.55 x 10^{-3} % and 4.96 x 10^{-2} %. Even these values are quite low compared to the concentrations of natural hematite in the red sandstones of Case Study 2 that caused significant decreases in permeability.

Finally although the comparison between the two case studies gave favorable results they should be taken with a grain of salt, as the two studies had overall different reservoir conditions. The hematite nanoparticles were naturally occurring in a relatively low permeability gas reservoir while the maghemite synthetic nanoparticles were injected (as a stabilized suspension) in relatively high permeability sandpacks in a laboratory setting. Thus further work would be required to affirm the previously drawn conclusions with greater confidence.

Table 5.1: Calculated volume percentage concentrations of initially injected (3rd pore volume) and subsequently retained maghemite nanoparticles following the 4th pore volume water-flush of different nano-fluid suspensions injections performed by Khan (2012).

Figure # and Experimental Details from Khan (2012)	Injected Nanoparticle Volume Concentration of Solids (%)	Retained Nanoparticle Volume Concentration of Solids (%)	Retained Nanoparticles Compared to Injected Nanoparticles (%)
Figure 5-3, φ 0.339, Glass Beads, k 2.3 Darcy	4.89×10^{-02}	4.59×10^{-03}	10.7
Figure 5-4, φ 0.34, Glass Beads, k 2.25 Darcy	1.64×10^{-02}	2.30×10^{-03}	7.1
Figure 5-5, φ 0.352, Glass Beads, k 2.4 Darcy	6.91×10^{-03}	1.03×10^{-03}	6.7
Figure 5-6, φ 0.352, Glass Beads, k 2.25 Darcy	6.91×10^{-03}	4.85×10^{-04}	14.2
Figure 5-7, φ 0.346, Glass Beads, k 2.4 Darcy	6.73×10^{-03}	1.02×10^{-03}	6.6
Figure 5-8, φ 0.35, Glass Beads, k 2.3 Darcy	6.85×10^{-03}	1.24×10^{-03}	5.5
Figure 5-9, φ 0.34, Glass Beads, k 2.25 Darcy	6.55×10^{-03}	4.60×10^{-04}	14.2
Figure 5-10, φ 0.37, Glass Beads, k 6.35 Darcy	7.47×10^{-03}	4.67×10^{-04}	16.0
Figure 5-11, φ 0.368, Glass Beads, k 22.8 Darcy	7.41×10^{-03}	2.43×10^{-04}	30.5
Figure 5-13, φ 0.367, Sand, k 20 Darcy	7.38×10^{-03}	2.63×10^{-04}	28.0
Figure 5-14, φ 0.368, Glass Beads, k 22.8 Darcy	7.41×10^{-03}	2.43×10^{-04}	30.5
Figure 5-15, φ 0.352, Glass Beads, k 2.25 Darcy	6.91×10^{-03}	4.77×10^{-04}	14.5
Figure 5-19, φ 0.342, Glass Beads, k 2.48 Darcy	4.96×10^{-02}	4.05×10^{-03}	12.2

5.4 Conclusions

This chapter first analyzed two previous case studies of gas reservoirs (Potter et al., 2009) located in the North Sea, where the reservoirs were comprised of white and red sandstones (and where the red sandstones contained nanoparticle hematite). In the case of the tight gas reservoir (Case Study 1) the red sandstones exhibited lower permeabilities when compared to the adjacent white sandstones. The permeabilities in the white sandstones were controlled by the illite clay content. The permeability of the red sandstones was predominantly controlled by the naturally occurring hematite nanoparticles rather than the illite clay. From the further analysis carried out in this chapter the following conclusions were drawn:

1. In the other gas reservoir (Case Study 2) new measurements on core plugs demonstrated how small concentrations of nanoparticle hematite correlated with dramatic decreases in permeability. Hematite volume concentrations of over 0.16% can significantly decrease the permeability in this reservoir.
2. This thesis analyzed the water-flushes undertaken by Khan (2012) of porous media initially injected with maghemite nanoparticle suspensions. The analysis revealed that the volume percentage of retained nanoparticles was between 2.43×10^{-4} % and 4.59×10^{-3} %. This appears to be sufficiently low so as not to degrade the quality of the porous media by not significantly reducing the permeability.

5.5 References

- Caldelas, F. M., 2010. Experimental parameter analysis of the nanoparticle retention in porous media. M.S. thesis, University of Texas at Austin, Austin, USA, 145 pp.
- Hunt, C. P., Moskowitz, B. M., and Banerjee, S. K., 1995. Magnetic properties of rocks and minerals. In: Thomas J. Ahrens (ed.) Rock Physics and Phase Relations: a Handbook of Physical Constants, AGU reference shelf 3, 189-204.
- Ivakhenko, O. P., 2006. Magnetic analysis of petroleum reservoir fluids, matrix mineral assemblages and fluid-rock interactions. Ph.D. thesis, Heriot-Watt University, Institute of Petroleum Engineering, Edinburgh, UK, 210 pp.

- Khan, S., 2012. A laboratory study of the stability and flow of nanoparticle suspensions through porous media using magnetic techniques. M.S. thesis, University of Alberta, Department of Civil and Environmental Engineering, Edmonton, Canada, 147 pp.
- Murphy, M. J., 2012. Experimental analysis of electrostatic and hydrodynamic forces affecting nanoparticle retention in porous media. M.S. thesis, University of Texas at Austin, Austin, USA, 153 pp.
- Potter, D. K., 2005. Magnetic susceptibility as rapid non-destructive technique for improved RCAL and SCAL parameter prediction. Proceedings of the International Symposium of the Society of Core Analysts, Toronto, Canada. Paper SCA2005-02 (12 pages).
- Potter, D. K., 2007. Magnetic susceptibility as rapid, non-destructive technique for improved petrophysical parameter prediction. Petrophysics, **48**, 191-201.
- Potter, D. K., Ali, A., and Ivakhenko, O. P., 2009. Quantifying the relative roles of illite and hematite on permeability in red and white sandstones using low and high field magnetic susceptibility. Proceedings of the International Symposium of the Society of Core Analysts, Noordwijk, Netherlands. Paper SCA2009-11 (12 pages).
- Potter, D. K., Corbett, P. W. M., Barclay, S. A., and Haszeldine, R. S., 2004. Quantification of illite content in sedimentary rocks using magnetic susceptibility – a rapid complement or alternative to X-ray diffraction. Journal of Sedimentary Research, Research Methods Papers Section, **74**, 730-735.
- Richardson, S. 2005. Bleaching and diagenesis affecting reservoir quality in the upper Slochteren (ROLSU), Lauwerszee trough, the Netherlands. Summer intern student, The University of Durham, England. Internship at NAM (Nederlandse Aardolie Maatschappij) building in Assen.
- Yu, H., 2012. Transport and retention of surface-modified nanoparticles in sedimentary rocks. Ph.D. thesis, University of Texas at Austin, Austin, USA, 257 pp.
- Zhang, T., Murphy, M., Yu, H., Huh, C., and Bryant, S. L., 2016. Mechanic model for nanoparticle retention in porous media. Transport in Porous Media, **115**, 387-406.

Chapter 6

DIAMAGNETIC BEHAVIOUR IN NANOPARTICLE HEMATITE?

A version of this chapter has been published as follows:

Petrov, P. A., Ali, A., and Potter, D. K., 2017. Diamagnetic behaviour in nanoparticle hematite? Journal of Modern Physics, **8**, 1013-1019. (Special Issue on "Magnetism and Magnetic Materials").

6.1 Introduction

The spherical 30 nm hematite nanoparticles produced by the SOL-GEL method were initially considered as a fifth potential candidate for hydrocarbon reservoir applications and for understanding natural nano-sized hematite particles in reservoirs (the latter discussed in **Chapter 5**). Their potential as contrast agents, however, was quickly dismissed due to their low magnetic susceptibility. However, an initial observation of apparently diamagnetic behaviour in the 30 nm hematite nanoparticles dilutely dispersed in resin led to an interesting separate study.

Hematite has a variable magnetic behaviour which is dependent on the temperature conditions as well as the particle size of the material. Hematite has two transitional temperature boundaries for its magnetic behaviour. The Néel temperature of hematite is at approximately 948 K (Dunlop and Özdemir 1997), while the low temperature transition occurs just below room temperature and is referred to as the Morin transition. The exact temperature of the Morin transition is variable and highly dependent upon the size of the hematite particles. Özdemir et al. (2008) found the Morin transition temperatures for submicron synthetic hematite particles with sizes between 120 nm and 520 nm to be between 241 K and 256 K, with a tendency for the Morin transition temperature to decrease with decreasing particle size. The magnetic behaviour of hematite is such that below the Morin transition the material has antiferromagnetic behaviour, above the Morin transition and below the Néel temperature it has canted antiferromagnetic behaviour, while above its Néel temperature hematite has paramagnetic behaviour.

The initial observation of a diamagnetic susceptibility response in the 30 nm hematite nanoparticles dilutely dispersed in resin seemed very unusual. Therefore a search was conducted in the literature to see if diamagnetic behaviour in nanoparticle hematite had been reported by anyone else. There was a paper by Mi et al. (2006) which reported diamagnetic hysteresis curve behaviour in spindle-type hematite nanoparticles with dimensions of 200 nm length and 80nm width (**Figure 6.1**). Diamagnetic behaviour would not be expected in hematite and was thus investigated further. Two possible explanations for the observed diamagnetic behaviour of the hematite nanoparticles were considered: either (1) the hematite particles exhibit some unusual diamagnetic behaviour for certain sizes or shapes of nanoparticles, possibly due to their proximity to the stable single domain/superparamagnetic boundary (Bando et al., 1965; Banerjee, 1971, **Table 2.6** in **Chapter 2**) or due to their "spindle" shape in the Mi et al. (2006) work, or (2) the diamagnetic hysteresis behaviour in Mi et al.'s (2006) work and the initial results on the 30 nm hematite observed here were the result of a diamagnetic particle dispersant overwhelming the weak canted antiferromagnetic hematite magnetic signal of the nanoparticles at room temperature. The latter explanation seemed more plausible, and was the focus of experiments detailed in this chapter.

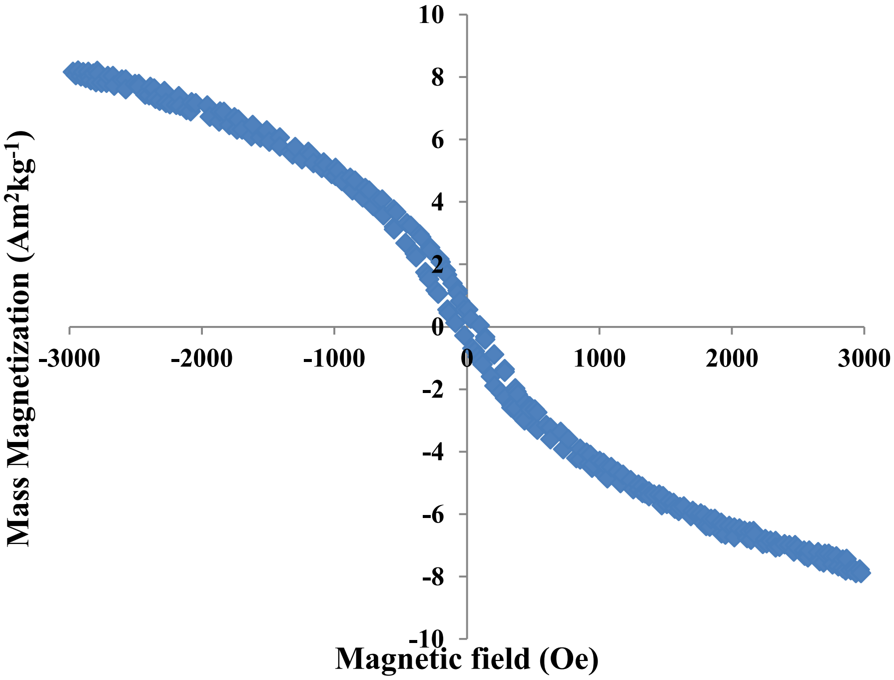

Figure 6.1: Hysteresis curve of 80 nm x 200 nm spindle-type hematite nanoparticles reported by Mi et al. (2006).

6.2 Characterization of Hematite Nanoparticles

6.2.1 X-Ray Diffraction (XRD) and Transmission Electron Microscopy (TEM)

An XRD analysis was used to confirm the chemical composition of the 30 nm hematite nanoparticles synthesized by the SOL-GEL method (**Figure 6.2**). Here the experimental diffraction peaks (black) clearly coincided with those expected for hematite (red). Following the compositional confirmation the size of the nanoparticles was also verified with the manufacturers specifications using a TEM. The TEM photomicrograph of the 30 nm hematite nanoparticles indicated an average particle size of approximately 30 nm in agreement with the manufacturer specifications (**Figure 6.3**). The overall shape of the nanoparticles was also spherical, although some other shapes can also be seen. The particles themselves revealed a tendency to form into larger agglomerates, although the agglomerates are believed to have formed during the air drying process prior to the conduction of the TEM imaging.

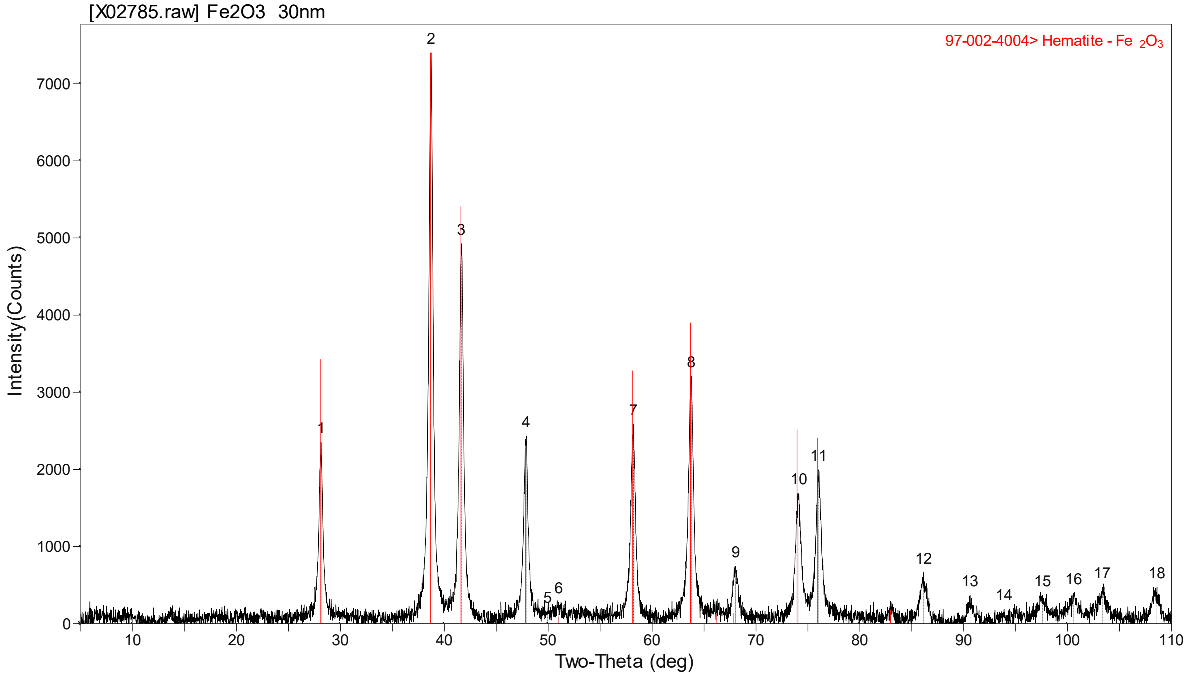

Figure 6.2: X-ray diffraction spectra of the spherical 30 nm hematite nanoparticles. The black line trace shows the observed spectra while the red vertical lines indicate the expected peaks for hematite.

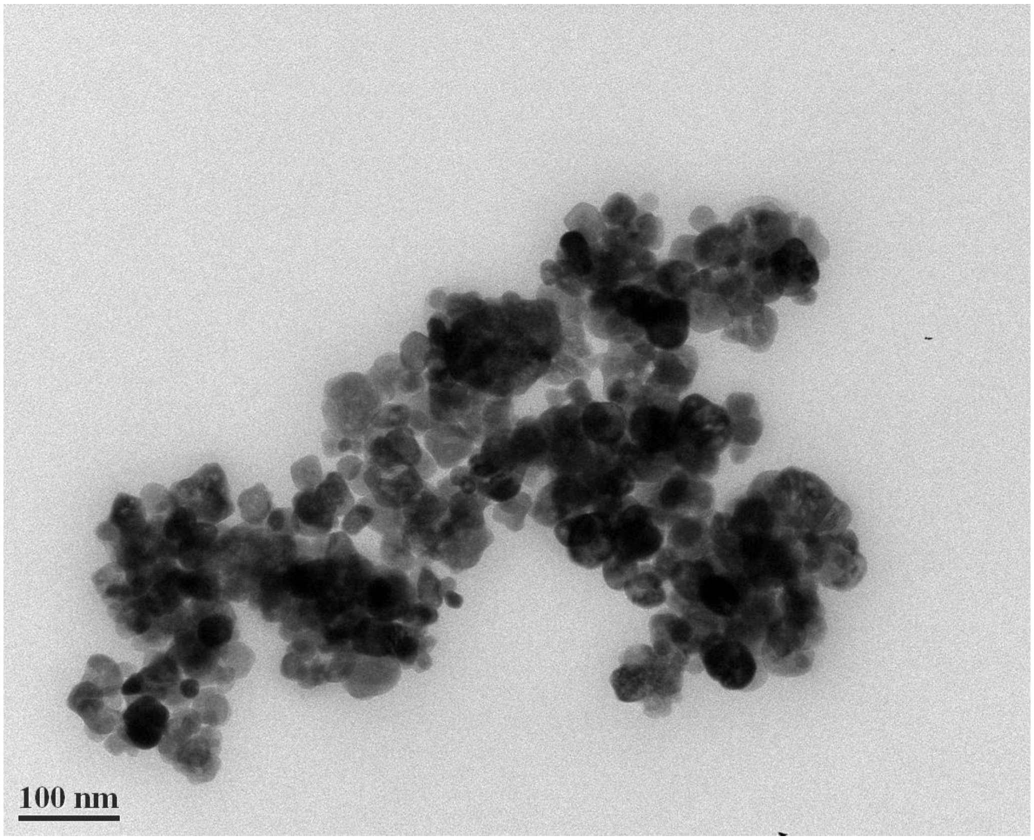

Figure 6.3: TEM photomicrograph of the spherical 30 nm hematite nanoparticles, scale bar 100 nanometers. The observed darker areas are caused by some nanoparticles overlaying one another.

6.2.2 Magnetic Susceptibility and Magnetic Hysteresis

A sample of the 30 nm hematite nanoparticles dilutely dispersed (the sample contained 50.6 mg of nanoparticles, at 0.08% volume concentration) in resin gave a volume magnetic susceptibility of -1.47×10^{-5} SI. Since hematite is widely accepted to be a canted antiferromagnetic mineral at room temperature the diamagnetic value obtained was unusual. It was therefore questioned if the resin was diamagnetic and whether that was dominating the magnetic susceptibility signal. Therefore a sample of the hardened resin matrix was obtained and measured giving a volume magnetic susceptibility value of -1.48×10^{-5} SI. This suggested that the resin was indeed dominating the magnetic susceptibility of the sample.

Therefore an accurate independent volume magnetic susceptibility measurement was made on a 10 ml volume sample containing a larger mass of the 30 nm hematite nanoparticles dispersed in calcium fluoride (the sample contained 231 mg of nanoparticles, at 0.48% volume concentration) using a Bartington MS2B low field sensor. This gave a reading of 0.5×10^{-5} SI. Using the mass of the sample the mass magnetic susceptibility was calculated to be 21×10^{-8} m^3kg^{-1}. This indicated that the hematite nanoparticles were not diamagnetic. A further independent volume magnetic susceptibility measurement was made using a Bartington MS2E probe sensor on a similar sample to that used for the MS2B sensor measurement. The MS2E sensor is slightly less accurate than the MS2B sensor but still gave a positive volume magnetic susceptibility reading of 1.0×10^{-5} SI. This again meant that the nanoparticles themselves were not diamagnetic.

The magnetic hysteresis properties of the spherical 30 nm hematite nanoparticles were also investigated using a Variable Field Translation Balance (VFTB). The VFTB measured the hysteresis curve of the nanoparticles at room temperature (**Figure 6.4**). The curve showed a positive magnetization for positive applied magnetic field strength, which was consistent with the bulk susceptibility measurements of the MS2E and MS2B sensors. The magnetic hysteresis curve therefore also demonstrated that the hematite nanoparticles were not diamagnetic.

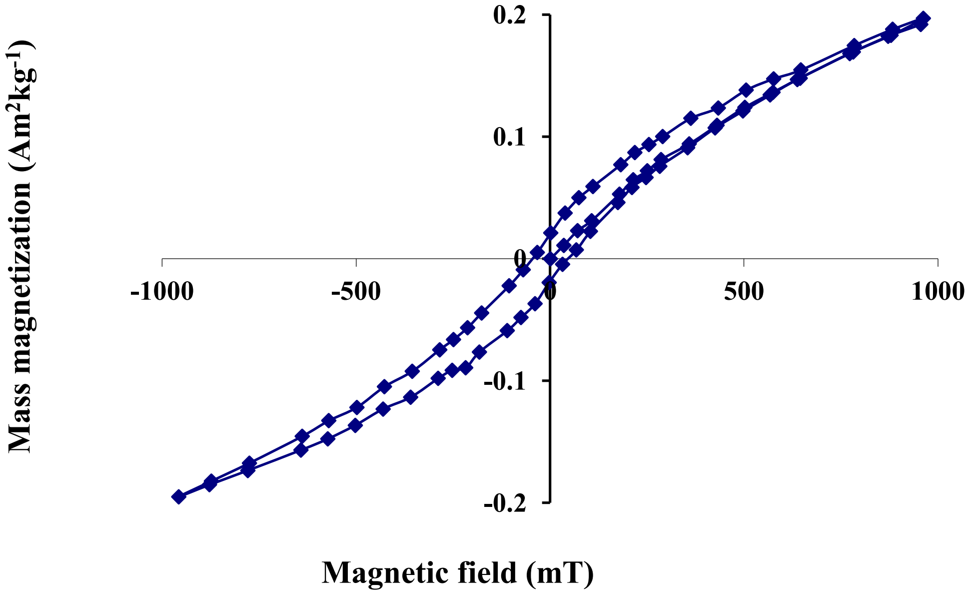

Figure 6.4: Magnetic hysteresis loop of the spherical 30 nm hematite nanoparticles dispersed in calcium fluoride (concentration: 13 wt. %).

In order to further test the magnetic properties of nanosized hematite two more samples were analyzed. In this case the particles were synthesized via the laser ablation method with average sizes of 40 nm for one sample and 8 nm for the other. Their sizes were accurately determined by a Malvern laser particle size analyzer. Both samples were dilutely dispersed (160 mg L^{-1} and 140 mg L^{-1}) in diamagnetic water. As these samples were dilutely dispersed in water the first magnetic hysteresis curve determined was that of the water dispersant by itself (**Figure 6.5**). The water dispersant exhibited a pure diamagnetic signal of a straight line with a negative slope passing through the origin.

The magnetic hysteresis curve of the dilutely dispersed 40 nm hematite nanoparticle sample is shown in **Figure 6.6**. At first glance it resembles the hysteresis curve of the water dispersant (**Figure 6.5**). The diamagnetic response of the water clearly dominates the signal at high applied fields. The significant difference between **Figures 6.5 and 6.6** is the small kink in the hysteresis curve of the 40 nm hematite sample (**Figure 6.6**) that is present at low applied fields. This kink reveals a hysteresis curve with a positive slope at applied fields of up to 70 mT. Such behaviour is not indicative of a diamagnetic material, and is attributed to the 40 nm hematite nanoparticles. This experiment demonstrates how a very dilutely dispersed sample of hematite nanoparticles can at first glance appear to exhibit a diamagnetic behaviour, while in fact the diamagnetic features (seen at applied fields greater than 70 mT in this case) are caused entirely by the diamagnetic dispersant dominating the magnetic signal of the sample. The low applied field curve (seen at applied fields less that 70 mT) on the other hand displayed a positive magnetization to applied field, which is what one would normally expect from hematite.

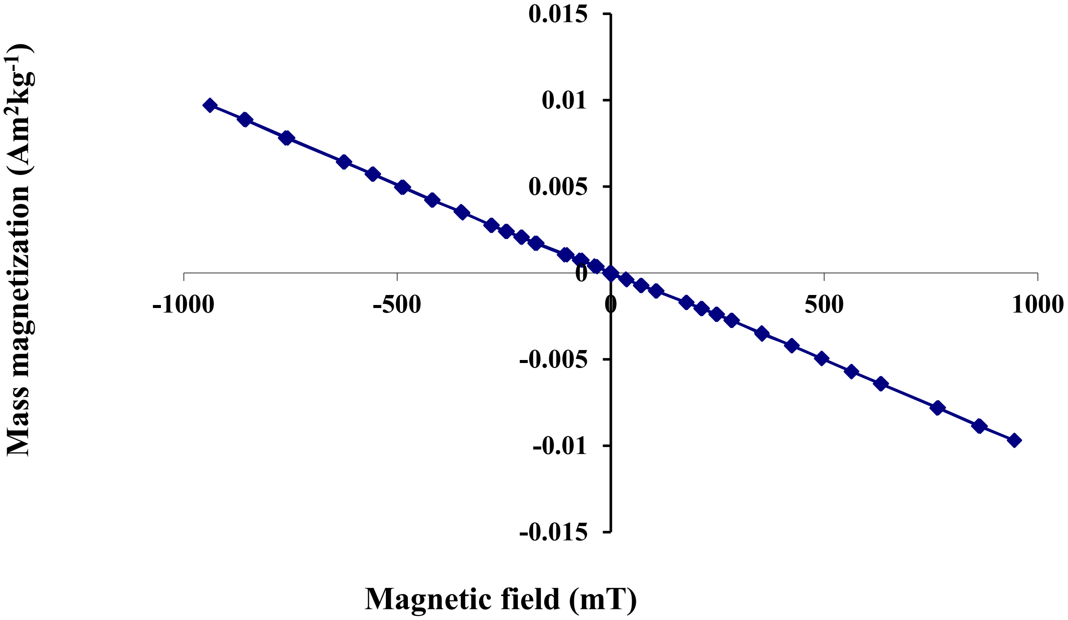

Figure 6.5: Magnetic hysteresis curve of the diamagnetic water that was used as a dispersant for the 40 nm and 8 nm hematite nanoparticle samples.

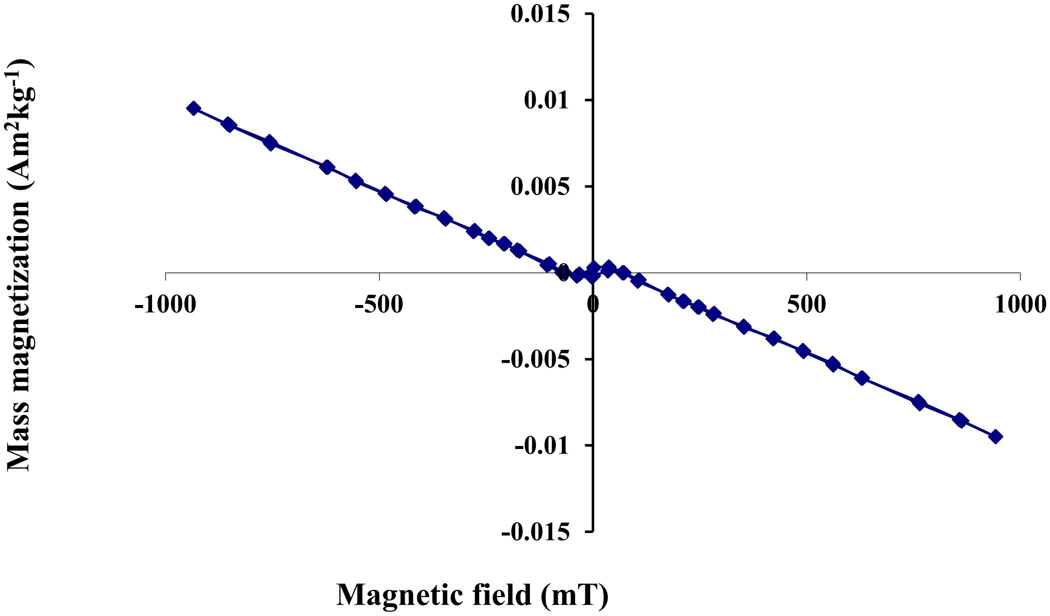

Figure 6.6: Magnetic hysteresis curve of the 40 nm hematite nanoparticles dilutely dispersed in water (concentration: 0.016 wt. %).

In the case of the 8 nm hematite sample (**Figure 6.7**) dilutely dispersed in water the magnetic hysteresis curve was identical to that of the water dispersant (**Figure 6.5**), and thus completely dominated by the diamagnetic signal of the water. The reason for the absence of a kink at low applied fields is not entirely clear. One explanation could be due to the difference in nanoparticle concentrations between the two samples. The concentration of the dilutely dispersed 40 nm hematite sample was 160 mg L^{-1} while the concentration of the 8 nm hematite sample was slightly lower at 140 mg L^{-1}. It is plausible that the lower concentration of hematite in the 8 nm sample results in the magnetic response being completely dominated by the diamagnetic water dispersant. Also the intrinsic magnetic susceptibility of the 8 nm nanoparticles could be lower than that of the 40 nm hematite nanoparticles.

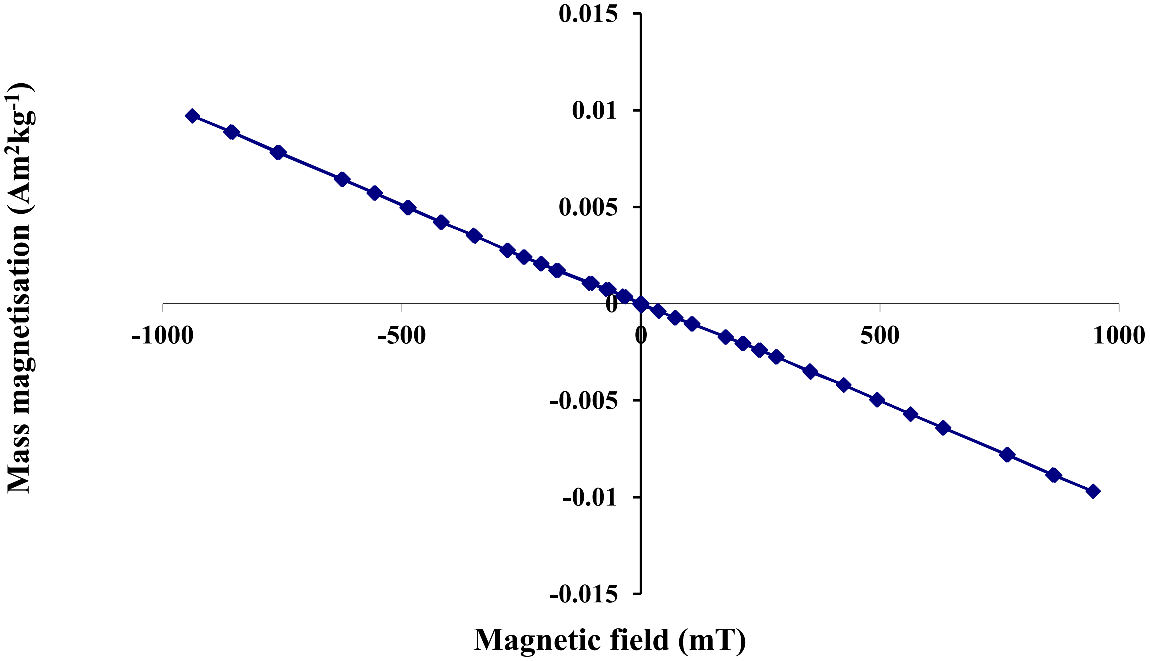

Figure 6.7: Magnetic hysteresis curve of the 8 nm hematite nanoparticles dilutely dispersed in water (concentration: 0.014 wt. %).

All the results therefore suggest that the “diamagnetic” behaviour of hematite that was observed in the 30 nm sample and the Mi et al. (2006) sample were due to the hematite nanoparticles being dilutely dispersed in a diamagnetic dispersant which dominated the overall magnetic signal. Mi et al. (2006) did not identify the type of dispersant that they used for the nanoparticle hematite sample that showed a “diamagnetic” response. Nevertheless the magnetic hysteresis curve which they used as their basis for “diamagnetic” behaviour of nanosized hematite did not display a pure diamagnetic response. It was not a single straight line with a negative slope as one would expect of a pure diamagnetic material (**Figure 6.1**). Instead the curve shows a distinct loop with a change of slope at low applied field strengths. It is therefore suspected that the change of slope might be related to the weak hematite nanoparticle signal. The dominant diamagnetic signal, however, is almost certainly due to a diamagnetic dispersant. It may also be relevant to note that their sample which showed the “diamagnetic” behaviour was the sample that was produced from the lowest concentration (0.01 mol L^{-1}) of ferric nitrate ($Fe(NO_3)_3$).

6.3 Conclusions

After investigating the magnetic behaviour of three different hematite nanoparticle sizes the following conclusions could be drawn:

1. The observed “diamagnetic” behaviour for the 30 nm hematite nanoparticles, as well as those reported by Mi et al. (2006), was very likely due to a diamagnetic dispersant dominating the magnetic signal of the dispersion, rather than any intrinsic diamagnetic behaviour of the hematite nanoparticles themselves.
2. The magnetic hysteresis of the dilutely dispersed 40 nm hematite nanoparticles clearly demonstrated how the magnetic signal of a dispersion can be dominated by the diamagnetic dispersant at high applied fields, while still exhibiting a positive magnetic response from the hematite nanoparticles themselves at low applied fields (seen as the kink in the curve at low fields).
3. The hysteresis curve of the 8 nm hematite nanoparticles was entirely dominated by the diamagnetic signal of the water dispersant, which was believed to be due to the lower nanoparticle concentration of the suspension.

4. The high concentration samples containing 30 nm hematite nanoparticles clearly displayed a positive magnetization under all applied field conditions on the hysteresis curve, and showed positive magnetic susceptibility from independent measurements using two other sensors. Those measurements were consistent with the accepted view that hematite is a canted antiferromagnetic mineral at room temperature. The only sample containing 30 nm hematite nanoparticles that gave a "diamagnetic" response was the one where the particles were dilutely dispersed in resin. The diamagnetic resin in this case appears to have dominated the magnetic susceptibility signal.
5. The "diamagnetic" hysteresis curve reported by Mi et al. (2006) was not consistent with pure diamagnetic behaviour as it clearly displayed the presence of a hysteresis loop with a change of slope at low applied fields.

6.4 References

- Bando, Y., Kiyama, M., Yamamoto, N., Takada, T., Sjinjo, T., and Takaki, H., 1965. Magnetic properties of α-Fe_2O_3 fine particles. Journal of the Physical Society of Japan, **20**, 2086.
- Banerjee, S. K., 1971. New grain size limits for palaeomagnetic stability in hematite. Nature Physical Science, **232**, 15-16.
- Dunlop, D. J., and Özdemir, Ö., 1997. Rock Magnetism. Cambridge University Press, 565 pp.
- Mi, Y., Zhang, X., Luo, J., Zhou, S., Zhang, H., Cheng, J. and Liu, F., 2006. Hydrothermal fabrication of spindle-type α-Fe2O3 nanoparticle and its magnetic property. Proceedings of the 1st IEEE International Conference on Nano/Micro Engineered and Molecular Systems, Zhuhai, 519-522.
- Özdemir, Ö., Dunlop, D. J., and Berquó, T.S., 2008. Morin transition in hematite: size dependence and thermal hysteresis. Geochemistry, Geophysics, Geosystems, **9**, 1-12.

Chapter 7

CONCLUSIONS AND RECOMMENDATIONS

7.1 Conclusions

The main focus of this thesis was to investigate the potential of magnetic nanoparticles as contrast agent tracers for reservoir applications. One specific application was focused on, that of monitoring the progression of waterflooding of heavy oil in real time from the magnetic susceptibility signal of a suspension of the dispersed magnetic nanoparticles. The following main conclusions were drawn from the results of the experiments:

1. The SEM and TEM microscopy confirmed the particle sizes of the individual nanoparticles of each composition, but also revealed the formation of nanoparticle agglomerates and the subsequent need to disperse the nanoparticles if they were to be used successfully as magnetic contrast agents.
2. The room temperature magnetic characterization of the nanoparticles revealed that three of the nanoparticle compositions (20 nm magnetite, 20 nm maghemite and 30 nm nickel ferrite) exhibited superparamagnetic behaviour and high magnetic susceptibilities. The 40 nm cobalt ferrite nanoparticles, on the other hand, exhibited stable single domain behaviour with a significantly lower magnetic susceptibility.
3. The 20 nm maghemite nanoparticles displayed the most stable behaviour from room temperature to reservoir temperatures when dispersed in different types of matrix. There was little difference in the magnetic susceptibility heating and cooling curves in every case. On the basis of their high magnetic susceptibility and stable behaviour at reservoir temperatures the maghemite nanoparticles were chosen as the most favourable candidate as a magnetic contrast agent tracer for the waterflood experiments.
4. The stability experiments were able to produce a stable suspension of dispersed maghemite nanoparticles in deionized water with the use of sodium dodecylbenzenesulfonate (DDBS) surfactant (confirming previous work by Khan, 2012a, and Khan et al., 2015). They also confirmed a previous study (Khan, 2012b) that

suspensions which had high ionic strength would lead to the formation of nanoparticle agglomerates that would settle and destabilize the dispersion.

5. In waterflood 1 both monitoring methods (magnetic susceptibility and CT scanning) were not very effective at tracking the progression of the waterflooding process in real time. Whilst the magnetic scans were able to distinguish small changes in the injected nanoparticle content over the two days, the results were hindered by the instability of the nano-fluid and the presence of a large background magnetic susceptibility signal from the metal end fittings. The CT scanner was only able to detect minor changes during the waterflooding process.
6. The magnetic susceptibility scans in waterflood 2 showed the formation, growth and movement of a magnetic susceptibility peak, which was consistent with the collection of maghemite nanoparticles at the main water-heavy oil interface(s). The results suggest that the magnetic technique can provide a quantitative means to track the progression of the water-heavy oil waterflood in real time. Furthermore, the shape of the magnetic susceptibility scans collected after the main water-heavy oil interface(s) had passed through the production end of the sandpack were relatively consistent and reflected the porosity profile of the sandpack. This suggested that the magnetic susceptibility scans collected after the passing of the main water-heavy oil interface(s) can be used to quantitatively measure the water saturation of the sandpack. The CT scans, on the other hand, did not show any clear water-heavy oil contrast during the nano-fluid injection. The reason was most likely due to the low CT contrast between the nano-fluid and the heavy oil.
7. To understand the potential effect on reservoir quality (in terms of degrading the permeability) of any retained nanoparticles two previous reservoir case studies were first examined. New core plug measurements for one of the reservoirs demonstrated how small concentrations of hematite nanoparticles (above about 0.16%) could significantly reduce the permeability. Also, calculations were made of the retained maghemite nanoparticles after water-flushing the nano-fluid from glass bead or sandpacks using data from experiments by Khan (2012a). The percentage volume concentrations (of the solids only) of the retained nanoparticles were calculated to be between 2.43 x 10^{-4} % and 4.59 x 10^{-3} %. It was concluded that water-flushing could remove sufficient nanoparticles so

as not to pose a significant threat of degrading the porous media used in Khan's (2012a) experiments.

8. Apparent "diamagnetic" behaviour observed in some nanoparticle hematite samples (one of the samples studied in this thesis, and a sample studied by Mi et al., 2006) was examined. The experimental analysis showed that hematite nanoparticles were not in fact diamagnetic, but had a positive magnetic susceptibility response. The cases where they appeared to behave "diamagnetically" arose from the magnetic signal being dominated by the diamagnetic dispersing matrix, which overwhelmed the weak canted antiferromagnetic signal from the hematite nanoparticles.

7.2 Recommendations

The recommendations for future studies are as follows:

1. Further maghemite nanoparticle stability experiments should be conducted to test the stability of the dispersed nanoparticle suspensions over time intervals of months required in a real reservoir rather than days. The procedure should also be modified to produce the large quantity of nano-fluid required for an actual hydrocarbon reservoir waterflood.
2. More waterflood experiments should be conducted, which would include examining nanoparticle retention by conducting a water-flush to remove as many of the nanoparticles as possible. If possible the waterfloods should be conducted at a higher temperature to better represent real reservoir conditions. Experiments simulating other types of reservoirs could also be undertaken. The permeability before and after the waterfloods could be measured and compared to see if the retained nanoparticles have any effect.
3. Although enhanced oil recovery (EOR) was not the main goal of this thesis many studies have indicated that nanoparticles have potential in improving the oil recovery of a reservoir. A study should be devised such that the nanoparticles in the nano-fluid used would not only act as a tracer but would also improve the oil recovery during the waterflooding process. This dual functionality could potentially be very cost effective.

4. Once the above experiments have been conducted with satisfactory results a small scale field study could be designed. The study should test the waterflooding potential of the nano-fluid in real reservoir conditions by injecting them through an injection well and then collecting them at a production well. Ideally there should be some monitoring wells for magnetic data collection between the injection and production wells.
5. New stabilizing procedures would need to be devised for magnetite and nickel ferrite nanoparticles if they are to be used for waterflooding, as the one devised was specifically for maghemite nanoparticles.
6. The 40 nm cobalt ferrite nanoparticles proved to be unsuitable as magnetic contrast agents for hydrocarbon reservoir applications due to their lower magnetic susceptibilities. This is believed to be due to their stable single domain behaviour. If smaller cobalt ferrite nanoparticles were synthesized such that they behaved superparamagnetically they could be revaluated. This would be beneficial as the cobalt ferrite nanoparticles appeared to be relatively stable during the reservoir temperature experiments showing little to no chemical changes when heated and cooled.

7.3 References

- Khan, M. M., 2012b. A laboratory study of the effect of ionic strength on the stability of nanoparticle suspensions using a magnetic technique. M. Eng. report, University of Alberta, Department of Civil and Environmental Engineering, Edmonton, Canada, 25 pp.
- Khan, S., 2012a. A laboratory study of the stability and flow of nanoparticle suspensions through porous media using magnetic techniques. M.S. thesis, University of Alberta, Department of Civil and Environmental Engineering, Edmonton, Canada, 147 pp.
- Khan, S., Potter, D. K., and Kuru, E., 2015. Quantifying the transport of superparamagnetic nanoparticles in porous media using an acrylic flow cell and integrated magnetic susceptibility sensor technique. Transport in Porous Media, **106**, 691-705.
- Mi, Y., Zhang, X., Luo, J., Zhou, S., Zhang, H., Cheng, J. and Liu, F., 2006. Hydrothermal fabrication of spindle-type α-Fe2O3 nanoparticle and its magnetic

property. Proceedings of the 1st IEEE International Conference on Nano/Micro Engineered and Molecular Systems, Zhuhai, 519-522.

BIBLIOGRAPHY

- Abrams A., SPE-AIME and Shell Development Co., 1977. Mud Design to Minimize Rock Impairment Due to Particle Invasion. Journal of Petroleum Technology, **29**, 586-592.
- Argyle, K. S., and Dunlop, D. J., 1984. Theoretical domain structure in multidomain magnetite particles. Geophysical Research Letters, **95**, 7069-7083.
- Auge, A., Weddemann, A., Vogel, D., Wittbracht, F., and Hutten, A., 2010. A level set base approach for modeling oxidation processes of ligand stabilized metallic nanoparticles. Applied Physics Letters, **96**, ID093111, 3 pp.
- Bando, Y., Kiyama, M., Yamamoto, N., Takada, T., Sjinjo, T., and Takaki, H., 1965. Magnetic properties of α-Fe_2O_3 fine particles. Journal of the Physical Society of Japan, **20**, 2086.
- Banerjee, S. K., 1971. New grain size limits for palaeomagnetic stability in hematite. Nature Physical Science, **232**, 15-16.
- Barron, A. R., Tour, J. M., Busnaina, A. A., Jung, Y. J., Somu, S., Kanj, M. Y., Potter, D. K., Resasco, D., and Ullo, J., 2010. Big things in small packages. Oilfield Review, Schlumberger, **22**, 38-49.
- Bennion, B. D., Thomas, B. F., Crowell, E. C., amd Freeman B., 1995. Applications for tracers in reservoir conformance predictions and initial saturation determinations. Annual International Conference on Reservoir Conformance, Profile Control Water and Gas Shutoff, Houston, 14 pp.
- Butler, R. F., 1992. Paleomagnetism, magnetic domains to geologic terranes. Blackwell Scientific Publications, 319 pp.
- Butler, R. F., and Banerjee, S. K., 1975. Theoretical single-domain grain-size rangein magnetite and titanomagnetite. Journal of Geophysical Research, **80**, 4049-4058.
- Caldelas, F. M., 2010. Experimental parameter analysis of the nanoparticle retention in porous media. M.S. thesis, University of Texas at Austin, Austin, USA, 145 pp.
- Chinnasamy, C. N., Jeyadevan, B., Shinoda, K., Djayaprawira, D. J., Takahashi, M., Joseyphus, R. J., and Narayanasamy, A., 2003. Unusually high coercivity and critical

singe-domain size of nearly monodisperesed $CoFe_2O_4$ nanoparticles. Applied Physics Letters, **83**, 2862-2864.

- Da Costa e Silva, A. 1995. Analysis of viscous fingering reproducibility in consolidated natural porous media. Society of Core Analysts conference, Paper Number 9504, 1–10.
- Dunlop, D. J., 1973. Superparamagnetic and single-domain threshold sizes in magnetite. Journal of Geophysical Research, **78**, 1780-1793.
- Dunlop. D. J., 1974. Thermal enhancement of magnetic susceptibility. Journal of Geophysiscs, **40**, 439-451.
- Dunlop, D. J., and Bina, M-M. 1977. The coercive force spectrum of magnetite at high temperatures: evidence for thermal activation below blocking temperature. Geophysical Journal International, **51**, 121-147.
- Dunlop, D. J., and Özdemir, Ö., 1997. Rock Magnetism. Cambridge University Press, 565 pp.
- French, R. A., Jacobson, A. R., Kim, B., Isley, S. L., Penn, R. L., and Baveye P. C., 2009. Influence of ionic strength, pH and cation valence on aggregation kinetics of titanium dioxide nanoparticles. Environmental Science and Technology, **43**, 1354-1359.
- Ghazanfari, M. R., Kashefi, M., Shams, S. F., and Jaafari, M. R., 2016. Perspective of Fe_3O_4 nanoparticles role in biomedical applications. Biochemistry Research International, **2016**, Article ID 7840161, 32 pp.
- Halbreich, A., Roger, J., Pons, J. N., Geldwerth, D., Da Silva, M. F., Roudier, M., and Bacri, J. C., 1998. Biomedical applications of maghemite ferrofluid. Biochimie, **80**, 5-6, 379-390.
- Hong S. J., Pyun J., Park W. Y., Kim S. C. and Shim I., 2009. Oxidation Effect in Cobalt Nanoparticles Magnetic Fluids, IEEE Transactions on Magnetics, **45**, 2464-2466.
- Hunt, C. P., Moskowitz, B. M., and Banerjee, S. K., 1995. Magnetic properties of rocks and minerals. In: Thomas J. Ahrens (ed.) Rock Physics and Phase Relations: a Handbook of Physical Constants, AGU reference shelf 3, 189-204.
- Ivakhenko, O. P., 2006. Magnetic analysis of petroleum reservoir fluids, matrix mineral assemblages and fluid-rock interactions. Ph.D. thesis, Heriot-Watt University, Institute of Petroleum Engineering, Edinburgh, UK, 210 pp.

- Ivakhenko, O. P., and Potter, D. K., 2004. Magnetic susceptibility of petroleum reservoir fluids. Physics and Chemistry of the Earth, **29**, 899-907.
- Jamaloei, B. Y., Babolmorad, R., and Kharrat, R., 2016. Correlations of viscous fingering in heavy oil waterflooding. Fuel, **179**, 97-102.
- Jensen, J., 1999. Fate and effects of linear alkylbenzene sulphonates (LAS) in the terrestrial environment. Science of The Total Environment, **226**, 2-3, 93-111.
- Jiang, J. and Yang, Y-M., 2007. Facile synthesisof nanocrystalline spinel $NiFe_2O_4$ via a novel soft chemistry route. Material Letters, **61**, 4276-4279.
- Jingkun, J., Günter, O., and Pratim, B., 2009. Characterization of size, surface charge, and agglomeration state of nanoparticle dispersions for toxicological studies. Journal of Nanoparticle Research, **11**, 79-89.
- Johnson, K., 2010. Advances in nanotechnology hold huge potential promise in upstream applications. The American Oil & Gas Reporter, 113-123.
- Joshi, G. K., Khot, A. Y., and Sawant, S. R., 1986. Magnetization, Curie temperature and Y-K angle studies of Cu substituted and non substituted Ni-Zn mixed ferrites. Solid State Communications, **65**, 1593-1595.
- Kamble, R. B., Varade, V., Ramesh, K. P., and Prasad, V., 2015. Domain size correlated magnetic properties and electrical impedance of size dependent nickel ferrite nanoparicles. AIP Advances, **5**, 017119-1 – 017119-13.
- Khan, M. M., 2012. A laboratory study of the effect of ionic strength on the stability of nanoparticle suspensions using a magnetic technique. M. Eng. report, University of Alberta, Department of Civil and Environmental Engineering, Edmonton, Canada, 25 pp.
- Khan, S., 2012. A laboratory study of the stability and flow of nanoparticle suspensions through porous media using magnetic techniques. M.S. thesis, University of Alberta, Department of Civil and Environmental Engineering, Edmonton, Canada, 147 pp.
- Khan, S., Potter, D. K., and Kuru, E., 2015. Quantifying the transport of superparamagnetic nanoparticles in porous media using an acrylic flow cell and integrated magnetic susceptibility sensor technique. Transport in Porous Media, **106**, 691-705.

- Kothari, N., Raina, B., Chandak, K. B., Iyer, V., and Mahajan, H. P., 2010. Application of ferrofluids for enhanced surfactant flooding in IOR. Society of Petroleum Engineers, SPE EUROPEC/EAGE Annual Confenrece and Exhibition, Barcelona, 14-17.
- Krishnan, K. M., 2010. Biomedical Nanomagnetics: a spin through possibilities in imaging, diagnostics, and therapy. IEEE Transactions on Magnetics, **46**, 2523-2558.
- MacNab, T. K., Fox, R. A., and Boyle, A. J. F., 1968. Some magnetic properties of magnetite (Fe_3O_4) microcrystals. Journal of Applied Physics, **39**, 5703-5711.
- Marinova, K. G., Alargova, R. G., Dencov, N. D., Velev, O. D., Petsev, D. N., Ivanov, I. B., and Borwankar, R. P. 1996. Charging of oil-water interfaces due to spontaneous adsorption of hydroxyl ions. Langmiur, **12**, 2045-2051.
- Mi, Y., Zhang, X., Luo, J., Zhou, S., Zhang, H., Cheng, J. and Liu, F., 2006. Hydrothermal fabrication of spindle-type α-Fe2O3 nanoparticle and its magnetic property. Proceedings of the 1st IEEE International Conference on Nano/Micro Engineered and Molecular Systems, Zhuhai, 519-522.
- Morrish, A. H., and Yu, S. P., 1955. Dependance of the coercive force on the density of some iron oxide powders. Journal of Applied Physics, **26**, 1049-1055.
- Morrow, L., Potter, D. K., and Barron, A. R., 2015. Detection of magnetic nanoparticles against proppant and shale reservoir rocks. Journal of Experimental Nanoscience, **10**, 1028-1041.
- Murphy, M. J., 2012. Experimental analysis of electrostatic and hydrodynamic forces affecting nanoparticle retention in porous media. M.S. thesis, University of Texas at Austin, Austin, USA, 153 pp.
- Negin, C., Ali, S., and Xie, Q., 2016. Application of nanotechnology for enhancing oil recovery – A review. Petroleum, **2**, 324-333.
- Nordin, M., and Frankel, V. H., 2001. Basic biomechnics of the musculoskeletal system. Lippincott Williams and Wilkins, 467 pp.
- Ogolo, N. A., Olafuyi, O. A., and Onyekonwu, M. O., 2012. Enhanced oil recovery using nanoparticles. Society of Petroleum Engineers, SPE Saudi Arabia Section Technical Symposium and Exhibition, Al-Khobar, 9 p.

- Onyekonwu, M. O., and Ogolo, N. A., 2010. Investigating the use of nanoparticles in enhancing oil recovery. Society of Petroleum Engineers, Nigeria Annual International Conference and Exhibition, Tinapa-Calabar, 14 pp.
- Özdemir, Ö., Dunlop, D. J., and Berquó, T.S., 2008. Morin transition in hematite: size dependence and thermal hysteresis. Geochemistry, Geophysics, Geosystems, **9**, 1-12.
- Paulsen, J. A., Lo, C. C. H., Snyder, J. E., Ring, P., Jones, L. L., and Jiles, D. C., 2003. Study of the curie temperature of cobalt ferrite based composites for stress sensor applications. IEEE Transactions on Magnetics, **39**, 3316-3318.
- Ponmani, S., Nagarajan, R., and Sandwai, J., 2013. Applications of nanotechnology for upstream oil and gas industry. Journal of Nano Research, **24**, 7-15.
- Potter, D. K., 2005. Magnetic susceptibility as rapid non-destructive technique for improved RCAL and SCAL parameter prediction. Proceedings of the International Symposium of the Society of Core Analysts, Toronto, Canada. Paper SCA2005-02 (12 pages).
- Potter, D. K., 2007. Magnetic susceptibility as rapid, non-destructive technique for improved petrophysical parameter prediction. Petrophysics, **48**, 191-201.
- Potter, D. K., Ali, A., and Ivakhenko, O. P., 2009. Quantifying the relative roles of illite and hematite on permeability in red and white sandstones using low and high field magnetic susceptibility. Proceedings of the International Symposium of the Society of Core Analysts, Noordwijk, Netherlands. Paper SCA2009-11 (12 pages).
- Potter, D. K., Corbett, P. W. M., Barclay, S. A., and Haszeldine, R. S., 2004. Quantification of illite content in sedimentary rocks using magnetic susceptibility – a rapid complement or alternative to X-ray diffraction. Journal of Sedimentary Research, Research Methods Papers Section, **74**, 730-735.
- Prigiobbe, V., Ko, S., Huh, C., and Bryant, S. L., 2015. Measuring and modeling the magnetic settling of superparamagnetic nanoparticle dispersions. Journal of Colloid and Interface Science, **447**, 58-67.
- Richardson, S. 2005. Bleaching and diagenesis affecting reservoir quality in the upper Slochteren (ROLSU), Lauwerszee trough, the Netherlands. Summer intern student, The

University of Durham, England. Internship at NAM (Nederlandse Aardolie Maatschappij) building in Assen.

- Roger, J., Pons, J. N., Massart, R., and Halbreich A., 1999. Some biomefical applications of ferrofluids. The European Physical Journal Applied Physics, **5**, 321-325.
- Rong, C., Li, D., Nandwana, V., Poudyal, N., Ding, Y., Wang, Z. L., Zeng, H., and Liu, J. P., 2006. Size-dependant chemical and magnetic ordering in $L1_0$-FePt nanoparticles. Advanced Materials, **18**, 2984-2988.
- Schubert, H., 1981. Principles of agglomeration. International Chemical Engineering, **21**, 363-377.
- Stauch, C., Spath, S., Ballweg, T., Luxenhofer, R., and Mandel, K., 2017. Nanostructured micro-raspberries from superparamagnetic iron oxide nanoparticles: studying agglomeration degree and redispersibility of nanoparticulate powders via magnetization measurements. Journal of Colloid and Interface Science, **505**, 605-614.
- Thompson, R., and Oldfield, F., 1986. Environmental Magnetism. Allen and Unwin, London, 243 pp.
- Yu, H., 2012. Transport and retention of surface-modified nanoparticles in sedimentary rocks. Ph.D. thesis, University of Texas at Austin, Austin, USA, 257 pp.
- Zhang, T., Murphy, M. J., Yu, H., Bagaria. H. G., Yoon, K. Y., Neilson, B. M., Bielawski, C. W., Johnston, K. P., Huh, C., and Bryant, S. L., 2015. Investigation of nanoparticle adsorption during transport in porous media. Society of Petroleum Engineers, SPE Annual Technical Conference and Exhibition, New Orleans, 667-677.
- Zhang, T., Murphy, M., Yu, H., Huh, C., and Bryant, S. L., 2016. Mechanic model for nanoparticle retention in porous media. Transport in Porous Media, **115**, 387-406.